ABSTRACT

SMITH, ERICK MARTIN. SAR Imaging Through the Earth's Ionosphere. (Under the direction of Semyon Tsynkov.)

Imaging of the Earth's surface by spaceborne synthetic aperture radars (SAR) may be adversely affected by the ionosphere, as the temporal dispersion of radio waves gives rise to distortions of signals emitted and received by the radar antenna. Those distortions lead to a mismatch between the actual received signal and its assumed form used in the signal processing algorithm (known as the matched filter). In turn, the discrepancy between the filter and the signal causes a deterioration of the image.

In this dissertation, we conduct a thorough mathematical analysis of transionospheric SAR imaging, and accurately quantify the distortions of images due to the ionosphere. In doing so, we model the ionosphere as a dilute cold plasma. Then, to mitigate the ionospheric distortions of SAR images, we propose to probe the terrain, and hence the ionosphere, on two distinct carrier frequencies. The resulting two images appear shifted with respect to one another, and the magnitude of the shift allows one to evaluate the total electron content (TEC) in the ionosphere. Knowing the TEC, one can correct the matched filter, and hence improve the quality of the image. Robustness of the proposed approach can subsequently be improved by applying an area-based image registration technique to the two images obtained on two frequencies. The latter enables a very accurate evaluation of the shift, which, in turn, translates into a very accurate estimate of the TEC.

We also analyze a host of additional factors that affect the spaceborne SAR performance. Those include the Ohm conductivity of the ionosphere, which is due to the collisions of electrons with other particles, the horizontal variation of the ionospheric parameters, and the random fluctuations of the electron number density, i.e., the ionospheric turbulence. The effect of the latter on the SAR resolution is evaluated in the statistical sense.

Finally, we devote special attention to anisotropic phenomena. The ionospheric plasma becomes anisotropic (gyrotropic) due to the magnetic field of the Earth. The propagation of radio waves in a gyrotropic medium is accompanied by the Faraday rotation. For spaceborne SAR, the Faraday rotation presents an additional source of mismatch between the received signal and the filter, and hence causes additional image distortions. We propose to use the image autocorrelation analysis to quantify the impact of the Faraday rotation and obtain its parameters, which then allows us to correct the filter accordingly.

Scattering of radar signals at the target may also be affected by anisotropy. We interpret the target as a weakly conductive birefringent dielectric, and derive a necessary and sufficient condition under which this model allows one to reconstruct all the degrees of freedom in the

scattered signal that the previous studies in the literature have introduced phenomenologically. This development can help construct a full-fledged radar ambiguity theory for polarimetric SAR imaging, i.e., the type of imaging that exploits individual polarizations of the transmitted and received signals.

This dissertation is based on four journal articles published or submitted for publication between 2011 and 2013. Although every effort has been made to streamline the overall presentation, unify the notations and cross-references, and remove the redundancies, still the structure and content of individual chapters may inherit the style of those journal publications whence they originate.

SAR Imaging Through the Earth's Ionosphere

by
Erick Martin Smith

A dissertation submitted to the Graduate Faculty of
North Carolina State University
in partial fulfillment of the
requirements for the Degree of
Doctor of Philosophy

Applied Mathematics

Raleigh, North Carolina

2013

APPROVED BY:

Mansoor Haider	Mark Hoefer
Ralph Smith	Semyon Tsynkov Chair of Advisory Committee

DEDICATION

To my parents, for always encouraging and believing in me.

BIOGRAPHY

The author graduated summa cum laude from the University of Tennessee, Knoxville with a bachelor of science in mathematics (honors) and physics. He was born in Knoxville, Tennessee, raised around the suburb of Farragut, and lived there until moving to North Carolina to pursue his graduate studies, where he received a masters of science in applied mathematics while in pursuit of a doctoral degree in the same subject.

He has loved math ever since he was small and remembers a particular time in the first grade when, during a lesson on subtraction, he corrected his teacher when she stated that one can only subtract smaller numbers from larger ones. He was unaware that he was not supposed to know about negative numbers at that point! Besides mathematics, he has always had a keen interest in many branches of science and gaining knowledge. In fact, his friends might claim that he knows at least a little something about everything (except for music, sports, and popular culture). He appreciates his Creator's handiwork everywhere in nature and loves to spend time enjoying the outdoors on hikes or just quietly learning and observing the surrounding natural wonders. Animals also bring much joy and amusement to his life. He loves living in the southeastern United States but is additionally fond of the summertime in Wyoming, which he got to experience during a research internship in astronomy in 2005. He would have a hard time living in a place where nature was not easily accessible such as a large city and generally tries to avoid areas with high population densities.

The author enjoys being challenged and working hard but also knows the value in a quiet, simple life and that it is crucial to have balance; one's career is important, but it is not all there is in life. It is vital to take the time and effort to be able to step away from everything and enjoy other things. Still, his professional interests besides the topic of this dissertation include physics based problems with a heavy mathematical emphasis, especially when the work is more analytical than numerical in nature. Although naturally curious about the world around him, the motivation for his endeavors additionally comes from knowing that he is working with a purpose and that his results will be helpful to others in some way.

ACKNOWLEDGEMENTS

I first want to thank my advisor, Dr. Semyon Tsynkov for giving me the opportunity to work for him over these past few years and for being patient and understanding with me whenever I had problems. His constant guidance and encouragement was invaluable. I also appreciate him going above and beyond when it came to funding me overall but also during times when he could have easily not.

I also want to thank Dr. Mikhail Gilman for spending so much time helping me over the course of the research ever since I first met him. He was like a second, unofficial advisor, and his knowledge of the subject was immensely helpful. I do not think nearly as much would have gotten done without his help.

Without the abundant help I received from my main undergraduate advisor, Dr. Conrad Plaut, I know I would not be where I am today. Although my years as an undergraduate were what I consider to be the worst time in my life, he definitely made it better. I will always be grateful for his guidance along with the assistance during the countless hours I spent struggling during his office hours and for bringing the very existence of NC State to my attention.

My high school precalculus / calculus 1 & 2 teacher, Mr. John Beckett also deserves mention. His enthusiasm for making sure his students understood and appreciated math as well as him giving me the privilege of being the only student in the history of his teaching career to earn a 6 out of 5 on a homework problem inspired me to push myself to fulfill my potential.

I want to thank the people of the Over the Horizon Radar group at the United States Naval Research Laboratory in Washington, D.C. for allowing me to work there and gain valuable experience during the summer of 2011.

Denise Seabrooks deserves a special mention for all the work she does and especially for helping me over the years here at NC State and always answering my questions. I also want to thank Carolyn Gunton for all the assistance she provided me, especially towards the end.

Dr. Stephen Campbell and Dr. Ernest Stitzinger have helped me numerous times over my graduate career, especially one particular time when things looked bleak.

The input and advice from my committee members, Dr. Mansoor Haider, Dr. Mark Hoefer, and Dr. Ralph Smith is also greatly appreciated.

This work was made possible by support from the United States Air Force Office of Scientific Research through grants No. FA9550-07-0170 and No. FA9550-10-1-0092.

On the personal side of things, my family has always been there for me with love and support. I do not know what more I can say except, “Thank you, and I love you all!”

In the years that I have been involved with it, the math grad student Bible study has been a blessing because I could relate to others on professional, personal, and spiritual levels.

All of the people I have come to know and love through Colonial Baptist Church mean more to me than they will ever know. It had been many years since I had had any close friendships, and the relationships I have formed there have helped me to see what is truly important in life. In particular, I want to recognize Tom and Courtney Wadsworth, Dr. Eli Owens, Nathan Johnson, and Sam Trogdon. There are others I want to acknowledge, as well, but they are too numerous to list. Don Sandberg's leadership, kindness, and unique niche in life is also deserving of a special mention.

Finally, I want to acknowledge my personal Lord and Savior, the Creator and Sustainer of the universe, without Whom I would not even exist. Galileo once said, "Mathematics is the language with which God has written the universe." I am humbled and eternally grateful to be a student of that language.

TABLE OF CONTENTS

LIST OF TABLES

LIST OF FIGURES

Chapter 1

Introduction

Synthetic aperture radar (SAR) is a coherent imaging technology that uses microwave electromagnetic pulses primarily for imaging the surface of the Earth from airplanes or satellites, but it is also used to image the surfaces of other planets like Venus or even moons like Titan. It is based predominantly on the phase information of the emitted and received waves (as opposed, say, to conventional photography, which is based on the amplitude). In particular, spaceborne SAR imaging of the Earth's surface involves sending specially shaped pulses of radio waves from a satellite to the ground, receiving the scattered response, and processing it by means of a matched filter [Che01, CB09]. In doing so, the received signal can, in some approximate sense, be interpreted as a Fourier transform of the ground reflectivity function,[1] whereas filtering that yields the image is analogous to the inverse transform. The filter is called matched because its phase is supposed to match that of the received signal.

However, when the signal of a spaceborne radar travels between the satellite and the ground, it becomes subject to the temporal dispersion in the Earth's ionosphere [Gin64]. This causes delays in arrival times and advances in the phases of the waves; the dispersion distorts the signal, and if the filter does not account for that, a mismatch of the phase occurs and the quality of the image deteriorates [Tsy09a]. The extent of deterioration depends on the carrier frequency of the radar, or more precisely, on its ratio to the Langmuir frequency of the ionospheric plasma. The higher the carrier frequency the less prone the image to ionospheric distortions, requiring less processing of the data received. Also, higher frequencies correspond to shorter wavelengths, so the physical size of the system itself can be smaller than one operating with longer wavelengths. Therefore, many modern spaceborne SAR sensors operate on the frequencies of around $10\,GHz$. For example, the European satellite TerraSAR-X operates in the X-band, on the frequency of $9.65\,GHz$.

[1] In the simplest formulation [Che01], the ground reflectivity function is the difference between the reciprocal of the square of the speed of light and the reciprocal of the square of the local propagation speed.

Nonetheless, radars operating on lower carrier frequencies, in particular, in the UHF or even VHF band, i.e., in the range of hundreds of megahertz (also referred to as the P-band [Par02]), have at least one key advantage, which is a better surface/foliage penetrating capability. At the same time, their images are much more sensitive to ionospheric distortions. Hence, an effort is justified aimed at correcting the matched filter and reducing or removing those distortions. That brings us to the work presented in this dissertation, as well as in the preceding paper [Tsy09a].[2]

We also emphasize that the matched filter must be corrected precisely for the time and place the image is taken. The reason is that the extent of correction will depend on the current state of the ionosphere, and the Earth's ionosphere is not steady. Its characteristics such as the total electron content depend on many factors, e.g., time of the day, time of the year, geographic location, level of Solar activity, etc., and may change rapidly, namely, considerably faster than the period of one revolution of the satellite around the Earth.

Remark. This dissertation stems from three published journal papers: [ST11], [GST12], and [GST13a], and another paper [GST13b] that has recently been submitted for publication. Although every effort has been made to streamline the overall presentation, unify the notations and cross-references, and remove the redundancies, still the structure and content of individual chapters may inherit the style of those journal publications upon which they are based.

1.1 Trans-ionospheric SAR fundamentals

In [Tsy09a], the author analyzed the distortions for the case of SAR imaging by means of a scalar field (in the form of linear upchirps) that propagates through the inhomogeneous ionosphere modeled as weakly dispersive dilute cold plasma. The transverse electric field in such a medium is governed by the Klein-Gordon equation (dispersive wave equation), see formula (2.8). The scattering at the target in [Tsy09a] was considered in the framework of the first Born approximation. The latter enables linearization and thus makes the inverse problem of reconstructing the target properties (i.e., the ground reflectivity function) from the observable quantities amenable to solution. Continuing the work started in that paper, repeating and enhancing the results given in [ST11, GST13a], we begin in Chapter 2 with investigating the distortions of SAR images due to the propagation of radar signals through a dispersive medium.

Our analysis allows for both a homogeneous and an inhomogeneous ionosphere where the inhomogeneity can be vertical and horizontal (as analyzed in [GST13a, Section 3]). We also consider a dissipative ionosphere, i.e., one where Ohmic losses are present. However, these losses attenuate the signal nearly uniformly and have no noticeable effect on the phase, so they are not a major part of this study. Overall, the analysis enables an accurate quantification of the

[2] Some performance criteria for the correction of ionospheric effects in SAR images obtained on low frequencies are discussed in [Mey11].

group delay and phase advance that characterize the propagation, as well as of the changes in the chirp duration and rate. As such, it leads to a precise description of the ionosphere-induced mismatches between the received signal and the matched filter. Those mismatches are shown to be the primary source of image distortions, and the distortions are quantified in terms of how the image resolution, sharpness, and displacement depend on the parameters of the ionospheric plasma, primarily its total electron content (TEC) along the signal trajectory.

This part of the study involves building and analyzing the generalized ambiguity function (GAF) for the radar that takes into account the dispersive propagation in the ionosphere. We note that in Sections 2.2, 2.3, 2.4, 2.5, and later 2.10 (with the addition of another type of distortion, due to turbulence) we basically develop a full-fledged radar ambiguity theory [CB09] for the SAR sensor operating through the Earth's ionosphere (monostatic, scalar case). To the best of our knowledge, prior to [Tsy09a], a mathematical analysis of this type has not been reported in the literature, even though there were a number of publications discussing the effects of the ionosphere on SAR imaging, see, e.g., [GMS00] or [XWW04] (a review). An analysis similar to ours is presented in [IKL$^+$99], however, only for the case of a homogeneous background ionosphere. Knowing what the distortions in the image caused by ionospheric dispersion are is only the first step, though. To improve the image, mismatch between the matched filter and the received data must be removed.

In addition to analyzing the distortions in SAR images caused by the ionosphere, it was also proposed in [Tsy09a] to probe the terrain, and hence the ionosphere, on two distinct carrier frequencies. We expand upon this idea in Section 2.6 and show in Section 2.7 that the resulting two images, while both incorrect per se, can be used to reconstruct the unknown TEC along the line of sight, and the matched filter can be corrected accordingly. Specifically, a given object or feature in the scene will be displaced from its true position if imaged through the ionosphere. Considering the same object or feature imaged on two carrier frequencies, we can write down a system of equations, in which the two observed distances to the object will be the data, and the true distance and the TEC will be the unknowns. Solving for the TEC, we can get it as a function of the shift between the two images. In addition, for a horizontally inhomogeneous ionosphere, this method can be used to reconstruct the first moment of the azimuthal gradient of the electron number density. We correct the matched filter by introducing the actual phase and group travel times, as well as the new chirp rate, computed via the TEC. Then, by reprocessing the raw data with the new filter, we can obtain an improved image. By evaluating and analyzing the new GAF that is built with the help of the corrected filter, we show that the quality of the image indeed becomes better, see [ST11].

It is to be noted that the idea of dual carrier probing for quantifying the ionospheric distortions of satellite radio signals has been used in the GPS community for quite some time. For example, the near-realtime GPS-derived global TEC maps are available on-line at

http://swaciweb.dlr.de. In the literature, work [DS02] discusses general effects of the ionosphere on the satellite to land radio propagation in the UHF and L bands. Work [vdKCT09] exploits the TEC data obtained from GPS-based measurements for evaluating the extent of defocusing in space-based SAR images. Similarly, work [CZ12] exploits the GPS derived TEC data to determine the nature of phase artifacts in interferometric SAR images. The fundamental difference between the GPS and SAR though is that in GPS there is a "sufficiently smart" receiver on the ground that can interpret the data it receives on two frequencies. In SAR, on the other hand, the imaged terrain is assumed completely passive. Moreover, no artificial targets with a priori known characteristics are, generally speaking, available, and the parameters of the ionosphere must be determined from the same data that are used to form the image itself (scattered field received by the antenna on the orbit).

Unlike in GPS, the application of dual carrier probing for quantifying and mitigating the distortions of spaceborne SAR images in the formulation above is new, see [Tsy09a, ST11]. The key consideration is precisely the use of the same (redundant) data for both the image formation and the TEC reconstruction. Indeed, as stated before, if the TEC data are acquired at a different location and/or different time, they may reflect on a different state of the ionosphere and hence appear not particularly helpful for correcting the matched filter to be used for a given image.

Prior to the work in [Tsy09a, ST11], we are aware of only one paper [WQWH03] that briefly touches upon the idea of two frequencies for SAR, and also of an equally brief comment in [CM91, page 381]. The authors of [WQWH03] suggest that the two frequencies can be taken from the available bandwidth but never actually develop the approach beyond mentioning it as a potential strategy for obtaining the TEC. Another group of publications [MBJF06, RHC10, BPE+10, BPE+11] discusses and demonstrates the use of two sub-bands in the context of SAR interferometry. Some of the methods of [MBJF06, RHC10, BPE+10, BPE+11] also utilize the aforementioned difference in the displacement between the two images. The interferometric approach, however, allows one to reconstruct only the differential TEC,[3] although with very high accuracy [BPE+10, BPE+11]. Given the satellite revisit time of several days that characterizes both existing and future SAR systems, and the volatility of the ionosphere, the requirement of having a repeat acquisition makes the acquired information less valuable for many practical applications.

Several alternative approaches to deriving the ionospheric TEC have also been proposed in the literature. Some of them are motivated by the launch of the Japanese Advanced Land Observation Satellite (ALOS) that carries a phased array SAR instrument (PALSAR) operating in the L-band. In [JRZ+09] and [PFC+11], it is proposed to use the Faraday rotation (see Chapter 3) for retrieving the TEC information from the the fully polarimetric quad-channel SAR data, in case the corresponding SAR sensor provides this capability (which ALOS PALSAR

[3] It is the difference between the TEC distributions for two successive data acquisitions.

does, see [LP09, Section 10.4]). The authors of [JRZ$^+$09] also present the estimates of the group delays and phase advances for a non-turbulent ionosphere similar to those obtained in the previous paper in this study [Tsy09a]. An even earlier publication discussing the effect of Faraday rotation on polarimetric SAR is [Gai98]. Of course, if the fully polarimetric data are not available (or, otherwise, if polarimetry puts too high of a demand on storage, downlink capacity, etc.), then the approach based on the Faraday rotation is not going to work. For example, the authors of [WQWH03] also rely on the Faraday rotation for TEC reconstruction (in fact, they consider it the only source of image distortions), but emphasize that for other types of sensors (e.g., single-channel), an explicit a priori estimate of the Faraday rotation is needed for introducing corrections. The authors of [MBJF06] indicate that in the absence of external information one can use autofocus algorithms (see [FL99, Section 3.9.1] or [EJJ89, WEGJJ94]) to obtain the TEC, which is not a very reliable approach though, whereas the SAR system itself (L-band) can be efficient in obtaining the difference of the TEC distributions between the two radar acquisitions. The authors of [LL08] present two approaches; the first one involves a spaceborne radar operating on a very low frequency, below the Langmuir value, and is similar to the traditional ground-based sounding. The second one uses a higher frequency and derives the TEC information by analyzing the returns from the specially chosen bright point targets. The authors of [MG02] employ a model known as the ionospheric phase screen to analyze the effect of auroral arcs (special electron density irregularities) on spaceborne SAR images taken in the polar regions of the Earth. Finally, the authors of [JFSM10] introduce two methods for measuring the ionospheric TEC based on single-polarized data. The first one estimates the TEC from the phase error of the filter mismatch and requires high contrast strong point targets such as corner reflectors within an otherwise dark area; the second one requires two different interrogating waveforms, up and down linear chirps, and estimates the TEC from the path-delay differences between them. We note that none of these papers, see [JRZ$^+$09, Gai98, MBJF06, RHC10, BPE$^+$10, BPE$^+$11, LL08, MG02, JFSM10], provides a comprehensive analysis of how the reconstructed TEC can be used for correcting the filter and subsequently improving the image.

As far as our own work, after demonstrating (as seen in [ST11]) that the filter corrected by dual carrier probing indeed helps improve the image, we proceed in Section 2.8 (as seen in [GST13a]) to analyzing the robustness and accuracy of the TEC reconstruction itself. The goal is to see what happens if the TEC is reconstructed not precisely, but with some error. One of the reasons the TEC reconstruction may be prone to an error is that the formula for the TEC derived in [Tsy09a, ST11] by taking the two distances to a given object as the data appears poorly conditioned with respect to each individual distance. The first obvious remedy is to use several distinct objects instead of just one. In this case, the overall error can be reduced by a factor of $\sqrt{L}$, where L is the number of objects (under a natural assumption that the

values of the TEC computed for individual objects can be interpreted as independent random variables). However, a more promising approach is to use the technique known as area-based image registration [ZF03]. It allows one to superimpose the two shifted images and obtain the shift as an independent quantity that is not related to the distance from the satellite. The accuracy of the modern registration techniques can be as high as a few percent of the resolution pixel, see, e.g., [FZB02, SOCM01, GSTF08, TH86, Abd99].

Thus, we show that if an area-based image registration approach (see, e.g., [KH75, KBP79]) is employed for evaluating the shift, then the robustness, and hence the accuracy of the TEC reconstruction, considerably improves. In Section 2.9, for the phase correlation method, we obtain specific quantitative estimates of how the error in the value of the shift affects the error in the TEC and how the latter, in turn, affects the final quality of the image. Of course, these results withstand a natural "backward compatibility check." If we assume that there is no error in the value of the shift, then there will be no error in the value of the TEC, and eventually all the deterministic distortions of the image will be completely removed, as in [ST11].

Although most of the thesis focuses on the distortions caused by the deterministic part of the ionospheric phenomena, we also look at the distortions of SAR images due to the ionospheric randomness (caused by turbulence). These distortions are related to the fluctuations of the electron number density of the ionosphere and can be quantified reasonably well, see, e.g., [Tsy09a], as well as [QL86, IKL$^+$99, LKI$^+$03, Arm05, GS13]. However, mitigating those distortions requires a substantial additional effort: obtaining the statistics of radio waves based on the statistics of the medium (turbulent ionosphere), see, e.g., [RKT89a, RKT89b, Tat68], and then modifying the signal processing algorithm (the matched filter) accordingly, and even then all of the distortions may still not be mitigated. We investigate the issue of ionospheric turbulence in Section 2.10 and find that it is much more of an issue for the azimuthal (parallel to the flight track) resolution than the range (normal to the flight track) resolution. In fact, the distortions in range are completely removed by correcting the filter for the deterministic errors alone. This "unevenness" between the range and azimuth stems from the performance of a spaceborne SAR in range being practically not affected by the ionospheric turbulence due to the ergodicity of the random field that represents the fluctuations, whereas the performance in azimuth being sensitive to both the deterministic and random component of the electron number density. In the literature, the subject of mitigating the distortions caused by turbulence has not received too much attention; among the relevant publications we mention [BG88, GB88], where the authors propose several approaches to reducing the random component of the phase error.

For the rest of the dissertation, we will assume that the SAR imaging is done in the stripmap mode, and that it is broadside, i.e., that the antenna always points in the direction normal to the orbit, see Figure 1.1. We will also employ the start-stop approximation for our analysis [Che01, Tsy09b]. In Table 1.1, we present the key parameters and their typical values that we

Table 1.1: Typical values of parameters throughout most of this dissertation.

Parameter	**Notation**	**Typical value**	**Reference**
Radar carrier frequency	$\frac{\omega_0}{2\pi}$	$300MHz$	(2.4)
Carrier wavelength	$\lambda_0 = \frac{2\pi c}{\omega_0}$	$1m$	(2.4)
Bandwidth	$\frac{B}{2\pi}$	$8MHz$	(2.18)
Pulse (chirp) duration	τ	$5 \cdot 10^{-5}s$	(2.18)
Pulse repetition frequency	f_{p}	$2KHz$	page 23
Total electron content in the ionosphere	N_H	$5 \cdot 10^{13}cm^{-2}$	(D.8)
Plasma electron (Langmuir) frequency	$\frac{\omega_{\mathrm{pe}}}{2\pi}$	$9MHz$	(2.8)
Collision frequency in the ionosphere	ν_e	$10^5 Hz$	(2.55), (E.1)
Satellite velocity	v_{SAT}	$7.6km/s$	page 23
Length of synthetic aperture	L_{SA}	$50km$	page 24
One-way distance from orbit to target	R	$1000km$	(2.76), Fig. 1.1
Orbit altitude	H	$500km$	Figure 1.1
Incidence angle	$\cos\theta = \frac{H}{R}$	$60°$	Figure 1.1
Registration accuracy, in resolution units	ζ_R, ζ_A	0.05	(2.119), (2.126)
Carrier frequency separation factor	Z	10%	(2.121)
Relative magnitude of fluctuations	M	$5 \cdot 10^{-3}$	(2.11)
Outer scale of ionospheric turbulence	r_0	$1km$ — $10km$	(2.15)
Integral squared mean electron density	$N_{2,H}$	$5 \cdot 10^{19}cm^{-5}$	(2.139)
Magnetic field of the Earth, CGS units	$\lvert\boldsymbol{H}_0\rvert$	0.31 — 0.58 G	(J.4)
Electron cyclotron (Larmor) frequency	$\frac{\lvert\Omega\rvert}{2\pi}$	0.87 — 1.6 MHz	(J.4)

use hereafter (excluding Chapter 4). Note that along with the physical units of the TEC, cm^{-2}, used in Table 1.1, engineering units defined as $1TECU$=$10^{12}cm^{-2}$ can often be found in the literature. We also use the electrostatic CGS units throughout this dissertation.

1.2 Anisotropy as it relates to SAR

In Chapter 2, we deal with inhomogeneity of the mean electron number density, but this is done within an isotropic framework. Namely, the permittivity of the plasma, which is due to the interaction of the impinging electromagnetic field with the electrons, may vary both horizontally and vertically, but may not vary as a function of the local propagation direction. The matched filter in this case is corrected by introducing a total electron content (TEC) over the ray path.

Looking at anisotropy both in the propagating medium and at the target are the logical next steps in adding complexity to the model introduced in the isotropic framework. In Chapter

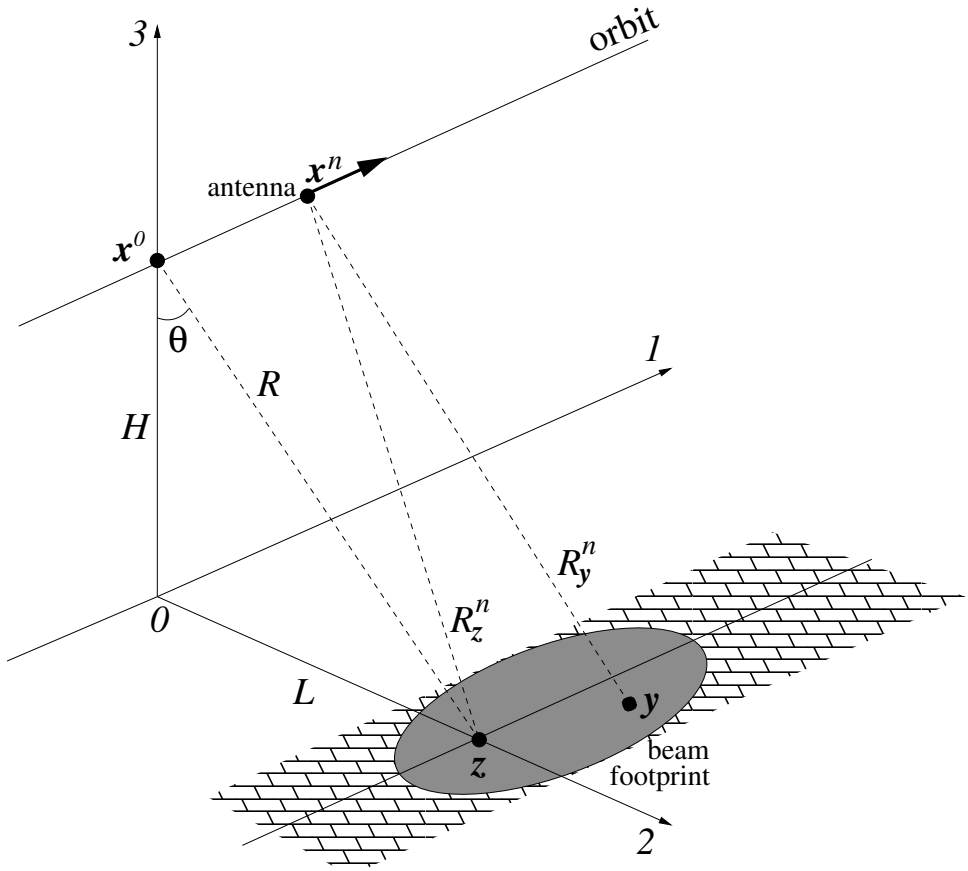

Figure 1.1: Schematic for the broadside stripmap SAR imaging.

3, we study the electromagnetic propagation in a plasma with the presence of a magnetic field, and in Chapter 4 we take into account the anisotropy of the target material. These add new levels of complexity to the model but are significant steps toward improving the interpretation of spaceborne SAR images obtained on the frequencies low enough where the ionosphere is a major issue.

1.2.1 Anisotropic medium — an external magnetic field

Chapter 3 is an extension of the main focal point of the study: the SAR imaging through the ionosphere and construction of the generalized ambiguity function. However, we are no longer ignoring the polarization of the radar pulses. Typical SAR systems emit linearly polarized signals. Knowing that the waves are linearly polarized allows us to consider the anisotropy of the medium in which they propagate. The Earth's magnetic field introduces a significant

anisotropy in the ionosphere (gyrotropy), and therefore it is vital to analyze its effect on the ambiguity theory that is being developed. Analysis of the Faraday rotation,[4] which is the change in a wave's plane of polarization due to propagation in a magnetized plasma, is thus warranted. While it was mentioned in Section 1.1 that others have proposed using it to obtain the TEC [JRZ+09, PFC+11], this capability is limited to the fully polarimetric SAR data. In a single polarization framework though, the Faraday rotation must be accounted for as it has the potential of severely distorting the received signal and hence the image.

Chapter 3 is the first step in this direction. We construct the generalized ambiguity function for single polarization images in the presence of Faraday rotation. As expected, additional parameters dependent on the external magnetic field arise that are not present in the isotropic case. We are able to identify these parameters and show how the effect of Faraday rotation varies along the length of the chirp. As for the GAF, we show that the Faraday rotation only affects the range part; the azimuthal part is identical to that in the isotropic case analyzed in Chapter 2.

Although the Faraday rotation affects the propagation of a chirp, the magnitude of the effect can vary depending on the values of the parameters involved. It can sometimes be difficult to detect the Faraday rotation by a single-polarization instrument. In Chapter 3, we present three possible scenarios as far as how much the rotation affects the chirp, and analyze the one for which the rotation is neither too small nor too large. Within the specifications of this intermediate case, we propose a method to determine the parameters that characterize the Faraday rotation given the image obtained. Once these values are known, a new corrected filter can be constructed to improve the SAR performance in range. These corrections can be applied on top of the corrections derived in Chapter 2, providing compensation of both dispersion and Faraday rotation effects.

1.2.2 Anisotropic target material

Chapter 4 deals with the scattering at the target, which could also be anisotropic, with the focus being on the degrees of freedom in the scattering model. Ultimately, we are able to provide a necessary and sufficient condition under which interpreting the target material as a weakly conductive uniaxial crystal allows one to reconstruct all the degrees of freedom contained in the complex 2×2 Sinclair scattering matrix[5]. As in the previous parts of our study, we are assuming that the scattering is weak, i.e., the scattered field is much smaller than the incident field. This, again, allows us to invoke the first Born approximation, which is a very

[4] The rotation is named after Michael Faraday, a prominent 19th century scientist and pioneer in the field of electromagnetism.

[5] This matrix is widely used to describe the relation between incident and scattered monochromatic waves since the concept was first introduced by George Sinclair in [Sin50].

important simplification, as otherwise the nonlinear inverse problem would be very difficult, if at all possible, to solve [Che01, CB09].

Using the first Born approximation, we start in Section 4.2 with the most basic kind of scatterer: an isotropic dielectric, and slowly add layers of complexity. The next framework we analyze is that of a perfect birefringent dielectric. We restrict ourselves with a uniaxial crystal model because it is the simplest. Following this, we repeat the studies of isotropic and uniaxial scatters but allow them to have a finite conductivity, making them lossy dielectrics. The study of lossy uniaxial dielectrics is broken down further because the conductivity can also be isotropic or anisotropic. Again, we are only considering the uniaxial anisotropy. After adding the final level of complexity, i.e., anisotropic conductivity, we find that all of the degrees of freedom of the Sinclair matrix are recovered.

It turns out though this problem does not have a solution for every combination of possible entries for the scattering matrix. However, we are able to provide a necessary and sufficient condition for the solution to exist and demonstrate that the presence of a "region of nonexistence", so to speak, for the solution is not due to the first Born approximation that we use but rather is an inherent feature of scattering off the target material with the chosen structure.

Furthermore, all these scenarios of increasing complexity assume that the wave is coming from a vacuum and is being scattered off a half-space with certain properties. However, for SAR imaging, the target material is usually considered concentrated only on the surface of the half-space [Che01]. We show in Section 4.3 that the two setups are equivalent in the sense that the reflected fields for both are the same in the first Born approximation.

Modern practical applications of radar polarimetry employ different empirical and semi-empirical criteria that rely on the entries of the Sinclair scattering matrix. Examples include a co-polaraized phase difference-based study of oil spills [MNG09], an algorithm for reconstructing the ocean surface slopes that utilizes all four channels [SLKP04], several soil moisture retrieval algorithms analyzed in [MMP10], and a vegetation classification technique that uses multi-frequency polarimetric data [LFT$^+$11]. Additional references can be found in [LP09]. In contradistinction to all those techniques that interpret the entries of the scattering matrix phenomenologically, we are able to reconstruct the physical characteristics of the scattering material within the adopted model, namely the principal values of the permittivities and conductivities, i.e. those associated with the principal axes, and the orientation of the optical axes in regards to the plane of incidence.

Chapter 2

SAR in an isotropic framework

2.1 Chapter layout

The current chapter is based on [ST11] and [GST13a] and is organized as follows. In Section 2.2, we introduce the physical model for the propagation of radio waves in the ionosphere. This model has a deterministic and a stochastic component. The stochastic component is due to turbulence, and in Section 2.2 we also present the basic formulas that we use to describe the turbulence. In Section 2.3 we introduce the generalized ambiguity function, or GAF. The concept of GAF appears when considering the matched filter applied to the SAR signal scattered off the target and received by the antenna, and then summing up the contributions from all the pulses along the synthetic array. As seen in [Che01], the GAF can be interpreted as the image of a point target. It provides a convenient way to assess the radar performance. In Section 2.3 we assume that the shape of the pulse that the radar transmits is a linear upchirp, which is common, and investigate how these pulses travel between the antenna and the target in three separate scenarios: unobstructed non-dispersive propagation, dispersive propagation in a homogeneous ionosphere, and dispersive propagation in an inhomogeneous ionosphere. We also look at how the latter two scenarios affect the GAF.

The effect of the ionosphere on the SAR performance is analyzed in detail in Sections 2.4 and 2.5, where we show that temporal dispersion in the ionosphere can lead to image displacement and can also result in a loss of image resolution and sharpness in both range and azimuth. The distortions caused by the ionospheric dispersion can actually be quantified, demonstrating the significance of the issue and why mitigation of the distortions would be greatly beneficial.

Following the idea put forth in [Tsy09a, Section 3], Section 2.6 proposes to probe the terrain, and hence the ionosphere, on two distinct carrier frequencies. From the information gathered from this double probing, one can set up a system of equations and solve for the total electron content, TEC, of the ionosphere along the ray path. The resulting TEC can then be used to

construct a corrected matched filter for the GAF. If the reconstruction is accurate, then, as seen in Section 2.7, the images obtained through the new matched filter are greatly improved from their non-corrected counterparts in Sections 2.4 and 2.5.

However, the original approach of [Tsy09a] to TEC reconstruction based on dual carrier probing appears poorly conditioned, meaning that it is sensitive to errors in the input data. We discuss this in Appendix G. In Section 2.8, we show that probing the ionosphere on two carrier frequencies can rather be combined with image registration, which yields an accurate and robust procedure for TEC reconstruction. Still, even with the best registration techniques, the TEC will not be reconstructed *exactly*, and it is important to see how the errors in the reconstruction affect the performance of the corrected matched filter. We look into this in Section 2.9.

Finally, in Section 2.10 we turn our attention to ionospheric turbulence, which is a crucial feature of the ionosphere. We quantify the distortions of the image due to the turbulent fluctuations of the ionosphere and find that the azimuthal resolution is much more sensitive to the turbulence than the range resolution. However, the issue of mitigating the distortions due to the turbulent fluctuations is left for future study.

Appendices A through I correspond to this chapter and are arranged in the order they are referenced (for the most part).

2.2 The model

2.2.1 Fundamentals

For the discussion in the current chapter we adopt the same model as in [Tsy09a]. We analyze the standard (as opposed to interferometric) SAR images [FL99], i.e., all the images are considered two-dimensional (range and azimuth), and the elevation is not taken into account. We also assume that the images are rendered by scalar propagating fields, i.e., that the polarization can be disregarded [Che01, CB09]. All the targets are assumed deterministic (no randomness is involved in describing them) and dispersionless (the scattering properties are not frequency-dependent within the spectrum of the radar signal); scattering of radar signals off the targets is linearized and interpreted using the first Born approximation. The start-stop approximation is employed to describe the synthetic antenna; its applicability to spaceborne SAR sensors is justified in [Tsy09b].

The ionosphere is modeled as a layer of inhomogeneous dilute plasma: the mean concentration (number density) of electrons can depend on both the altitude and the horizontal coordinates (as seen in section 2.5). In this chapter we disregard the effect of the magnetic field of the Earth on the propagating waves. This implies, in particular, that the Faraday rotation is not taken into account. On top of its mean value, the electron number density has a

stochastic component due to the ionospheric turbulence, which is a quasi-homogeneous random field [MY71, RKT89a]. The effect of the Earth's magnetic field on the ionospheric turbulence is disregarded, and the turbulence is assumed isotropic.

The propagation of electromagnetic waves in the ionosphere is analyzed with the help of the cold plasma approximation [Gin64], which requires that the phase speed of the waves be much faster than the thermal speed of the electrons. The cold plasma approximation is equivalent to disregarding spatial dispersion and taking into account only temporal dispersion of radio waves in the plasma [MM91]. Moreover, the propagation is assumed linear, because the power of signals emitted by spaceborne antennas is typically much lower than that needed for setting off the nonlinear effects, see [GG60, Gur78, Gur07], as well as [Gin64, Ch. VIII].

We use the classical Helmholtz theorem [MF53] to partition the overall electric field into the longitudinal and transverse components. Then, from the full Maxwell's equations and the equation of motion of electrons in the electric field one can derive the Klein-Gordon equation (see [Tsy09a, App. A]) that governs the propagation of high frequency transverse[1] electromagnetic waves in dilute plasma:

$$\frac{\partial^2 \boldsymbol{E}_\perp}{\partial t^2} - c^2 \Delta \boldsymbol{E}_\perp + \omega_{\mathrm{pe}}^2 \boldsymbol{E}_\perp = \boldsymbol{0}. \tag{2.1}$$

The quantity ω_{pe} in equation (2.1) is the Langmuir frequency, or plasma electron frequency. It characterizes temporal responses of the plasma and is given by:

$$\omega_{\mathrm{pe}} = \sqrt{\frac{4\pi e^2 N_{\mathrm{e}}}{m_{\mathrm{e}}}}, \tag{2.2}$$

where e and m_{e} are the charge and mass of the electron, and N_{e} is the electron number density. The behavior of ω_{pe}^2 in the ionosphere follows that of N_{e}; it has an altitude-dependent deterministic component and a stochastic component due to the turbulence. Typical values of the Langmuir frequency in the Earth's ionosphere range between 19 and 94 *megaradians/s*, which corresponds to between 3 and 15 *MHz*.

Unlike in a vacuum, the propagation speed of electromagnetic waves in the ionosphere depends on the frequency. This phenomenon is known as temporal dispersion; it is due to the presence of the last, non-differentiated, term in equation (2.1). The dispersion relation for the Klein-Gordon equation reads:

$$\omega^2 = \omega_{\mathrm{pe}}^2 + c^2 k^2, \tag{2.3}$$

which is derived by substituting the form of a plane electromagnetic wave,

$$\varphi \sim e^{i(\omega t - kr)}, \tag{2.4}$$

[1] The corresponding longitudinal oscillations are known as Langmuir waves, in a cold plasma they have zero group velocity [MM91].

into (2.1). We emphasize that according to (2.3) the short waves are weakly dispersive, whereas the long waves are subject to stronger dispersion. Indeed, the phase and group velocity of the propagation (ω/k and $d\omega/dk$, respectively) are given by:

$$v_{\mathrm{ph}} = c\left(1 + \omega_{\mathrm{pe}}^2/c^2k^2\right)^{\frac{1}{2}} \tag{2.5}$$

and

$$v_{\mathrm{gr}} = c\left(1 + \omega_{\mathrm{pe}}^2/c^2k^2\right)^{-\frac{1}{2}}, \tag{2.6}$$

so that the shorter the wave (the larger the k), the closer both velocities to the non-dispersive limit $v = c$. Also, (2.3) yields the following expression for the dielectric constant ε of a cold plasma:

$$\frac{k^2c^2}{\omega^2} = \varepsilon = 1 - \frac{\omega_{\mathrm{pe}}^2}{\omega^2}. \tag{2.7}$$

In the Cartesian coordinates we can consider equation (2.1) for individual field components:

$$\frac{\partial^2 E}{\partial t^2} - c^2\Delta E + \omega_{\mathrm{pe}}^2 E = 0. \tag{2.8}$$

In the rest of the chapter, we will use the scalar governing equation (2.8) to describe the propagation of electromagnetic waves in the ionosphere. For a comprehensive account of the propagation of radio waves in plasma we refer the reader to the monographs [Gin64] and [Bud85].

2.2.2 Turbulence basics

To characterize the ionospheric turbulence, we write the electron number density as follows:

$$N_{\mathrm{e}} = \langle N_{\mathrm{e}}\rangle + \mu(\boldsymbol{x}), \tag{2.9}$$

where the angular brackets $\langle\,\cdot\,\rangle$ denote the expected value (mean) and μ represents the fluctuations: $\langle\mu\rangle = 0$. In the simplest case of constant $\langle N_{\mathrm{e}}\rangle$, $\mu(\boldsymbol{x})$ is a homogeneous and isotropic random field, and its correlation function depends only on the distance $r = |\boldsymbol{x}_1 - \boldsymbol{x}_2|$ and not on the individual locations $\boldsymbol{x}_1 \in \mathbb{R}^3$ and $\boldsymbol{x}_2 \in \mathbb{R}^3$:

$$V(\boldsymbol{x}_1, \boldsymbol{x}_2) \stackrel{\mathrm{def}}{=} \langle\mu(\boldsymbol{x}_1)\mu(\boldsymbol{x}_2)\rangle = V(|\boldsymbol{x}_1 - \boldsymbol{x}_2|) \equiv V(r). \tag{2.10}$$

In reality, however, $\langle N_{\mathrm{e}}\rangle$ is a function of the altitude h. At the same time, the ratio

$$M = \frac{\sqrt{\langle\mu^2\rangle}}{\langle N_{\mathrm{e}}\rangle} \tag{2.11}$$

is assumed constant. A typical numerical value of M is $5 \cdot 10^{-3}$, and in extreme situations it may reach 10^{-1} [Arm05]. Hence, $\sqrt{\langle \mu^2 \rangle}$ also depends on x_1 and h, which makes $\mu(\boldsymbol{x})$ a quasi-homogeneous (rather than truly homogeneous) random field. While in this case we still keep the same notation (2.10) for the correlation function, in fact we have $V = V(x_1, h, r)$, where the dependence on x_1 and h is slow and the dependence on r (local variable) is fast.

For the Kolmogorov-Obukhov turbulence, the spectrum is (see [MY75, Section 12.1]):

$$\hat{V}(q) = \frac{C}{(1 + q^2/q_0^2)^\kappa}, \quad \text{where} \quad \kappa = \frac{11}{6} \quad \text{and} \quad C = \text{const}. \tag{2.12}$$

Hence, the correlation function evaluates to

$$\begin{aligned} V(r) &\stackrel{\text{def}}{=} \iiint_{-\infty}^{\infty} \hat{V}(\boldsymbol{q}) e^{i\boldsymbol{q}\boldsymbol{r}} d\boldsymbol{q} = 4\pi \int_0^\infty \frac{\sin qr}{qr} \hat{V}(q) q^2 dq \\ &= \frac{1}{\Gamma(\kappa)} 2^{\frac{5}{2}-\kappa} C \pi^{\frac{3}{2}} q_0^{\frac{3}{2}+\kappa} r^{-\frac{3}{2}+\kappa} K_{\kappa-\frac{3}{2}}(q_0 r), \end{aligned} \tag{2.13}$$

where $K_{\kappa-\frac{3}{2}}$ is the Macdonald function, or modified Bessel function of the second kind (see, e.g., [LS87, Chapter VII, § 3]). Asymptotically for large r, we have $K_{\kappa-\frac{3}{2}}(q_0 r) \approx \sqrt{\frac{\pi}{2q_0 r}} e^{-q_0 r}$, so that the correlation function decays exponentially:

$$V(r) \approx \frac{2^{2-\kappa}}{\Gamma(\kappa)} C \pi^2 \left(\frac{q_0}{r}\right)^{\frac{3}{2}} (q_0 r)^{\kappa-\frac{1}{2}} e^{-q_0 r}. \tag{2.14}$$

This means that effectively we are taking into account only short-range phenomena in the ionosphere. The quantity q_0 in formulae (2.12)–(2.14) helps define the correlation length r_0, or the outer scale of turbulence:

$$r_0 \stackrel{\text{def}}{=} \frac{1}{V(0)} \int_0^\infty V(r) dr = \left(C \pi^{\frac{3}{2}} \frac{\Gamma(\kappa - \frac{3}{2})}{\Gamma(\kappa)} q_0^3 \right)^{-1} \frac{C \pi^2 q_0^2}{\kappa - 1} = \frac{\sqrt{\pi}\Gamma(\kappa)}{(\kappa-1)\Gamma(\kappa - \frac{3}{2})} \frac{1}{q_0}, \tag{2.15}$$

where we have taken into account that

$$V(0) = \iiint_{-\infty}^{\infty} \hat{V}(\boldsymbol{q}) d\boldsymbol{q} = \int_0^\infty \int_0^{2\pi} \int_0^\pi V(q) q^2 \sin\theta d\theta d\phi dq = C \pi^{3/2} q_0^3 \frac{\Gamma\left(\kappa - \frac{3}{2}\right)}{\Gamma(\kappa)}. \tag{2.16}$$

The value of r_0 in (2.15) ranges between $1km$ and $10km$ according to different sources in the literature. The value of the constant C in (2.12) is related to the variance $\langle \mu^2 \rangle$ of $\mu(\boldsymbol{x})$, which

follows immediately the definition (2.10) and normalization (2.16):

$$\iiint_{-\infty}^{\infty} \hat{V}(\boldsymbol{q})d\boldsymbol{q} = \langle \mu^2 \rangle \quad \Rightarrow \quad C = \frac{\langle \mu^2 \rangle \Gamma(\kappa)}{\pi^{\frac{3}{2}} q_0^3 \Gamma(\kappa - \frac{3}{2})}. \tag{2.17}$$

Moreover, because of (2.14), the correlation function (2.13) clearly satisfies the necessary and sufficient condition for ergodicity of $\mu(\boldsymbol{x})$ known as the Slutskii theorem (1938), see [MY71, Section 4.7]:

$$\lim_{S\to\infty} \frac{1}{S} \int_0^S V(s)ds = 0.$$

Hence, we can substitute statistical means for spatial averages of μ when averaging over long distances. In [Bel08, Section 5.1] one can find some experimental data on the spectra of the ionospheric turbulence.

For the purpose of obtaining specific quantitative estimates, we will use the typical values given in Table 1.1. The effects of turbulence on a SAR image are analyzed in Section 2.10.

2.3 The generalized ambiguity function

The generalized ambiguity function offers a convenient way of assessing the radar performance. It is basically the image of a point target, i.e., that of a delta-type scatterer. In the ideal world, this image would be a delta-function as well. In reality, however, it is smeared out (by the nature of the radar signal processing, even when there is no ionosphere and no dispersion), and the extent of this smearing provides the limits of radar resolution.

The interrogating pulses emitted by the antenna of a SAR are taken as linear upchirps[2] of the form:

$$P(t) = A(t)e^{i\omega_0 t}, \quad \text{where} \quad A(t) = \chi_\tau(t)e^{i\alpha t^2}. \tag{2.18}$$

In formula (2.18), $\chi_\tau(t)$ is the indicator function of the interval of duration τ:

$$\chi_\tau(t) = \begin{cases} 1, & t \in [-\tau/2, \tau/2], \\ 0, & \text{otherwise}, \end{cases} \tag{2.19}$$

and $\alpha = B/(2\tau)$, where $\frac{B}{2\pi}$ is the bandwidth of the chirp (for an upchirp, $\alpha > 0$). Accordingly, the instantaneous frequency of the chirp [Che01, CB09], $\frac{\omega(t)}{2\pi}$, is given by

$$\omega(t) = \omega_0 + \frac{Bt}{\tau}, \quad t \in [-\tau/2, \tau/2], \tag{2.20}$$

[2] High-range resolution waveforms, see [CB09].

where $\frac{\omega_0}{2\pi}$ is the center carrier frequency. The modulating function $A(t)$ in formula (2.18) is assumed slowly varying compared to the fast carrier oscillation $e^{i\omega_0 t}$:

$$\left|\frac{dA}{dt}\right| = |2\alpha t \chi_\tau(t)| \leq 2\alpha\frac{\tau}{2} = \alpha\tau = \frac{B}{2} \ll \omega_0 = \left|\frac{d}{dt}e^{i\omega_0 t}\right|.$$

Hereafter, the radar is assumed to operate in the stripmap mode, see [CGM95], when the antenna points in a fixed direction relative to that of the satellite motion.[3] Hence, the footprint of the beam emitted by the antenna sweeps a strip on the Earth's surface parallel to the flight track, i.e., to the orbit.

To obtain the image, the antenna emits a series of pulses (2.18) when moving along the orbit. Those pulses travel to the Earth's surface, get scattered off the ground, and propagate back toward the satellite where they are received by the same antenna (in the case of a monostatic SAR [CGM95]). In doing so, clearly, both the emission and the reception of pulses are done by a moving antenna (which gives rise to the Doppler frequency shift) and moreover, the satellite travels a certain distance along the orbit during the pulse round-trip time between the antenna and the ground. However, in a simplified framework of the start-stop approximation those effects are disregarded. Instead, we assume that the pulse is emitted and the scattered response received while the antenna is at standstill at one and the same position, after which it moves to its next sending/receiving position along the orbit. This assumption has been used extensively in the SAR literature as it renders the corresponding analysis much easier. A full justification for the use of start-stop approximation for spaceborne SAR imaging can be found in [Tsy09b].

2.3.1 Non-dispersive propagation

Following [Che01], we first reproduce the derivation of the generalized ambiguity function for the case of unobstructed propagation with the speed c. In this case, the field is governed by the standard d'Alembert equation, which is obtained from the Klein-Gordon equation (2.8) by dropping the last term, i.e., by setting $\omega_{\text{pe}} = 0$. As indicated in Section 2.2, all images are assumed two-dimensional with range and azimuth (i.e., cross-range) being the coordinates, and the elevation of the target above the Earth's surface is not taken into account. This applies to the analysis of both non-dispersive and dispersive cases.

Suppose that the antenna is a motionless point source located at $\boldsymbol{x} \in \mathbb{R}^3$. Then, the propagating field due to the emitted chirp (2.18) is given by the standard retarded potential of the d'Alembert operator:

$$\varphi(t, \boldsymbol{z}) = \frac{1}{4\pi}\frac{P(t - |\boldsymbol{z} - \boldsymbol{x}|/c)}{|\boldsymbol{z} - \boldsymbol{x}|}. \tag{2.21}$$

[3] When this direction is normal to the flight track, the imaging is referred to as broadside.

Let us assume that the imaged terrain, which is also motionless, is characterized by the variable refraction index $n = n(\boldsymbol{z})$. Under the first Born approximation [BW99, Sec. 13.1.4], which is elaborated on in Section 4.1.2 and Appendix M, scattering is linearized so that the terrain is interpreted as a secondary waves' source due to the incident field $\varphi(t, \boldsymbol{z})$ of (2.21):

$$\frac{1 - n^2(\boldsymbol{z})}{c^2} \frac{\partial^2 \varphi}{\partial t^2} \stackrel{\text{def}}{=} \nu(\boldsymbol{z}) \frac{\partial^2 \varphi}{\partial t^2},$$

and each point $\boldsymbol{z}$ of the target is considered a source of the scattered field with intensity

$$\nu(\boldsymbol{z}) \frac{\partial^2 \varphi(t, \boldsymbol{z})}{\partial t^2} \approx -\omega_0^2 \nu(\boldsymbol{z}) \varphi(t, \boldsymbol{z}). \tag{2.22}$$

In Chapter 4 we extend the consideration of specular reflection to the backscattering, potentially bringing in some issues which will be part of a future study. The scattered field at the location $\boldsymbol{x}$ of the antenna and the moment of time t is given by the Kirchhoff integral, as derived in [Che01]:

$$\begin{aligned}
\psi(t, \boldsymbol{x}) &= \iiint \int \frac{\delta\left(t - \tau - |\boldsymbol{x} - \boldsymbol{z}|/c\right)}{4\pi |\boldsymbol{x} - \boldsymbol{z}|} \nu(\boldsymbol{z}) \frac{\partial^2 (\varphi + \psi)}{\partial t^2}(\tau, \boldsymbol{z}) d\tau d\boldsymbol{z} \\
\text{(Born approximation)} &\approx \iiint \int \frac{\delta\left(t - \tau - |\boldsymbol{x} - \boldsymbol{z}|/c\right)}{4\pi |\boldsymbol{x} - \boldsymbol{z}|} \nu(\boldsymbol{z}) \frac{\partial^2 (\varphi)}{\partial t^2}(\tau, \boldsymbol{z}) d\tau d\boldsymbol{z} \\
\text{(using } \delta\text{-function in } \int \ldots d\tau) &= \frac{1}{4\pi} \iiint \frac{\nu(\boldsymbol{z})}{|\boldsymbol{x} - \boldsymbol{z}|} \frac{\partial^2 \varphi}{\partial t^2}\left(t - |\boldsymbol{x} - \boldsymbol{z}|/c, \boldsymbol{z}\right) d\boldsymbol{z}.
\end{aligned} \tag{2.23}$$

As the amplitude $A(t)$ in (2.18) is slowly varying, it can be left out when differentiating the incident field (2.21) for substitution into (2.23), which yields:

$$\frac{\partial^2 \varphi}{\partial t^2}(t, \boldsymbol{z}) \approx -\frac{\omega_0^2}{4\pi} \frac{P(t - |\boldsymbol{z} - \boldsymbol{x}|/c)}{|\boldsymbol{z} - \boldsymbol{x}|}. \tag{2.24}$$

Consequently,

$$\begin{aligned}
\psi(t, \boldsymbol{x}) &\approx \iiint \tilde{\nu}(\boldsymbol{x}, \boldsymbol{z}) P\left(t - 2|\boldsymbol{x} - \boldsymbol{z}|/c\right) d\boldsymbol{z} \\
&= \iiint \tilde{\nu}(\boldsymbol{x}, \boldsymbol{z}) A\left(t - 2|\boldsymbol{x} - \boldsymbol{z}|/c\right) e^{i\omega_0 (t - 2|\boldsymbol{x} - \boldsymbol{z}|/c)} d\boldsymbol{z},
\end{aligned} \tag{2.25}$$

where

$$\tilde{\nu}(\boldsymbol{x}, \boldsymbol{z}) = -\frac{\omega_0^2}{16\pi^2} \frac{\nu(\boldsymbol{z})}{|\boldsymbol{x} - \boldsymbol{z}|^2}. \tag{2.26}$$

According to (2.25), the scattered field $\psi(t, \boldsymbol{x})$ can be interpreted as a result of application of

a Fourier integral operator (FIO) to the ground reflectivity function

$$\nu(\boldsymbol{z}) = \frac{1 - n^2(\boldsymbol{z})}{c^2}, \tag{2.27}$$

see, e.g., [CN04, NC04, CB08, CB09]. The FIO is approximately inverted by applying a matched filter to ψ and accumulating the information due to multiple interrogating pulses (2.18) emitted from and received by the antenna at different locations on the orbit. This procedure is similar to application of the adjoint operator, which would have coincided with the true inverse if the mapping (2.25) was a standard Fourier transform.

The matched filter is defined as follows. Assume that there is a point scatterer at the reference location $\boldsymbol{y}$, then the resulting field at $(t, \boldsymbol{x})$ is obtained by substituting $\nu(\boldsymbol{z}) = \delta(\boldsymbol{z} - \boldsymbol{y})$ into formula (2.25):

$$\psi_1(t, \boldsymbol{x}) = -\frac{\omega_0^2}{16\pi^2} \frac{P(t - 2|\boldsymbol{x} - \boldsymbol{y}|/c)}{|\boldsymbol{x} - \boldsymbol{y}|^2}. \tag{2.28}$$

The filter is essentially a complex conjugate of ψ_1 given by (2.28); for simplicity, the constant factor $-\omega_0^2/16\pi^2$, as well the entire denominator, which is a slowly varying function (compared to the fast oscillation $e^{i\omega_0 t}$), are disregarded. What remains is merely $\overline{P(t - 2|\boldsymbol{x} - \boldsymbol{y}|/c)}$, where the overbar denotes complex conjugation. The idea of building the filter this way, i.e., the idea of matching, is to have the large phase cancel in the exponent, see formula (2.18). The application of this filter yields an image from a single chirp:

$$\begin{aligned} I(\boldsymbol{y}) &= \int_\chi \overline{P(t - 2|\boldsymbol{x} - \boldsymbol{y}|/c)} \psi(t, \boldsymbol{x}) dt \\ &= \iiint \underbrace{\int_\chi \overline{P(t - 2|\boldsymbol{x} - \boldsymbol{y}|/c)} P(t - 2|\boldsymbol{x} - \boldsymbol{z}|/c) dt}_{W(\boldsymbol{y}, \boldsymbol{z})} \tilde{\nu}(\boldsymbol{x}, \boldsymbol{z}) d\boldsymbol{z}. \end{aligned} \tag{2.29}$$

where we have changed the order of integration after substituting expression (2.25) for $\psi(t, \boldsymbol{x})$. The interior integral $W(\boldsymbol{y}, \boldsymbol{z})$ in formula (2.29) is called the point spread function, see [Che01, CB09], and its limits are determined by the indicator function(s) χ_τ under the integral, see (2.18) and (2.19). Up to a slowly varying denominator, the point spread function $W(\boldsymbol{y}, \boldsymbol{z})$ yields a single-chirp image of the point scatterer located at $\boldsymbol{z}$, i.e., it is the field due to a unit magnitude delta-function at $\boldsymbol{z}$ processed with the matched filter $\overline{P(\,\cdot\,)}$.

Let us consider a sequence of emitting/receiving times and locations $(t^n, \boldsymbol{x}^n)$. For each n,

we build the point spread function following (2.29):

$$W^n(\boldsymbol{y},\boldsymbol{z}) = \int_\chi \overline{P(t-t^n-2|\boldsymbol{x}^n-\boldsymbol{y}|/c)}P(t-t^n-2|\boldsymbol{x}^n-\boldsymbol{z}|/c)dt \tag{2.30}$$
$$= \int_\chi \overline{P(u^n_{\boldsymbol{y}})}P(u^n_{\boldsymbol{z}})dt,$$

where the notation in the second line is used below in Chapter 3. The generalized ambiguity function of a SAR system takes into account the information from multiple interrogating pulses by summing up the corresponding contributions (2.30):

$$W(\boldsymbol{y},\boldsymbol{z}) = \sum_n \vartheta(\boldsymbol{z},\boldsymbol{x}^n)W^n(\boldsymbol{y},\boldsymbol{z}). \tag{2.31}$$

The factor $\vartheta(\boldsymbol{z},\boldsymbol{x}^n)$ under the sum in (2.31) determines the range of summation; it may come from the directivity pattern of the antenna. If so, the quantity $\vartheta(\boldsymbol{z},\boldsymbol{x}^n)$ can be approximated as follows:

$$\vartheta(\boldsymbol{z},\boldsymbol{x}^n) = \begin{cases} 1, & \text{if the target } \boldsymbol{z} \text{ is in the beam emitted from } \boldsymbol{x}^n, \\ 0, & \text{otherwise.} \end{cases} \tag{2.32a}$$

Often, the synthetic aperture is smaller than this, though, due to technical limitations.

The antenna of longitudinal dimension L emits a beam of angular width of about $2\lambda/L$ provided that the carrier wavelength $\lambda = 2\pi c/\omega_0$ is much shorter than L. Consequently, the longitudinal size of the antenna footprint on the ground in the case of broadside imaging is

$$R\tan\frac{\lambda}{L} \approx R\frac{\lambda}{L} \geqslant L_{\mathrm{SA}}, \tag{2.32b}$$

where R is the distance from the location of the antenna $\boldsymbol{x}^n$ to the center of the footprint. Let the subscript "1" denote the coordinate along the flight track (orbit), and Δx_1 be the distance along the orbit between the successive emissions of pulses. We can also take $z_1 = 0$ with no loss of generality. Then, we have $-\frac{L_{SA}}{2} \leq x_1^n \leq \frac{L_{SA}}{2}$, or $-\frac{N}{2} \leq n \leq \frac{N}{2}$, where $N = \left[\frac{L_{SA}}{\Delta x_1}\right] \leqslant \left[\frac{2\lambda R}{\Delta x_1 L}\right]$, see (2.32b), and $[\cdot]$ denotes the integer part. Consequently, we recast (2.30), (2.31), and (2.32a) as

$$W(\boldsymbol{y},\boldsymbol{z}) = \sum_{-N/2}^{N/2} \int_\chi \overline{A(t-t^n-2|\boldsymbol{y}-\boldsymbol{x}^n|/c)}e^{2i\omega_0|\boldsymbol{y}-\boldsymbol{x}^n|/c} \times A(t-t^n-2|\boldsymbol{z}-\boldsymbol{x}^n|/c)e^{-2i\omega_0|\boldsymbol{z}-\boldsymbol{x}^n|/c}dt. \tag{2.33}$$

Next, we change the integration variable from t to $t-t^n$ in each term of the sum (2.33) and realize that neither $\overline{A(t-2|\boldsymbol{y}-\boldsymbol{x}^n|/c)}$ nor $A(t-2|\boldsymbol{z}-\boldsymbol{x}^n|/c)$ depends on n explicitly, except

for the dependence via $\boldsymbol{x}^n$. The latter is weak, because for large R both $|\boldsymbol{y}-\boldsymbol{x}^n|$ and $|\boldsymbol{z}-\boldsymbol{x}^n|$ are slowly varying functions of $\boldsymbol{x}^n$, and they appear as arguments of another slowly varying function, A. Hence, the factors $\bar{A}$ and A can be taken out of the sum (2.33), and $\boldsymbol{x}^n$ inside $\overline{A(\,\cdot\,)}$ and $A(\,\cdot\,)$ can be replaced by $\boldsymbol{x}^0$ for definiteness, which yields:

$$W(\boldsymbol{y},\boldsymbol{z}) \approx \Big(\underbrace{\int_\chi \overline{A(t-2|\boldsymbol{y}-\boldsymbol{x}^0|/c)}A(t-2|\boldsymbol{z}-\boldsymbol{x}^0|/c)dt}_{W_R(\boldsymbol{y},\boldsymbol{z})}\Big)\Big(\underbrace{\sum_{-N/2}^{N/2} e^{2i\omega_0(|\boldsymbol{y}-\boldsymbol{x}^n|/c-|\boldsymbol{z}-\boldsymbol{x}^n|/c)}}_{W_A(\boldsymbol{y},\boldsymbol{z})}\Big). \tag{2.34}$$

Hence, the generalized ambiguity function gets approximately split into the product of the range factor:

$$W_R(\boldsymbol{y},\boldsymbol{z}) = \int_\chi \overline{A(t-2|\boldsymbol{y}-\boldsymbol{x}^0|/c)}A(t-2|\boldsymbol{z}-\boldsymbol{x}^0|/c)dt \tag{2.35}$$

and the azimuthal factor:

$$W_A(\boldsymbol{y},\boldsymbol{z}) = \sum_{n=-N/2}^{N/2} e^{2i\omega_0(|\boldsymbol{y}-\boldsymbol{x}^n|/c-|\boldsymbol{z}-\boldsymbol{x}^n|/c)}. \tag{2.36}$$

These control the range and azimuthal resolution of the radar,[4] respectively, see [Che01, CB09], for the case of an unobstructed propagation between the orbit and the ground. For a more complete argument and analysis of the error introduced with this approximation, see Appendix A. The actual calculation of the range and azimuthal factors of the GAF (2.35) and (2.36) is also done in Appendix A. In particular, the azimuthal factor (2.36) evaluates to

$$\begin{gathered} W_A(\boldsymbol{y},\boldsymbol{z}) \approx e^{i\Phi_0} N \operatorname{sinc}\Big(\pi\frac{y_1}{\Delta_A}\Big), \\ \text{where}\quad \Phi_0 = 2\frac{\omega_0(R_{\boldsymbol{y}}^0 - R_{\boldsymbol{z}}^0)}{c} \quad\text{and}\quad \Delta_A = \frac{\pi R c}{\omega_0 L_{\mathrm{SA}}}. \end{gathered} \tag{2.37}$$

The quantity Δ_A in (2.37) is the azimuthal resolution. The sinc function in (2.37) defines the shape of the GAF in the azimuthal direction. While azimuthal resolution is determined by the width of synthetic aperture, the range resolution depends on the properties of the interrogating pulse, i.e., $P(t)$. The analysis for chirp waveforms is given in Section 2.4.1 and Appendix A.

Remark. The quantity $e^{i\Phi_0}$ in W_A, see (2.37), is a factor of magnitude one in front of the sum. It may not have received proper attention in the earlier accounts of the SAR ambiguity theory, including [Tsy09a] and those of our own [ST11, GST13a]. This factor rapidly oscillates in range. While an inconvenience at a first glance, it actually helps redefine the ground reflectivity

[4] Resolution is a capability of the radar to distinguish between two different targets located a certain distance apart.

function so that to enable backscattering via the Bragg mechanism.[5] This is done by means of a windowed Fourier transform (WFT) on an intermediate scale [GT13] (much longer than the carrier wavelength yet much shorter than the resolution). In doing so, the geometrical spreading of spherical waves, which is accounted for by the denominator in formula (2.26), can be included into the definition of the ground reflectivity prior to applying the WFT. Indeed, for $\boldsymbol{x}$ within a given synthetic aperture, the denominator of (2.26) varies slowly and produces only insignificant changes in the signal amplitude. Therefore, for the rest of the dissertation we will omit the rapidly oscillating factor $e^{i\Phi_0}$ in (2.37) and disregard the dependence of $\tilde{\nu}$ on $\boldsymbol{x}$. This is equivalent to assuming ahead of time that $\tilde{\nu}(\boldsymbol{z})$ has already been transformed, and needs to be interpreted as the local backscattering coefficient at the target rather than the plain variation of the refraction index, as in (2.27).

The generalized ambiguity function (2.34) is the image of a delta-type scatterer. Hence, if we could make it equal to a delta-function as well, $W(\boldsymbol{y}, \boldsymbol{z}) = \delta(\boldsymbol{y} - \boldsymbol{z})$, then the radar would have had perfect resolution. In reality this is never achieved, and instead $W(\boldsymbol{y}, \boldsymbol{z})$ has a peak of finite height and finite width as the reference point $\boldsymbol{y}$ approaches the target $\boldsymbol{z}$. The sharper (i.e., the narrower) this peak the better the resolution, because two sharper peaks can be told apart if they are closer.

2.3.2 Dispersive propagation in the homogeneous medium

In the case of propagation through the ionosphere, the shape of the pulse changes in time and space because of the dispersion. The simplest case to analyze is that of a homogeneous ionosphere; a detailed analysis (based on the Fourier transform and linearization of the dispersion relation around the carrier frequency) is provided in Appendix B. The form of the propagating pulse emitted by the antenna at $\boldsymbol{x}$ is given by equation (B.19) [cf. formula (2.21)]:

$$\begin{gathered}\varphi(t, \boldsymbol{z}) = \frac{A'(t - |\boldsymbol{z} - \boldsymbol{x}|/v_{\mathrm{gr}}(\omega_0))}{4\pi|\boldsymbol{z} - \boldsymbol{x}|} e^{i\omega_0(t - |\boldsymbol{z}-\boldsymbol{x}|/v_{\mathrm{ph}}(\omega_0))}, \\ \text{where} \quad A'(t) = \chi_{\tau'}(t) e^{i\alpha' t^2},\end{gathered} \tag{2.38}$$

or more compactly as

$$\varphi(t, \boldsymbol{z}) = \frac{1}{4\pi} \frac{P'(\boldsymbol{x}, \boldsymbol{z}, \omega_0, t)}{|\boldsymbol{z} - \boldsymbol{x}|}, \tag{2.39}$$

where

$$P'(\boldsymbol{x}, \boldsymbol{z}, \omega_0, t) = A'\left(t - \frac{|\boldsymbol{z} - \boldsymbol{x}|}{v_{\mathrm{gr}}(\omega_0)}\right) e^{i\omega_0\left(t - \frac{|\boldsymbol{z}-\boldsymbol{x}|}{v_{\mathrm{ph}}(\omega_0)}\right)}. \tag{2.40}$$

[5] Allowing for backscattering at the target is critical for the analysis of a monostatic SAR. Yet formulae (2.25), (2.26), (2.27) show some physical inconsistency as they may yield non-zero backscattering even where it does not exist, e.g., for the scattering off a half-space with $\nu(\boldsymbol{z}) = \text{const}$, which is known to be specular.

The variables τ' and α' are the new chirp duration and rate given by equations (B.17) and (B.18), respectively:

$$\tau' = \tau - \delta\tau = \tau - \frac{|\boldsymbol{z} - \boldsymbol{x}|}{c} \frac{\omega_{\rm pe}^2}{\omega_0^2} \frac{B}{\omega_0}, \tag{2.41}$$

and

$$\alpha' = \alpha + \delta\alpha = \alpha + \frac{|\boldsymbol{z} - \boldsymbol{x}|}{2c} \frac{\omega_{\rm pe}^2}{\omega_0^3} \frac{B^2}{\tau^2} = \alpha + \frac{\delta\tau}{2} \frac{B}{\tau^2} = \frac{B}{2\tau} \left(1 + \frac{\delta\tau}{\tau}\right). \tag{2.42}$$

According to (2.41) and (2.42), the longer the distance $|\boldsymbol{z}-\boldsymbol{x}|$ that the pulse travels, the more it gets compressed (τ' becomes shorter) and the more its rate increases (α' becomes larger). We also emphasize that as formula (2.38) indicates, the chirp itself, i.e., its slowly varying envelope A', which represents energy distribution in the pulse, travels with the group velocity $v_{\rm gr}(\omega_0)$ that corresponds to the center carrier frequency ω_0. For the high frequency case that we are interested in, i.e., $\omega_0 \gg \omega_{\rm pe}$, the group velocity (2.6) can also be linearized:

$$v_{\rm gr} = v_{\rm gr}(\omega) \approx c \left(1 - \frac{1}{2} \frac{\omega_{\rm pe}^2}{c^2 k^2}\right) = c \left(1 - \frac{1}{2} \frac{\omega_{\rm pe}^2}{\omega^2 - \omega_{\rm pe}^2}\right) \approx c \left(1 - \frac{1}{2} \frac{\omega_{\rm pe}^2}{\omega^2}\right). \tag{2.43}$$

At the same time, the carrier phase travels with the corresponding phase velocity $v_{\rm ph}(\omega_0)$ and can also be linearized:

$$v_{\rm ph} = v_{\rm ph}(\omega) \approx c \left(1 + \frac{1}{2} \frac{\omega_{\rm pe}^2}{c^2 k^2}\right) = c \left(1 + \frac{1}{2} \frac{\omega_{\rm pe}^2}{\omega^2 - \omega_{\rm pe}^2}\right) \approx c \left(1 + \frac{1}{2} \frac{\omega_{\rm pe}^2}{\omega^2}\right). \tag{2.44}$$

Using the notions of the group and phase velocity (2.43) and (2.44), we can introduce the group and phase travel times, respectively, in the homogeneous ionosphere:

$$T_{\rm gr}(\boldsymbol{x}, \boldsymbol{z}, \omega) = \frac{|\boldsymbol{x} - \boldsymbol{z}|}{v_{\rm gr}(\omega)} \quad \text{and} \quad T_{\rm ph}(\boldsymbol{x}, \boldsymbol{z}, \omega) = \frac{|\boldsymbol{x} - \boldsymbol{z}|}{v_{\rm ph}(\omega)}, \tag{2.45}$$

and recast formula (2.38) as follows:

$$\varphi(t, \boldsymbol{z}) = \frac{A'(t - T_{\rm gr}(\boldsymbol{x}, \boldsymbol{z}, \omega_0))}{4\pi|\boldsymbol{z} - \boldsymbol{x}|} e^{i\omega_0(t - T_{\rm ph}(\boldsymbol{x}, \boldsymbol{z}, \omega_0))}. \tag{2.46}$$

It is important to point out that the group velocity $v_{\rm gr}$ of (2.43) is slower than the speed of light c. However, the phase velocity $v_{\rm ph}$ (2.44) is faster than the speed of light c. Hence, if we introduce the neutral (non-dispersive) travel time $T = T(\boldsymbol{x}, \boldsymbol{z}) = |\boldsymbol{x} - \boldsymbol{z}|/c$, then, according to

(2.43) and (2.44), for the group and phase travel time we can write:

$$T_{\mathrm{gr}}(\boldsymbol{x},\boldsymbol{z},\omega) = T(\boldsymbol{x},\boldsymbol{z}) + \Delta T \quad \text{and} \quad T_{\mathrm{ph}}(\boldsymbol{x},\boldsymbol{z},\omega) = T(\boldsymbol{x},\boldsymbol{z}) - \Delta T,$$
$$\text{where} \quad \Delta T = \Delta T(\boldsymbol{x},\boldsymbol{z},\omega) = \frac{|\boldsymbol{x}-\boldsymbol{z}|}{c}\frac{1}{2}\frac{\omega_{\mathrm{pe}}^2}{\omega^2}. \tag{2.47}$$

In other words, the group delay and the phase advance in formula (2.46) are equal to one another. Given (2.47), we can recast formula (2.41) for the pulse contraction as follows:

$$\delta\tau = 2\Delta T(\boldsymbol{x},\boldsymbol{z},\omega_0)\frac{B}{\omega_0}. \tag{2.48}$$

2.3.3 Dispersive propagation in the inhomogeneous medium

In the actual ionosphere, the electron number density N_{e} is not constant, and this is going to affect the propagation times (2.45). For the current analysis, we will assume that the mean electron number density $\langle N_{\mathrm{e}}\rangle$ depends on the altitude above the Earth's surface, but does not depend on the horizontal coordinates. A typical dependence of the mean electron number density on the altitude h is non-monotonic. The maximum is reached in the F-layer somewhere between $200km$ and $300km$ above the Earth's surface, and the characteristic scale h_0 of the variations of $\langle N_{\mathrm{e}}\rangle$ is on the order of tens of kilometers, see [Gin64, Ch. VI]. Clearly, $h_0 \gg \lambda$, where λ is the wavelength, which suggests that we can use the approximation of geometrical optics to analyze the propagation of SAR pulses in the inhomogeneous ionosphere.

We should remember, however, that the total electron number density N_{e} also has a stochastic component $\mu(\boldsymbol{x})$, see formula (2.9). It depends on all spatial coordinates, and can be interpreted as a quasi-homogeneous random field. To justify the use of geometrical optics for the study of pulse propagation through the turbulent ionosphere, the wavelength λ must be much shorter than the characteristic scale of turbulent inhomogeneities. If the latter is taken as r_0 (the outer scale of turbulence), the constraint $\lambda \ll r_0$ is obviously met. There is, however, a more subtle criterion for applicability of the geometrical optics. The characteristic scale of inhomogeneities must be much longer than the size of the first Fresnel zone $\sqrt{\lambda R_{\boldsymbol{z}}}$, where $R_{\boldsymbol{z}} = |\boldsymbol{z}-\boldsymbol{x}|$ is the propagation distance between the antenna and the target. The quantity $\sqrt{\lambda R_{\boldsymbol{z}}}$ comes to $1km$ for $\lambda = 1m$ and $R_{\boldsymbol{z}} = 1000km$, which is roughly r_0 according to [Arm05] or $\frac{1}{10}r_0$ according to [BG88]. Technically speaking, this makes the geometrical optics a borderline approximation for the class of problems we are considering. It is known however, that there are fewer shorter scale inhomogeneities in the spectrum of ionospheric turbulence than longer scale inhomogeneities, which still leaves the main conclusions of geometrical optics valid even outside its formal applicability range, see [RKT89b, Ch. I].

The expressions for travel times in the inhomogeneous ionosphere that replace formulae

(2.45) are derived in Appendix C for the deterministic case and in Appendix D for the stochastic case. Further analyzing the case of an inhomogeneous dispersive ionosphere, where the Langmuir frequency $\omega_{\rm pe}$ depends on the altitude, we see that while the form of the propagating signal (2.38), (2.40) in this case does not change, the travel times become [cf. formula (2.45)]

$$T_{\rm gr}(\boldsymbol{x},\boldsymbol{z},\omega_0)=\frac{|\boldsymbol{x}-\boldsymbol{z}|}{\bar{v}_{\rm gr}(\omega_0)}\quad\text{and}\quad T_{\rm ph}(\boldsymbol{x},\boldsymbol{z},\omega_0)=\frac{|\boldsymbol{x}-\boldsymbol{z}|}{\bar{v}_{\rm ph}(\omega_0)}. \tag{2.49}$$

The modified phase and group velocities $\bar{v}_{\rm ph}$ and $\bar{v}_{\rm gr}$ in (2.49) are [cf. formulae (2.44) and (2.43)]

$$\bar{v}_{\rm ph}(\omega_0)=c\left(1+\frac{1}{2}\frac{\bar{\omega}_{\rm pe}^2}{\omega_0^2}\right)\quad\text{and}\quad \bar{v}_{\rm gr}(\omega_0)=c\left(1-\frac{1}{2}\frac{\bar{\omega}_{\rm pe}^2}{\omega_0^2}\right), \tag{2.50}$$

where $\bar{\omega}_{\rm pe}^2$ is the square of the Langmuir frequency averaged over the straightened signal path between the antenna and the target:

$$\bar{\omega}_{\rm pe}^2=\frac{1}{|\boldsymbol{x}-\boldsymbol{z}|}\int_{\boldsymbol{z}}^{\boldsymbol{x}}\omega_{\rm pe}^2(s)ds\equiv\frac{1}{R_{\boldsymbol{z}}}\int_0^{R_{\boldsymbol{z}}}\omega_{\rm pe}^2(s)ds. \tag{2.51}$$

The quantity $\bar{\omega}_{\rm pe}^2$ of (2.51) also helps re-define the new chirp duration and rate for the stratified ionosphere [cf. formulae (2.41) and (2.42)]:

$$\tau'=\tau-\delta\tau=\tau-\frac{|\boldsymbol{x}-\boldsymbol{z}|}{c}\frac{\bar{\omega}_{\rm pe}^2}{\omega_0^2}\frac{B}{\omega_0}\quad\text{and}\quad \alpha'=\alpha+\delta\alpha=\frac{B}{2\tau}\left(1+\frac{\delta\tau}{\tau}\right). \tag{2.52}$$

Note that in integral (2.51), s is the distance along the straight line connecting $\boldsymbol{z}$ and $\boldsymbol{x}$. In the case where the electron number density depends only on the altitude h: $N_{\rm e}=N_{\rm e}(h)$, integral (2.51) reduces to (see Figure 1.1):

$$\bar{\omega}_{\rm pe}^2=\frac{1}{|\boldsymbol{x}-\boldsymbol{z}|}\int_0^H\omega_{\rm pe}^2(h)\frac{dh}{\cos\theta}=\frac{1}{H}\int_0^H\omega_{\rm pe}^2(h)dh=\frac{4\pi e^2}{m_{\rm e}}\frac{N_H}{H}, \tag{2.53}$$

where H is the orbit altitude and

$$N_H\stackrel{\rm def}{=}\int_0^H N_{\rm e}(h)dh \tag{2.54}$$

is the total electron content (TEC) in the ionosphere.[6] A more realistic case, where the ionosphere has a horizontal inhomogeneity as well, is analyzed in Section 2.5, whereas the ionospheric turbulence is accounted for in Section 2.10.

In addition to temporal dispersion, the propagation of radio waves in the ionosphere may

[6] In many ionospheric studies, the upper integration limit in (D.8) is formally taken as ∞.

be subject to Ohmic losses. In Appendix E we show that in the case of a lossy ionosphere, the propagating chirp (2.18) still has the form (2.38), but instead of (2.40) the numerator is given by [see formula (E.4)]

$$P'(\boldsymbol{x},\boldsymbol{z},\omega_0,t) = A'(t - T_{\mathrm{gr}}(\boldsymbol{x},\boldsymbol{z},\omega_0))e^{i\omega_0(t-T_{\mathrm{ph}}(\boldsymbol{x},\boldsymbol{z},\omega_0))}e^{-\frac{1}{2}\frac{|\boldsymbol{x}-\boldsymbol{z}|}{c}\frac{\nu_e\omega_{\mathrm{pe}}^2}{\omega_0^2}}, \tag{2.55}$$

where ν_e is the effective frequency of the particle collisions in the ionosphere [Gin64]. For the typical parameters presented in Table 1.1, including $|\boldsymbol{x}-\boldsymbol{z}| \sim R$, the last exponential factor in (2.55) evaluates to $e^{-0.15} \approx 0.86$, which means that the one-way signal attenuation due to the Ohmic losses in the ionosphere is about 14%. While not negligible by itself, this attenuation affects only the amplitude of the propagating chirp and does not affect its phase. Therefore, we will not be taking the Ohmic losses into account hereafter [as we effectively do not take into account the geometric attenuation, i.e., the denominator in formula (2.22)], and will always be using the ionospheric propagator in the form (2.38), (2.40) rather than (2.38), (2.55).

Neglecting the turbulence for now (see Section 2.10), we can write (2.49) in a way that corresponds to (C.20) and (C.21):

$$T_{\mathrm{gr}}(\boldsymbol{x},\boldsymbol{z},\omega) = \frac{R_{\boldsymbol{z}}}{c}\left[1 + \frac{1}{2}\frac{4\pi e^2}{m_{\mathrm{e}}\omega^2}\frac{N_H}{H}\right], \tag{2.56a}$$

$$T_{\mathrm{ph}}(\boldsymbol{x},\boldsymbol{z},\omega) = \frac{R_{\boldsymbol{z}}}{c}\left[1 - \frac{1}{2}\frac{4\pi e^2}{m_{\mathrm{e}}\omega^2}\frac{N_H}{H}\right]. \tag{2.56b}$$

Similarly to (2.47), we can also write:

$$\begin{aligned} &T_{\mathrm{gr}}(\boldsymbol{x},\boldsymbol{z},\omega) = T(\boldsymbol{x},\boldsymbol{z}) + \Delta T \quad \text{and} \quad T_{\mathrm{ph}}(\boldsymbol{x},\boldsymbol{z},\omega) = T(\boldsymbol{x},\boldsymbol{z}) - \Delta T, \\ &\text{where} \quad T(\boldsymbol{x},\boldsymbol{z}) = \frac{R_{\boldsymbol{z}}}{c} \quad \text{and} \quad \Delta T = \Delta T(\boldsymbol{x},\boldsymbol{z},\omega) = \frac{R_{\boldsymbol{z}}}{c}\frac{1}{2}\frac{4\pi e^2}{m_{\mathrm{e}}\omega^2}\mathcal{N}, \end{aligned} \tag{2.57}$$

where we introduce the notation

$$\mathcal{N} \stackrel{\mathrm{def}}{=} \frac{N_H}{H}. \tag{2.58}$$

Given the travel times (2.57), we can evaluate the contraction of the pulse on its way between the antenna $\boldsymbol{x}$ and the target $\boldsymbol{z}$ using formula (2.48):

$$\delta\tau = 2\Delta T(\boldsymbol{x},\boldsymbol{z},\omega_0)\frac{B}{\omega_0} = \frac{R_{\boldsymbol{z}}}{c}\frac{4\pi e^2}{m_{\mathrm{e}}\omega_0^2}\frac{B}{\omega_0}\mathcal{N}. \tag{2.59}$$

Finally, we can modify the generalized ambiguity function derived in Section 2.3.1, see formula (2.34), by substituting the actual travel times (2.56) instead of the unobstructed travel

time $|\boldsymbol{z}-\boldsymbol{x}|/c$ into those factors that correspond to the received signal. According to the form (2.46) of the propagating pulse, the group travel time $T_{\rm gr}(\boldsymbol{x}^0,\boldsymbol{z},\omega_0)$ of (2.56a) shall be substituted into $W_R(\boldsymbol{y},\boldsymbol{z})$ and the phase travel time $T_{\rm ph}(\boldsymbol{x}^n,\boldsymbol{z},\omega_0)$ of (2.56b) shall be substituted into $W_A(\boldsymbol{y},\boldsymbol{z})$. Then, instead of formulae (2.35) and (2.36) we have:

$$W'_R(\boldsymbol{y},\boldsymbol{z}) = \int_\chi \overline{A(t-2|\boldsymbol{y}-\boldsymbol{x}^0|/c)} A'_{2\delta}(t-2T_{\rm gr}(\boldsymbol{x}^0,\boldsymbol{z},\omega_0))dt \tag{2.60}$$

and

$$W'_A(\boldsymbol{y},\boldsymbol{z}) = \sum_{n=-N/2}^{N/2} e^{2i\omega_0(|\boldsymbol{y}-\boldsymbol{x}^n|/c-T_{\rm ph}(\boldsymbol{x}^n,\boldsymbol{z},\omega_0))}. \tag{2.61}$$

Similarly, for the scattered field received by the antenna, we can replace (2.25) by

$$\psi(t,\boldsymbol{x}) \approx \iiint \tilde{\nu}(\boldsymbol{x},\boldsymbol{z}) A'_{2\delta}(t-2T_{\rm gr}(\boldsymbol{x},\boldsymbol{z},\omega_0)) e^{i\omega_0(t-2T_{\rm ph}(\boldsymbol{x},\boldsymbol{z},\omega_0))} d\boldsymbol{z}. \tag{2.62}$$

The subscript 2δ in formulae (2.60) and (2.62) indicates that the round trip pulse contraction is twice the $\delta\tau$ of (2.59).

We emphasize that in formulae (2.60) and (2.61) the factors that correspond to the actual field received by the antenna take into account the dispersion of radio waves in the ionosphere. However, the factors that represent the matched filter remain the same as in the non-dispersive case. This creates a mismatch, and as it will be shown, it is precisely this mismatch that is responsible for the deterioration of the image.

2.4 Radar resolution and ionospheric distortions of SAR images

2.4.1 Range resolution

Expression (2.60) for the range ambiguity function, accurate to a constant factor, is given by the following integral:

$$W'_R(\boldsymbol{y},\boldsymbol{z}) \propto \int_{\max\{-\tau/2+2R_{\boldsymbol{y}}/c,\, -\tau''/2+2T_{\rm gr}(\boldsymbol{x}^0,\boldsymbol{z},\omega_0)\}}^{\min\{\tau/2+2R_{\boldsymbol{y}}/c,\, \tau''/2+2T_{\rm gr}(\boldsymbol{x}^0,\boldsymbol{z},\omega_0)\}} e^{i(\alpha''-\alpha)t^2} e^{4i(\alpha R_{\boldsymbol{y}}/c-\alpha'' T_{\rm gr}(\boldsymbol{x}^0,\boldsymbol{z},\omega_0))t} dt, \tag{2.63}$$

where [cf. formula (2.52)]

$$R_{\boldsymbol{y}} = |\boldsymbol{x}^0-\boldsymbol{y}|, \quad \tau'' = \tau - 2\delta\tau, \quad \text{and} \quad \alpha'' = \alpha + 2\delta\alpha = \frac{B}{2\tau}\left(1+\frac{2\delta\tau}{\tau}\right). \tag{2.64}$$

Changing the integration variable in (2.63) to $u = t - \left(\frac{R_{\boldsymbol{y}}}{c} + T_{\mathrm{gr}}(\boldsymbol{x}^0, \boldsymbol{z}, \omega_0)\right)$, removing the higher order terms, and denoting

$$a = \alpha'' - \alpha \quad \text{and} \quad b = 2(\alpha + \alpha'')(R_{\boldsymbol{y}}/c - T_{\mathrm{gr}}(\boldsymbol{x}^0, \boldsymbol{z}, \omega_0)), \tag{2.65}$$

we can convert integral (2.63) to

$$w(a, b) = \int_{-\tau/2}^{\tau/2} e^{iau^2 + ibu} du. \tag{2.66}$$

Note that the exact integration limits are approximated by simpler expressions in (2.66), which introduces a small relative error $\sim \frac{\delta\tau}{\tau}$. A comprehensive analysis can be found in Appendix F, where we consider all possible scenarios of how the intervals $\chi_\tau(t - 2|\boldsymbol{y} - \boldsymbol{x}^0|/c)$ and $\chi_{\tau''}(t - 2T_{\mathrm{gr}}(\boldsymbol{x}^0, \boldsymbol{z}, \omega_0))$ can be positioned with respect to one another.

Integrals of type (2.66) commonly appear in the analysis of the radar ambiguity functions and their properties [JWE+96, CW05]. The quadratic phase error (QPE) for (2.66) is defined as the maximum absolute value of the quadratic term in the exponent (see, e.g., [CW05, Chapter 3.5] or [JWE+96, Chapter 2.6]):

$$\phi_{\mathrm{q}} = |a| \left(\frac{\tau}{2}\right)^2. \tag{2.67}$$

The QPE characterizes the mismatch between the chirp rates in the direct (2.62) and inverse (2.29) operators. If the QPE is small, then w of (2.66) can be represented as

$$w(a, b) \approx w_0(b) + w_1(a, b), \tag{2.68}$$

where

$$w_0(b) = \tau \operatorname{sinc}\left(\frac{b\tau}{2}\right) \equiv \tau \frac{\sin(b\tau/2)}{b\tau/2} \quad \text{and} \quad |w_1| \ll |w_0|. \tag{2.69}$$

With no dispersion at all, formula (2.65) yields $a = 0$ and $b = 4\alpha(R_{\boldsymbol{y}} - R_{\boldsymbol{z}})/c$, because $T_{\mathrm{gr}} = R_{\boldsymbol{z}}/c$. In this case, the semi-width of the main lobe of $w_0(b)$, which is given by the conditions $\frac{b\tau}{2} = \pm\pi$, determines the undistorted radar resolution in range, $\Delta_R = \frac{\pi c}{B}$, see [Che01], while the sidelobes of w_0 determine the image contrast.

In the dispersive case, the term w_0 in (2.68) represents the effect of the filter with the group delay of the signal taken into account, but with no rate mismatch, i.e., no QPE. Substituting b of (2.65) into w_0 of (2.69) and keeping only the first term on the right-hand side of (2.68), we approximate (2.63) as follows:

$$W'_R(\boldsymbol{y}, \boldsymbol{z}) \propto \tau \operatorname{sinc}\left([(\alpha'' + \alpha)R_{\boldsymbol{y}}/c - (\alpha'' + \alpha)T_{\mathrm{gr}}(\boldsymbol{x}^0, \boldsymbol{z}, \omega_0)]\tau\right). \tag{2.70}$$

The range resolution Δ_R is also given by the semi-width of the main lobe of the sinc in (2.70). Setting $\frac{(\alpha''+\alpha)\Delta_R\tau}{c} = \pi$, we derive with the help of (2.64):

$$\Delta_R = \frac{\pi c}{B}\left(1 - \frac{\delta\tau}{\tau}\right). \tag{2.71}$$

Formula (2.71) yields roughly $19m$ for the values of the parameters listed in Table 1.1. The term $\frac{\delta\tau}{\tau}$ is formally kept in (2.71) only because it comes from the analysis of (2.70) with no simplifications. Otherwise, this term is small, about 0.15%, and of the same order as the terms dropped when simplifying the integration limits in (2.66). Thus, it can be neglected, and the range resolution in the dispersive case remains practically unchanged.

The term w_1 in (2.68) leads to the broadening of the main lobe of $w(a,b)$ and increase of its sidelobes, both of which add to the image blurring. Quantitatively, the role of w_1 has been estimated in [Tsy09a, Appendix C].[7] Specifically, it has been shown[8] that at the edge of the main lobe we have $|w| \neq 0$ due to the presence of w_1, so that

$$\frac{1}{\max|w|}|w|_{\frac{b\tau}{2}=\pi} \approx \frac{|w_1|_{\frac{b\tau}{2}=\pi}}{|w_0|_{\frac{b\tau}{2}=0}} \approx \frac{a\tau^2}{2\pi^2} = \frac{2}{\pi^2}\phi_{\mathrm{q}}, \tag{2.72}$$

where the QPE ϕ_{q} is defined by (2.67) and should be small for (2.72) to hold. A non-zero value in (2.72) suggests that the image is smeared, because the main lobe is not so well defined compared to the case where $|w|_{\frac{b\tau}{2}=\pi} = 0$. For the typical parameters given in Table 1.1, the extent of the smearing in the sense of (2.72) is $\sim 40\%$, assuming that for the definition of $\delta\tau$ in (2.52) we take $|\boldsymbol{x} - \boldsymbol{z}| \sim R$. An alternative measure for image imperfections due to the QPE is called the integrated side lobe ratio (ISLR). The ISLR is defined as a ratio of the power (i.e., integral of $|w|^2$) in the sidelobes to that in the main lobe, see [CW05, Section 2.8]. It is usually expressed in decibels, and can be calculated numerically. The increase of ISLR that corresponds to the data in Table 1.1 is $\sim 1.8dB$.

The ionosphere also causes a displacement of the image. Formula (2.69) indicates that w_0 attains its maximum at $b = 0$. In the non-dispersive case, we have $T_{\mathrm{gr}}(\boldsymbol{x}^0, \boldsymbol{z}, \omega_0) = R_{\boldsymbol{z}}/c$ where $R_{\boldsymbol{z}} = |\boldsymbol{x}^0 - \boldsymbol{z}|$, and according to (2.65), $b = 0$ for $R_{\boldsymbol{y}} = R_{\boldsymbol{z}}$. In other words, the sinc reaches its maximum value precisely when the reference location $\boldsymbol{y}$ and the target $\boldsymbol{z}$ are at the same distance away from the orbit in the normal direction. In the dispersive case though, $b = 0$ when $R_{\boldsymbol{y}}(\boldsymbol{z}) = cT_{\mathrm{gr}}(\boldsymbol{x}^0, \boldsymbol{z}, \omega_0)$, where T_{gr} is given by (2.49). This is not equivalent to $R_{\boldsymbol{y}} = R_{\boldsymbol{z}}$, and hence the image of a point scatterer at $\boldsymbol{z}$ will be displaced in range with respect to its true

[7] The effect of QPE can, to some degree, be controlled by introducing the weight functions into integral (2.29), see, e.g., [CW05]; we do not consider this approach here.

[8] At this point we should note that there are some arithmetic errors in that appendix, but the end result of the analysis is the same.

position. The displacement is given by

$$S_R \stackrel{\text{def}}{=} R_{\boldsymbol{y}}(\boldsymbol{z}) - R_{\boldsymbol{z}} = cT_{\text{gr}}(\boldsymbol{x}^0, \boldsymbol{z}, \omega_0) - R_{\boldsymbol{z}} = R_{\boldsymbol{z}} \frac{1}{\omega_0^2} \frac{4\pi e^2}{2m_{\text{e}}} \frac{N_H}{H} = \frac{1}{2} R_{\boldsymbol{z}} \frac{\bar{\omega}_{\text{pe}}^2}{\omega_0^2}. \tag{2.73}$$

For the parameters in Table 1.1, formula (2.73) yields approximately $450m$, assuming that $R_{\boldsymbol{z}} \approx R$. The origin of this displacement is the group delay, i.e., the mismatch between the actual propagation velocity $\bar{v}_{\text{gr}}$ of (2.50), which is used in the direct operator (2.62), and the speed of light in the inverse operator (2.29). Although the displacement of the image in range is a distortion per se, it appears of key importance for the reconstruction of the ionospheric TEC by means of dual-carrier probing (see Section 2.8).

2.4.2 Azimuthal resolution

To analyze the azimuthal factor of the GAF, we first introduce the notation

$$\Psi_n = \frac{|\boldsymbol{y} - \boldsymbol{x}^n| - cT_{\text{ph}}(\boldsymbol{x}^n, \boldsymbol{z}, \omega_0)}{R} \tag{2.74}$$

so that the sum (2.61) is recast as

$$W'_A(\boldsymbol{y}, \boldsymbol{z}) = \sum_{n=-N/2}^{N/2} e^{\frac{2i\omega_0 R}{c}\Psi_n}. \tag{2.75}$$

When calculating the distances in (2.74), we will use the subscripts "1" and "2" to denote the horizontal coordinates along the orbit (azimuth) and across the orbit (range), respectively, leaving the index "3" for the altitude, so that for the points on the orbit we will have $\boldsymbol{x} = (x_1, 0, H)$. For the target $\boldsymbol{z} = (z_1, z_2, 0)$ we will assume with no loss of generality that $z_1 = 0$, see Figure 1.1; we also take $y_2 = z_2$ when analyzing azimuthal resolution. Then, we can linearize the travel distances:

$$\begin{aligned} R_{\boldsymbol{z}} = |\boldsymbol{z} - \boldsymbol{x}| &= \sqrt{R^2 + (z_1 - x_1)^2} \approx R\Big(1 + \frac{1}{2}\frac{x_1^2}{R^2}\Big), \\ R_{\boldsymbol{y}} = |\boldsymbol{y} - \boldsymbol{x}| &= \sqrt{R^2 + (y_1 - x_1)^2} \approx R\Big(1 + \frac{1}{2}\frac{(y_1 - x_1)^2}{R^2}\Big), \end{aligned} \tag{2.76}$$

because $|x_1^n| \ll R$ and $|y_1 - x_1^n| \ll R$, where $R = \sqrt{H^2 + z_2^2}$. Substituting (2.76) into (2.74), we get

$$\Psi_n = \frac{1}{2}\frac{y_1^2}{R^2} - \frac{y_1 x_1^n}{R^2} + \frac{1}{2}\frac{\bar{\omega}_{\text{pe}}^2}{\omega_0^2} + \frac{\bar{\omega}_{\text{pe}}^2}{\omega_0^2}\frac{(x_1^n)^2}{4R^2}. \tag{2.77}$$

For the azimuthal coordinate x_1 in formula (2.77) we can write: $x_1^n = n \cdot \Delta x_1$, where Δx_1 is the distance that the satellite travels along the orbit between the successive emission of pulses: $\Delta x_1 = v_{\mathrm{SAT}}/f_{\mathrm{p}}$. Introducing

$$\hat{a} = \frac{\omega_0 (\Delta x_1)^2}{2Rc} \frac{\bar{\omega}_{\mathrm{pe}}^2}{\omega_0^2} \quad \text{and} \quad \hat{b} = \frac{2\omega_0 y_1 \Delta x_1}{Rc}, \tag{2.78}$$

and ignoring the proportionality constant that results from the first and third terms in (2.77), we can approximate the sum (2.75) by the integral:

$$W'_A(y_1, 0) \stackrel{\mathrm{def}}{=} W'_A(\boldsymbol{y}, \boldsymbol{z})\Big|_{\substack{z_1=0,\\ y_2=z_2}} = \sum_{n=-N/2}^{N/2} e^{i\hat{a}n^2 - i\hat{b}n} \approx \int_{-N/2}^{N/2} e^{i\hat{a}n^2 - i\hat{b}n} du. \tag{2.79}$$

The integral in (2.79) is of the type (2.66). Thus, the calculation of the azimuthal w_0 is equivalent to keeping only the first term on the right-hand side of (2.77) for the sum (2.75):

$$W'_A(y_1, 0) \approx \sum_{n=-N/2}^{N/2} e^{-\frac{2i\omega_0}{c}\frac{y_1 x_1^n}{R}} \approx N \operatorname{sinc} \frac{\omega_0 y_1 \Delta x_1 N}{Rc}. \tag{2.80}$$

The semi-width of the main lobe of the sinc in (2.80) yields the azimuthal resolution:

$$\Delta_A = \frac{1}{2} \frac{\lambda_0 R}{L_{\mathrm{SA}}}, \tag{2.81}$$

which is another way of writing what appears in (2.37). It appears approximately equal to $10m$ for the typical parameters given in Table 1.1.

The azimuthal w_1 is due to $\hat{a}$ of (2.78), i.e., to the second term on the right-hand side of (2.77). This second term accounts for the difference between the phase velocity in the dispersive propagator (2.40), (2.49) and the speed of light in the non-dispersive filter in (2.29). Similarly to (2.67), the expression for the azimuthal QPE is

$$\phi_{\mathrm{qA}} = \frac{\hat{a}N^2}{4} = \frac{1}{2}\frac{\omega_0}{Rc}\frac{\bar{\omega}_{\mathrm{pe}}^2}{\omega_0^2}\frac{1}{4}(N\Delta x_1)^2 = \frac{1}{8}\frac{\omega_0 L_{\mathrm{SA}}^2}{Rc}\frac{\bar{\omega}_{\mathrm{pe}}^2}{\omega_0^2}, \tag{2.82}$$

and the same argument that leads to equation (2.72) yields the deterioration of the GAF contrast of approximately 35% for the the typical parameters given in Table 1.1. Note though that such a substantial deterioration implies that the main lobe of the sinc absorbs the first sidelobe, the resolution drops, and the measure of image defects based on formula (2.72) essentially loses its original meaning. On the other hand, the ISLR still provides an adequate measure, and the corresponding increase is about $4dB$.

2.5 Azimuthal displacement due to horizontal variation of the ionosphere

In Section 2.4, we have assumed that the electron number density does not depend on the horizontal coordinates. Then, the only characteristic of the ionospheric plasma that enters into the expression for the propagator (2.38) is the constant TEC given by (2.54).

In order to account for the horizontally inhomogeneous ionosphere, we will let the electron number density N_e depend not only on the altitude h but also on the azimuthal coordinate ξ_1. In doing so, we will assume that the dependence is predominantly linear and truncate the Taylor expansion of N_e in the direction ξ_1 after the second term:

$$N_\mathrm{e}(\xi_1, h) \approx N_\mathrm{e}(0, h) + \xi_1 \frac{\partial N_\mathrm{e}}{\partial \xi_1}(0, h), \quad \text{where} \quad |\xi_1| \ll R. \tag{2.83}$$

Following Appendix C, for $\omega^2 \gg \omega_\mathrm{pe}^2$ (see Table 1.1) we can calculate the phase travel time by integrating the reciprocal phase velocity of (2.44) along the straight line connecting $\boldsymbol{x}$ and $\boldsymbol{z}$ (i.e., ignoring the ray curvature) [cf. formulae (2.51) and (2.53)]:

$$\begin{aligned} T_\mathrm{ph}(\boldsymbol{x}, \boldsymbol{z}, \omega) &= \int_0^{R_z} \frac{ds}{v_\mathrm{ph}(s)} = \frac{1}{\cos\theta} \int_0^H \frac{dh}{v_\mathrm{ph}(\xi_1(h), h)} \\ &\approx \frac{R_z}{c} - \frac{1}{c\cos\theta} \int_0^H \frac{1}{2} \frac{\omega_\mathrm{pe}^2(\xi_1(h), h)}{\omega^2}\, dh. \end{aligned} \tag{2.84}$$

Here, $\xi_1(h)$ is the azimuthal coordinate of the point on the line between $\boldsymbol{x}$ and $\boldsymbol{z}$ that has altitude h (see Figure 1.1):

$$\xi_1(h) \equiv \xi_1(\boldsymbol{x}, \boldsymbol{z}, h) = \frac{h}{H} x_1 + \frac{H-h}{H} z_1 = \frac{h}{H} x_1, \tag{2.85}$$

and we again assume $z_1 = 0$. Substituting (2.85) into (2.84), we get:

$$T_\mathrm{ph}(\boldsymbol{x}, \boldsymbol{z}, \omega) = \frac{R_z}{c} - \frac{1}{2c\omega^2\cos\theta} \int_0^H \left(\omega_\mathrm{pe}^2(0, h) + \frac{x_1}{H} \frac{4\pi e^2}{m_\mathrm{e}} \frac{\partial N_\mathrm{e}}{\partial \xi_1}(0, h) h \right) dh. \tag{2.86}$$

Then, using formulae (2.50)–(2.54), we transform expression (2.86) into

$$T_\mathrm{ph}(\boldsymbol{x}, \boldsymbol{z}, \omega) = \frac{R_z}{\bar{v}_\mathrm{ph}(\omega)} - \frac{R_z}{c} \frac{\bar{\omega}_\mathrm{pe}^2}{2\omega^2} \mathcal{Q}(\boldsymbol{x}^0, \boldsymbol{z}) x_1, \tag{2.87}$$

where

$$\mathcal{Q}(\boldsymbol{x}^0, \boldsymbol{z}) \stackrel{\mathrm{def}}{=} \frac{1}{H^2} \int_0^H \frac{4\pi e^2}{m_\mathrm{e} \bar{\omega}_\mathrm{pe}^2} \frac{\partial N_\mathrm{e}}{\partial \xi_1}(0, h) h\, dh \tag{2.88}$$

is essentially the first vertical moment of the azimuthal gradient of N_{e}. The quantities $\bar{\omega}_{\mathrm{pe}}^2$ and $\bar{v}_{\mathrm{ph}}(\omega)$ in formulae (2.87) and (2.88) are evaluated according to (2.53) and (2.50), respectively, for $\xi_1 = 0$, i.e., for $\omega_{\mathrm{pe}}^2 = \omega_{\mathrm{pe}}^2(0,h)$, or $N_{\mathrm{e}} = N_{\mathrm{e}}(0,h)$. Substituting (2.88), (2.87), and (2.76) into (2.74), we have [cf. formula (2.77)]:

$$\Psi_n = -\frac{y_1 x_1^n}{R^2} + \frac{\bar{\omega}_{\mathrm{pe}}^2}{\omega_0^2}\frac{(x_1^n)^2}{4R^2} + \frac{\bar{\omega}_{\mathrm{pe}}^2}{2\omega_0^2}\mathcal{Q}x_1. \tag{2.89}$$

With the third term on the right-hand side of (2.89) taken into account, and the second term temporarily disregarded, we obtain instead of formula (2.80):

$$W_A'(y_1,0) \approx \sum_{n=-N/2}^{N/2} e^{-\frac{2i\omega_0}{c}\left(\frac{y_1}{R} - R\frac{\bar{\omega}_{\mathrm{pe}}^2}{2\omega_0^2}\mathcal{Q}\right)x_1^n} \approx N\,\mathrm{sinc}\left[\frac{\omega_0}{c}\left(\frac{y_1}{R} - R\frac{\bar{\omega}_{\mathrm{pe}}^2}{2\omega_0^2}\mathcal{Q}\right)\Delta x_1 N\right].$$

Consequently, a non-zero value of $\mathcal{Q}$ of (2.88), which is due to the azimuthal gradient of N_{e}, see (2.83), results in an azimuthal displacement of the entire image by

$$S_A = \frac{1}{2}\frac{\bar{\omega}_{\mathrm{pe}}^2}{\omega_0^2}\mathcal{Q}R^2. \tag{2.90}$$

As in the case of the displacement in range, see formula (2.73), the origin of the azimuthal displacement (2.90) is a mismatch between the filter in (2.29) and the propagator (2.40). The presence of the azimuthal displacement (2.90) allows us to reconstruct the value of $\mathcal{Q}$ by means of the dual-carrier probing (see Section 2.8) and subsequently use this value to correct the matched filter in (2.29).

The effect of the second term on the right-hand side of (2.89) is exactly the same for the horizontally inhomogeneous ionosphere as it is for the horizontally homogeneous ionosphere. Namely, the QPE leads to a deterioration of the GAF contrast, see (2.82).

It is also to be noted that in the literature one sometimes uses a simplified model based on the so-called phase screens to describe the propagation of radar pulses through the ionosphere, see, e.g., [MG02, Bel08, BPE+10].

2.6 Dual carrier probing

To remove the mismatches that cause distortions of the image, one needs to correct the filter, i.e., replace the unobstructed travel times $|\boldsymbol{y}-\boldsymbol{x}^n|/c$ by $T_{\mathrm{gr}}(\boldsymbol{x}^n, \boldsymbol{y}, \omega_0)$ in (2.60) and by $T_{\mathrm{ph}}(\boldsymbol{x}^n, \boldsymbol{y}, \omega_0)$ in (2.61), and also adjust the chirp duration and chirp rate in the filter factor under the integral (2.60). However, unlike in the received field, which is a physical observable, the correction in the filter must be done theoretically. Therefore, one needs to know the quantity $\mathcal{N}$, see formulas

(2.57) and (2.58), that characterizes the ionosphere. The availability of $\mathcal{N}$ will allow one to calculate the dilation (2.59) and the new chirp rate (2.42), as well as travel times for any reference location $\boldsymbol{y}$.

In the literature, many estimates are available for the electron number density and the TEC in the ionosphere, see, e.g., [Gin64] or [Bud85]. Those estimates, however, can only provide a typical range of values, especially as the parameters of the ionosphere are known to vary in space and in time. This will not allow one to correct the filter with a sufficient degree of reliability. More accurate values of the ionospheric parameters can be obtained with the help of the specialized techniques, such as those described in the papers surveyed in Chapter 1. It is to be emphasized though that even if the TEC is known accurately, but not for the exact same state of the ionosphere that corresponds to a given image, it may still be not very useful for mitigating the image distortions. What is rather needed is an accurate value of $\mathcal{N}$ exactly at the time and place the image is taken. The technique we describe hereafter provides just that.

Namely, we exploit the idea of dual carrier probing as it applies to the determination of $\mathcal{N}$ for the given specific state of the ionosphere. Let us assume that there is an object or feature in the scene that can be clearly identified on the image. This object does not have to be artificial. It does not have to dominate the scene, say, by having the highest reflectivity. Its location does not have to be known ahead of time. It merely has to be something that can be fairly easily picked out and matched on different images that represent the same terrain. For example, it can be some landmark, such as a hilltop, a building, a road intersection, etc.

Let ω_1 and ω_2 be two distinct carrier frequencies, $\omega_1 \neq \omega_2$, and let $R_{\boldsymbol{y}}^{(1)}$ and $R_{\boldsymbol{y}}^{(2)}$ be the corresponding ranges of the aforementioned object measured by the radar, whereas its true range is $R_{\boldsymbol{z}}$ (unknown yet). Then, we can consider the corresponding two equations (2.73) as a system:

$$\begin{aligned} R_{\boldsymbol{y}}^{(1)} &= cT_{\mathrm{gr}}(\boldsymbol{x}^0, \boldsymbol{z}, \omega_1), \\ R_{\boldsymbol{y}}^{(2)} &= cT_{\mathrm{gr}}(\boldsymbol{x}^0, \boldsymbol{z}, \omega_2), \end{aligned} \tag{2.91}$$

where the group travel time T_{gr} is given by formula (2.56a). With the data $R_{\boldsymbol{y}}^{(1)}$ and $R_{\boldsymbol{y}}^{(2)}$ available, system (2.91) can be solved with respect to the two unknown quantities: the true range $R_{\boldsymbol{z}}$ and the integral quantity $\mathcal{N}$ that characterizes the plasma.

Let us reintroduce (see (2.51) and (2.58)) the following notation for brevity:

$$\bar{\omega}_{\mathrm{pe}}^2 = \frac{4\pi e^2}{m_{\mathrm{e}}}\mathcal{N}. \tag{2.92}$$

Using this notation, system (2.91) with the expression for T_{gr} given by (2.56a) is recast as

$$\begin{aligned} R_{\boldsymbol{y}}^{(1)} &= R_{\boldsymbol{z}} \left(1 + \frac{\bar{\omega}_{\mathrm{pe}}^2}{2\omega_1^2}\right), \\ R_{\boldsymbol{y}}^{(2)} &= R_{\boldsymbol{z}} \left(1 + \frac{\bar{\omega}_{\mathrm{pe}}^2}{2\omega_2^2}\right). \end{aligned} \tag{2.93}$$

The range $R_{\boldsymbol{z}}$ can be eliminated from system (2.93) by dividing the equations by one another. Then, after simple transformations, we have:

$$\bar{\omega}_{\mathrm{pe}}^2 = \frac{2\omega_1^2\omega_2^2\Delta R_{\boldsymbol{y}}}{\omega_2^2 R_{\boldsymbol{y}}^{(2)} - \omega_1^2 R_{\boldsymbol{y}}^{(1)}}, \quad \text{where} \quad \Delta R_{\boldsymbol{y}} \equiv R_{\boldsymbol{y}}^{(1)} - R_{\boldsymbol{y}}^{(2)}. \tag{2.94}$$

Once the frequency $\bar{\omega}_{\mathrm{pe}}^2$ has been obtained, the actual electron content N_H can be determined using (2.92). Moreover, if there is a need to know the true range $R_{\boldsymbol{z}}$ of the chosen reference object, it can be easily found from any of the equations (2.93).

Let us emphasize that formula (2.94) does not degenerate in the sense that its denominator does not turn into zero. Indeed, if it were equal to zero, then system (2.93) would immediately yield $\omega_1 = \omega_2$. However, the quantity $\bar{\omega}_{\mathrm{pe}}^2$ computed according to (2.94) appears sensitive to the errors in the data $R_{\boldsymbol{y}}^{(1)}$ and $R_{\boldsymbol{y}}^{(2)}$. A rigorous analysis of this sensitivity, i.e., of the conditioning [RT07, Chapter 1] of formula (2.94), can be found in Appendix G. It shows that the conditioning is only weakly affected by how far the probing frequencies ω_1 and ω_2 are chosen from each other. For the most part, $\bar{\omega}_{\mathrm{pe}}^2$ appears sensitive to errors because there is a difference between two large numbers that are close to one another ($R_{\boldsymbol{y}}^{(1)}$ and $R_{\boldsymbol{y}}^{(2)}$) in the numerator of (2.94). The overall conditioning of $\bar{\omega}_{\mathrm{pe}}^2$ can be improved though by using several reference locations instead of one. In Appendix G, we are showing that this approach indeed helps reduce the resulting error. But there is an even better way to reduce the error, image registration, and we look into this in Section 2.8.

It is also to be noted that the idea of using two frequencies for determining the TEC is briefly mentioned in [WQWH03], without analyzing the resulting performance. The authors of [WQWH03] suggest however that the two frequencies be taken from the existing SAR bandwidth. In the context of our approach, we analyze the split-band technique in Appendix I.

2.7 Correcting the matched filter when the exact TEC is known

Let us recall that the distortions of the SAR image are due to the mismatch between the actual field received by the radar antenna and the assumptions made about this field when designing the signal processing algorithm, i.e., the matched filter. In this section, we assume that we are

able to reconstruct the TEC exactly. Analysis of the case where there is some error in the reconstructed TEC is done in Section 2.9. Once the quantity N_H has been found, one can use formulae (2.56) and accurately evaluate the travel times $T_{\rm ph}(\boldsymbol{x}^n, \boldsymbol{y}, \omega_0)$ and $T_{\rm gr}(\boldsymbol{x}^n, \boldsymbol{y}, \omega_0)$ for any location $\boldsymbol{y}$. Then, one can also compute the pulse dilation for the reference point $\boldsymbol{y}$ using formula (2.59), and the new pulse rate according to (2.42). This allows to correct the matched filter, i.e., to modify its definition in formulae (2.60) and (2.61) by substituting the travel times that account for the ionospheric dispersion.

2.7.1 Range resolution

With the above correction in place, the range factor of the generalized ambiguity function becomes [cf. formula (2.63)]:

$$\begin{aligned} W'_R(\boldsymbol{y}, \boldsymbol{z}) &= \int_{\max\{-\tau''(\boldsymbol{y})/2+2T_{\rm gr}(\boldsymbol{y}),\, -\tau''(\boldsymbol{z})/2+2T_{\rm gr}(\boldsymbol{z})\}}^{\min\{\tau''(\boldsymbol{y})/2+2T_{\rm gr}(\boldsymbol{y}),\, \tau''(\boldsymbol{z})/2+2T_{\rm gr}(\boldsymbol{z})\}} e^{-i\alpha''(\boldsymbol{y})(t-2T_{\rm gr}(\boldsymbol{y}))^2} e^{i\alpha''(\boldsymbol{z})(t-2T_{\rm gr}(\boldsymbol{z}))^2} dt \\ &\propto \int_{\max\{-\tau''(\boldsymbol{y})/2+2T_{\rm gr}(\boldsymbol{y}),\, -\tau''(\boldsymbol{z})/2+2T_{\rm gr}(\boldsymbol{z})\}}^{\min\{\tau''(\boldsymbol{y})/2+2T_{\rm gr}(\boldsymbol{y}),\, \tau''(\boldsymbol{z})/2+2T_{\rm gr}(\boldsymbol{z})\}} e^{i(\alpha''(\boldsymbol{z})-\alpha''(\boldsymbol{y}))t^2} e^{4i(\alpha''(\boldsymbol{y})T_{\rm gr}(\boldsymbol{y})-\alpha''(\boldsymbol{z})T_{\rm gr}(\boldsymbol{z}))} dt, \end{aligned} \tag{2.95}$$

where we have introduced the abbreviated notation $T_{\rm gr}(\boldsymbol{z}) = T_{\rm gr}(\boldsymbol{x}^0, \boldsymbol{z}, \omega_0)$. The double primed quantities τ'' and α'' in formula (2.95) are to be evaluated for the pulse round-trip between the antenna and the target [cf. formulae (2.52) and (2.42)]:

$$\tau'' = \tau - 2\delta\tau \quad \text{and} \quad \alpha'' = \alpha + \delta\tau \frac{B}{\tau^2} = \frac{B}{2\tau}\left(1 + \frac{2\delta\tau}{\tau}\right), \tag{2.96}$$

where $\delta\tau$ is given by formula (2.59). For the integral (2.95), we consider the integration limits $\mp\tau''(\boldsymbol{y})/2 + 2T_{\rm gr}(\boldsymbol{y})$, and, changing the integration variable: $u = t - 2T_{\rm gr}(\boldsymbol{y})$, obtain:

$$\begin{aligned} W'_R(\boldsymbol{y}, \boldsymbol{z}) &\propto \int_{-\tau''(\boldsymbol{y})/2}^{\tau''(\boldsymbol{y})/2} e^{-i\alpha''(\boldsymbol{y})u^2} e^{i\alpha''(\boldsymbol{z})(u+2T_{\rm gr}(\boldsymbol{y})-2T_{\rm gr}(\boldsymbol{z}))^2} du \\ &\propto \int_{-\tau''(\boldsymbol{y})/2}^{\tau''(\boldsymbol{y})/2} e^{i(\alpha''(\boldsymbol{z})-\alpha''(\boldsymbol{y}))u^2} e^{4i\alpha''(\boldsymbol{z})(T_{\rm gr}(\boldsymbol{y})-T_{\rm gr}(\boldsymbol{z}))u} du, \end{aligned} \tag{2.97}$$

where the constant factors of magnitude one in front of the integrals are dropped.

Following the analysis of Section 2.4, we first disregard the quadratic term $\sim u^2$ in the exponent under the integral (2.97), because this term is small. Then, integral (2.97) evaluates to

$$W'_R(\boldsymbol{y}, \boldsymbol{z}) \propto \tau''(\boldsymbol{y}) \operatorname{sinc}[2\alpha''(\boldsymbol{z})(T_{\rm gr}(\boldsymbol{y}) - T_{\rm gr}(\boldsymbol{z}))\tau''(\boldsymbol{y})]. \tag{2.98}$$

The range resolution of the radar is defined as the semi-width of the sinc function (2.98)

interpreted as a function of $R_{\boldsymbol{y}} - R_z$, and hence can be obtained by setting the argument of the sinc equal to π:

$$2\alpha''(\boldsymbol{z})(T_{\mathrm{gr}}(\boldsymbol{y}) - T_{\mathrm{gr}}(\boldsymbol{z}))\tau''(\boldsymbol{y}) = \pi.$$

With the help of (2.96), the previous equality transforms into

$$\frac{B}{\tau}\left(1 + \frac{2\delta\tau}{\tau}\right)(T_{\mathrm{gr}}(\boldsymbol{y}) - T_{\mathrm{gr}}(\boldsymbol{z}))\tau\left(1 - \frac{2\delta\tau}{\tau}\right) = \pi. \tag{2.99}$$

Per our discussion in Appendix F, we can disregard the terms $\frac{\delta\tau}{\tau}$ in the expression for resolution and instead of (2.99) write:

$$B(T_{\mathrm{gr}}(\boldsymbol{y}) - T_{\mathrm{gr}}(\boldsymbol{z})) = \pi. \tag{2.100}$$

Then, we can use formulae (2.56a) and (2.92), and express the difference between the group travel times in (2.100) as follows:

$$T_{\mathrm{gr}}(\boldsymbol{y}) - T_{\mathrm{gr}}(\boldsymbol{z}) = \frac{R_{\boldsymbol{y}} - R_{\boldsymbol{z}}}{c}\left(1 + \frac{1}{2}\frac{\bar{\omega}_{\mathrm{pe}}^2}{\omega_0^2}\right). \tag{2.101}$$

Thus, substituting the result into (2.100), we arrive at the following expression for the range resolution:

$$\Delta_R = R_{\boldsymbol{y}} - R_{\boldsymbol{z}} \approx \frac{\pi c}{B}\left(1 - \frac{1}{2}\frac{\bar{\omega}_{\mathrm{pe}}^2}{\omega_0^2}\right). \tag{2.102}$$

The resolution given by formula (2.102) is an improvement over the non-corrected case (2.71) because it is basically as good as the non-dispersive resolution $\Delta_R = \pi c/B$. However, as indicated in Section 2.4.1, the range resolution of a SAR sensor does not suffer much from the ionospheric dispersion in any event. Therefore, what is even more important is that when the filter is corrected, the target is no longer shifted in range from its true position as in formula (2.73). That is because the maximum of the sinc in formula (2.98) is attained precisely at $R_{\boldsymbol{y}} = R_{\boldsymbol{z}}$.

What is also very important is that the degradation of image sharpness becomes negligible once the filter has been corrected. To analyze this effect, we bring back the quadratic term in the exponent under the integral (2.97). First, we recast this integral in the form

$$W_R'(\boldsymbol{y}, \boldsymbol{z}) \propto \int_{-\tau''(\boldsymbol{y})/2}^{\tau''(\boldsymbol{y})/2} e^{i\gamma u^2} e^{i\zeta u} du, \tag{2.103}$$

where

$$\gamma = \alpha''(\boldsymbol{z}) - \alpha''(\boldsymbol{y}) = \frac{B}{\tau^2}(\delta\tau(\boldsymbol{y}) - \delta\tau(\boldsymbol{z})) = \frac{B}{\tau^2}\frac{2(R_{\boldsymbol{y}} - R_z)}{c}\frac{4\pi e^2}{m_{\mathrm{e}}\omega_0^2}\frac{B}{\omega_0}\mathcal{N}, \tag{2.104}$$

$$\zeta = 4\alpha''(\boldsymbol{z})(T_{\mathrm{gr}}(\boldsymbol{y}) - T_{\mathrm{gr}}(\boldsymbol{z})), \tag{2.105}$$

and the quantity $\mathcal{N}$ is defined in formula (2.58). The quadratic term in the exponent under the integral (2.103) is small: $|\gamma u^2| \ll 1$ for $u \in [-\tau''(\boldsymbol{y})/2, \tau''(\boldsymbol{y})/2]$, and consequently we have:

$$\begin{aligned} W'_R(\boldsymbol{y}, \boldsymbol{z}) &\approx \int_{-\tau''(\boldsymbol{y})/2}^{\tau''(\boldsymbol{y})/2} (1 + i\gamma u^2) e^{i\zeta u} du \\ &= \tau'' \operatorname{sinc}[2\alpha'(\boldsymbol{z})(T_{\mathrm{gr}}(\boldsymbol{y}) - T_{\mathrm{gr}}(\boldsymbol{z}))\tau''] + i\gamma \frac{4\zeta\tau'' \cos\frac{\zeta\tau''}{2} + (-8 + \zeta^2\tau''^2)\sin\frac{\zeta\tau''}{2}}{2\zeta^3}, \end{aligned} \tag{2.106}$$

where $\tau'' = \tau''(\boldsymbol{y})$. The first term on the right-hand side of (2.106) obviously coincides with (2.98), and the second term represents a correction. According to (2.104) and (2.105), (2.101), both γ and ζ vanish as $R_{\boldsymbol{y}}$ approaches $R_{\boldsymbol{z}}$. However, the fraction on the right-hand side of (2.106) remains bounded as $\zeta \to 0$ (and $\gamma \to 0$). It is, in fact, easy to see that

$$W'_R(\boldsymbol{y}, \boldsymbol{z}) \approx \tau'' \operatorname{sinc}[2\alpha''(\boldsymbol{z})(T_{\mathrm{gr}}(\boldsymbol{y}) - T_{\mathrm{gr}}(\boldsymbol{z}))\tau''] + \frac{3}{16} i\gamma\tau''^3. \tag{2.107}$$

As the first term on the right-hand side of (2.107) is proportional to τ'', the relative magnitude of the correction is about $\gamma\tau''^2$ (this is a dimensionless quantity). There is no correction at the central peak of the sinc, because $\gamma = 0$ when $R_{\boldsymbol{y}} = R_{\boldsymbol{z}}$. To quantify the extent to what the image sharpness is affected, we estimate the correction at the first zero of the sinc. Using formulae (2.104) and (2.96), we obtain:

$$\gamma\tau''^2 = B\frac{2(R_{\boldsymbol{y}} - R_z)}{c}\frac{4\pi e^2}{m_{\mathrm{e}}\omega_0^2}\frac{B}{\omega_0}\mathcal{N}\left(1 - \frac{2\delta\tau}{\tau}\right)^2,$$

where the value of $R_{\boldsymbol{y}} - R_{\boldsymbol{z}}$ shall be taken according to formula (2.102). For the typical values of the parameters involved, Table 1.1, we have

$$\frac{4\pi e^2}{m_{\mathrm{e}}\omega_0^2}\mathcal{N} \approx \frac{\bar{\omega}_{\mathrm{pe}}^2}{\omega_0^2} \sim 9 \times 10^{-4} \quad \text{and} \quad \frac{B}{\omega_0} \sim 10^{-2},$$

so that altogether we can write:

$$\frac{3}{16}\gamma\tau''^2 \approx \frac{3\pi}{8}\frac{\bar{\omega}_{\mathrm{pe}}^2}{\omega_0^2}\frac{B}{\omega_0}\left(1 - \frac{1}{2}\frac{\bar{\omega}_{\mathrm{pe}}^2}{\omega_0^2}\right)\left(1 - \frac{4\delta\tau}{\tau}\right) \sim \frac{3\pi}{4} \cdot 10^{-5}.$$

We therefore conclude that the degradation of image contrast in range decreases to approximately 0.003% as opposed to 20% in the non-corrected case, see formula (2.72). Again, this is assuming that the TEC is reconstructed exactly.

2.7.2 Azimuthal resolution

Once the matched filter has been corrected, expression (2.61) for the azimuthal component of the generalized ambiguity function becomes

$$W'_A(\boldsymbol{y},\boldsymbol{z}) = \sum_{n=-N/2}^{N/2} e^{2i\omega_0(T_{\mathrm{ph}}(\boldsymbol{x}^n,\boldsymbol{y},\omega_0)-T_{\mathrm{ph}}(\boldsymbol{x}^n,\boldsymbol{z},\omega_0))}. \tag{2.108}$$

Then, using formulae (2.56b) and (2.76), we can transform expression (2.108) into:

$$W'_A(\boldsymbol{y},\boldsymbol{z}) \propto \sum_{n=-N/2}^{N/2} e^{\frac{2i\omega_0}{c}\left[-\frac{y_1 x_1^n}{R}\left(1-\frac{1}{2}\frac{4\pi e^2}{m_{\mathrm{e}}\omega_0^2}\mathcal{N}\right)\right]}, \tag{2.109}$$

where the constant factor of unit magnitude in front of the sum was dropped. The result is another sinc function, and it leads to the following estimate of the azimuthal resolution in the case of a non-fluctuating ionosphere:

$$2y_1 \approx \frac{L}{2}\left(1+\frac{1}{2}\frac{4\pi e^2}{m_{\mathrm{e}}\omega_0^2}\mathcal{N}\right) = \frac{L}{2}\left(1+\frac{1}{2}\frac{\bar{\omega}_{\mathrm{pe}}^2}{\omega_0^2}\right).$$

This value is only marginally worse than that obtained in the non-dispersive case: $2y_1 = L/2$. Even more important, correction of the filter restores the sharpness of the image for the non-fluctuating ionosphere, so that there is no deterioration like in the non-corrected case, see formula (2.80). The reason is that unlike in formula (2.75), there is no quadratic term with respect to x_1^n in the exponent in the sum (2.109).

We have seen that dual carrier probing can dramatically improve the quality of a SAR image. However, the analysis in this section neglects one important detail: in practice, the TEC will never be reconstructed exactly. As seen in Appendix G, formula (2.94) is poorly conditioned. Any errors in $R_y^{(1)}$ and $R_y^{(2)}$ will significantly affect the determined Langmuir frequency $\bar{\omega}_{\mathrm{pe}}^2$ and thus the determined TEC. A method to improve the conditioning and accuracy of the TEC reconstruction is proposed in Section 2.8; it is based on image registration [ZF03]. However, even the most advanced registration techniques carry a certain error, which, in turn, will affect the computed value of the TEC. In Section 2.9, we analyze the resulting errors in the corrected matched filter and the residual distortions of the image that occur when the TEC is not reconstructed exactly.

2.8 Robust evaluation of ionospheric parameters by dual-carrier probing combined with image registration

In the previous sections, it has been demonstrated how mismatches between the direct and inverse operators (formulae (2.62) and (2.29), respectively) result in image distortions of various kinds. For a horizontally homogeneous ionosphere (Section 2.4), these mismatches include a substantial displacement of the entire image in range, as well as both range and azimuthal smearing. Horizontal inhomogeneity of the ionosphere (Section 2.5) adds an azimuthal displacement that may sometimes be of the same magnitude as the range displacement. Our goal is to remove (or reduce) the mismatches and thus reduce the image distortions. The mismatches originate from the difference between the actual phase and group travel times of radar signals in the ionosphere [formulae (2.38)–(2.52)] and the expression $|\boldsymbol{x} - \boldsymbol{z}|/c$ in (2.29) that is based on the speed of light in vacuum. Hence, it is necessary to evaluate the parameters of the ionospheric plasma that appear in formulae (2.50), (2.53), and (2.87).

The approach to correcting the ionospheric distortions based on dual-carrier probing assumes that at the first stage, two SAR images of the same area at the same time are acquired using two different carrier frequencies and a filter with no correction. Each of the two images will be displaced from the ground truth, but the magnitude of the displacement will depend on the carrier frequency, see (2.73). In doing so, the difference between the two values of the displacement allows one to estimate the parameter $\bar{\omega}_{\mathrm{pe}}^2$ given by (2.92). This has been demonstrated in section 2.6. The next step is that $\bar{\omega}_{\mathrm{pe}}^2$ is substituted into formulae (2.50), which helps determine the phase and group travel times (2.49) and the new chirp rate and length (2.52). These quantities, in turn, are used to build a new filter $\overline{P'}$ based on (2.40) that would match the actual signal that propagates through the ionosphere (2.38). The distortions of the image obtained with the help of the new filter will be reduced or removed. We have seen this in Section 2.7 but there are still more effects to account for, namely the horizontal inhomogeneity of the ionosphere introduced in Section 2.5.

Following the argument used previously, we assume that there exists a point-like object in the scene that is imaged at two different slant distances $R_{\boldsymbol{y}}^{(1)}$ and $R_{\boldsymbol{y}}^{(2)}$ using carrier frequencies ω_1 and ω_2. Then, a similar approach to that used in section 2.6 can be used to reconstruct the horizontal inhomogeneity parameter $\mathcal{Q}$ from the measurements of the azimuthal displacement S_A on two images. According to (2.90), the azimuthal coordinates $y_1^{(1)}$ and $y_1^{(2)}$ of a given object

on two images are related to its true azimuthal coordinate z_1 by

$$y_1^{(1)} = z_1 + \frac{1}{2}\frac{\bar{\omega}_{\rm pe}^2}{\omega_1^2}\mathcal{Q}R^2,$$
$$y_1^{(2)} = z_1 + \frac{1}{2}\frac{\bar{\omega}_{\rm pe}^2}{\omega_2^2}\mathcal{Q}R^2,$$

which yields

$$\bar{\omega}_{\rm pe}^2\mathcal{Q}R^2 = \frac{2\omega_1^2\omega_2^2\Delta y_1}{\omega_2^2-\omega_1^2}, \quad \text{where} \quad \Delta y_1 \equiv y_1^{(1)} - y_1^{(2)}. \tag{2.110}$$

Formulae (2.94) and (2.110) allow one to reconstruct the ionospheric parameters $\bar{\omega}_{\rm pe}^2$ and $\mathcal{Q}$ that are responsible for the filter mismatch between $\overline{P}$ in (2.29) and P' in (2.40). The deficiencies of this method include the following:

(i) Formula (2.94) involves a small quantity $\Delta R_{\boldsymbol{y}} = R_{\boldsymbol{y}}^{(1)} - R_{\boldsymbol{y}}^{(2)}$ defined as a difference of two large quantities. Hence, this formula is poorly conditioned, i.e., sensitive to errors in the input data $R_{\boldsymbol{y}}^{(1)}$ and $R_{\boldsymbol{y}}^{(2)}$, see [ST11].

(ii) The method of (2.91)–(2.94) requires having point-like objects in the scene. Yet the initial images built using the uncorrected filter may be smeared because of the chirp rate mismatches (Section 2.4). With no sharp objects, the measurements of $R_{\boldsymbol{y}}^{(1)}$ and $R_{\boldsymbol{y}}^{(2)}$ should use diffuse objects and/or brightness gradients, which reduces the accuracy and further aggravates the problem outlined in item (i). Additional complication comes from the fact that the extent of smearing depends on the radar frequency, and thus one and the same object may appear different in two images.

(iii) Expression (2.94) yields a single value of $\bar{\omega}_{\rm pe}^2$, whereas the electron number density may, in fact, vary over the scale of the image, so that different values of the TEC may be needed for different parts of the image.

In Appendix G, which follows up on our prior work [ST11], we address the issue of conditioning of formula (2.94) by exploiting multiple pairs of $(R_{\boldsymbol{y}}^{(1)}, R_{\boldsymbol{y}}^{(2)})$ chosen over the image, so that the result given by (2.94) is averaged over the set of those pairs. If the values of $\bar{\omega}_{\rm pe}^2$ obtained for individual pairs are interpreted as independent random variables, then this approach may reduce the total error by a factor of $\sqrt{L}$, where L is the number of pairs. It, however, puts an even higher demand on the availability of sharp objects (item (ii)), whereas if the TEC varies over the image (item (iii)), there will be little or no improvement.

In the current section, instead of determining the range values $R_{\boldsymbol{y}}$ from individual images, we follow the approach of [GST13a] and propose to calculate the shift between the two images using registration techniques [ZF03]. The key advantage of the registration approach is that

it determines the value of $\Delta R_{\boldsymbol{y}}$ directly, as opposed to computing it as the difference of two much larger values. While there is still a need to know $R_{\boldsymbol{y}}^{(1)}$ and $R_{\boldsymbol{y}}^{(2)}$ individually to calculate the denominator in (2.94), it has been shown in Section 2.6 that it is the quantity $\Delta R_{\boldsymbol{y}}$ in the numerator of (2.94) that is primarily responsible for the poor conditioning of the formula.

A particular registration method that can be used is known as phase correlation [KH75, KBP79]. It belongs to the family of area-based image registration techniques [ZF03].[9] Consider two functions of a single real argument: $u(x)$ and $v(x) \equiv u(x-s)$, where s is the unknown shift. Then, for the Fourier transforms of u and v we have:

$$\hat{u}(\kappa) = \int_{-\infty}^{\infty} u(x) e^{-i\kappa x} dx \quad \Rightarrow \quad \hat{v}(\kappa) = \int_{-\infty}^{\infty} u(x-s) e^{-i\kappa x} dx = e^{-i\kappa s} \hat{u}(\kappa). \tag{2.111}$$

Therefore,

$$\tilde{\delta}(x) \stackrel{\text{def}}{=} \int_{-\infty}^{\infty} \frac{\hat{u}^*(\kappa)\hat{v}(\kappa)}{|\hat{u}^*(\kappa)\hat{v}(\kappa)|} e^{i\kappa x} d\kappa = \int_{-\infty}^{\infty} e^{-i\kappa s} e^{i\kappa x} d\kappa = 2\pi\delta(x-s), \tag{2.112}$$

where asterisk (*) denotes complex conjugation. The idea of phase correlation for the area-based image registration is to look for the value of x that delivers the maximum to $\tilde{\delta}(x)$ of (2.112). In the ideal world, $\tilde{\delta}(x)$ peaks exactly at s, so the approach immediately yields the shift. Moreover, one can interpret the shift obtained this way as an independent quantity rather than the difference $\Delta R_{\boldsymbol{y}}$ of two large distances, as in the original formula (2.94). In the real world, one uses a discrete Fourier transforms instead of both (2.111) and (2.112). This leads to the usual ambiguities due to the finite size of the image and finite size of the grid, on which the discrete transform is done, and the result is not a pure δ-function any more. It is rather a grid function with its maximum at the node closest to $x = s$, see Appendix H. This brings the accuracy of determining the shift s to half the grid size, which has a lower bound of half the pixel size. Additional steps can be taken to improve this accuracy further, and also to mitigate the component of the error due to the presence of noise, see [MM93]. Altogether, the error of determining the shift s by phase correlation decreases as $L^{-1/2}$, see formula (H.8), where L is the dimension of the discrete Fourier transform.[10] It is fundamentally the same "inverse square root" behavior as appears in the feature-based registration. The advantage of the area-based approach is that by involving areas without distinct point-like features it helps increase the effective number of "pairs of the reference points," and thus improves the accuracy and robustness of the shift estimation. In practice, the best techniques currently available in the literature report the accuracy of the area-based image registration of only a few percent of the resolution cell, see [TH86, SOCM01, GSTF08, FZB02, Abd99].

We note that the functions $u(x)$ and $v(x)$ in formula (2.111), as well as in Appendix H,

[9] The technique of Appendix G, which exploits multiple objects, is an example of the feature-based registration.
[10] The value of L may not exceed the overall number of pixels in a given direction, see Appendix H.

represent the absolute value of the complex image $I(\boldsymbol{y})$. Correlation of complex images, called coherent cross correlation in [BE05], provides a better registration accuracy, but is only possible if frequency bands of the two images substantially overlap.

In Section 2.9, we show how the accuracy of registration affects the accuracy of TEC reconstruction by dual-carrier probing. We also analyze the residual distortions of SAR images. When making numerical estimates, we will assume that the registration accuracy, in both range and azimuthal direction, is 5% of the corresponding resolution.

2.9 Performance of the matched filter with ionospheric corrections

2.9.1 Implementation of ionospheric corrections into the matched filter

Let us recall that the goal of reconstructing the parameters of the ionosphere $\bar{\omega}_{\rm pe}^2$ and $\mathcal{Q}$ is to correct formula (2.29) [as well as formulae (2.30) and (2.31)], i.e., replace the filter $\overline{P(\boldsymbol{x},\boldsymbol{y},\omega_0)}$ by the complex conjugate of $P'(\boldsymbol{x},\boldsymbol{y},\omega_0)$ of (2.40), so that the mismatch between the filter and the dispersive propagator is removed. If $\bar{\omega}_{\rm pe}^2$ is known, then P' can be obtained by evaluating the travel times $T_{\rm ph}(\boldsymbol{x}^n,\boldsymbol{y},\omega_0)$ and $T_{\rm gr}(\boldsymbol{x}^n,\boldsymbol{y},\omega_0)$ with the help of formulae (2.49), (2.50), and also computing corrections to the chirp rate and duration using (2.52). Furthermore, if $\mathcal{Q}$ is known, then an additional correction to the phase travel time is given by formula (2.87), and a similar formula can be easily derived for the group travel time by flipping the sign in front of $\mathcal{Q}$ and replacing $\bar{v}_{\rm ph}$ by $\bar{v}_{\rm gr}$.

The ionospheric parameters $\bar{\omega}_{\rm pe}^2$ and $\mathcal{Q}$ are reconstructed using the dual-carrier approach of Section 2.8, i.e., by means of formulae (2.94) and (2.110). The values of $\Delta R_{\boldsymbol{y}}$ and Δy_1 entering these formulae are obtained by evaluating the shift between the two SAR images with the help of image registration (see Section 2.8 and Appendix H). In doing so, the accuracy of reconstructing $\bar{\omega}_{\rm pe}^2$ and $\mathcal{Q}$ will obviously depend on the accuracy of registration. The latter is discussed in Appendix H, and for the rest of this section we will analyze the effect of the registration errors on the performance of the corrected matched filter. In Section 2.7, we conducted similar analysis for a horizontally homogeneous ionosphere under the assumption that the TEC is reconstructed exactly.

2.9.2 Residual errors of corrected filter

Throughout this section, we are using the tilde above the symbol (e.g., $\tilde{\omega}_{\rm pe}^2$, $\tilde{\alpha}$, $\tilde{W}_R$) to denote the quantities computed with the help of the reconstructed TEC.

2.9.2.1 Range factor.

The analysis of the range factor of the GAF will be based on formula (2.60) with the replacement

$$\overline{A(t-2|\boldsymbol{y}-\boldsymbol{x}^0|/c)} \mapsto \overline{A_{2\delta}(t-2|\boldsymbol{y}-\boldsymbol{x}^0|/\tilde{v}_{\mathrm{gr}})}, \quad \text{where} \quad \tilde{v}_{\mathrm{gr}} = c\left(1-\frac{1}{2}\frac{\tilde{\omega}_{\mathrm{pe}}^2}{\omega_0^2}\right).$$

Note that the quantity Q does not contribute to $\tilde{T}_{\mathrm{gr}}(\boldsymbol{x}^0,\boldsymbol{y},\omega_0)$ because $x_1^0 = 0$, so that $\tilde{T}_{\mathrm{gr}}(\boldsymbol{x}^0,\boldsymbol{y},\omega_0) = |\boldsymbol{y}-\boldsymbol{x}^0|/\tilde{v}_{\mathrm{gr}}(\omega_0)$ [cf. formula (2.87)]. Changing the integration variable from t to $u = t-\big(\tilde{T}_{\mathrm{gr}}(\boldsymbol{x}^0,\boldsymbol{y},\omega_0)+T_{\mathrm{gr}}(\boldsymbol{x}^0,\boldsymbol{z},\omega_0)\big)$, we obtain [similarly to obtaining (2.66) from (2.63)]:

$$\tilde{W}_R(\boldsymbol{y},\boldsymbol{z}) \propto \int_{-\tilde{\tau}/2}^{\tilde{\tau}/2} e^{i\tilde{a}u^2+i\tilde{b}u}du, \tag{2.113}$$

where [cf. formulae (2.52), (2.64), and (2.65)]

$$\begin{gathered}\tilde{\tau} = \tau - 2\delta\tilde{\tau}(\boldsymbol{y}) = \tau - 2\frac{|\boldsymbol{y}-\boldsymbol{x}^0|}{c}\frac{\tilde{\omega}_{\mathrm{pe}}^2}{\omega_0^2}\frac{B}{\omega_0}, \quad \tilde{\alpha} = \alpha + 2\delta\tilde{\alpha}(\boldsymbol{y}) = \alpha + 2\frac{\delta\tilde{\tau}}{2}\frac{B}{\tau^2}, \\ \tilde{a} = \alpha'' - \tilde{\alpha}, \quad \text{and} \quad \tilde{b} = \tilde{b}(\boldsymbol{y},\boldsymbol{z}) = 2(\alpha''+\alpha)\left(\frac{|\boldsymbol{y}-\boldsymbol{x}^0|}{\tilde{v}_{\mathrm{gr}}} - \frac{|\boldsymbol{z}-\boldsymbol{x}^0|}{\bar{v}_{\mathrm{gr}}}\right).\end{gathered} \tag{2.114}$$

As in Section 2.4, we first disregard the quadratic phase term under the integral in (2.113), in which case it approximately evaluates to [cf. formula (2.69)]

$$\tilde{W}_R(\boldsymbol{y},\boldsymbol{z}) \propto \tilde{\tau}\,\mathrm{sinc}\left(\frac{\tilde{b}\tilde{\tau}}{2}\right). \tag{2.115}$$

From (2.115) and (2.114), we obtain the new overall displacement of the image in range:

$$\tilde{S}_R = R_{\boldsymbol{y}}(\boldsymbol{z}) - R_{\boldsymbol{z}} \approx R_{\boldsymbol{z}}\frac{1}{2}\frac{\bar{\omega}_{\mathrm{pe}}^2 - \tilde{\omega}_{\mathrm{pe}}^2}{\omega_0^2}, \tag{2.116}$$

where $R_{\boldsymbol{y}}(\boldsymbol{z}) = c\tilde{T}_{\mathrm{gr}}\left(\boldsymbol{x}^0,\boldsymbol{z},\omega_0\right)$ and $R_{\boldsymbol{z}} = |\boldsymbol{z}-\boldsymbol{x}^0|$. Formula (2.116) shows that the displacement $\tilde{S}_R$ is directly proportional to the error of the reconstructed TEC. The two "extreme" cases here are no correction at all, i.e., no attempt to reconstruct the TEC, and the exact reconstruction of the TEC. If no filter correction is implemented, then one can set $\tilde{\omega}_{\mathrm{pe}}^2 = 0$ and formula (2.116) reduces to (2.73), whereas if the TEC is reconstructed exactly, then $\tilde{\omega}_{\mathrm{pe}}^2 = \bar{\omega}_{\mathrm{pe}}^2$ and $\tilde{S}_R = 0$, which is a result from Section 2.7.

To derive the new range resolution from (2.115) and (2.114), we set $\frac{(\alpha''+\alpha)\tilde{\Delta}_R\tilde{\tau}}{\tilde{v}_{\rm gr}} = \pi$ and get:

$$\tilde{\Delta}_R \approx \frac{\pi c}{B}\left(1 - \frac{(\delta\tau - \delta\tilde{\tau})}{\tau}\right)\left(1 - \frac{1}{2}\frac{\tilde{\omega}_{\rm pe}^2}{\omega_0^2}\right). \tag{2.117}$$

Again, with no correction $\tilde{\omega}_{\rm pe}^2 = 0$ and $\delta\tilde{\tau} = 0$, so that formula (2.117) reduces to (2.71).

To obtain quantitative estimates for (2.116) and (2.117), we need to relate the accuracy of reconstructing the TEC to the accuracy of registering the two images, i.e., accuracy of obtaining the shift $\Delta R_{\boldsymbol{y}}$ (Section 2.8 and Appendix H). Let us denote by $\delta(\bar{\omega}_{\rm pe}^2)$ and $\delta(\Delta R_{\boldsymbol{y}})$ the errors in determining $\bar{\omega}_{\rm pe}^2$ and $\Delta R_{\boldsymbol{y}}$, respectively. Then, according to (2.94) we can write:

$$\delta(\bar{\omega}_{\rm pe}^2) \stackrel{\rm def}{=} \bar{\omega}_{\rm pe}^2 - \tilde{\omega}_{\rm pe}^2 \approx \frac{2\omega_1^2\omega_2^2\delta(\Delta R_{\boldsymbol{y}})}{\omega_2^2 R_{\boldsymbol{y}}^{(2)} - \omega_1^2 R_{\boldsymbol{y}}^{(1)}}. \tag{2.118}$$

In turn, the error in evaluating the shift $\Delta R_{\boldsymbol{y}}$ can be taken as a fraction of the undistorted range resolution or, equivalently, a fraction of the pixel size (see Appendix H):

$$\delta(\Delta R_{\boldsymbol{y}}) \stackrel{\rm def}{=} \zeta_R \frac{\pi c}{B}. \tag{2.119}$$

Hence, combining formulae (2.116), (2.118), and (2.119), we can write:

$$\tilde{S}_R \approx R_{\boldsymbol{z}} \frac{\omega_2^2}{\omega_2^2 R_{\boldsymbol{y}}^{(2)} - \omega_1^2 R_{\boldsymbol{y}}^{(1)}} \zeta_R \frac{\pi c}{B}, \tag{2.120}$$

where we have identified the central carrier frequency ω_0 with one of the two carrier frequencies used for dual-carrier probing, namely, ω_1.[11] Next, let us introduce the carrier frequency separation factor

$$Z \stackrel{\rm def}{=} \frac{|\omega_2 - \omega_1|}{\omega_1}, \tag{2.121}$$

and assume that $Z \ll 1$, which also implies $\frac{\omega_2+\omega_1}{\omega_1} \approx 2$. Then, given that $R_{\boldsymbol{z}} \approx R_y^{(1)} \approx R_{\boldsymbol{y}}^{(2)} \approx R$, formula (2.120) yields:

$$\tilde{S}_R \approx \frac{\zeta_R}{2Z}\frac{\pi c}{B}. \tag{2.122}$$

Remarkably, this estimate of the residual displacement given as a fraction of the range resolution $\frac{\pi c}{B}$ does not depend on the TEC. If, for example, $Z = 10\%$ ($\omega_1/2\pi = 300MHz$ as in Table 1.1 and $\omega_2/2\pi = 330MHz$), and the dimensionless factor $\zeta_R = 0.05 = 5\%$, which is reasonable for sub-pixel registration, then formula (2.122) yields $\tilde{S}_R \approx 5.5m$. This is a most noticeable improvement over $S_R \approx 450m$ given by formula (2.73). In other words, with the filter correction in effect, the

[11] In fact, ω_0 can be identified either with ω_1 or with ω_2.

displacement of the image in range is practically removed. As for the range resolution (2.117), it shows little change compared to either (2.71) or the undistorted value $\frac{\pi c}{B}$.

What the correction of the filter helps improve very substantially is the contrast/sharpness of the GAF. The corresponding estimate is given by formula (2.72) with the following QPE [see (2.64), (2.67), (2.114), (2.116), and (2.122)]:

$$\begin{aligned}\tilde{\phi}_{\mathrm{q}} &= |\tilde{a}|\frac{\tilde{\tau}^2}{4} = |\alpha'' - \tilde{\alpha}|\frac{\tilde{\tau}^2}{4} = 2|\delta\alpha - \delta\tilde{\alpha}|\frac{\tilde{\tau}^2}{4} = 2\alpha\frac{|\delta\alpha - \delta\tilde{\alpha}|}{\alpha}\frac{\tilde{\tau}^2}{4} = \frac{B}{\tau}\frac{|\delta\tau - \delta\tilde{\tau}|}{\tau}\frac{\tilde{\tau}^2}{4} \\ &\approx \frac{B}{\tau^2}\frac{R}{c}\left|\frac{\tilde{\omega}_{\mathrm{pe}}^2}{\omega_0^2} - \frac{\bar{\omega}_{\mathrm{pe}}^2}{\omega_0^2}\right|\frac{B}{\omega_0}\frac{\tilde{\tau}^2}{4} \approx \frac{B}{\tau^2}\frac{R}{c}\left|\frac{2\tilde{S}_R}{R}\right|\frac{B}{\omega_0}\frac{\tilde{\tau}^2}{4} = \frac{B}{\tau^2 c}2\frac{\zeta_R}{2Z}\frac{\pi c}{B}\frac{B}{\omega_0}\frac{\tilde{\tau}^2}{4} \approx \frac{\zeta_R}{4Z}\frac{\pi B}{\omega_0},\end{aligned} \tag{2.123}$$

which yields only about 0.2% of contrast deterioration for the parameters in Table 1.1, as opposed to 20% in the non-corrected case (2.72). If the TEC is reconstructed exactly, then the correction yields about 4 orders of magnitude of improvement, see Section 2.7.

Remark. Another way of comparing the initial shift and the residual shift (formulae (2.73) and (2.122), respectively) is to determine the TEC sensitivity, i.e., the minimal value of the TEC for which the correction is still beneficial. The carrier frequency separation factor Z in (2.122) cannot be made very large because of the technical limitations. In Appendix I, we analyze the extreme situation where the separation of carrier frequencies is capped by the single bandwidth. This is called a split bandwidth configuration. The analysis shows that in this case, the formulae for the residual shift and the TEC sensitivity have an inverse square dependence on the system bandwidth, see (I.4) and (I.5), as opposed to the inverse dependence on the bandwidth in (2.122).

2.9.2.2 Azimuthal factor.

The azimuthal factor of the GAF $\tilde{W}_A(\boldsymbol{y}, \boldsymbol{z})$ with the corrected filter will still be given by formula (2.75), where instead of (2.74) we substitute

$$\tilde{\Psi}_n = \frac{c(\tilde{T}_{\mathrm{ph}}(\boldsymbol{x}^n, \boldsymbol{y}, \omega_0) - T_{\mathrm{ph}}(\boldsymbol{x}^n, \boldsymbol{z}, \omega_0))}{R}. \tag{2.124}$$

Then, using formulae (2.50), (2.76), and (2.87) we can write:

$$\begin{aligned}\tilde{\Psi}_n \approx &\left(1 + \frac{(y_1 - x_1^n)^2}{2R^2}\right)\left(1 - \frac{1}{2}\frac{\tilde{\omega}_{\mathrm{pe}}^2}{\omega_0^2}[1 + \tilde{\mathcal{Q}}(x_1^n - y_1)]\right) \\ &- \left(1 + \frac{(x_1^n)^2}{2R^2}\right)\left(1 - \frac{1}{2}\frac{\bar{\omega}_{\mathrm{pe}}^2}{\omega_0^2}(1 + \mathcal{Q}x_1^n)\right) \\ \approx &- \frac{y_1 x_1^n}{R^2}\left(1 - \frac{1}{2}\frac{\tilde{\omega}_{\mathrm{pe}}^2}{\omega_0^2}\right) + \frac{\bar{\omega}_{\mathrm{pe}}^2 - \tilde{\omega}_{\mathrm{pe}}^2}{\omega_0^2}\frac{(x_1^n)^2}{4R^2} + \frac{\bar{\omega}_{\mathrm{pe}}^2\mathcal{Q} - \tilde{\omega}_{\mathrm{pe}}^2\tilde{\mathcal{Q}}}{2\omega_0^2}x_1^n + \mathrm{const},\end{aligned} \tag{2.125}$$

where we have dropped the small term $\frac{1}{2}\frac{\tilde{\omega}_{\rm pe}^2}{\omega_0^2}\frac{y_1 x_1^n}{R^2}\tilde{Q}(x_1^n - y_1)$, as well as all the terms $\sim (x_1^n)^3$, which are also small. The first term on the last line of (2.125) corresponds to the first term on the right-hand side of (2.89), whereas the second and third terms show the effect of the corrected filter on the azimuthal QPE and azimuthal displacement of the image, respectively. The term "const" combines everything that does not depend on n.

To evaluate the azimuthal displacement for the corrected filter using formula (2.125), we first introduce the dimensionless registration accuracy ζ_A as a fraction of the undistorted azimuthal resolution (2.81) [cf. formula (2.119)]:

$$\delta(\Delta y_1) \stackrel{\rm def}{=} \zeta_A \Delta_A = \zeta_A \frac{R}{2}\frac{\lambda}{L_{\rm SA}}. \tag{2.126}$$

Then, the error of reconstructing the quantity $\bar{\omega}_{\rm pe}^2 \mathcal{Q}$ can be obtained from formula (2.110) with the help of formulae (2.126) and (2.121):

$$\delta(\bar{\omega}_{\rm pe}^2 \mathcal{Q}) \stackrel{\rm def}{=} \bar{\omega}_{\rm pe}^2 \mathcal{Q} - \tilde{\omega}_{\rm pe}^2 \tilde{\mathcal{Q}} \approx \frac{1}{R^2}\frac{\omega_1^2\omega_2^2}{\omega_2^2 - \omega_1^2}\zeta_A R \frac{\lambda}{L_{\rm SA}} \approx \frac{\zeta_A}{2Z}\omega_0^2 \frac{\lambda}{R L_{\rm SA}}. \tag{2.127}$$

Formula (2.127), combined with (2.75) and (2.125), yields the residual azimuthal displacement of the image in the case of a corrected filter [cf. formula (2.90)]:

$$\tilde{S}_A = \frac{1}{2}R^2 \frac{\delta(\bar{\omega}_{\rm pe}^2 \mathcal{Q})}{\omega_0^2} = \frac{\zeta_A}{2Z}\frac{R}{2}\frac{\lambda}{L_{\rm SA}}, \tag{2.128}$$

which is approximately $2.5m$ for the typical parameters given in Table 1.1. Note that formulae (2.122) and (2.128) are similar in the sense that both use the factors $\zeta_{R,A}/(2Z)$ to relate the residual displacement of the image $\tilde{S}_R$ and $\tilde{S}_A$ to the range and azimuthal resolution given by formulae (2.71) and (2.81), respectively.

Similarly to the range resolution (2.117), the new azimuthal resolution obtained with the help of formulae (2.75) and (2.125)

$$\tilde{\Delta}_A = \frac{1}{2}\frac{\lambda_0 R}{L_{\rm SA}}\left(1 + \frac{1}{2}\frac{\tilde{\omega}_{\rm pe}^2}{\omega_0^2}\right)$$

shows little change after the correction of the filter [i.e., little change compared to (2.81)]. Yet the GAF contrast in the azimuthal direction improves very substantially. Indeed, the new value of the parameter $\hat{a}$ [see formulae (2.78) and (2.79)] due to the second term on the last line of (2.125) differs from the one that corresponds to (2.77) [or (2.89)] by a factor of $\delta(\bar{\omega}_{\rm pe}^2)/\bar{\omega}_{\rm pe}^2$. Hence, the same will be the reduction of the azimuthal QPE, and using formulae (2.118),

(2.119), and (2.82) we get:

$$\tilde{\phi}_{\mathrm{qA}} = \phi_{\mathrm{qA}} \frac{\delta(\bar{\omega}_{\mathrm{pe}}^2)}{\bar{\omega}_{\mathrm{pe}}^2} = \frac{\zeta_R}{8Z} \frac{\pi \omega_0 L_{\mathrm{SA}}^2}{R^2 B}. \tag{2.129}$$

Expression (2.129) leads to only about 0.4% of deterioration of the GAF contrast in azimuth, as opposed to 35% given by formula (2.82).

2.10 The effect of ionospheric turbulence

In our previous analysis regarding correcting the matched filter we have assumed that the electron number density in the ionosphere was a regular function of the altitude h and, maybe, the horizontal coordinate x_1: $N_{\mathrm{e}} = N_{\mathrm{e}}(x_1, h)$, see Sections 2.4 and 2.5, as well as Appendices B and E. The actual Earth's ionosphere, however, is a turbulent medium, see Appendix D.

Turbulent fluctuations of the ionosphere will affect the group and phase travel times that are otherwise derived in Sections 2.4 and 2.5 with no account for randomness. Specifically, in the framework of Section 2.4, we assume that the mean electron number density depends only on the altitude: $\langle N_{\mathrm{e}} \rangle = \langle N_{\mathrm{e}}(h) \rangle$. Then, expressions (2.49) for T_{gr} and T_{ph} keep their form, and so do expressions (2.50) that introduce the average velocities. However, according to (2.9) (and (D.15), (D.16)), instead of formula (2.92) for the quantity $\bar{\omega}_{\mathrm{pe}}^2$ that enters into (2.50), we now need to write:

$$\begin{aligned} \bar{\omega}_{\mathrm{pe}}^2 &= \frac{1}{R_{\boldsymbol{z}}} \int_0^{R_{\boldsymbol{z}}} \omega_{\mathrm{pe}}^2(s) ds = \frac{4\pi e^2}{m_{\mathrm{e}} R_{\boldsymbol{z}}} \left[\int_0^H \langle N_{\mathrm{e}}(h) \rangle \frac{dh}{\cos\theta} + \int_0^{R_{\boldsymbol{z}}} \mu(s) ds \right] \\ &= \frac{4\pi e^2}{m_{\mathrm{e}} H} \int_0^H \langle N_{\mathrm{e}}(h) \rangle dh + \frac{4\pi e^2}{m_{\mathrm{e}} R_{\boldsymbol{z}}} \int_0^{R_{\boldsymbol{z}}} \mu(s) ds = \frac{4\pi e^2}{m_{\mathrm{e}}} \frac{N_H}{H} + \frac{4\pi e^2}{m_{\mathrm{e}} R_{\boldsymbol{z}}} \int_0^{R_{\boldsymbol{z}}} \mu(s) ds, \end{aligned} \tag{2.130}$$

where the new definition of the TEC is [cf. formula (2.54)]

$$N_H \stackrel{\mathrm{def}}{=} \int_0^H \langle N_{\mathrm{e}}(h) \rangle dh. \tag{2.131}$$

In the case of a horizontally inhomogeneous ionosphere (Section 2.5), for the group travel time T_{gr} we can write following (C.20) and taking into account (2.9):

$$\begin{aligned} T_{\mathrm{gr}}(\boldsymbol{x}, \boldsymbol{z}, \omega) &= \int_0^{R_{\boldsymbol{z}}} \frac{ds}{v_{\mathrm{ph}}(s)} \approx \frac{R_{\boldsymbol{z}}}{c} + \frac{1}{2c} \int_0^{R_{\boldsymbol{z}}} \frac{4\pi e^2}{m_{\mathrm{e}} \omega^2} (\langle N_{\mathrm{e}}(s) \rangle + \mu(s)) ds \\ &= \frac{R_{\boldsymbol{z}}}{c} + \frac{1}{2c \cos\theta} \int_0^H \frac{4\pi e^2}{m_{\mathrm{e}} \omega^2} \langle N_{\mathrm{e}}(\xi_1(h), h) \rangle dh + \frac{1}{2c} \int_0^{R_{\boldsymbol{z}}} \frac{4\pi e^2}{m_{\mathrm{e}} \omega^2} \mu(s) ds, \end{aligned} \tag{2.132}$$

which is slightly modified from (D.15) to account for the horizontal inhomogeneity. Similarly, for the phase travel time $T_{\rm ph}$ we can use (C.21) and (2.9) to modify (D.16):

$$\begin{aligned} T_{\rm ph}(\boldsymbol{x},\boldsymbol{z},\omega) &= \int_0^{R_z} \frac{ds}{v_{\rm ph}(s)} \approx \frac{R_{\boldsymbol{z}}}{c} - \frac{1}{2c}\int_0^{R_z} \frac{4\pi e^2}{m_{\rm e}\omega^2}(\langle N_{\rm e}(s)\rangle + \mu(s))ds \\ &= \frac{R_{\boldsymbol{z}}}{c} - \frac{1}{2c\cos\theta}\int_0^{H} \frac{4\pi e^2}{m_{\rm e}\omega^2}\langle N_{\rm e}(\xi_1(h),h)\rangle dh - \frac{1}{2c}\int_0^{R_z} \frac{4\pi e^2}{m_{\rm e}\omega^2}\mu(s)ds. \end{aligned} \tag{2.133}$$

The Taylor formula for $\langle N_{\rm e}\rangle = \langle N_{\rm e}(\xi_1,h)\rangle$ yields [cf. formula (2.83)]:

$$\langle N_{\rm e}(\xi_1,h)\rangle \approx \langle N_{\rm e}(0,h)\rangle + \xi_1\frac{\partial}{\partial\xi_1}\langle N_{\rm e}(0,h)\rangle, \tag{2.134}$$

and substituting the right-hand side of (2.134) into (2.132), we arrive at the same formula (2.87) as in Section 2.5, but with the new definitions of some of the expressions that it is comprised of. Namely, the quantity $\bar\omega_{\rm pe}^2$ enters into formula (2.87) through the average velocity $\bar v_{\rm ph}(\omega) = c\left(1+\frac{1}{2}\frac{\bar\omega_{\rm pe}^2}{\omega^2}\right)$, see (2.50), and according to (2.132), it should now be evaluated as follows [cf. formula (2.130)]:

$$\bar\omega_{\rm pe}^2 = \frac{4\pi e^2}{m_{\rm e}}\left[\frac{1}{H}\int_0^H \langle N_{\rm e}(0,h)\rangle dh + \frac{1}{R_{\boldsymbol{z}}}\int_0^{R_z}\mu(s)ds\right] = \frac{4\pi e^2}{m_{\rm e}}\frac{N_H}{H} + \frac{4\pi e^2}{m_{\rm e}R_{\boldsymbol{z}}}\int_0^{R_z}\mu(s)ds, \tag{2.135}$$

so that the TEC is re-defined again, this time via $\langle N_{\rm e}(0,h)\rangle$ [cf. formula (2.131)]:

$$N_H \stackrel{\rm def}{=} \int_0^H \langle N_{\rm e}(0,h)\rangle dh. \tag{2.136}$$

Moreover, the first moment $\mathcal{Q}(\boldsymbol{x}^0,\boldsymbol{z})$ that also enters into formula (2.87) is re-defined in the presence of turbulence according to (2.134) [cf. formula (2.88)]:

$$\mathcal{Q}(\boldsymbol{x}^0,\boldsymbol{z}) \stackrel{\rm def}{=} \frac{1}{H^2}\int_0^H \frac{4\pi e^2}{m_{\rm e}\bar\omega_{\rm pe}^2}\frac{\partial}{\partial\xi_1}\langle N_{\rm e}(0,h)\rangle h\, dh. \tag{2.137}$$

In doing so, we emphasize that the factor $\bar\omega_{\rm pe}^2$ appears in the second term on the right-hand side of (2.87) only for the convenience of notation. In fact, this second term does not depend on $\bar\omega_{\rm pe}^2$ because this quantity also appears in the denominator in (2.137). Hence, randomness contributes only to the first term on the right-hand side of (2.87) via (2.135).

Along with the travel times, turbulent fluctuations may impact the contraction and rate of the propagating pulse. Specifically, formulae (2.52) and (2.64) will remain unchanged, but the expression for $\delta\tau$ will now depend on $\bar\omega_{\rm pe}^2$ given by (2.130) or (2.135). Altogether, the new quantities will affect the dispersive propagator (2.38), (2.40), and through it, both the range

and azimuthal factor of the GAF, see formulae (2.60) and (2.61).

It turns out that the overall effect of turbulent fluctuations on the performance of the SAR sensor in range is small. More precisely, even though the quantity $\bar{\omega}_{\rm pe}^2$ that determines the shape of the propagating pulse (2.52), (2.64), as well as the displacement of the target in range (2.73), contains a stochastic component $\sim \int_0^{R_z} \mu(s)ds$, see (2.130), (2.135), this component is small because μ is ergodic and $\langle \mu \rangle = 0$. Indeed, let

$$\varphi_0 = \int_0^{R_z} \mu(s)ds, \qquad \langle \varphi_0 \rangle = 0, \tag{2.138}$$

denote the random contribution to the eikonal (up to a constant factor). Then, following [RKT89b, Chapter I], in the case of a homogeneous plasma we obtain with the help of (2.17) and (2.15):

$$\begin{aligned} \langle \varphi_0^2 \rangle &= \pi^2 R_{\boldsymbol{z}} \int_0^\infty \hat{V}(q) q dq = \pi^2 R_{\boldsymbol{z}} \frac{C q_0^2}{2(\kappa - 1)} \\ &= R_{\boldsymbol{z}} \langle \mu^2 \rangle \frac{\sqrt{\pi}\Gamma(\kappa)}{2 q_0 \Gamma(\kappa - \frac{3}{2})(\kappa - 1)} = \frac{R_z r_0}{2} \langle \mu^2 \rangle. \end{aligned}$$

For the inhomogeneous plasma, we can write following [RKT89b, Chapter I] and using (2.11):

$$\begin{aligned} \langle \varphi_0^2 \rangle &\approx \frac{r_0}{2} \int_0^{R_z} \langle \mu^2(s) \rangle ds = \frac{r_0}{2} M^2 \int_0^{R_z} \langle N_{\rm e}(s) \rangle^2 ds \\ &= \frac{r_0}{2} \frac{M^2}{\cos\theta} \int_0^H \langle N_{\rm e}(\xi_1(h), h) \rangle^2 dh \stackrel{\rm def}{=} \frac{r_0}{2} \frac{M^2}{\cos\theta} N_{2,H}, \end{aligned} \tag{2.139}$$

where according to [Arm05], the value of $N_{2,H}$ for high altitudes H is between $9.3 \cdot 10^{18} cm^{-5}$ and $9.9 \cdot 10^{20} cm^{-5}$, with the average of about $5 \cdot 10^{19} cm^{-5}$.

Next, we return to formula (2.132) for the travel time in the turbulent ionosphere and realize that the second term on its right hand side accounts for the contribution of the baseline, i.e., deterministic, dispersion, whereas the third term is responsible for that of the turbulent fluctuations. The magnitude of the second term is $\sim \frac{1}{c} \frac{4\pi e^2}{m_{\rm e}\omega^2} N_H$, while the magnitude of the third, random, term shall be estimated via its standard deviation, which yields $\sim \frac{1}{c} \frac{4\pi e^2}{m_{\rm e}\omega^2} \sqrt{\langle \varphi_0^2 \rangle}$. Hence, the ratio of the third term to the second one is

$$\frac{\sqrt{\langle \varphi_0^2 \rangle}}{N_H} \sim \frac{M \sqrt{r_0 N_{2,H}}}{N_H} \ll 1. \tag{2.140}$$

Indeed, the ratio (2.140) is approximately between $2 \cdot 10^{-4}$ and $7 \cdot 10^{-4}$ for the typical parameters listed in Table 1.1, including the correlation length r_0 that ranges between $10^5 cm$ and $10^6 cm$. Similarly, to see what the role of randomness is in determining the shape of the propagating

pulse we need to compare the standard deviation $\sqrt{\langle \delta\tau^2 \rangle}$ to the mean $\langle \delta\tau \rangle$, where $\delta\tau$ is defined by formula (2.52) and $\bar{\omega}_{\rm pe}^2$ is defined by formula (2.135). It is easy to see that the ratio $\frac{\sqrt{\langle \delta\tau^2 \rangle}}{\langle \delta\tau \rangle}$ evaluates to the same quantity as given by formula (2.140). We therefore conclude that the contribution of turbulent fluctuations to travel times, as well as to the change of the pulse duration and rate in the course of its propagation in the ionosphere, is much smaller than that of the baseline dispersion.

To evaluate the azimuthal factor (2.61) of the GAF, we denote similarly to (2.138)

$$\varphi_n = \int_0^{R_{\boldsymbol{z}}} \mu(s) ds, \tag{2.141}$$

and instead of (2.75) obtain:

$$W_A'(\boldsymbol{y}, \boldsymbol{z}) = \sum_{n=-N/2}^{N/2} e^{\frac{2i\omega_0}{c}\left(R\Psi_n + \frac{1}{2}\frac{4\pi e^2}{m_{\rm e}\omega_0^2}\varphi_n\right)}, \tag{2.142}$$

where [cf. formula (2.89)]

$$\Psi_n = -\frac{y_1 x_1^n}{R^2} + \frac{4\pi e^2}{m_{\rm e}\omega_0^2}\frac{N_H}{H}\frac{(x_1^n)^2}{4R^2} + \frac{\bar{\omega}_{\rm pe}^2}{2\omega_0^2}\mathcal{Q}x_1. \tag{2.143}$$

Formula (2.143) is written under the same assumptions of $z_1 = 0$ and $y_3 = z_3$ as in Section 2.4, and the TEC N_H is given by (2.136). Again, we note that the last term on the right-hand side of (2.143) does not depend on $\bar{\omega}_{\rm pe}^2$ because of the definition of Q (2.137).

Due to the central limit theorem [CH06, Chapter 2], each eikonal φ_n of (2.141) is a Gaussian random variable with zero mean, $\langle \varphi_n \rangle = 0$. Hence, the mean of each term of (2.142) is

$$\begin{aligned} \left\langle e^{\frac{2i\omega_0}{c}\left(R\Psi_n + \frac{1}{2}\frac{4\pi e^2}{m_e\omega_0^2}\varphi_n\right)} \right\rangle &= e^{\frac{2i\omega_0 R}{c}\Psi_n} \frac{1}{\sqrt{2\pi \langle \varphi_n^2 \rangle}} \int_{-\infty}^{\infty} e^{\frac{i\omega_0}{c}\frac{4\pi e^2}{m_e\omega_0^2}\xi} e^{-\frac{\xi^2}{2\langle \varphi_n^2 \rangle}} d\xi \\ &= e^{\frac{2i\omega_0 R}{c}\Psi_n} e^{-\frac{1}{2}\frac{\omega_0^2}{c^2}\left(\frac{4\pi e^2}{m_e\omega_0^2}\right)^2 \langle \varphi_n^2 \rangle}. \end{aligned} \tag{2.144}$$

The variances of all individual φ_n can be assumed approximately equal to one another because the variation of the integration distance $R_{\boldsymbol{z}}$ in (2.141) with respect to n is small compared to R, see (2.76):

$$\frac{\omega_0^2}{c^2}\left(\frac{4\pi e^2}{m_{\rm e}\omega_0^2}\right)^2 \langle \varphi_n^2 \rangle \approx \sigma^2, \qquad n = -N/2, \ldots, N/2.$$

Then, as shown in [Tsy09a], we have:

$$\langle W'_A(y_1,0)\rangle \;\propto\; e^{-\sigma^2/2} \sum_{n=-N/2}^{N/2} e^{\frac{2i\omega_0 R}{c}\Psi_n}, \tag{2.145}$$

where Ψ_n is given by (2.143) or, equivalently, (2.89) in the non-turbulent case. The factor $e^{-\sigma^2/2}$ in front of the sum on the right hand side of (2.145) represents the phenomenon of extinction, see [RKT89b, Chapter I]. The value of σ^2 for the typical parameters we have chosen, see Table 1.1, is $\sigma^2 \approx 0.058$ if $r_0 = 1km$, and $\sigma^2 \approx 0.58$ if $r_0 = 10km$. Other than the extinction, the sum on the right hand side of (2.145) is the same as that in (2.75); it controls the SAR performance in azimuth in the case of a non-fluctuating ionosphere.

While formula (2.145) shows that the mean value of the azimuthal factor of the GAF essentially coincides with its deterministic counterpart, the ionospheric turbulence still manifests itself through the presence of random eikonals φ_n in the exponents on the right-hand side of (2.142). The effect of randomness on the azimuthal resolution is stronger than that on the range resolution. The reason is that the range resolution is basically determined by a single look, and because of the ergodicity the contribution of turbulent fluctuations into the radar reading averages out, see formulae (2.138)–(2.140). On the contrary, azimuthal resolution is built using multiple looks, $n = -N/2, \ldots, N/2$, and whereas the contribution of randomness into each individual reading is still small, it can get amplified when those readings are summed up.

To quantify this "un-averaging" effect [Tsy09a], one needs to estimate the variance of the sum (2.142). Each term in this sum is a random variable with a logarithmically normal distribution [Gne97], and as long as those variables are uncorrelated, they are also independent [Tsy09a, Appendix F]. Therefore, the covariance of the received signals will also provide a measure of independence for the random variables in the sum (2.142). If the fluctuations of the phase are small, which is the case for our study, then the correlation function of the field is approximately equal to the correlation function of the electron number density (2.10), see [RKT89b, Chapter I]. Therefore, the correlation length r_0 given by formula (2.15) also provides a characteristic scale of how rapidly the received field decorrelates along the synthetic antenna. Roughly speaking, for the locations that are further apart than r_0 the received pulses will be uncorrelated and hence independent, whereas for the locations that are closer than r_0 they will not be independent.

Therefore, we follow the argument given in [Tsy09a]: the variances of the individual terms in the sum (2.142) are close to one another. Thus we can artificially split the synthetic array into several clusters of elements with the length r_0, and assume that the random variables from the sum (2.142) that belong to a given cluster are identical, whereas for different clusters they

are independent, see the argument between (2.144) and (2.145). An estimation for the total length of the array, L_{SA}, is given in Table 1.1 at $50km$. Therefore the number of clusters is $\sim \frac{L_{SA}}{r_0}$, and the number of elements in each cluster is

$$N_c \approx (N+1)\frac{r_0}{L_{SA}} \approx \frac{r_0}{\Delta x_1}.$$

This yields the variance of (2.142):

$$\sigma_\Sigma^2 = \frac{L_{SA}}{r_0} N_c^2 \sigma^2 \approx \frac{r_0}{L_{\mathrm{SA}}}(N+1)^2\sigma^2, \tag{2.146}$$

and as also shown in [Tsy09a], the corresponding relative change of the azimuthal resolution is $\sim \frac{\sigma}{2}\sqrt{\frac{r_0}{L_{\mathrm{SA}}}}$. For the typical parameters (see Table 1.1), this quantity is about 1.7% if $r_0 = 1km$, and 17% if $r_0 = 10km$. It may get even higher if the instantaneous values for M and $N_{2,H}$, see (2.11) and (2.139), happen to be larger than their typical averages.

The fact that the performance of the SAR system in range is only weakly sensitive to turbulent fluctuations indicates that the ionospheric turbulence will basically not affect any of the considerations of Sections 2.8 and 2.9 related to reconstructing the TEC with the help of formula (2.94), improving the robustness of reconstruction by means of the image registration, and assessing the quality of the image obtained with the corrected filter. At the same time, as the random contribution to individual travel times averages out, the proposed filter correction is essentially based on deterministic quantities only. As such, we do not expect that it will provide an efficient means for reducing the ionospheric distortions of the image that are due to the turbulence.

It is also to be noted that the conditioning of formula (2.110) may be better than that of formula (2.94) because the individual quantities $y_1^{(1)}$ and $y_1^{(2)}$ may not be as large compared to the azimuthal shift Δy_1. There may, however, be a potential difficulty of a different nature in evaluating $\mathcal{Q}$ by formula (2.110), because unlike the range resolution, the azimuthal resolution of a SAR system is sensitive to the turbulent fluctuations of the ionosphere, see formula (2.146). This sensitivity may induce larger errors in $y_1^{(1)}$ and $y_1^{(2)}$. Addressing the accuracy considerations for $\mathcal{Q}$ will be a subject of future study.

2.11 Chapter Summary

In this chapter, we have seen how the Earth's ionosphere can affect the performance of a satellite based SAR system operating in the P-band. The analysis was conducted for the simplest case of a scalar interrogating field propagating in an isotropic ionosphere. It was shown that the images generated by the system will be distorted in a number of ways due to a mismatch between the

received signal and the matched filter. Then, we have introduced and analyzed a method of probing the target, and hence the ionosphere, on two distinct carrier frequencies [ST11]. It can provide an accurate estimate of the ionospheric TEC, which subsequently helps correct the filter. However, this method appears poorly conditioned, meaning that small errors in the input data may result in large errors in the estimate of the TEC. The use of image registration can alleviate this issue and make the procedure both accurate and robust [GST13a]. There is no *perfect* reconstruction method for the TEC though, and thus we investigated how the errors of the reconstruction affect the performance of the corrected matched filter. We concluded this chapter with quantifying the effect of the ionospheric turbulence on spaceborne SAR images, which was done in the statistical sense. We saw, in particular, that turbulence mainly affects the azimuthal performance of the system. This analysis may help develop the future mitigation strategies for image distortions due to the ionospheric turbulence.

In the following chapter, we extend our approach to the case of polarized SAR signals propagating in an anisotropic (gyrotropic) ionosphere.

Chapter 3

Single-polarization SAR imaging in the presence of Faraday rotation

3.1 Introduction

This chapter is based on [GST13b].

As we have already seen, the Earth's ionosphere may have an adverse effect on spaceborne synthetic aperture radar (SAR) imaging. In [Tsy09a] and the previous chapter, it was shown that this adverse effect shall be attributed to the mismatch between the actual radar signal affected by the dispersion of radio waves in the ionospheric plasma, and the matched filter used for signal processing. Accordingly, to improve the image one should correct the filter, which requires knowledge of the total electron content (TEC) in the ionosphere along the signal path. The TEC, in turn, can be reconstructed by probing the ionosphere on two distinct carrier frequencies and exploiting the resulting redundancy in the data.

The analysis in [Tsy09a] and Chapter 2 was done under the assumption that the interrogating field is scalar, and that it propagates in an isotropic medium. In reality, however, the electromagnetic field is represented by vector quantities, and the ionospheric plasma is anisotropic (gyrotropic) due to the magnetic field of the Earth. The primary effect of gyrotropy on a linearly polarized electromagnetic wave is the Faraday rotation (FR). The FR is a slow rotation of the polarization plane due to the accumulating phase difference between the doubly refracted circularly polarized waves that form the original linear polarization. The phase difference accumulates because the two circularly polarized waves propagate with slightly different phase speeds in a gyrotropic plasma [Gin64, LL84].

The Faraday rotation may have both a positive and negative effect on the transionospheric SAR imaging. If the full polarimetric data are available, then one can reconstruct the FR angle for the radar pulse round-trip between the antenna on the orbit and the

target on the ground. The latter, in turn, can be used to obtain the TEC, see, e.g., [Gai98, WQWH03, FS04, MN08, JRZ+09] and [LP09, Section 10.4], although the resulting value of the TEC will be subject to ambiguities in the FR angle that can only be determined up to a constant multiple of 2π. If the full polarimetric data are not available, then, according to [WQWH03, FS04], an explicit a priori estimate of the Faraday rotation is required for understanding how the ionosphere affects the image. For single-polarization imaging, the FR yields an additional mismatch between the received signal and the filter. This mismatch can cause an adverse effect if, e.g., the returned linear polarization is (nearly) perpendicular to the emitted polarization, and hence perpendicular to the field direction that the antenna can receive efficiently. The previous scenario is by no means impossible, because the rotation angle in the P-band[1] can be quite large.

Even if the emitted and received polarizations are not close to perpendicular, the FR may still be detrimental for imaging. Indeed, the rotation angle may vary substantially along the radar chirp, in which case one can qualitatively think of the received signal as "twisted." This happens, in particular, when the carrier frequency is low (P-band) and the bandwidth is high (for better resolution). To the best of our knowledge, the twisting phenomenon has not received any attention in the previous studies of the Faraday rotation for SAR, see [Gai98, WQWH03, FS04, MN08, JRZ+09, LP09]. It is, however, very important, as it can cause substantial image artifacts, such as split intensity peaks, see Section 3.5.

To quantify the overall effect of the Faraday rotation on a spaceborne SAR image, we first notice that the impact of the magnetic field of the Earth on the dispersion of radio waves in the ionosphere is negligible, and therefore, the dispersive propagation and the Faraday rotation can be studied independently. Moreover, it turns out that the matched filter corrected for dispersion in the scalar framework, see [Tsy09a] and Chapter 2, will still eliminate the dispersion-induced distortions in the presence of gyrotropy, while leaving the FR effect intact. Hence, the latter can be analyzed regardless of the dispersion, i.e., as if the rotation accompanied a plain non-dispersive propagation (see Appendix K).

In the current chapter, we use the image autocorrelation analysis to quantify the effect of the Faraday rotation on a single-polarization spaceborne SAR image, and correct for the corresponding distortions. The presentation is organized as follows.

We briefly revisit the SAR ambiguity theory in Section 3.2. Section 3.3 describes the modification of the radar ambiguity function due to the FR. In Sections 3.4 and 3.5, we discuss how one can use the information from a given SAR image in order to detect the Faraday rotation and characterize its variation over the frequency band of the radar. Subsequently, the SAR filter can be corrected to match the actual received signal in the presence of the Faraday rotation

[1] Recall that P-band is the range of frequencies that partially overlaps with VHF and UHF, and which may be of interest for a number of SAR applications that require, say, some ground and/or foliage penetration.

and thus improve the quality of the image (Section 3.6). As in Chapter 2, a number of lengthy derivations have been moved to Appendices. Specifically, the FR of a chirped signal is analyzed in Appendix J, and the properties of the SAR ambiguity function in the presence of both the dispersion and FR are studied in Appendix K and Appendix L. Appendix A is also revisited.

3.2 Review of the SAR ambiguity theory

Referring back to Chapter 2, we recall that the sum (2.31) is called the generalized ambiguity function (GAF) of the SAR. The constant t^n in (2.30) can be removed by changing the integration variable (shifting). Then, noticing that the dependence of $\overline{A(u_{\boldsymbol{y}}^n)}$ and $A(u_{\boldsymbol{z}}^n)$ on n is through $\boldsymbol{x}^n$ and is therefore weak, we can pull these terms out of the summation over n, so that the GAF (2.31) can be factorized (see [ST11, GST13a, Che01, Cut90]):

$$W(\boldsymbol{y},\boldsymbol{z}) \approx W_A(\boldsymbol{y},\boldsymbol{z}) \cdot W_R(\boldsymbol{y},\boldsymbol{z}). \tag{3.1}$$

In formula (3.1),

$$W_A(\boldsymbol{y},\boldsymbol{z}) = \sum_{n=-N/2}^{N/2} e^{2i\omega_0(R_{\boldsymbol{y}}^n - R_{\boldsymbol{z}}^n)/c}, \tag{3.2}$$

$$W_R(\boldsymbol{y},\boldsymbol{z}) = \int_\chi \overline{A(u_{\boldsymbol{y}}^0)} A(u_{\boldsymbol{z}}^0)\, dt, \tag{3.3}$$

and the superscript "0" refers to formulae (2.30) for $\boldsymbol{x} = \boldsymbol{x}^0$. We emphasize that representation (3.1)–(3.3) is only approximate. The error of the factorization is analyzed in Appendix A and is shown to be small, of the order of $\frac{B}{\omega_0}$, see formula (A.19). Moreover, this error becomes even smaller (insignificant) if the target $\boldsymbol{z}$ and the reference point $\boldsymbol{y}$ have either the same range coordinate or the same azimuthal coordinate.

The range factor W_R of (3.3) is expressed as

$$W_R(\boldsymbol{y},\boldsymbol{z}) \approx \tau w_p(\xi) \equiv \tau w_p\Big(\pi \frac{R_{\boldsymbol{y}}^0 - R_{\boldsymbol{z}}^0}{\Delta_R}\Big), \quad \text{where} \quad \Delta_R = \frac{\pi c}{B}. \tag{3.4}$$

The quantity Δ_R in formula (3.4) is the range resolution, and

$$\begin{gathered} w_p(\xi) = \frac{1}{\tau}\int_\chi \overline{A(u_{\boldsymbol{y}}^0)} A(u_{\boldsymbol{z}}^0)\, dt \approx \frac{1}{\tau}\int_{-\tau/2}^{\tau/2} e^{ibu} du = \operatorname{sinc}\xi, \\ b = \frac{4\alpha(R_{\boldsymbol{y}}^0 - R_{\boldsymbol{z}}^0)}{c}, \quad \xi = \frac{b\tau}{2} = \pi\frac{R_{\boldsymbol{y}}^0 - R_{\boldsymbol{z}}^0}{\Delta_R} \approx \pi\frac{(y_2 - z_2)\sin\theta}{\Delta_R}. \end{gathered} \tag{3.5}$$

The function $w_p(\xi)$ of (3.5) defines the shape of the GAF in the range direction. Also note that $w_p(\xi) = \frac{1}{\tau} w_0\left(\frac{2\xi}{\tau}\right)$, where w_0 was used in the previous chapter and defined in (2.69).

Remark. In formula (3.5) [as well as in (3.18) below], we use $\pm\tau/2$ as the integration limits. In Appendix A, more accurate expressions for these limits are introduced: $\pm\tau^0/2$, where $\tau^0 = \tau - 2|R^0_{\boldsymbol{y}} - R^0_{\boldsymbol{z}}|/c$ [see formulae (A.4)–(A.5)]. Since for the high range resolution chirp we are assuming $B\tau \gg 1$ [CW05, JWE+96], one can show that

$$\frac{|\tau - \tau^0|}{\tau} = \frac{2|R^0_{\boldsymbol{y}} - R^0_{\boldsymbol{z}}|}{c\tau} \sim \frac{\Delta_R}{c\tau} = \frac{\pi}{B\tau} \ll 1,$$

so the difference is insignificant.

3.3 Ambiguity function in the presence of the Faraday rotation

The propagation of radar signals in the ionospheric plasma affects the SAR imaging in two ways. First, the temporal dispersion of radio waves alters the envelope and phase of the received signal, see [Tsy09a] and Chapter 2. Second, the magnetic field of the Earth causes the Faraday rotation, see [Gin64, WQWH03, DS02]. These distortions, if not accompanied by the proper corrections of the filter, lead to image deterioration due to the filter mismatch.

In Appendix J, we consider the effect of the FR on the chirped signals. For an antenna operating on a single linear polarization, the effective antenna signal in the presence of the rotation is related to the non-rotated signal $\psi(t, \boldsymbol{x})$ of (2.25) as

$$\psi_F(t, \boldsymbol{x}) = \psi(t, \boldsymbol{x}) \cos \varphi_F(\omega), \tag{3.6}$$

where φ_F is the rotation angle [see the top row of (J.18)]. For the two-way propagation in a magnetized plasma, the angle φ_F depends on the instantaneous frequency as

$$\varphi_F(\omega) = 2 \cdot \frac{R}{2c} \frac{\omega_{\mathrm{pe}}^2 \Omega \cos\beta}{\omega^2} \propto \omega^{-2} \tag{3.7}$$

[see also (J.19)], where R is the distance from the target to the orbit (300–1000 km), ω_{pe} is the Langmuir frequency, Ω is the electron cyclotron frequency, and β is the angle between the ray path and the magnetic field. For the actual ionosphere, the quantity $\omega_{\mathrm{pe}}^2 \Omega \cos\beta$ in (3.7) should be averaged over the ray path. Formula (3.7) shows that the low frequency and high frequency parts of the chirp (2.18) will be rotated by different angles and, according to (3.6), attenuated by different factors when received by the antenna.

Next, we approximate $\cos\varphi_F$ in (3.6) by the first two terms of its Taylor expansion w.r.t.

$u = t - 2R/c$, and, using (2.20), obtain:

$$\cos\varphi_F(u) \equiv \cos\varphi_F(\omega(u)) \approx p + \frac{2q}{\tau}u, \tag{3.8}$$

where

$$\begin{aligned} p =& \cos\varphi_F(\omega_0), \\ q =& \frac{\tau}{2}\frac{d\cos\varphi_F}{du}(\omega_0) = -\frac{\tau}{2}\sin\varphi_F\frac{d\varphi_F}{d\omega}\frac{d\omega}{du}(\omega_0) \\ \approx& \frac{BR}{c}\frac{\omega_{\rm pe}^2\Omega\cos\beta}{\omega_0^3}\sin\varphi_F(\omega_0) = \frac{B}{\omega_0}\varphi_F(\omega_0)\sin\varphi_F(\omega_0). \end{aligned} \tag{3.9}$$

Thus, the FR manifests itself by an additional attenuation of the signal received by the antenna, with the attenuation coefficient, $\cos\varphi_F$, varying over the chirp [see (3.6) and (3.8)]. Two non-dimensional constants, p and q, are introduced in (3.8), (3.9) to describe this effect. If we take the amplitude of the non-rotated antenna signal as 1, then, with the FR present, the amplitude at the center of the chirp is p, while the end-to-end variation over the chirp is $2q$. We have $|p| \leqslant 1$ by definition, and $|q| \ll 1$ as a condition of applicability of the Taylor linearization, see (3.8).

Of course, the use of linear approximation in (3.8) is justified only if the variation of $\cos\varphi_F$ over the chirp is small, i.e., $|q| \ll 1$. The Faraday rotation angle for $\omega_0/2\pi \lesssim 0.5\,GHz$ may reach $\pi/2$ for ionospheric propagation, see [DS02]. Taking $B/\omega_0 \sim 5\%$, we have about $0.1 \cdot \pi/2$ variation of the Faraday rotation angle over the chirp, see (3.9), which we consider sufficiently small for linearization.

As mentioned in Section 3.1, the cause of the FR is double circular refraction in a gyrotropic medium [LL84, Chapter XI], which results in different propagation speeds for two circular waves that form the original linear polarization, see also Appendix J for detail. In the dispersive yet rotation-less case, see [Tsy09a] and Chapter 2, correcting the filter for dispersive effects helps remove the corresponding image distortions, and the expression for the GAF becomes similar to that for the non-dispersive case. In Appendix K, we show that in the presence of both the dispersion and gyrotropy, such a filter will still eliminate the dispersion-related part of distortions, leaving the rotation effect intact. For that reason, for the rest of this chapter we assume that the FR accompanies a plain non-dispersive propagation of the radar signals described in Chapter 2. In a comprehensive setting, this means that the compensation of the Faraday rotation in the SAR filter discussed in Section 3.6 should be applied on top of the dispersion correction.

In the presence of the Faraday rotation, the imaging formula (2.29) transforms into

$$\begin{aligned} I_F(\boldsymbol{y}) &= \int_\chi \overline{P(t-2|\boldsymbol{x}-\boldsymbol{y}|/c)}\psi_F(t,\boldsymbol{x})\,dt \\ &= \int \tilde{\nu}(\boldsymbol{z})W_F(\boldsymbol{y},\boldsymbol{z})d\boldsymbol{z}, \end{aligned} \tag{3.10}$$

where $\psi_F(t,\boldsymbol{x})$ is given by (3.6) and the kernel $W_F(\boldsymbol{y},\boldsymbol{z})$ takes into account (3.8):

$$\begin{aligned} W_F(\boldsymbol{y},\boldsymbol{z}) &= \int_\chi \overline{P(u_{\boldsymbol{y}})}P(u_{\boldsymbol{z}})\cos\varphi_F(u_{\boldsymbol{z}})\,dt \\ &= pW(\boldsymbol{y},\boldsymbol{z}) + q\frac{2}{\tau}W_q(\boldsymbol{y},\boldsymbol{z}). \end{aligned} \tag{3.11}$$

In formula (3.11), $W(\boldsymbol{y},\boldsymbol{z})$ coincides with that of (2.29), and

$$W_q(\boldsymbol{y},\boldsymbol{z}) = \int_\chi \overline{P(u_{\boldsymbol{y}})}u_{\boldsymbol{z}}P(u_{\boldsymbol{z}})\,dt. \tag{3.12}$$

Remark. In the rest of this chapter, we will be using the subscript "q" to denote contributions due to the Faraday rotation, as in (3.12); in the isotropic case (i.e., when there is no magnetic field), these terms vanish. The subscript "F" will be used to denote the characteristics affected by the Faraday rotation, i.e., having both rotational and non-rotational "components," as on the left-hand side of (3.11); in the isotropic case, these expressions reduce to their isotropic counterparts, e.g., $W_F(\boldsymbol{y},\boldsymbol{z})$ in (3.11) reduces to $W(\boldsymbol{y},\boldsymbol{z})$ in (2.29).

For the sequence of emitted and received signals, definition (2.31) is replaced by (K.4) with primes dropped:

$$W_F(\boldsymbol{y},\boldsymbol{z}) = \sum_{n=-N/2}^{N/2} W_F^n(\boldsymbol{y},\boldsymbol{z}), \tag{3.13}$$

where $W_F^n(\boldsymbol{y},\boldsymbol{z})$ is given by the first line of (3.11). Using approximation (3.8), we can write:

$$W_F^n(\boldsymbol{y},\boldsymbol{z}) = pW^n(\boldsymbol{y},\boldsymbol{z}) + q\frac{2}{\tau}\int_\chi \overline{P(u_{\boldsymbol{y}}^n)}u_{\boldsymbol{z}}^n P(u_{\boldsymbol{z}}^n)\,dt, \tag{3.14}$$

where $W^n(\boldsymbol{y},\boldsymbol{z})$ is the same as in (2.30). An approximate factorization of the GAF (3.13), (3.14) similar to (3.1) is also possible:

$$W_F(\boldsymbol{y},\boldsymbol{z}) \approx W_A(\boldsymbol{y},\boldsymbol{z}) \cdot W_{RF}(\boldsymbol{y},\boldsymbol{z}), \tag{3.15}$$

where the azimuthal factor $W_A(\boldsymbol{y}, \boldsymbol{z})$ does not change and is still defined by (3.2), and

$$W_{RF}(\boldsymbol{y}, \boldsymbol{z}) = pW_R(\boldsymbol{y}, \boldsymbol{z}) + q\frac{2}{\tau}W_{qR}(\boldsymbol{y}, \boldsymbol{z}). \tag{3.16}$$

In formula (3.16), $W_R(\boldsymbol{y}, \boldsymbol{z})$ is given by (3.3), and

$$W_{qR}(\boldsymbol{y}, \boldsymbol{z}) = \int_\chi \overline{A(u^0_{\boldsymbol{y}})}u^0_{\boldsymbol{z}}A(u^0_{\boldsymbol{z}})\,dt. \tag{3.17}$$

Thus, the effect of the Faraday rotation results in a modification of the range factor in the approximate formula (3.15) compared to (3.1): $W_{RF}(\boldsymbol{y}, \boldsymbol{z})$ of (3.16), (3.17) replaces $W_R(\boldsymbol{y}, \boldsymbol{z})$ of (3.3). It is shown in Appendix L that the error due to the factorization (3.15) is small — of the same order as that for (3.1), i.e., about $\frac{B}{\omega_0}$, see formula (L.5).

Introducing a new dimensionless function

$$\begin{aligned} w_q(\xi) &\stackrel{\text{def}}{=} \frac{2}{i\tau^2}\int_\chi \overline{A(u^0_{\boldsymbol{y}})}u^0_{\boldsymbol{z}}A(u^0_{\boldsymbol{z}})\,dt \approx \frac{2}{i\tau^2}\int_{-\tau/2}^{\tau/2} ue^{ibu}du \\ &= \frac{2}{\tau^2}\frac{1}{i^2}\frac{d}{db}\int_{-\tau/2}^{\tau/2} e^{ibu}du = -\frac{d}{d\xi}w_p(\xi) = -w_p'(\xi), \end{aligned} \tag{3.18}$$

we can represent W_{RF} of (3.16) as

$$W_{RF}(\boldsymbol{y}, \boldsymbol{z}) = W_{RF}(\xi) = \tau\big(pw_p(\xi) + iqw_q(\xi)\big), \tag{3.19}$$

where w_p, b, and ξ are given by (3.5).

Remark. When integrating in (3.18), we have replaced τ^0 with τ, similarly to how we did it for w_p, see formula (3.5) and the subsequent remark. This introduces a small error. The formulae with no simplification can be found in Appendix L, see (L.4).

3.4 Detection of the Faraday rotation

The Faraday rotation affects the GAF $W_F(\boldsymbol{y}, \boldsymbol{z})$ via the range factor (3.19). It is to be noted that while the real part of the range ambiguity function W_{RF} in (3.19) is an even function of its argument, see (3.5), the imaginary part is proportional to $w_q = -w_p'$ and is therefore an odd function, see Figure 3.1 (the singularity of w_q at $\xi = 0$ is removable by setting $w_q(0) = 0$). As far as the relative contribution of w_p and w_q into W_{RF}, there are several qualitatively different regimes determined by the range of variation of the attenuation coefficient $\cos\varphi_F$ over the bandwidth, see (3.8).

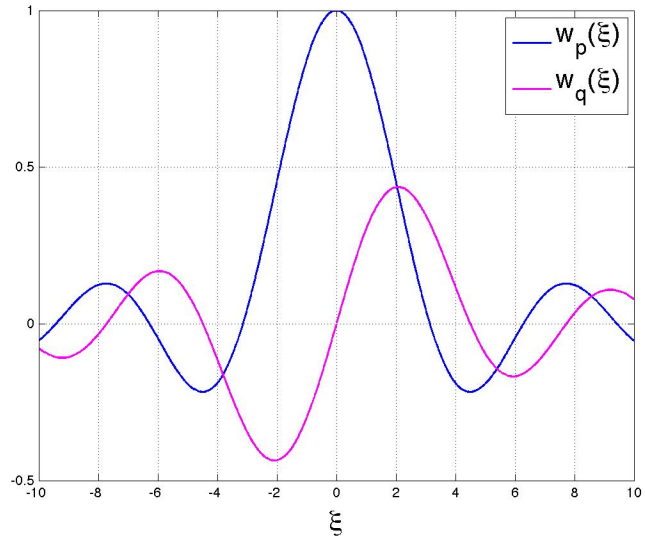

Figure 3.1: Components of the range factor (3.19) in the presence of the Faraday rotation.

(a) $|q| \ll |p|$: This is the case of nearly uniform attenuation where all possible φ_F's lie in a narrow range of angles, see Figure 3.2(a). In essence, it is this case that has been previously assumed in the literature when studying the Faraday rotation for SAR applications [Gai98, WQWH03, FS04, MN08, JRZ+09, LP09]. As the relative contribution of w_q is small, the correction for the Faraday rotation is not necessary. This is also the case where the detection of the Faraday rotation by a single-polarization instrument is difficult.

(b) $|p| \lesssim |q|$: The case of an intermediate range of φ_F, see Figure 3.2(b), that presents a challenge — the image is both attenuated and distorted by the Faraday rotation; yet if $p \neq 0$, the "double peak" feature of $w_q(\xi)$ is smeared out by the $pw_p(\xi)$ term in (3.19) and may not be easily observable.

(c) $|q| \gtrsim 1$: The range of φ_F is wide, see Figure 3.2(c), which is the opposite to case (a). The correction is required; however, the linearization of $\cos\varphi_F(u)$ in (3.8) is not valid. We do not consider this case hereafter.

The foregoing three cases can be very roughly discriminated by means of the sub-band processing. Assume that the entire bandwidth B of the signal is split, say, into three sub-bands of bandwidth $B/3$ each. The average of $\cos\varphi_F$ over a sub-band will be approximately the same for all sub-bands for case (a) and will vary substantially from one sub-band to another for cases (b) and (c), see Figure 3.2. Lower resolution images can be obtained by sub-band

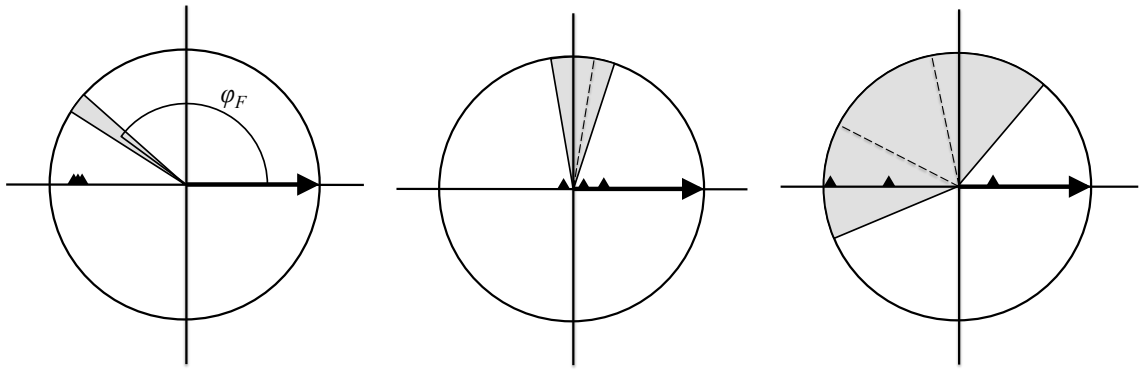

(a) Narrow range of φ_F (b) Intermediate range of φ_F (c) Wide range of φ_F

Figure 3.2: Examples of possible ranges of φ_F for the chirp propagating through a gyrotropic medium shown in a plane normal to the direction of propagation. The thick arrow indicates the polarization of the emitted field. The ranges for φ_F for $B/3$ sub-bands are shown by dashed lines according to (3.8), while the values of $\cos\varphi_F$ averaged over the sub-bands are indicated by triangles on the horizontal axis.

processing as seen in Appendix I, and a substantial variation between their intensities can be indicative of the presence of a significant Faraday rotation.

All subsequent analysis in this chapter applies primarily to the intermediate case (b).

3.5 Evaluation of the Faraday rotation effect

If the reflectivity of the target is not known, then in the problem of reconstruction of the Faraday rotation parameters from the image I_F we have one equation [cf. (2.29)]:

$$I_F(\boldsymbol{y}) = \int W_F(\boldsymbol{y}, \boldsymbol{z})\tilde{\nu}(\boldsymbol{z})d\boldsymbol{z} \tag{3.20}$$

with two unknowns: W_F of (3.15) and $\tilde{\nu}$. The information about the Faraday rotation is contained in W_F, but in order to retrieve this information from (3.20), we should make certain assumptions about the other unknown, i.e., $\tilde{\nu}$. Specifically, we adopt the model of a homogeneous distributed scatterer for $\tilde{\nu}(\boldsymbol{z})$, and subsequently employ the image autocorrelation analysis. Alternatively, see Section 2.8, one can use point scatterers: $\tilde{\nu}(\boldsymbol{z}) = \sum_m \nu_m \delta(\boldsymbol{z} - \boldsymbol{z}_m)$ so that (3.20) yields: $I_F(\boldsymbol{y}) = \sum_m \nu_m W_F(\boldsymbol{y}, \boldsymbol{z}_m)$. Considering $I_F(\boldsymbol{y})$ at sufficiently many reference locations $\boldsymbol{y}$ as given data, and taking into account that w_p and w_q in (3.19) are known analytically, one can obtain an overdetermined system of equations and solve it in a weak sense with respect to

p and q. In a practical setting, however, the problem with dominant point scatterers is their availability. That's why we subsequently focus on the approach suitable for distributed scatterers. Our goal is to find the parameters p and q that characterize the Faraday rotation, see (3.8) and (3.16). It turns out that only the ratio of those parameters can be obtained, but it proves sufficient to correct the filter, see Section 3.6.

We first notice that imaging in azimuth is not affected by the Faraday rotation, see (3.1) and (3.15), (3.16). Hence, we can exploit the decoupling between azimuth and range due to the factorization of the GAF. In other words, we can process the image in azimuth ahead of time and subsequently focus on the one-dimensional imaging with respect to the range coordinate only. To do so, we recast (3.20) as

$$I(y_1, y_2) = \iint_{-\infty}^{\infty} W_A(y_1, z_1) W_{RF}(R^0_{\boldsymbol{y}}, R^0_{\boldsymbol{z}}) \tilde{\nu}(z_1, z_2) dz_1 dz_2, \tag{3.21}$$

where W_A is given by (3.2), (2.37), W_{RF} is given by (3.16), (3.3), (3.17), and the arguments of W_A and W_{RF} in (3.21) emphasize their dependence on the azimuthal and range variables, respectively. We also assume that the function $\tilde{\nu}(z_1, z_2)$ in (3.21) already accounts for the transition from the volumetric reflectivity $\tilde{\nu}(\boldsymbol{z}) \equiv \tilde{\nu}(z_1, z_2, z_3)$ to the single layer $\tilde{\nu}(z_1, z_2)\delta(z_3)$ on the surface $z_3 = 0$, see Section 4.3 below.

The difference $R^0_{\boldsymbol{y}} - R^0_{\boldsymbol{z}}$, which enters the argument of W_{RF} via (3.19) and (3.5), does not depend on either y_1 or z_1, see formula (A.11) for $x_1^n = 0$. Therefore, equation (3.21) transforms into:

$$I(y_1, y_2) = \int_{-\infty}^{\infty} W_{RF}(y_2, z_2) \underbrace{\int_{-\infty}^{\infty} W_A(y_1, z_1) \tilde{\nu}(z_1, z_2) dz_1}_{\nu_R(y_1, z_2)} dz_2, \tag{3.22}$$

where $\nu_R(y_1, z_2)$ is already an image in the azimuthal direction, but still retains the meaning of a ground reflectivity in the range direction. Equation (3.22) can be considered independently for each y_1, which effectively implies one-dimensional imaging in range only. As such, we will henceforth use the plain non-indexed variables (y, z) instead of (y_2, z_2), and also drop y_1 from the arguments of I and ν_R. Then, formula (3.22) yields:

$$I(y) = \int_{-\infty}^{\infty} W_{RF}(y, z) \nu_R(z) dz, \tag{3.23}$$

where W_{RF} is, in fact, a single variable function: $W_{RF} = W_{RF}(y - z)$, see (3.19), (3.5).

To model a homogeneous distributed scatterer, we assume that $\nu_R(z)$ has a rapidly decaying

autocorrelation function (ACF) that we approximate by the delta function:

$$V_\nu(z) \stackrel{\text{def}}{=} \int_{-\infty}^{\infty} \nu_R(y-z)\bar{\nu}_R(y)dy \approx \sigma^2\delta(z). \tag{3.24}$$

The quantity σ^2 in formula (3.24) is the average backscattering intensity. The approximation in (3.24) shall be understood in the sense of distributions, so that for any appropriate test function $\phi(z)$ we have $\int V_\nu(z)\phi(z)dz \approx \sigma^2\phi(0)$. The assumption that the ground reflectivity has a short range autocorrelation function is common in the literature, see, e.g., [Que90, OQ98]. In practice, it means that the characteristic scale of the ACF of (3.24) is much shorter than the range resolution Δ_R.

With the help of (3.24), we can easily compute the ACF of the image $I(y)$ of (3.23):

$$\begin{aligned}
&\int_{-\infty}^{\infty} I(y)\bar{I}(y+h)dy \\
&= \int_{-\infty}^{\infty}\int_{-\infty}^{\infty} W_{RF}(y-z)\nu_R(z)dz \int_{-\infty}^{\infty} \bar{W}_{RF}(y+h-z')\bar{\nu}_R(z')dz'dy \\
&= \int_{-\infty}^{\infty}\int_{-\infty}^{\infty} W_{RF}(z)\nu_R(y-z)dz \int_{-\infty}^{\infty} \bar{W}_{RF}(z'+h)\bar{\nu}_R(y-z')dz'dy \\
&= \iiint_{-\infty}^{\infty} W_{RF}(z)\bar{W}_{RF}(z'+h)\nu_R(y-z)\bar{\nu}_R(y-z')dzdz'dy \\
&= \iint_{-\infty}^{\infty} W_{RF}(z)\bar{W}_{RF}(z'+h) \int_{-\infty}^{\infty} \nu_R(y-z)\bar{\nu}_R(y-z')dydzdz' \\
&= \iint_{-\infty}^{\infty} W_{RF}(z)\bar{W}_{RF}(z'+h)V_\nu(z-z')dzdz' \\
&= \sigma^2 \int_{-\infty}^{\infty} W_{RF}(z)\bar{W}_{RF}(z+h)dz.
\end{aligned} \tag{3.25}$$

Next, introduce a shorthand notation

$$w_1 * w_2 \equiv (w_1 * w_2)(\zeta) \stackrel{\text{def}}{=} \int_{\infty}^{\infty} w_1(\xi)w_2(\xi+\zeta)\,d\xi,$$

where $w_{1,2}$ denote any of the functions w_p or w_q, and $\zeta = Bh\sin\theta/c$. Then, using (3.19), we can transform the integral on the right-hand side of (3.25) as follows:

$$\int_{-\infty}^{\infty} W_{RF}(z)\bar{W}_{RF}(z+h)dz = \tau^2\frac{c}{B\sin\theta}\Big(p^2 w_p * w_p + q^2 w_q * w_q + ipq\big(w_q * w_p - w_p * w_q\big)\Big). \tag{3.26}$$

Using contour integration on the complex plane, one can show that the function $w_p * w_p$ from

(3.26) takes the form

$$w_p * w_p = \int_{-\infty}^{\infty} \frac{\sin\xi}{\xi} \frac{\sin(\xi+\zeta)}{(\xi+\zeta)} d\xi = \pi \operatorname{sinc}\zeta, \tag{3.27a}$$

while for the remaining three terms on the right-hand side of (3.26), we have:

$$-w_p * w_q = w_q * w_p = \frac{d}{d\zeta}\big(w_p * w_p\big), \tag{3.27b}$$

and

$$w_q * w_q = -\frac{d}{d\zeta}\big(w_q * w_p\big) = -\frac{d^2}{d\zeta^2}\big(w_p * w_p\big). \tag{3.27c}$$

Substituting (3.26)–(3.27) into (3.25), we arrive at

$$\int_{-\infty}^{\infty} I(y)\bar{I}(y+h)dy = \pi D\tau^2 \frac{c}{B\sin\theta}(\operatorname{sinc}\zeta + 2iQ\operatorname{sinc}'\zeta - Q^2\operatorname{sinc}''\zeta), \tag{3.28}$$

where

$$D = p^2\sigma^2 \quad \text{and} \quad Q = \frac{q}{p}.$$

The left-hand side of equation (3.28) represents the data. For any given value of h, the ACF of $I(y)$ can be evaluated directly from the image, although in practice the integration limits are, of course, finite. The right-hand side of equation (3.28) is rather a function of h defined by an analytic expression (recall, $\zeta = Bh\sin\theta/c$); this function also depends on two unknown parameters, D and Q. By choosing sufficiently many distinct values of h, we can obtain an overdetermined system of equations that can be solved with respect to D and Q in a weak sense. For example, one can use an appropriate form of nonlinear least squares, see [Kel99]. We leave the issues of conditioning of the aforementioned overdetermined system and robustness of its least squares solution for the future study. Instead, in this chapter we show how the reconstructed parameters of the Faraday rotation p and q can help correct the matched filter and thus improve the image. It is to be noted that the individual values of p and q can only be determined from D and Q up to a common factor $\sim \frac{1}{\sigma}$. However, knowing their ratio Q proves sufficient for implementing the filter correction, see Section 3.6.

3.6 Reducing image distortions due to the Faraday rotation

In the presence of the Faraday rotation, the filter $\overline{P(t-2|\boldsymbol{x}-\boldsymbol{y}|/c)}$ does not match the received signal $\psi_F(t,\boldsymbol{x})$ in (3.10). The distortions created by this mismatch can be reduced by using

the filter $\overline{P_F(t-2|\boldsymbol{x}-\boldsymbol{y}|/c)}$ that will match $\psi_F(t,\boldsymbol{x})$. The expression for $P_F(t)$ involves the parameter $Q=\frac{q}{p}$ that characterizes the Faraday rotation (see Section 3.5), and is given by [cf. (2.18)]

$$P_F(t)=A_F(t)e^{i\omega_0 t},\quad \text{where}\quad A_F(t)=\chi_\tau(t)e^{i\alpha t^2}\Big(1+\frac{2Q}{\tau}t\Big). \tag{3.29}$$

Using formulae (3.6) and (3.8), the factorization (3.15), and the corrected filter given by the conjugate of (3.29), we obtain the following expression for the new range ambiguity function [cf. (3.3) and (3.16), (3.17)]:

$$\widetilde{W}_{RF}(\boldsymbol{y},\boldsymbol{z})=\int_\chi \overline{A_F(u^0_{\boldsymbol{y}})}A(u^0_{\boldsymbol{z}})\Big(p+\frac{2q}{\tau}u^0_{\boldsymbol{z}}\Big)\,dt. \tag{3.30}$$

Knowing that $t_n=0$ for $n=0$ and performing the integration in (3.30), we get instead of (3.19):

$$\widetilde{W}_{RF}(\xi)=p\tau\Big((1+Q^2)w_p(\xi)+2iQw_q(\xi)-2Q^2w_{qq}(\xi)\Big),$$

where the new dimensionless function $w_{qq}(\xi)\overset{\text{def}}{=}w_q(\xi)/\xi$ has a removable singularity at $\xi=0$ if we set $w_{qq}(0)=1/3$.

To demonstrate the superiority of the corrected ambiguity function $\widetilde{W}_{RF}$ over its unmodified form (3.19), we plot the corresponding normalized range intensity PSFs

$$\frac{|W_{RF}(\xi)|^2}{\max|W_{RF}|^2}\quad\text{and}\quad\frac{|\widetilde{W}_{RF}(\xi)|^2}{\max|\widetilde{W}_{RF}|^2} \tag{3.31}$$

for several values of $Q=q/p$, see Figure 3.3. The dashed vertical lines indicate a 3dB drop of intensity from the maximum. It can be readily seen that the resolution is improved in all cases, however, a more significant improvement is observed for larger Q, as expected.

3.7 Discussion

In the current chapter, we have introduced a mathematical model and analyzed the effect of the Faraday rotation on single-polarization transionospheric SAR imaging. Unlike in all other studies of the Faraday rotation in the SAR literature (that exploit either single-polarization or polarimetric framework), our analysis takes into account the variation of the rotation angle along the interrogating chirp, and offers a venue for correcting the matched filter in those cases where the impact of the Faraday rotation on the image is deemed detrimental. Specifically, we first propose an approach to rough detection of the Faraday rotation based on sub-band image processing. Then, we employ the image autocorrelation analysis to relate the parameters of the Faraday rotation defined within our mathematical model to certain observable quantities. This

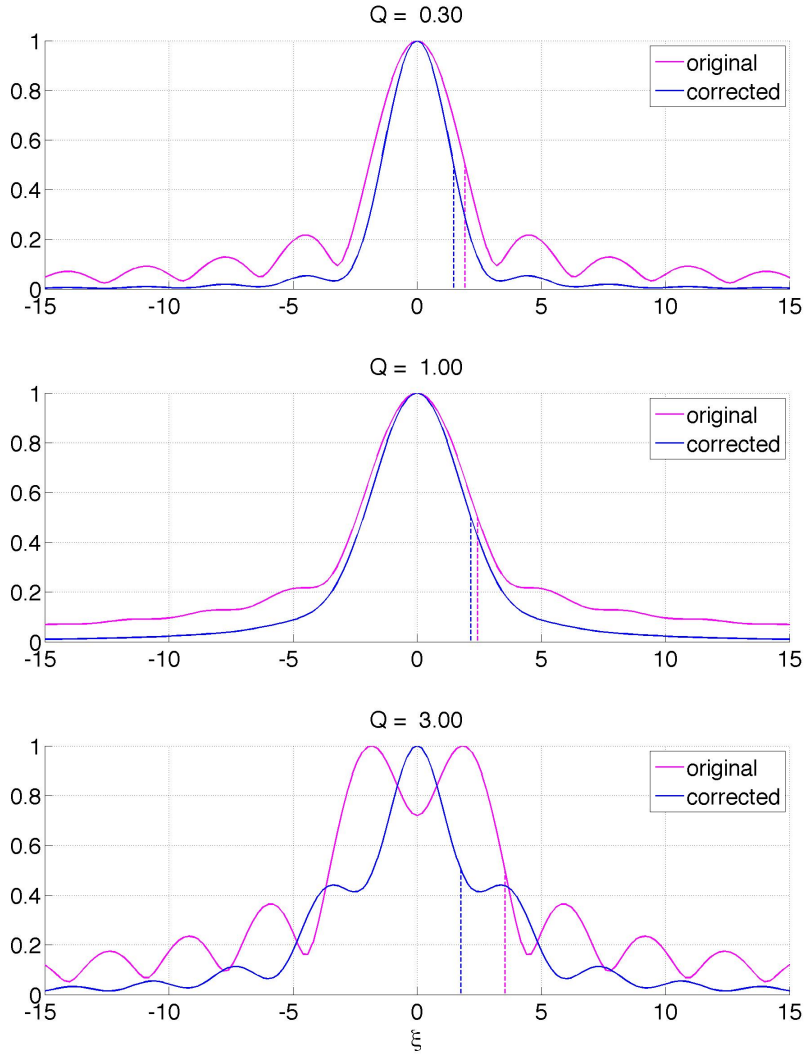

Figure 3.3: The original and corrected range intensity PSF curves (3.31) and -3dB resolution for different values of Q.

allows us to reconstruct the foregoing parameters and subsequently correct the matched filter. The corrected filter is shown to reduce the distortions of the image due to the Faraday rotation. This correction is applied on top of the corrections developed previously for the dispersive propagation, see [Tsy09a] and Chapter 2.

Another important aspect of the system is the anisotropy of the target. Scattering of the

polarized radio waves off an anisotropic target material is the topic of Chapter 4.

Chapter 4

A linearized inverse scattering problem for polarized waves and anisotropic targets

4.1 Background

This chapter is based on [GST12]. Its objective is to analyze the scattering of the linearly polarized electromagnetic waves off anisotropic targets in the framework of the first Born approximation. This analysis will help relate the observable quantities, i.e., the characteristics of the scattered field, to the physical properties of the target, such as the permittivity and conductivity of its composition material. Hence, it will generalize to the vector case the relations between the received field and the ground reflectivity function obtained in Chapter 2 for the scalar setting. In the future, the results of this chapter may help build a full-fledged SAR ambiguity theory for multi-channel imaging.

Appendices M through Q correspond to Chapter 4.

4.1.1 Direct and inverse scattering problems

Maxwell's equations of electromagnetism in CGS units [LL75, LL84]:

$$\begin{aligned} &\frac{1}{c}\frac{\partial \boldsymbol{H}}{\partial t} + \nabla \times \boldsymbol{E} = \boldsymbol{0}, && \nabla \cdot \boldsymbol{H} = 0, \\ &\frac{1}{c}\frac{\partial \boldsymbol{D}}{\partial t} - \nabla \times \boldsymbol{H} = -\frac{4\pi}{c}(\boldsymbol{j} + \boldsymbol{j}^{(\mathrm{ex})}), && \nabla \cdot \boldsymbol{D} = 0, \end{aligned} \tag{4.1}$$

govern the electromagnetic field driven by the extraneous electric current with the density $\boldsymbol{j}^{(\mathrm{ex})} = \boldsymbol{j}^{(\mathrm{ex})}(\boldsymbol{x}, t)$. In system (4.1), c is the speed of light in vacuum, $\boldsymbol{E}$ and $\boldsymbol{H}$ denote the

vectors of the electric and magnetic field, respectively, and $\boldsymbol{D}$ is the vector of electric induction, which is related to the electric field via the permittivity tensor $\boldsymbol{\varepsilon} = \boldsymbol{\varepsilon}(\boldsymbol{x})$ (hereafter, the dot "$\cdot$" denotes the tensor convolution):

$$\boldsymbol{D} = \boldsymbol{\varepsilon} \cdot \boldsymbol{E}. \tag{4.2}$$

The total current in system (4.1) is a sum of $\boldsymbol{j}^{(\mathrm{ex})}$ and the conductivity current $\boldsymbol{j}$ given by

$$\boldsymbol{j} = \boldsymbol{\sigma} \cdot \boldsymbol{E}. \tag{4.3}$$

The quantity $\boldsymbol{\sigma}$ in (4.3) denotes the conductivity tensor, which may also vary in space: $\boldsymbol{\sigma} = \boldsymbol{\sigma}(\boldsymbol{x})$. We are assuming that the current $\boldsymbol{j}^{(\mathrm{ex})}$ does not lead to the accumulation of the extraneous electric charge, so that the second steady-state equation in system (4.1) (the Gauss law of electricity) is homogeneous. The magnetic permeability is assumed equal to one (for the range of phenomena of interest) so that there is no need to distinguish between the magnetic field and magnetic induction.

Let $\boldsymbol{E}^{(\mathrm{inc})}$ and $\boldsymbol{H}^{(\mathrm{inc})}$ denote the incident fields that satisfy system (4.1) in vacuum:

$$\begin{aligned} &\frac{1}{c}\frac{\partial \boldsymbol{H}^{(\mathrm{inc})}}{\partial t} + \nabla \times \boldsymbol{E}^{(\mathrm{inc})} = \boldsymbol{0}, && \nabla \cdot \boldsymbol{H}^{(\mathrm{inc})} = 0, \\ &\frac{1}{c}\frac{\partial \boldsymbol{E}^{(\mathrm{inc})}}{\partial t} - \nabla \times \boldsymbol{H}^{(\mathrm{inc})} = -\frac{4\pi}{c}\boldsymbol{j}^{(\mathrm{ex})}, && \nabla \cdot \boldsymbol{E}^{(\mathrm{inc})} = 0. \end{aligned} \tag{4.4}$$

Then, the total fields that solve (4.1) can be represented as

$$\boldsymbol{E} = \boldsymbol{E}^{(\mathrm{inc})} + \boldsymbol{E}^{(\mathrm{sc})} \quad \text{and} \quad \boldsymbol{H} = \boldsymbol{H}^{(\mathrm{inc})} + \boldsymbol{H}^{(\mathrm{sc})}, \tag{4.5}$$

where the corrections $\boldsymbol{E}^{(\mathrm{sc})}$ and $\boldsymbol{H}^{(\mathrm{sc})}$ shall be attributed to the variation of $\boldsymbol{\varepsilon}$ and $\boldsymbol{\sigma}$ against the background vacuum values $\boldsymbol{\varepsilon} = \mathcal{I}$ (identity tensor) and $\boldsymbol{\sigma} = \boldsymbol{0}$, respectively. Those corrections are referred to as the scattered fields. The direct electromagnetic scattering problem is the problem of determining the scattered fields $\boldsymbol{E}^{(\mathrm{sc})}$ and $\boldsymbol{H}^{(\mathrm{sc})}$ if $\boldsymbol{\varepsilon} = \boldsymbol{\varepsilon}(\boldsymbol{x})$ and $\boldsymbol{\sigma} = \boldsymbol{\sigma}(\boldsymbol{x})$ are given. The inverse electromagnetic scattering problem rather consists of determining the variable electric permittivity $\boldsymbol{\varepsilon} = \boldsymbol{\varepsilon}(\boldsymbol{x})$ and conductivity $\boldsymbol{\sigma} = \boldsymbol{\sigma}(\boldsymbol{x})$ under the assumption that the scattered fields $\boldsymbol{E}^{(\mathrm{sc})}$ and $\boldsymbol{H}^{(\mathrm{sc})}$ are available. The region of space where $\boldsymbol{\varepsilon} = \boldsymbol{\varepsilon}(\boldsymbol{x})$ and $\boldsymbol{\sigma} = \boldsymbol{\sigma}(\boldsymbol{x})$ are to be reconstructed is called the target. The inverse scattering problem may have multiple solutions.

4.1.2 The first Born approximation

In the literature, the foregoing scattering problems are often studied using second order governing equations for the individual fields. Moreover, the inverse scattering problem can be simplified

by means of the linearization based on the first Born approximation, see [BW99, Chapter XIII]. It is typically used when the scattered field is much smaller than the incident field, i.e., when the scattering is weak. This, in turn, can be expected to be the case when the deviation of the material parameters at the target from the background parameters in vacuum is small. In Appendix M, we show that when the target material is isotropic, i.e., when both the permittivity and conductivity tensors are spherical, the governing equation for the scattered electric field under the first Born approximation becomes [see equation (M.8)]:

$$\frac{1}{c^2}\frac{\partial^2 \boldsymbol{E}^{(\mathrm{sc})}}{\partial t^2} - \Delta \boldsymbol{E}^{(\mathrm{sc})} = \nu \frac{\partial^2 \boldsymbol{E}^{(\mathrm{inc})}}{\partial t^2} - \frac{4\pi\sigma}{c^2}\frac{\partial \boldsymbol{E}^{(\mathrm{inc})}}{\partial t}, \tag{4.6}$$

where the scalar quantity ν is the ground reflectivity function [see formula (M.7)]:

$$\nu(\boldsymbol{x}) = \frac{1}{c^2} - \frac{1}{v(\boldsymbol{x})^2}. \tag{4.7}$$

In formula (4.7), $v = v(\boldsymbol{x})$ is the local propagation speed in the material. More rigorously, a solution by means of the first Born approximation can be obtained by truncating the corresponding Neumann series after its linear term [CB09, Chapter 6].

In the literature, the Born approximation (named after Max Born) is often discussed along with another approximation, named after Sergei Mikhailovich Rytov, see, e.g., [BW99, Chapter XIII] and [Ori85, LF92]. It is known that the Rytov approximation better describes the transmitted waves, i.e., the field inside the target material, whereas the Born approximation is better suited for the reflected waves, i.e., for the scattered field in vacuum (see, e.g., [LF92, Mar06] and references therein). We will focus on the first Born approximation for the rest of this chapter because it provides a linearized scattering model for the field reflected off the target into the vacuum region, which is convenient for SAR applications.

We also note that in the Cartesian coordinates the vector equation (4.6) decouples into three independent scalar wave equations for the individual field components. This enables studying the scattering problems in the scalar formulation [Che01], provided that the polarization of the field is not important.

4.1.3 Scalar vs. polarimetric SAR

As seen in Chapter 2, many currently operating SAR sensors use linear chirps in the form given by (2.18),

$$P(t) = A(t)e^{i\omega_0 t}, \quad \text{where} \quad A(t) = \chi_\tau(t)e^{i\alpha t^2},$$

as interrogating waveforms [Che01]. In this formula, ω_0 is the carrier frequency, $\chi_\tau(t)$ is the indicator function of the interval $[-\tau/2, \tau/2]$, and the modulating function $A(t)$ is varying slowly

compared to the fast oscillation $e^{i\omega_0 t}$.

Let us first disregard the polarization and identify the pulse (2.18) with the right-hand side of the scalar counterpart of equation (M.5). This right-hand side shall be interpreted as the time derivative of a given Cartesian component of the electric current at the emitting SAR antenna, which is taken as a point source[1] located at $\boldsymbol{x} \in \mathbb{R}^3$. Then, the corresponding component of the incident field due to the emitted chirp (2.18) is given by the standard retarded potential of the d'Alembert operator:

$$E^{(\mathrm{inc})}(\boldsymbol{z}, t) = \frac{1}{4\pi} \frac{P(t - |\boldsymbol{z} - \boldsymbol{x}|/c)}{|\boldsymbol{z} - \boldsymbol{x}|}, \tag{4.8}$$

which is (2.21) using new notation. It should be noted that we ignore the units of the electric field and currents because the governing equations are linear in E. When substituting $E^{(\mathrm{inc})}$ of (4.8) into the right-hand side of equation (4.6), we can leave $A(\cdot)$ out of the differentiation w.r.t. t, because $A(\,\cdot\,)$ varies slowly. Subsequently, a solution of equation (4.6) can be obtained with the help of the Kirchhoff integral (2.23). In particular, the scattered field back at the antenna $\boldsymbol{x}$ is given by the following expression, a modification of (2.25):

$$\begin{aligned} E^{(\mathrm{sc})}(\boldsymbol{x}, t) &\approx -\frac{\omega_0^2}{16\pi^2} \iiint\limits_{|\boldsymbol{x}-\boldsymbol{z}| \le ct} \frac{\hat{\nu}(\boldsymbol{z})}{|\boldsymbol{x} - \boldsymbol{z}|^2} P\left(t - 2|\boldsymbol{x} - \boldsymbol{z}|/c\right) d\boldsymbol{z} \\ &= -\frac{\omega_0^2}{16\pi^2} \iiint\limits_{|\boldsymbol{x}-\boldsymbol{z}| \le ct} \frac{\hat{\nu}(\boldsymbol{z})}{|\boldsymbol{x} - \boldsymbol{z}|^2} A\left(t - 2|\boldsymbol{x} - \boldsymbol{z}|/c\right) e^{i\omega_0 (t - 2|\boldsymbol{x}-\boldsymbol{z}|/c)} d\boldsymbol{z}, \end{aligned} \tag{4.9}$$

where

$$\hat{\nu}(\boldsymbol{z}) \stackrel{\mathrm{def}}{=} \nu(\boldsymbol{z}) + i \frac{4\pi\sigma(\boldsymbol{z})}{\omega_0 c^2}, \tag{4.10}$$

which differs from (M.7) due to the right hand term in (4.6). According to (4.9), the scattered field $E^{(\mathrm{sc})}$ can be interpreted as the result of application of a Fourier integral operator (FIO), see, e.g., [CN04,NC04,CB08,CB09], to the complex reflectivity function $\hat{\nu}(\boldsymbol{z})$ of (4.10) that combines the variation of the propagation speed c, see (4.7), and the variation of the conductivity σ. As discussed in Section 2.3.1, this FIO can be approximately inverted by applying a matched filter to $E^{(\mathrm{sc})}$ and accumulating the information due to multiple interrogating pulses (2.18) emitted from and received by the antenna at different locations along its trajectory. This is the procedure of SAR signal processing [Che01, CB09, FL99]; it allows one to reconstruct $\hat{\nu}(\boldsymbol{z})$, i.e., to obtain the image. Mathematically, this procedure is similar to application of the adjoint operator, which would have coincided with the true inverse of the FIO (4.9) if the latter were a genuine Fourier transform.

In general, $\hat{\nu}(\boldsymbol{z})$ is a function of three variables, because $\boldsymbol{z} \in \mathbb{R}^3$. As, however, the synthetic

[1] Actual SAR antennas have a special structure that enables narrowly directed radiation patterns [CB09].

antenna is aligned with the flight trajectory or orbit, which is one-dimensional, the conventional SAR data collection algorithm (in the case of a monostatic non-interferometric sensor) can generate only two-dimensional datasets, see [CB09]. At the same time, the primary task of all practical SAR systems is imaging of the surface of the Earth from aircraft or from satellites. The introduction of the Earth's surface as the geometric location (i.e., locus) of all the targets naturally eliminates the third coordinate (i.e., fixes the altitude) and hence makes the dimension of the dataset equal to that of the desired image. Mathematically, this corresponds to considering the reflectivity function (4.10) in the form

$$\hat{\nu}(\boldsymbol{z}) \equiv \hat{\nu}(z_1, z_2, z_3) = \hat{\nu}(z_1, z_2)\delta(z_3), \tag{4.11}$$

i.e., in the form of a single layer on the surface, where z_1 and z_2 are the two horizontal coordinates and z_3 is the vertical coordinate [Che01]. The resulting image then reconstructs $\hat{\nu}(z_1, z_2)$, i.e., yields the complex reflectivity function (4.10) on the surface of the Earth as a function of the two horizontal coordinates.

In real applications, however, disregarding the polarization may not be appropriate, as the field is always polarized, and its polarization may change due to the interaction with the target.[2] Even in the simplest possible scenario, when a linearly polarized incident wave impinges on a plane interface between the vacuum and an isotropic target material, the polarization angle, generally speaking, tilts. A more sophisticated target material gives rise to a broader variety of the possible changes in polarization of the scattered field, see Section 4.2. Mathematically, scattering off interfaces corresponds to a non-smooth permittivity $\boldsymbol{\varepsilon}(\boldsymbol{x})$ and/or conductivity $\boldsymbol{\sigma}(\boldsymbol{x})$, when the regions of their regular behavior (the vacuum and the target) are separated by a surface, at which these quantities (tensors) undergo jumps. Special boundary conditions are required at this surface for a proper description of the scattering mechanism.

The methodology of SAR imaging that takes into account the polarization of interrogating waves is known as polarimetric SAR, see [Mot07, LP09]. As the antenna is typically far away from the target, by the time the incident pulse reaches the target it can be sufficiently accurately approximated by a transverse plane wave. Likewise, the scattered field can be effectively thought of as a transverse plane wave by the time it reaches the antenna. Therefore, even though the field vectors in $\mathbb{R}^3$ are three-dimensional, it is sufficient to consider only their two transverse components if the third coordinate axis is chosen parallel to the direction of propagation. Accordingly, there are two independent linear polarizations for either incident or scattered wave.

At its current state, the theory of polarimetric SAR imaging is different from the scalar

[2] It may also change due to the propagation in a chiral medium, e.g., the magnetized ionosphere, which is considered in Chapter 3.

theory in that it exploits a completely phenomenological framework; the polarimetric SAR literature has been dominated by the phenomenological approach since the dissertation by Huynen [Huy70]. Namely, the vector of the incident electric field that has two (transverse) components and the vector of the scattered electric field that also has two components are considered related by means of a formal 2×2 matrix $\mathcal{S}$:

$$\boldsymbol{E}^{(\mathrm{sc})} = \mathcal{S}\boldsymbol{E}^{(\mathrm{inc})}, \tag{4.12}$$

called the Sinclair scattering matrix. The entries of the scattering matrix $\mathcal{S}$ are usually not related to any physical characteristics of the target; they are rather introduced as the coefficients of the transformation between $\boldsymbol{E}^{(\mathrm{inc})}$ and $\boldsymbol{E}^{(\mathrm{sc})}$. This is precisely what the phenomenological nature of the approach of [Huy70] means.

Note also that as the incident and scattered waves propagate in different directions, they will be represented in different coordinate systems in formula (4.12), and hence the scattering matrix $\mathcal{S}$ incorporates not only the transformation of the field per se, but the change of the coordinates as well. Moreover, as both fields related by (4.12) are assumed transverse plane waves, they are attributed to different spatial locations — the target for the incident field and the receiving antenna for the scattered field. In the time domain, which is common for SAR applications [CB09], this would have also implied that the incident and scattered field were evaluated at different moments in time.

Note that using formula (4.9) one can also obtain a scalar counterpart of relation (4.12). Consider a point scatterer of complex magnitude $\hat{\nu}$ located at $\boldsymbol{z}_0$ so that $\hat{\nu}(\boldsymbol{z}) = \hat{\nu}\delta(\boldsymbol{z} - \boldsymbol{z}_0)$. Then, instead of (4.9), we can write [with the help of (4.8)]:

$$E^{(\mathrm{sc})}(\boldsymbol{x}, t) \approx \underbrace{-\frac{\omega_0^2}{4\pi}\frac{\hat{\nu}}{|\boldsymbol{x} - \boldsymbol{z}_0|}}_{S} E^{(\mathrm{inc})}(\boldsymbol{z}_0, t - |\boldsymbol{x} - \boldsymbol{z}_0|/c). \tag{4.13}$$

However, unlike the reflectivity function (4.10) that enters into (4.13) and (4.9), the entries of the scattering matrix $\mathcal{S}$ of (4.12) do not directly represent any physics-based scattering mechanism or material characteristics of the target; they are introduced just as the coefficients of a linear transformation. Subsequently, various target decomposition techniques, see Section 4.4 and [LP09, Chapters 4, 6, 7] for more detail, attempt to attribute some physical properties of the target (e.g., its symmetry, convexity, etc.) to certain combinations of the entries of the observed matrix $\mathcal{S}$.

For SAR applications, one often considers two basic cases of a linearly polarized incident field: horizontal polarization corresponds to the electric field vector normal to the plane of incidence, whereas vertical polarization corresponds to the electric field vector parallel to the

plane of incidence. All other polarizations can be obtained as linear combinations of these two. Accordingly, the entries of the scattering matrix (that are also referred to as channels) are commonly denoted as

$$\mathcal{S} = \begin{bmatrix} S_{\mathrm{HH}} & S_{\mathrm{HV}} \\ S_{\mathrm{VH}} & S_{\mathrm{VV}} \end{bmatrix}, \tag{4.14}$$

where for each matrix entry, the first and second letter of the subscript denote the polarization of the scattered and incident field, respectively. In formula (4.14), S_{HH} and S_{VV} are the co-polarized channels, and S_{HV} and S_{VH} are the cross-polarized channels. Fully polarimetric SAR sensors produce four different images — one per channel.[3]

In the frequency domain, the components of the electric field vector become complex, and instead of the retarded time, as in formula (4.13), the solution acquires the corresponding phase factor. The Sinclair matrix can then be represented as follows:

$$\mathcal{S} = e^{i\phi_0} \begin{bmatrix} |S_{\mathrm{HH}}| & |S_{\mathrm{HV}}|e^{i\phi_{\mathrm{HV}}} \\ |S_{\mathrm{VH}}|e^{i\phi_{\mathrm{VH}}} & |S_{\mathrm{VV}}|e^{i\phi_{\mathrm{VV}}} \end{bmatrix}, \tag{4.15a}$$

where ϕ_0 is the common phase (also called absolute phase) that basically yields the distance (or time) that the scattered wave travels between the target and the receiving antenna, and ϕ_{HV}, ϕ_{VH}, and ϕ_{VV} are the relative phases. In particular, ϕ_{VV} is called the co-polarized phase difference (CPD). The absolute phase ϕ_0 is the principal quantity of interest in the case of the SAR imaging by means of a scalar field, see Chapter 2.

In the vector case, representation (4.15a) clearly shows that the complex-valued Sinclair scattering matrix offers a total of seven additional degrees of freedom — four amplitudes and three relative phases — on top of the scalar case. Consequently, eight independent quantities (1+7) associated with every location yield as much information as one can obtain from a polarimetric SAR image (i.e., four complex-valued images, one per channel) regardless of what the actual target is.

We should also mention that extracting the common phase ϕ_0 the way it is done in formula (4.15a) removes a certain degree of arbitrariness that otherwise exists in the definitions. Indeed, the scattering mechanism at the target can be such that every polarization undergoes a phase shift upon reflection, see Section 4.2. In this case, instead of (4.15a) we would have

$$\mathcal{S} = e^{i\tilde{\phi}_0} \begin{bmatrix} |S_{\mathrm{HH}}|e^{i\tilde{\phi}_{\mathrm{HH}}} & |S_{\mathrm{HV}}|e^{i\tilde{\phi}_{\mathrm{HV}}} \\ |S_{\mathrm{VH}}|e^{i\tilde{\phi}_{\mathrm{VH}}} & |S_{\mathrm{VV}}|e^{i\tilde{\phi}_{\mathrm{VV}}} \end{bmatrix} \stackrel{\mathrm{def}}{=} e^{i\tilde{\phi}_0}\tilde{\mathcal{S}}, \tag{4.15b}$$

where the entries of the matrix represent the actual complex reflection coefficients, and $\tilde{\phi}_0$

[3] In some inversion algorithms, the processing is not done channel-by-channel, but rather couples the channels, which may provide additional benefits, see, e.g., [VCY13].

accounts for the travel distance. The relation between the phases in (4.15a) and (4.15b) is obvious: $\phi_0 = \tilde{\phi}_0 + \tilde{\phi}_{\mathrm{HH}}$, but having only the overall matrix $\mathcal{S}$ as an observable, one cannot tell unambiguously how to split ϕ_0 into $\tilde{\phi}_0$ and $\tilde{\phi}_{\mathrm{HH}}$. Therefore, it is common in the literature to adopt normalization (4.15a) that keeps the HH entry of the matrix real.

4.1.4 Objectives of the chapter

Our primary objective is to build a material-based linearized scattering model for the case of vector propagation. In other words, using the first Born approximation we would like to relate the entries of the scattering matrix $\mathcal{S}$ to the material properties of the target (its permittivity and conductivity), similarly to how one defines the ground reflectivity function in the scalar case, see formulae (4.7), (4.10), and (4.13).

Note that in the framework of the first Born approximation, one can formulate both a direct and inverse scattering problem. The direct problem consists of obtaining the scattered field $\boldsymbol{E}^{(\mathrm{sc})}$, given the incident field $\boldsymbol{E}^{(\mathrm{inc})}$ and the material parameters $\boldsymbol{\varepsilon}$ and $\boldsymbol{\sigma}$, and assuming that the scattering is weak (see Section 4.1.2). Of our primary interest is the corresponding linearized inverse scattering problem, which consists of defining the channels (4.14) as functions of the material parameters, $S_{\mathrm{HH}} = S_{\mathrm{HH}}(\boldsymbol{\varepsilon}, \boldsymbol{\sigma})$, $S_{\mathrm{VV}} = S_{\mathrm{VV}}(\boldsymbol{\varepsilon}, \boldsymbol{\sigma})$, $S_{\mathrm{HV}} = S_{\mathrm{HV}}(\boldsymbol{\varepsilon}, \boldsymbol{\sigma})$, and $S_{\mathrm{VH}} = S_{\mathrm{VH}}(\boldsymbol{\varepsilon}, \boldsymbol{\sigma})$, so that $\boldsymbol{\varepsilon}$ and $\boldsymbol{\sigma}$ can subsequently be reconstructed given the fields $\boldsymbol{E}^{(\mathrm{inc})}$ and $\boldsymbol{E}^{(\mathrm{sc})}$ in formula (4.12), and again, assuming that the scattering is weak.

The desired linearized scattering model shall be minimally complex in terms of the structure of the tensors $\boldsymbol{\varepsilon}$ and $\boldsymbol{\sigma}$. This means that it should not aim at more than recovering the four complex reflection coefficients contained in the matrix $\tilde{\mathcal{S}}$ of (4.15b), which is a total of eight degrees of freedom, because what the polarimetric SAR methodology is capable of detecting is even one degree of freedom less, see formula (4.15a).

Availability of such a model may help develop the radar ambiguity theory for the polarimetric case similarly to how it is done in the scalar case, see [Che01], [CB09, Chapters 5 and 11], and Chapter 2. Besides, it may prove useful for the material identification SAR (miSAR) applications.

The application of the first Born approximation in the vector case is similar to that in the scalar case (discussed in Section 2.3.1). Replacing the total electric field $\boldsymbol{E}$ by the incident field $\boldsymbol{E}^{(\mathrm{inc})}$ on the right-hand side of equation (M.4) and taking into account the Gauss laws $\nabla \cdot \boldsymbol{D} = 0$ and $\nabla \cdot \boldsymbol{E}^{(\mathrm{inc})} = 0$, we obtain:

$$\frac{1}{c^2}\frac{\partial^2 \boldsymbol{E}^{(\mathrm{sc})}}{\partial t^2} - \Delta \boldsymbol{E}^{(\mathrm{sc})} = -\frac{\boldsymbol{\varepsilon} - \mathcal{I}}{c^2} \cdot \frac{\partial^2 \boldsymbol{E}^{(\mathrm{inc})}}{\partial t^2} - \frac{4\pi\boldsymbol{\sigma}}{c^2} \cdot \frac{\partial \boldsymbol{E}^{(\mathrm{inc})}}{\partial t}. \tag{4.16}$$

The main difference between this equation and its counterpart for the isotropic case, equation

(4.6), is that the material characteristics in equation (4.16) are tensors rather than scalars. This implies that generally speaking, the vector equation (4.16) cannot be decoupled into the independent scalar equations for the individual field components. Moreover, studying the scattering of electromagnetic waves off interfaces requires special boundary conditions in addition to the governing equations themselves. Those boundary conditions, mentioned earlier, play a key role in the construction of the first Born approximation for the case of vector fields, see Section 4.2.

In Section 4.2, we carefully develop and analyze the first Born approximation as it applies to scattering off a hierarchy of target materials. Starting with the simplest case of an isotropic dielectric, we gradually increase the complexity of the material by allowing for the anisotropy of $\boldsymbol{\varepsilon}$ and including the weak conductivity $\boldsymbol{\sigma}$ (anisotropic as well) so that finally we reach the same number of the degrees of freedom as in (4.15a). The resulting material is a uniaxial crystal (i.e., a birefringent medium) with the conductivity tensor that is also uniaxial, and with both axes allowed to have arbitrary directions with respect to the incidence plane and with respect to one another. We prove that the scattered field in vacuum obtained in this linearized framework approximates the true reflected field that one can obtain with no use of the Born approximation. We also obtain a necessary and sufficient condition for the existence of a solution to the foregoing linearized inverse scattering problem. Under this condition, the scattering matrix (4.15a) can be obtained by appropriately choosing the permittivities, conductivities, and angles that define the material and the orientation of its optical axis with respect to the plane of incidence.

The second objective of the current chapter is related to the first one. Namely, in the linearized framework that we have adopted for describing the scattering, a formal mathematical justification is needed for the possibility of taking the ground reflectivity function in the form of a single layer on the surface, see formula (4.11).

As of yet, the transition from the entire half-space occupied by the target material to the target material concentrated only on the surface has been motivated by the mere convenience of having the third coordinate removed from the radar dataset,[4] see the discussion around equation (4.11). This, however, is not a rigorous argument. One rather needs to prove that the linearized scattering off a material half-space can be equivalently reformulated as the linearized scattering off a layer of monopoles at its surface only.

In other words, we arrive at the following inverse source [Isa90] problem: for the linearized scattering off a half-space, find an equivalent surface reflectivity function of type (4.11) that would yield the same scattered field in the vacuum region. In Section 4.3 of the paper, we solve this inverse source problem and show that in the scalar case the resulting "density" $\hat{\nu}(z_1, z_2)$

[4]It is also supported by physical reasoning in the literature. For the microwave carrier frequencies ω_0, the penetration depth of the radar signals into the ground is very small, and all the reflections must be those off the surface. However, the first Born approximation may lead to a certain inconsistency for the ground reflectivity function in the form (4.11). Indeed, the single layer radiates in both directions, vacuum and material, which means that the scattered field actually penetrates into the ground.

indeed appears proportional to the target reflectivity function (4.10) on the surface. Moreover, we formulate and solve a similar inverse source problem in the vector case as well. With the polarization taken into account, the scattered field in the vacuum region can also be represented as a single-layer surface potential with tensor densities proportional to the jumps of the material characteristics at the interface. These topics are addressed in Section 4.3, whereas in Section 4.4 we discuss the relation between our analysis and polarimetric target decomposition.

The main notations that will be used hereafter are explained in Table 4.1.

4.2 Hierarchy of scattering models

4.2.1 Roadmap

In Section 4.2, we present a detailed derivation of the first Born approximation for the scattering of a linearly polarized electromagnetic wave off a material half-space. We consider several types of materials: a perfect isotropic dielectric, a perfect birefringent (uniaxial) dielectric, and lossy isotropic and birefringent dielectrics. In each case, our first goal is to determine the number of degrees of freedom associated with a given material in the linearized direct scattering problem. This number is determined by the functional dependence of the reflection coefficients on the material parameters.

In Section 4.2.3, the scattering coefficients are derived for the isotropic case. First, the Maxwell equations are transformed to the frequency domain, and the dependence of their solution on the tangential variables is factored out using the uniformity of the formulation along the interface. Then, the equations are linearized and reduced to a second-order ordinary differential equation (ODE) that governs the propagation of the scattered field in the direction normal to the interface. This equation is supplemented by the radiation conditions at infinity and the matching conditions at the interface. It turns out that the key difference between the horizontal and vertical polarization is precisely in the interface conditions. For the horizontal polarization, those conditions reduce to the continuity of the solution itself and its first derivative across the interface. For the vertical polarization, the condition for the first derivative becomes inhomogeneous, and this derivative undergoes a jump across the interface. Accordingly, the reflection coefficients are different for two polarizations, while the dielectric permittivity provides a single degree of freedom for this setting.

We note that the first Born approximation in the scalar (i.e., isotropic) case has been extensively studied in the literature, and also used in the context of SAR applications in Chapter 2. The reason we present its detailed analysis in the current chapter is two-fold. On one hand, it allows us to build the framework and introduce the solution methodology that subsequently applies to the cases with anisotropy and/or Ohmic losses. On the other hand, in its own right

Table 4.1: Key notations and their relations to be used in Chapter 4 and associated appendices.

Parameter name	**Notation**	**Relations**	**Reference**
Dielectric tensor and its reciprocal	$\boldsymbol{\varepsilon}, \boldsymbol{\eta}$	$\boldsymbol{D} = \boldsymbol{\varepsilon} \cdot \boldsymbol{E}$; $\boldsymbol{\varepsilon} \cdot \boldsymbol{\eta} = \mathcal{I}$	(4.17), (4.50)
Isotropic permittivity (or dielectric constant)	ε, $\varepsilon(z)$	$\varepsilon(z) = 1 + \theta(z)(\varepsilon - 1)$	(4.22)
Geometry and parameters of uniaxial dielectric tensor	$\varepsilon_\perp$, $\varepsilon_\parallel$, $\Delta\varepsilon$, α, β, γ	$\Delta\varepsilon = \varepsilon_\parallel - \varepsilon_\perp$, $\alpha^2 + \beta^2 + \gamma^2 = 1$	(4.47)–(4.49)
Entries of the reciprocal dielectric tensor	η_{ij}, $i, j = x, y, z$	$\eta_{ii} = 1/\varepsilon_{ii}$; $\eta_{ij} = -\varepsilon_{ij}$ for $i \neq j$	(4.51)
Conductivity tensor	$\boldsymbol{\sigma}$	$\boldsymbol{j} = \boldsymbol{\sigma} \cdot \boldsymbol{E}$	(4.3)
Isotropic conductivity	σ	$\boldsymbol{j} = \sigma \boldsymbol{E}$	(4.78)
Geometry and parameters of uniaxial conductivity tensor	$\sigma_\perp$, $\sigma_\parallel$, $\Delta\sigma$, α_σ, β_σ, γ_σ	$\Delta\sigma = \sigma_\parallel - \sigma_\perp$, $\alpha_\sigma^2 + \beta_\sigma^2 + \gamma_\sigma^2 = 1$	Section 4.2.5.1
Modified permittivity in frequency domain	$\tilde{\boldsymbol{\varepsilon}}$	$\tilde{\boldsymbol{\varepsilon}} = \boldsymbol{\varepsilon} + i\dfrac{4\pi}{\omega}\boldsymbol{\sigma}$	(4.80)
Small parameter for the first Born approximation	$\varkappa$	$\lVert\boldsymbol{\varepsilon} - \mathcal{I}\rVert \sim \varkappa$, $\lVert\boldsymbol{\sigma}\rVert \sim \varkappa\omega$, $\lvert u^{(\mathrm{sc})}\rvert \sim \varkappa\lvert u_0\rvert$	(4.21), (4.24c)
Differential operator describing scattering, right-hand side parameter	$\hat{L}$, r	$\hat{L} = \dfrac{d^2/dz^2 + q^2}{q^2}$	(4.27)
Electromagnetic field, its components, and amplitudes	U; $u^{(\mathrm{inc})}$, $u^{(\mathrm{sc})}$; u_0, $u(z)$	$U = u^{(\mathrm{inc})} + u^{(\mathrm{sc})}$, $u^{(\mathrm{inc})} = u_0 e^{i(qz+Kx)}$, $\lvert u^{(\mathrm{sc})}\rvert \sim \varkappa\lvert u_0\rvert$	(4.23)–(4.26)
Undetermined coefficients for a solution in two domains	A, B, C	$u^{(\mathrm{sc})}(z) = (Az + B)u_0 e^{iqz}$ for $z > 0$; $u^{(\mathrm{sc})}(z) = Cu_0 e^{-iqz}$ for $z < 0$	(4.32)
Free space and material sides of the interface at $z = 0$	(F), (M)	$(F) \equiv (z = -0)$ $(M) \equiv (z = +0)$	(4.19), Figure 4.1
Boundary condition parameter	R	$\left.\dfrac{du}{dz}\right\rvert_{(M)} = \left.\dfrac{du}{dz}\right\rvert_{(F)} + Ru_0$	(4.33), (4.34)
Wave vector and its components	k. K, q	$k^2 = K^2 + q^2$; $K = k\sin\theta_i$	(4.20), (4.40), Figure 4.1
Polarization ratio	Q	$S_{\mathrm{VV}} = S_{\mathrm{HH}}Q$,	(4.44), (4.73), (4.74), (4.76), (4.82), Figure 4.2

it helps us emphasize a very important distinction between the horizontal and vertical incident polarizations. In the case of a horizontal polarization, the linearized interface condition is homogeneous, and this is precisely the case that has received most of the attention in the literature, see, e.g., [Ori85]. For the vertical polarization though, the linearized interface condition becomes inhomogeneous and accordingly, the solution given by the first Born approximation is different even though the linearized governing equation is the same as in the case of a horizontal polarization.

In the lossless anisotropic case (Section 4.2.4), the polarizations are no longer independent, and Maxwell's equations reduce to a system of two coupled ODEs that govern the components of the electric and magnetic field normal to the plane of incidence. For this system, the first Born approximation appears very convenient to implement in two stages: first the equations are uncoupled, and then the resulting individual equations are linearized. The end result depends on the polarization of the incident wave. In each case (vertical or horizontal incident polarization), one of the uncoupled equations describes the co-polarized scattering and the other describes the cross-polarized scattering. The form of the resulting equations and interface conditions turns out to be similar to the isotropic case, although the actual expressions for the reflection coefficients are not the same and contain additional degrees of freedom.

In the case of a lossy material (Section 4.2.5), we show that the presence of a weak conductivity is equivalent to having a small imaginary part in the overall complex permittivity, which, in turn, makes the small parameter of the first Born approximation complex. This observation significantly simplifies the treatment of the lossy materials. In particular, the functional representation of the imaginary part of the scattering matrix turns out to be the same as that of the real part. Hence, the anisotropic conductivity yields the same number of degrees of freedom as does the anisotropic permittivity.

In Table 4.2, we provide the number of degrees of freedom and list the independent material parameters for each of the cases we have considered.

Having identified the degrees of freedom that characterize every material included into our analysis, we move on toward addressing the next goal of this chapter, which is to solve the corresponding linearized inverse scattering problem. Specifically, we would like to see whether a given scattering matrix can be obtained by adjusting the available degrees of freedom, i.e., by appropriately choosing the characteristics of the target material. In Theorem 1, we furnish a necessary and sufficient condition for the solvability of this inverse problem in the case of a lossless birefringent material, and in Corollary 1 we extend this result to the case of a lossy anisotropic material.

Table 4.2: Overview of scattering models and their properties: material parameters, non-zero reflection coefficients, and maximum number of degrees of freedom. The wavy underline in the third column means that the values may be complex.

Model of scatterer	**Independent material parameters**	**Non-zero reflection coefficients**	**Max. number of d.o.f.**	**Section #**
Perfect isotropic dielectric	ε	HH, VV	1	4.2.3
Lossy isotropic dielectric	ε, σ	HH, VV	1	4.2.5.2
Perfect uniaxial dielectric, interface in basal plane	$\varepsilon_\perp, \varepsilon_\parallel$	HH, VV	2	4.2.4.5
Lossy uniaxial dielectric with spherical conductivity tensor, interface in basal plane	$\varepsilon_\perp, \varepsilon_\parallel, \sigma$	HH, VV	3	4.2.5.3
Perfect uniaxial dielectric, arbitrary direction of optical axis	$\varepsilon_\perp, \varepsilon_\parallel, \alpha, \gamma$	HH, VV, HV, VH	4	4.2.4.7
Lossy uniaxial dielectric, arbitrary direction of optical axis	$\varepsilon_\perp, \varepsilon_\parallel, \alpha, \gamma$, $\sigma_\perp, \sigma_\parallel, \alpha_\sigma, \gamma_\sigma$	HH, VV, HV, VH	8	4.2.5.5

4.2.2 Problem of reflection of a plane wave by a material half-space

We consider the reflection of a monochromatic plane wave off a material half-space with permittivity tensor $\boldsymbol{\varepsilon}$ and conductivity tensor $\boldsymbol{\sigma}$. Since all the fields depend on time as $e^{-i\omega t}$, where ω is the frequency, we conduct the analysis in the frequency domain. For transverse electromagnetic waves with no extraneous currents,[5] the unsteady equations of system (4.1) with equation (4.3) taken into account reduce to

$$\nabla \times \boldsymbol{E} = ik\boldsymbol{H} \quad \text{and} \quad \nabla \times \boldsymbol{H} = -ik\boldsymbol{D} + \frac{4\pi}{c}\boldsymbol{\sigma} \cdot \boldsymbol{E}, \tag{4.17}$$

where $k = \omega/c$. Equation (4.2) and the Gauss laws of electricity and magnetism (steady-state equations in (4.1)) keep their form in the frequency domain.

Denote $\boldsymbol{x} = (x, y, z) \in \mathbb{R}^3$ and assume that the half-space $z < 0$ is occupied by vacuum, whereas the half-space $z > 0$ is filled with the material. The plane of incidence is defined as to contain the wave vector of the incident wave and the normal to the interface $z = 0$; with no loss of generality we take it as the (x, z) plane, see Figure 4.1. The problem is essentially

[5]The excitation in the problem will be provided by incident plane waves.

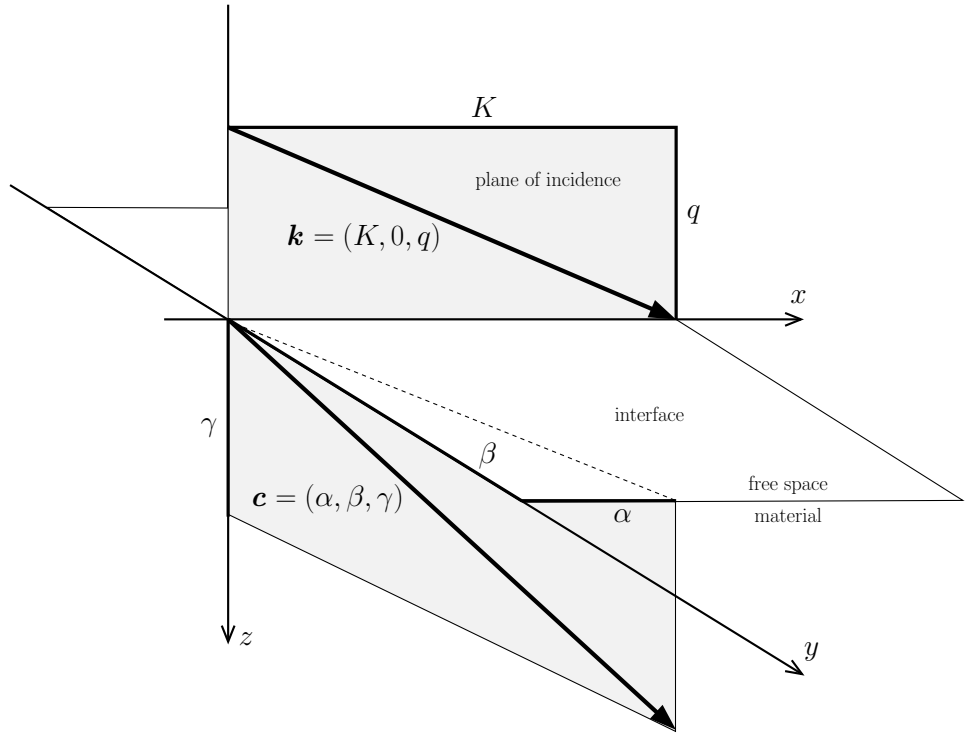

Figure 4.1: Schematic for the scattering problem off an anisotropic half-space. The vector $\boldsymbol{k} = (K, 0, q)$ is the incident wave vector, see formula (4.20). The vector $\boldsymbol{c} = (\alpha, \beta, \gamma)$ is a unit vector along the optical axis, see Section 4.2.4. Note that α, β, and γ denote the direction cosines rather than the actual angles.

two-dimensional, as the wave vectors of the incident, reflected, and transmitted waves all belong to the plane of incidence. Hence, the electromagnetic fields do not depend on the y coordinate (although the vectors may have y components).

Then, system (4.17) takes the form:

$$\begin{aligned} -\frac{\partial E_y}{\partial z} &= ikH_x, & -\frac{\partial H_y}{\partial z} &= -ik\tilde{D}_x, \\ \frac{\partial E_x}{\partial z} - \frac{\partial E_z}{\partial x} &= ikH_y, & \frac{\partial H_x}{\partial z} - \frac{\partial H_z}{\partial x} &= -ik\tilde{D}_y, \\ \frac{\partial E_y}{\partial x} &= ikH_z, & \frac{\partial H_y}{\partial x} &= -ik\tilde{D}_z, \end{aligned} \tag{4.18}$$

where $\tilde{D}_x$, $\tilde{D}_y$, and $\tilde{D}_z$ are components of the vector $\tilde{\boldsymbol{D}} = \boldsymbol{\varepsilon} \cdot \boldsymbol{E} + (4\pi i/\omega)\boldsymbol{\sigma} \cdot \boldsymbol{E}$. In the free space (vacuum), we have $\boldsymbol{\varepsilon} = \mathcal{I}$ and $\boldsymbol{\sigma} = \boldsymbol{0}$.

At the interface $z = 0$, the following boundary conditions are imposed on the tangential

components of the electric and magnetic field [LL84, Che83]:

$$E_x|_{(F)} = E_x|_{(M)}\,, \qquad E_y|_{(F)} = E_y|_{(M)}\,, \tag{4.19a}$$

$$H_x|_{(F)} = H_x|_{(M)}\,, \qquad H_y|_{(F)} = H_y|_{(M)}\,. \tag{4.19b}$$

The subscripts (F) and (M) in formulae (4.19) denote the free space ($z = -0$) and material ($z = +0$) side of the interface, respectively.

The incident field in formulae (4.5) is chosen as a plane wave:

$$(\boldsymbol{E}^{(\mathrm{inc})}, \boldsymbol{H}^{(\mathrm{inc})}) = (\boldsymbol{E}_0^{(\mathrm{inc})}, \boldsymbol{H}_0^{(\mathrm{inc})})e^{i(qz+Kx)}, \tag{4.20}$$

where K is the common horizontal wavenumber for all plane waves in the problem, and

$$q = (k^2 - K^2)^{1/2}$$

is the vertical component of the incident wave vector, see [LL84, Che83, Lek91].

In addition to the interface conditions (4.19) for the total field, the scattered field $(\boldsymbol{E}^{(\mathrm{sc})}, \boldsymbol{H}^{(\mathrm{sc})})$ should also satisfy the radiation conditions as $z \to \pm\infty$, see formulae (4.28).

In the textbook approach to problem (4.18)–(4.19) (see, e.g., [BW99, LL84]), the incident field (4.20) is restricted to the free space, while system (4.18) is solved with respect to the scattered field, and its solutions are found separately for the vacuum and material half-spaces. These solutions, called the reflected and transmitted field, respectively, are combined with the incident field, and then matched at the interface using boundary conditions (4.19). A comprehensive account of this approach can be found, e.g., in [Che83]. For the particular case of a perfect isotropic dielectric, amplitude and direction of the reflected and transmitted field are given by the classic Fresnel's equations and Snell's law; these expressions (see, e.g., [BW99, LL84]) are valid for arbitrary values of ε. Besides this, various simplifications can be considered depending on the specific structure of $\boldsymbol{\varepsilon}$ and $\boldsymbol{\sigma}$ [Lek91].

As indicated in Section 4.1.4, our goal is to analyze the linearized scattering case. Therefore, in the material domain $z > 0$ we assume that

$$\|\boldsymbol{\varepsilon} - \mathcal{I}\| \sim \varkappa \quad \text{and} \quad \|\boldsymbol{\sigma}\| \sim \varkappa\omega, \tag{4.21}$$

where $\varkappa$ is a small parameter, so that the scattering is weak. To study the existence of a solution to the resulting inverse scattering problem, we will use the first Born approximation to obtain a series of direct scattering solutions for a hierarchy of settings, starting from the simplest case, i.e., that of a perfect isotropic dielectric. The Fresnel and other exact solutions, linearized according to (4.21), will be used for validation of the solutions obtained with the help of the first Born approximation.

4.2.3 The first Born approximation for a perfect isotropic dielectric

4.2.3.1 Governing equations.

Assume that in the material the dielectric tensor is spherical, which means that the permittivity is scalar, and that the conductivity is zero. Since $\boldsymbol{\sigma} = \boldsymbol{0}$, the components of the vector $\tilde{\boldsymbol{D}}$ in (4.18) can be replaced by those of $\boldsymbol{D}$. Since $\boldsymbol{\varepsilon} = \varepsilon(z)\mathcal{I}$ in the entire space, the vectors $\boldsymbol{D}$ and $\boldsymbol{E}$ are proportional, i.e.,

$$D_i(x,z) = \varepsilon(z)E_i(x,z) \quad \text{for} \quad i = x, y, z,$$

where

$$\varepsilon(z) = 1 + \theta(z)(\varepsilon - 1), \tag{4.22}$$

$\theta(z)$ is a unit step function, and $\varepsilon > 1$ is the permittivity in the material domain $z > 0$, see [BW99, LL84]. In this case, the equations for the variables E_x, E_z, H_y and for H_x, H_z, E_y in system (4.18) are decoupled. This means that system (4.18) admits a solution with $E_x = E_z = H_y = 0$, which is called horizontal polarization, and another solution with $H_x = H_z = E_y = 0$, called vertical polarization. Each of these solutions is governed by the scalar Helmholtz equation:

$$\frac{\partial^2 U}{\partial x^2} + \frac{\partial^2 U}{\partial z^2} + \varepsilon(z)k^2 U = 0, \tag{4.23}$$

where $U(x,z)$ represents any nonzero Cartesian component of $\boldsymbol{E}$ or $\boldsymbol{H}$.

To build the first Born approximation for the scattering of a plane incident wave in either of the two basic polarizations defined above, we represent the total field U in (4.23) as a sum of the incident and scattered fields as in (4.5):

$$U = u^{(\mathrm{inc})} + u^{(\mathrm{sc})}, \tag{4.24a}$$

take the incident field in the form (4.20):

$$u^{(\mathrm{inc})} = u_0 e^{i(qz+Kx)}, \tag{4.24b}$$

and assume that

$$|u^{(\mathrm{sc})}| \sim \varkappa |u_0|, \tag{4.24c}$$

where the small parameter $\varkappa$ is introduced in (4.21). In doing so, both the incident and scattered components of the field occupy the entire space. Substituting equality (4.24a) into (4.23) and taking into account that $u^{(\mathrm{inc})}$ satisfies the same equation (4.23) but with $\varepsilon = 1$, we arrive at the equation for $u^{(\mathrm{sc})}$:

$$\frac{\partial^2 u^{(\mathrm{sc})}}{\partial x^2} + \frac{\partial^2 u^{(\mathrm{sc})}}{\partial z^2} + k^2 u^{(\mathrm{sc})} = -(\varepsilon(z) - 1)k^2(u^{(\mathrm{inc})} + u^{(\mathrm{sc})}). \tag{4.25}$$

The first Born approximation consists of disregarding the second-order term $(\varepsilon - 1)u^{(\mathrm{sc})}$, see formulae (4.21) and (4.24c), on the right-hand side of equation (4.25). Moreover, as everything in our formulation is uniform along the plane (x, y), see Figure 4.1, the dependence of the solution on x and y must be the same in the entire space, see [LL84, Chapter X]. This, in particular, implies that the horizontal component of the wave vector is the same for both the incident field (4.20), (4.24b) and the scattered field, so that we can take

$$u^{(\mathrm{sc})} = u(z)e^{iKx}. \tag{4.26}$$

Equation (4.26) helps us reduce (4.25) to the following equation for $u(z)$:

$$\frac{1}{u_0}\hat{L}u = g(z) \equiv -r\theta(z)e^{iqz}, \quad \hat{L} \stackrel{\mathrm{def}}{=} \frac{1}{q^2}\frac{d^2}{dz^2} + 1, \tag{4.27}$$

where $r = (\varepsilon - 1)k^2/q^2$. Note that the incident field satisfies the equation $\hat{L}u^{(\mathrm{inc})} = 0$. The solution $u(z)$ of equation (4.27) should also satisfy the radiation conditions at infinity:

$$\frac{1}{iq}\frac{du}{dz} - u = 0 \quad \text{as} \quad z \to \infty \qquad \text{and} \qquad \frac{1}{iq}\frac{du}{dz} + u = 0 \quad \text{as} \quad z \to -\infty. \tag{4.28}$$

The overall solution to equation (4.27) will be obtained as the sum of the general solution to the corresponding homogeneous equation and a particular solution to the inhomogeneous equation (4.27). For the general solution to the homogeneous equation $\hat{L}u = 0$ subject to the radiation conditions (4.28) we can write:

$$u^{(\mathrm{h})}(z) = \begin{cases} Bu_0e^{iqz}, & z > 0, \\ Cu_0e^{-iqz}, & z < 0, \end{cases} \tag{4.29}$$

where B and C are constants. A particular solution to the inhomogeneous equation (4.27), which accounts for the resonance between $\hat{L}$ and $g(z)$ on the material domain $z > 0$, is given by

$$u^{(\mathrm{p})}(z) = \begin{cases} Au_0ze^{iqz}, & z > 0, \\ 0, & z < 0, \end{cases} \tag{4.30}$$

where the value of A is obtained by the method of undetermined coefficients:

$$A = \frac{irq}{2}. \tag{4.31}$$

Combining (4.29) and (4.30), we obtain the overall scattering solution in the form

$$u^{(\mathrm{sc})}(z) = \begin{cases} (Az+B)u_0 e^{iqz}, & z>0 \quad \text{(material)}, \\ Cu_0 e^{-iqz}, & z<0 \quad \text{(vacuum)}, \end{cases} \tag{4.32}$$

where the constants B and C shall be determined with the help of the interface conditions (4.19). The constant C can be interpreted as the reflection coefficient.

In Sections 4.2.3.2 and 4.2.3.3 we will show that whereas the governing differential equation (4.27) and the value of r on its right-hand side are the same for both polarizations, the interface conditions (4.19), as expressed via the single unknown function u, appear different for the horizontal and vertical polarization. Specifically, in either case the interface conditions can be written as

$$u|_{(M)} = u|_{(F)}\,; \quad \left.\frac{du}{dz}\right|_{(M)} = \left.\frac{du}{dz}\right|_{(F)} + Ru_0, \tag{4.33}$$

where the constant R depends on the polarization (it may be equal to zero). Accordingly, the solution (4.32) also appears different for the horizontal and vertical polarization. In particular, substituting (4.32) and (4.31) into (4.33), we can express the reflection coefficient C via the parameters r and R:

$$C = B = -\frac{r}{4} + \frac{R}{2iq}, \tag{4.34}$$

which indicates that the reflection coefficient depends on the polarization via R.

Finally, let us note that equation (4.27) can also be solved by convolution with the fundamental solution, see, e.g., [Ori85]. As we explain in Section 4.3 though, the deficiency of this approach is precisely in that it offers no easy way of accounting for the different interface conditions (i.e., different values of R) that correspond to different polarizations.

4.2.3.2 Horizontal polarization.

In this case, the unknown quantity in equation (4.23) is usually taken as $U = E_y$, with the other two nonzero field components being H_x and H_z. The first equation (4.18) then implies:

$$H_x = \frac{i}{k}\frac{dE_y}{dz}, \tag{4.35}$$

so that boundary conditions (4.19) reduce to:

$$E_y|_{(F)} = E_y|_{(M)} \quad \text{and} \quad \left.\frac{dE_y}{dz}\right|_{(F)} = \left.\frac{dE_y}{dz}\right|_{(M)}. \tag{4.36}$$

Boundary conditions (4.36) imply the continuity of the total field (4.24a) and its first normal derivative at the interface. As the incident field (4.24b) and its derivative are continuous at

$z = 0$, so are the scattered field $u^{(\mathrm{sc})} = E_y^{(\mathrm{sc})}$ and its first derivative with respect to z:

$$E_y^{(\mathrm{sc})}\Big|_{(F)} = E_y^{(\mathrm{sc})}\Big|_{(M)} \quad \text{and} \quad \frac{dE_y^{(\mathrm{sc})}}{dz}\Big|_{(F)} = \frac{dE_y^{(\mathrm{sc})}}{dz}\Big|_{(M)}. \tag{4.37}$$

Conditions (4.37) are used to determine the constants B and C in (4.32). Comparison of (4.37) to (4.33) shows that $R = 0$, so, according to (4.34), the co-polarized reflection coefficient for the horizontal polarization is given by:[6]

$$S_{\mathrm{HH}} \stackrel{\mathrm{def}}{=} C = B = -\frac{r}{4} = -\frac{1}{4}\frac{k^2}{q^2}(\varepsilon - 1). \tag{4.38}$$

At the same time, the Fresnel solution [BW99, Chapter I] gives the following expression for the exact reflection coefficient in the case of horizontal polarization:

$$S_{\mathrm{HH}}^{(\mathrm{exact})} = -\frac{\sin(\theta_i - \theta_t)}{\sin(\theta_i + \theta_t)}, \tag{4.39}$$

where θ_i is the incidence angle and θ_t is the refraction angle (defined by Snell's law):

$$\sin\theta_i = \frac{K}{k}, \qquad \sin\theta_t = \frac{1}{\sqrt{\varepsilon}}\sin\theta_i. \tag{4.40}$$

Formulae (4.39), (4.40) do not involve linearization and are valid for arbitrary values of ε.

A comparison of the linearized solution (4.32), (4.31), and (4.38) to the Fresnel solution (4.39), (4.40) shows the deficiency of the former: in the material, it has a component that grows linearly as z increases, which is not physical. In addition, expression (4.32) does not provide the correct wavenumber and propagation direction of the refracted wave, which restricts the validity of the first Born approximation inside the material to the area [LF92]:

$$|z| \leqslant z_0 \sim \frac{\pi}{|q - q^{(\mathrm{exact})}|} \approx \frac{2\pi q}{k^2|\varepsilon - 1|},$$

where $q^{(\mathrm{exact})}$ is the z-component of the refracted wavenumber obtained from Snell's law:

$$q^{(\mathrm{exact})} = \sqrt{\varepsilon}k\cos\theta_t = k\sqrt{\varepsilon - \sin^2\theta_i},$$

see the second equation in formula (4.40).

However, formulae (4.32) and (4.38) are useful in the vacuum region: the wavenumber and propagation direction of the scattered field in vacuum are correct, and one can also see that the reflection coefficient (4.38) given by the first Born approximation coincides with the linear

[6] Hereafter, we identify the reflection coefficients with the entries of the scattering matrix $\mathcal{S}$ of (4.14), see Section 4.2.3.4.

term in the expansion of the exact reflection coefficient (4.39) in powers of $\varkappa = \varepsilon - 1$. Indeed, using equations (4.40) and taking into account that $\cos\theta_i = q/k$ and also

$$\varepsilon\cos^2\theta_t = \varepsilon - (1-\cos^2\theta_i) = \cos^2\theta_i\left(1+\varkappa\frac{k^2}{q^2}\right),$$

we can transform expression (4.39) as follows:

$$\begin{aligned} S_{\mathrm{HH}}^{(\mathrm{exact})} &= \frac{\frac{1}{\sqrt{\varepsilon}}\sin\theta_i\cos\theta_i - \frac{1}{\sqrt{\varepsilon}}\cos\theta_i\sin\theta_i(1+\varkappa k^2/q^2)^{1/2}}{\frac{1}{\sqrt{\varepsilon}}\sin\theta_i\cos\theta_i + \frac{1}{\sqrt{\varepsilon}}\cos\theta_i\sin\theta_i(1+\varkappa k^2/q^2)^{1/2}} \\ &= \frac{1-(1+\varkappa k^2/q^2)^{1/2}}{1+(1+\varkappa k^2/q^2)^{1/2}} = -\frac{1}{4}\frac{k^2}{q^2}\varkappa + \mathcal{O}(\varkappa^2) = S_{\mathrm{HH}} + \mathcal{O}(\varkappa^2). \end{aligned}$$

4.2.3.3 Vertical polarization.

In this case, we take $U = H_y$ in equation (4.23). The first interface condition for H_y at $z = 0$ is the continuity of H_y itself, see (4.19). The second interface condition is obtained from the continuity of E_x, using the relation

$$\varepsilon(z)E_x = -\frac{i}{k}\frac{dH_y}{dz} \tag{4.41}$$

that follows from (4.17), and taking into account that $\varepsilon = 1$ for $z < 0$, see formula (4.22). Altogether, this yields the following boundary conditions for H_y at $z = 0$:

$$H_y|_{(F)} = H_y|_{(M)}\,, \qquad \left.\frac{dH_y}{dz}\right|_{(F)} = \left.\left(\varepsilon^{-1}\frac{dH_y}{dz}\right)\right|_{(M)}. \tag{4.42}$$

The key difference between these boundary conditions and boundary conditions (4.36) that we have obtained for the horizontal polarization is the presence of the factor ε^{-1} in the condition for the normal derivative (i.e., z-derivative) in (4.42). Because of this factor, for the vertical polarization the normal derivative of the total field is no longer continuous, and rather undergoes a jump at $z = 0$, which is due to the jump of ε^{-1}, see (4.42). As the derivative of the incident field (4.24b) is still continuous, the discontinuity appears in the z-derivative of the scattered field:

$$\varepsilon^{-1}\left.\frac{dH_y^{(\mathrm{sc})}}{dz}\right|_{(M)} - \left.\frac{dH_y^{(\mathrm{sc})}}{dz}\right|_{(F)} = (1-\varepsilon^{-1})\left.\frac{dH_y^{(\mathrm{inc})}}{dz}\right|_{z=0}.$$

Multiplying both sides of this equality by ε and disregarding the quadratic term $(\varepsilon - 1)\left.\frac{dH_y^{(\mathrm{sc})}}{dz}\right|_{(F)} = \mathcal{O}(\varkappa^2)$ on the left-hand side, we arrive at the inhomogeneous linearized interface

condition for the normal derivative of $H_y^{(\mathrm{sc})}$:

$$\left.\frac{dH_y^{(\mathrm{sc})}}{dz}\right|_{(M)} - \left.\frac{dH_y^{(\mathrm{sc})}}{dz}\right|_{(F)} = (\varepsilon - 1)\left.\frac{dH_y^{(\mathrm{inc})}}{dz}\right|_{z=0}. \tag{4.43}$$

Comparing (4.43) to (4.33) while taking into account (4.24b) we get $R = iq(\varepsilon - 1)$. Hence, according to (4.34), we obtain [cf. formula (4.38)]:

$$S_{\mathrm{VV}} \stackrel{\mathrm{def}}{=} C = B = -\frac{r}{4} + \frac{\varepsilon - 1}{2} = S_{\mathrm{HH}}Q, \quad \text{where} \quad Q = \frac{K^2 - q^2}{k^2}. \tag{4.44}$$

The true reflection coefficient for this polarization is given by the Fresnel solution [BW99, Chapter I] [cf. formula (4.39)]:

$$S_{\mathrm{VV}}^{(\mathrm{exact})} = \frac{\tan(\theta_i - \theta_t)}{\tan(\theta_i + \theta_t)} = \frac{\sin\theta_i\cos\theta_i - \sin\theta_t\cos\theta_t}{\sin\theta_i\cos\theta_i + \sin\theta_t\cos\theta_t}, \tag{4.45}$$

where θ_i and θ_t are defined in (4.40). As in the case of the horizontal polarization, see Section 4.2.3.2, reflection coefficient (4.44) derived with the help of the first Born approximation can also be obtained by linearization of the exact reflection coefficient (4.45) with respect to $\varkappa$:

$$S_{\mathrm{VV}}^{(\mathrm{exact})} = \frac{\varepsilon - (1 + \varkappa k^2/q^2)^{1/2}}{\varepsilon + (1 + \varkappa k^2/q^2)^{1/2}} = -\frac{1}{4}\frac{k^2}{q^2}\varkappa + \frac{\varepsilon - 1}{2} + \mathcal{O}(\varkappa^2) = S_{\mathrm{VV}} + \mathcal{O}(\varkappa^2),$$

where we have used the same transformations as in Section 4.2.3.2.

The plots in Figure 4.2(a) show the exact and linearized reflection coefficients for both polarizations, as well as the polarization ratio Q, calculated using the first Born approximation and according to the Fresnel formulas. As expected, the accuracy of the first Born approximation decreases as the value of $(\varepsilon - 1)$ increases. Note that typical values of the refractive index $\sqrt{\varepsilon}$ are between 1 and 2 [BW99, Chapters I and II]. The method for constructing the plots in this figure is given in point 7h of Appendix P with the code itself given in Appendix Q.

Remark. The expression for the polarization ratio Q in formula (4.44) indicates that the scattered field in the vertical polarization vanishes if $|K| = |q|$, i.e., if the incidence angle is $\pi/4$. In other words, the Brewster angle in the linearized framework is equal to $\pi/4$. This should be expected for a weakly refractive material, in which the direction of the transmitted ray is close to that of the incident one (i.e., $|\theta_i - \theta_t| \sim \varkappa$, see formula (4.40)), and hence perpendicular to the direction of the reflected ray (see, e.g., [BW99, Chapter I]).

4.2.3.4 Discussion of the isotropic case.

Hereafter, we restrict our analysis to the scattering of plane transverse waves off a plane interface, so that the tangential components of the wave vectors for the incident, transmitted, and reflected fields are the same. Under these assumptions the reflection angle is known, and

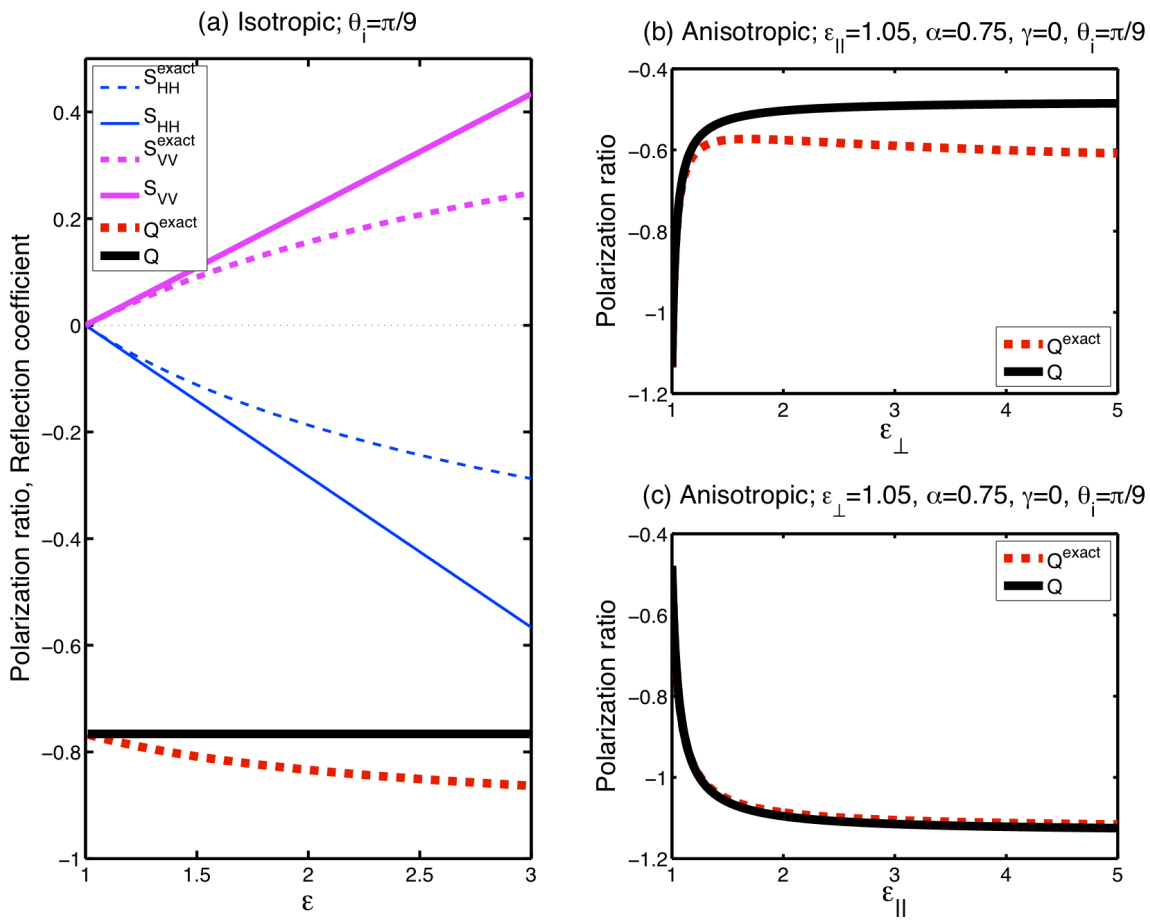

Figure 4.2: Reflection coefficients and polarization ratios for the linearized and full formulation: (a) lossless isotropic dielectric; (b) and (c): lossless birefringent dielectric with $\varepsilon_\perp$ and $\varepsilon_\parallel$ as independent variables, respectively.

hence the reflection coefficients computed in Sections 4.2.3.2 and 4.2.3.3 (and Sections 4.2.4 and 4.2.5 for other types of scatterers) already take into account the transformation between the coordinate systems used for representing the incident field and the reflected field, see the discussion after equation (4.12). Moreover, as we are considering only genuine plane waves, we can attribute both $\boldsymbol{E}^{(\mathrm{sc})}$ and $\boldsymbol{E}^{(\mathrm{inc})}$ in formula (4.12) to the same location right at the interface, rather than to different spatial locations in the far field (that allow one to approximate a more general wave form by a plane wave). Therefore, we may actually leave out the common phase ϕ_0, see (4.15a), that takes into account the propagation distance/time, and directly associate the reflection coefficients we compute with the corresponding entries of the scattering matrix $\mathcal{S}$. This approach will be adopted for the rest of the chapter.

Analysis of the reflection coefficients (4.38) and (4.44) shows that scattering off a perfect isotropic dielectric yields only one degree of freedom in the scattering matrix $\mathcal{S}$ of (4.14). At the same time, the reflection coefficients for two polarizations, S_{HH} and S_{VV}, differ by a factor of Q, see formula (4.44), that does not depend on the material properties at all. Therefore, when this type of scattering material is assumed, the only quantity that can be reconstructed from measurements is $\varepsilon - 1$, which also happens to be the only physical characteristic of the target, regardless of the received polarization(s). If, however, there is a mismatch between the observations and the predictions of the model (e.g., if the ratio of the received co-polarized signals differs substantially from Q, or if significant cross-polarized components are detected), then the use of a more comprehensive model for the scattering material may be justified, see Sections 4.2.4 and 4.2.5.

4.2.4 Perfect birefringent dielectric

4.2.4.1 Governing equations.

A perfect (i.e., lossless) anisotropic medium is characterized by the dielectric tensor $\boldsymbol{\varepsilon}$ that relates the components of $\boldsymbol{D}$ and $\boldsymbol{E}$:

$$D_i = \varepsilon_{ij} E_j, \quad i, j = x, y, z, \tag{4.46}$$

while $\boldsymbol{\sigma}$ is a zero tensor, so that $\tilde{\boldsymbol{D}}$ in (4.18) is still the same as $\boldsymbol{D}$. For a birefringent material (i.e., a uniaxial crystal), there exists a coordinate system x', y', z', in which the tensor $\boldsymbol{\varepsilon}$ is diagonal and the relation (4.46) simplifies to:

$$D_{x'} = \varepsilon_{\perp} E_{x'}, \quad D_{y'} = \varepsilon_{\perp} E_{y'}, \quad D_{z'} = \varepsilon_{\parallel} E_{z'}. \tag{4.47}$$

Let $\boldsymbol{c}$ be a unit vector along the z' axis, and let α, β, and γ be its x, y, and z components, respectively (see Figure 4.1). The components of a unit vector are related by

$$\alpha^2 + \beta^2 + \gamma^2 = 1. \tag{4.48}$$

Then, the entries of the tensor $\boldsymbol{\varepsilon}$ become (see [Lek91, Che83]):

$$\begin{aligned} &\varepsilon_{xx} = \varepsilon_{\perp} + \alpha^2 \Delta\varepsilon, \quad \varepsilon_{yy} = \varepsilon_{\perp} + \beta^2 \Delta\varepsilon, \quad \varepsilon_{zz} = \varepsilon_{\perp} + \gamma^2 \Delta\varepsilon, \\ &\varepsilon_{xy} = \varepsilon_{yx} = \alpha\beta\Delta\varepsilon, \quad \varepsilon_{xz} = \varepsilon_{zx} = \alpha\gamma\Delta\varepsilon, \quad \varepsilon_{yz} = \varepsilon_{zy} = \beta\gamma\Delta\varepsilon, \end{aligned} \tag{4.49}$$

where $\Delta\varepsilon = \varepsilon_{\parallel} - \varepsilon_{\perp}$. The diagonal terms in (4.49) are $\mathcal{O}(1)$, while the off-diagonal terms are $\mathcal{O}(\varkappa)$ [cf. the first relation in formula (4.21)].

The isotropic case considered in Section 4.2.3 is characterized by $\Delta\varepsilon = 0$. There, the off-diagonal terms in (4.49) vanish and the two basic polarizations (horizontal and vertical) in

system (4.18) separate. They are described individually by equation (4.23) for E_y and H_y, respectively. If $\Delta\varepsilon \neq 0$ though, then the two polarizations remain coupled. However, the treatment of this case is greatly simplified in the presence of a small parameter $\varkappa$. Namely, our assumption that the dielectric is weak implies that the coupling terms are small. For the case of weak coupling, it still makes sense to use E_y and H_y as the unknowns in the problem, because it simplifies the analysis of the Born approximation and makes the comparison to the isotropic case [equation (4.23)] easier.

To reduce system (4.18) to two equations for E_y and H_y, we will use the inverse dielectric tensor $\boldsymbol{\eta}$ defined as:

$$E_i = \eta_{ij} D_j, \quad i, j = x, y, z. \tag{4.50}$$

the entries of this tensor, *accurate to* $\mathcal{O}(\varkappa)$, are:

$$\begin{aligned} &\eta_{xx} = 1/\varepsilon_{xx}, && \eta_{yy} = 1/\varepsilon_{yy}, && \eta_{zz} = 1/\varepsilon_{zz}, \\ &\eta_{xy} = \eta_{yx} = -\varepsilon_{xy}, && \eta_{xz} = \eta_{zx} = -\varepsilon_{xz}, && \eta_{yz} = \eta_{zy} = -\varepsilon_{yz}. \end{aligned} \tag{4.51}$$

which can be proven by observing that all entries of the tensor $\boldsymbol{\varepsilon} \cdot \boldsymbol{\eta} - \mathcal{I}$ are $o(\varkappa)$. Then, we eliminate all field components except E_y and H_y from system (4.18) as follows:

1. The dependence (4.26) on the x coordinate is assumed for all field components, so in system (4.18) we replace $\partial/\partial x$ by iK and $\partial/\partial z$ by d/dz, respectively. This allows us to explicitly express the components D_x, D_z, H_x, and H_z via E_y, H_y, and their derivatives with respect to z:

$$D_x = -\frac{i}{k}\frac{dH_y}{dz}, \qquad D_z = -\frac{K}{k}H_y, \tag{4.52a}$$

$$H_x = \frac{i}{k}\frac{dE_y}{dz}, \qquad H_z = \frac{K}{k}E_y. \tag{4.52b}$$

2. Formulae (4.52b) are substituted into the expression for D_y in (4.18), which yields:

$$D_y = -\frac{1}{k^2}\Big(\frac{d^2E_y}{dz^2} - K^2E_y\Big). \tag{4.53}$$

3. Equations (4.52a) and (4.53) are substituted into formula (4.50), which leads to the following expressions for E_x and E_z:

$$E_x = -\eta_{xx}\frac{i}{k}\frac{dH_y}{dz} - \eta_{xy}\frac{1}{k^2}\Big(\frac{d^2E_y}{dz^2} - K^2E_y\Big) - \eta_{xz}\frac{K}{k}H_y, \tag{4.54a}$$

$$E_z = -\eta_{zz}\frac{K}{k}H_y - \eta_{xz}\frac{i}{k}\frac{dH_y}{dz} - \eta_{yz}\frac{1}{k^2}\Big(\frac{d^2E_y}{dz^2} - K^2E_y\Big), \tag{4.54b}$$

whereas for E_y we obtain:

$$(\eta_{yy}\frac{d^2}{dz^2} + k^2 - K^2\eta_{yy})E_y = -k(i\eta_{xy}\frac{d}{dz} + K\eta_{yz})H_y. \tag{4.55}$$

4. Expressions (4.54) are substituted into the y component of the Faraday law in (4.18) (the equation that relates E_x, E_z, and H_y). After simplifications, we arrive at

$$\begin{aligned}(\eta_{xx}\frac{d^2}{dz^2} + k^2 - K^2\eta_{zz})H_y \; &- 2i\eta_{xz}K\frac{dH_y}{dz} \\ &= -\frac{i}{k}\Big(i\eta_{yz}K - \eta_{xy}\frac{d}{dz}\Big)\Big(\frac{d^2E_y}{dz^2} - K^2E_y\Big).\end{aligned} \tag{4.56}$$

Note that the isotropic equation (4.23) can be derived from equation (4.55), or from equation (4.56), by setting $\Delta\varepsilon = 0$ in formulae (4.49) and (4.51). As will be seen in Sections 4.2.4.2 and 4.2.4.3, equations (4.55), (4.56) are particularly well suited for computing the scattered field because of the way they couple the components E_y and H_y. Specifically, for electromagnetic fields represented in the form (4.24a), it appears very convenient to carry out the Born approximation in two stages: first decouple equations (4.55) and (4.56) from one another, and then linearize the resulting individual equations.

System (4.55), (4.56) will also require boundary conditions at $z = 0$, see (4.19). The boundary conditions will be obtained with the help of relations for H_x and E_x in formulae (4.52b) and (4.54a). In the isotropic case, expression (4.54a) with (4.51) taken into account reduces to (4.41), as expected. In the anisotropic case, the right-hand side of expression (4.54a) will be responsible for the inhomogeneous boundary conditions (similar to (4.41) and (4.43) in isotropic case) for the vertical polarization of the scattered field.[7]

Let us now consider the two basic polarizations of the incident wave separately. For each one, the scattered field can also be polarized either vertically or horizontally.

4.2.4.2 Horizontal polarization of the incident wave.

In this case, the component H_y is present only in the scattered field, hence $H_y = \mathcal{O}(\varkappa)$ (see (4.24c)). Therefore, the right-hand side of equation (4.55) appears $\mathcal{O}(\varkappa^2)$ because according to (4.49) and (4.51), $\eta_{xy} \sim \Delta\varepsilon = \mathcal{O}(\varkappa)$ and $\eta_{yz} \sim \Delta\varepsilon = \mathcal{O}(\varkappa)$. As such, this right-hand side can be neglected, and the co-polarized scattering for the horizontal incident polarization is described by

$$(\eta_{yy}\frac{d^2}{dz^2} + k^2 - K\eta_{yy})E_y = 0.$$

[7]The inhomogeneous boundary condition will apply to the co-polarized component of the scattered field when the incident field is polarized vertically, and to the cross-polarized component of the scattered field when the incident field is polarized horizontally.

This equation can be transformed into

$$\hat{L}E_y = \frac{\eta_{yy}-1}{q^2}\Big(K^2 - \frac{d^2}{dz^2}\Big)E_y, \tag{4.57}$$

where the operator $\hat{L}$ is defined in (4.27). Linearization of (4.57) according to (4.24) yields:

$$\frac{1}{E_{0y}^{(\mathrm{inc})}}\hat{L}E_y^{(\mathrm{sc})} = \frac{(\eta_{yy}-1)k^2}{q^2}\theta(z)e^{iqz}, \tag{4.58}$$

which coincides with equation (4.27) for $r = -(\eta_{yy}-1)k^2/q^2$ and $u_0 = E_{0y}^{(\mathrm{inc})}$.

Since in the co-polarized case the scattered wave is also polarized horizontally, E_y and H_x must be continuous at $z = 0$, see (4.19), where the expression for H_x is given by the first equality of (4.52b). Recalling that the incident field is continuous at the interface along with its normal derivative, we obtain the continuity of $E_y^{(\mathrm{sc})}$ and $\frac{dE_y^{(\mathrm{sc})}}{dz}$:

$$E_y^{(\mathrm{sc})}\Big|_{(F)} = E_y^{(\mathrm{sc})}\Big|_{(M)}, \quad \frac{dE_y^{(\mathrm{sc})}}{dz}\Big|_{(F)} = \frac{dE_y^{(\mathrm{sc})}}{dz}\Big|_{(M)}, \tag{4.59}$$

so that in formula (4.33) we have $R = 0$. Interface conditions (4.59) are the same as (4.37) in the isotropic case. Using (4.34) for $E_y^{(\mathrm{sc})}$, we get the following reflection coefficient:

$$S_{\mathrm{HH}} = \frac{1}{4}\frac{k^2}{q^2}(\eta_{yy}-1). \tag{4.60}$$

For $\Delta\varepsilon = 0$, formula (4.60), with the help of (4.51), reduces to the isotropic expression in (4.38), as expected.

For the cross-polarized scattering, i.e., the vertical polarization of the scattered wave, we linearize equation (4.56) taking into account that $H_y^{(\mathrm{inc})} = 0$ and hence $H_y = H_y^{(\mathrm{sc})} = \mathcal{O}(\varkappa)$ according to (4.24c). Thus, on the left-hand side we may replace η_{xx} and η_{zz} by 1. The remaining off-diagonal terms of $\boldsymbol{\eta}$ are $\mathcal{O}(\varkappa)$; hence, we drop the η_{xz} term on the left-hand side and replace E_y by $E_y^{(\mathrm{inc})}$ on the right-hand side. This yields:

$$\Big(\frac{d^2}{dz^2}+q^2\Big)H_y^{(\mathrm{sc})} = -\frac{i}{k}\Big(i\eta_{yz}K - \eta_{xy}\frac{d}{dz}\Big)\Big(\frac{d^2E_y^{(\mathrm{inc})}}{dz^2} - K^2E_y^{(\mathrm{inc})}\Big). \tag{4.61}$$

Equation (4.61) can be transformed into

$$\frac{1}{E_{0y}^{(\mathrm{inc})}}\hat{L}H_y^{(\mathrm{sc})} = \frac{k}{q}\Big(\eta_{xy} - \frac{K}{q}\eta_{yz}\Big)\theta(z)e^{iqz}. \tag{4.62}$$

As the polarization of the scattered field is vertical, $H_y = H_y^{(\mathrm{sc})}$ and E_x must be continuous at $z = 0$, see (4.19). We use formula (4.54a) for E_x to express the interface conditions via the y-

components of the fields. Using $H_y^{(\mathrm{sc})} = \mathcal{O}(\varkappa)$ and recalling that the off-diagonal terms of $\boldsymbol{\eta}$ are also $\mathcal{O}(\varkappa)$, we can set $\eta_{xx} = 1$ in the first term and drop the third term on the right-hand side of that relation. Thus, we arrive at the following interface condition for the normal derivative of $H_y^{(\mathrm{sc})}$:

$$-\frac{i}{k}\frac{dH_y^{(\mathrm{sc})}}{dz}\bigg|_{(F)} = -\frac{i}{k}\frac{dH_y^{(\mathrm{sc})}}{dz}\bigg|_{(M)} + \eta_{xy}E_{0y}^{(\mathrm{inc})}. \tag{4.63}$$

It is inhomogeneous due to the second term on the right-hand side of (4.54a) [cf. (4.43)].

To define the cross-polarized reflection coefficient for this case, we use the following convention: if the scattered field in vacuum is given by $H_y^{(\mathrm{sc})} = H_{0y}^{(\mathrm{sc})}e^{iKx-iqz}$ (see equations (4.26) and (4.32)), then the reflection coefficient will be

$$S_{\mathrm{VH}} \stackrel{\mathrm{def}}{=} H_{0y}^{(\mathrm{sc})}/E_{0y}^{(\mathrm{inc})}. \tag{4.64}$$

Next, we introduce the notation

$$G^{\pm} \stackrel{\mathrm{def}}{=} -\Big(\eta_{xy} \pm \frac{K}{q}\eta_{yz}\Big) = \Delta\varepsilon\Big(\alpha\beta \pm \frac{K}{q}\beta\gamma\Big) \tag{4.65}$$

(see (4.51) for the components of $\boldsymbol{\eta}$) and match equation (4.62) to (4.27), which yields $u_0 \equiv E_{0y}^{(\mathrm{inc})}$ and $r = kG^-/q$ (note the minus sign in (4.65)). We also match the interface condition (4.63) to the second condition (4.33), which yields $R = -ik\eta_{xy}$. Substituting these values of r and R into (4.34), we express the cross-polarized reflection coefficient defined by (4.64) as

$$S_{\mathrm{VH}} = \frac{1}{4}\frac{k}{q}G^+. \tag{4.66}$$

4.2.4.3 Vertical polarization of the incident wave.

We start with the co-polarized scattering again. For this case, we have $E_y^{(\mathrm{inc})} = 0$ and, consequently, $E_y = E_y^{(\mathrm{sc})} = \mathcal{O}(\varkappa)$. As $\eta_{yz} \sim \eta_{xy} = \mathcal{O}(\varkappa)$, the right-hand side of equation (4.56) can be dropped, making this equation homogeneous:

$$\Big(\eta_{xx}\frac{d^2}{dz^2} + k^2 - K^2\eta_{zz}\Big)H_y - 2i\eta_{xz}K\frac{dH_y}{dz} = 0.$$

Linearization of this equation gives

$$\frac{1}{H_{0y}^{(\mathrm{inc})}}\hat{L}H_y^{(\mathrm{sc})} = \Big((\eta_{xx}-1) + \frac{K^2}{q^2}(\eta_{zz}-1) - 2\eta_{xz}\frac{K}{q}\Big)\theta(z)e^{iqz}, \tag{4.67}$$

where $H_{0y}^{(\mathrm{inc})}$ is the amplitude of the incident wave. The interface conditions for this co-polarized case require continuity of H_y and E_x at $z = 0$. Given the continuity of the incident field along

with its normal derivative, the second equation of (4.19b) yields the continuity of $H_y^{(\mathrm{sc})}$, while for E_x we employ formula (4.54a) and after the linearization obtain:

$$-\frac{i}{k}\frac{dH_y^{(\mathrm{sc})}}{dz}\bigg|_{(F)} = -\frac{i}{k}\frac{dH_y^{(\mathrm{sc})}}{dz}\bigg|_{(M)} + \frac{q}{k}(\eta_{xx}-1)H_{0y}^{(\mathrm{inc})} - \frac{K}{k}\eta_{xz}H_{0y}^{(\mathrm{inc})}. \tag{4.68}$$

Similarly to the isotropic case, see formula (4.43), the normal derivative of $H_y^{(\mathrm{sc})}$ is discontinuous at the interface. Comparing (4.67) and (4.68) to (4.27) and (4.33), we get:

$$r = -\Big((\eta_{xx}-1) + \frac{K^2}{q^2}(\eta_{zz}-1) - 2\eta_{xz}\frac{K}{q}\Big) \quad \text{and} \quad R = iK\eta_{xz} - iq(\eta_{xx}-1).$$

Then, using formula (4.34), we obtain:

$$S_{\mathrm{VV}} = -\frac{1}{4}\Big((\eta_{xx}-1) - \frac{K^2}{q^2}(\eta_{zz}-1)\Big). \tag{4.69}$$

For $\Delta\varepsilon = 0$, formula (4.69), with the help of (4.51), reduces to the isotropic expression in (4.44), as expected.

The cross-polarized field in this case is governed by the linearized equation (4.55):

$$\Big(\frac{d^2}{dz^2} + q^2\Big)E_y^{(\mathrm{sc})} = -k(i\eta_{xy}\frac{d}{dz} + K\eta_{yz})H_y^{(\mathrm{inc})},$$

which can be transformed into

$$\frac{1}{H_{0y}^{(\mathrm{inc})}}\hat{L}E_y^{(\mathrm{sc})} = \frac{k}{q^2}\Big(q\eta_{xy} - K\eta_{yz}\Big)\theta(z)e^{iqz}. \tag{4.70}$$

Remarkably, the value of r in (4.70) and (4.62) is the same, $r = kG^-/q$, where G^- is defined by (4.65). The difference between the cross-polarized case of Section 4.2.4.2 and the cross-polarized case considered here is in the boundary conditions. Indeed, for the current cross-polarized case we require the continuity of E_y and H_x at $z = 0$, which translates into the homogeneous boundary conditions (4.59) by taking into account that $E_y = E_y^{(\mathrm{sc})}$ and using the first equation of (4.52b) for H_x. Hence, $R = 0$, and using formula (4.34) for $E_y^{(\mathrm{sc})}$ with $u_0 \equiv H_{0y}^{(\mathrm{inc})}$, we arrive at the reflection coefficient

$$S_{\mathrm{HV}} = -\frac{1}{4}\frac{k}{q}G^-, \tag{4.71}$$

which is different from (4.66). In formula (4.71), S_{HV} is defined similarly to (4.64):

$$S_{\mathrm{HV}} \stackrel{\mathrm{def}}{=} E_{0y}^{(\mathrm{sc})}/H_{0y}^{(\mathrm{inc})} \quad \text{provided that} \quad E_y^{(\mathrm{sc})} = E_{0y}^{(\mathrm{sc})}e^{iKx-iqz} \quad \text{for} \quad z < 0.$$

4.2.4.4 Scattering coefficients for perfect birefringent dielectric.

For future reference, we present here the expressions for the reflection coefficients given by (4.60), (4.69), (4.66), and (4.71) in the following form (expressions (4.49), (4.51), and (4.65) have also been used):

$$
\begin{aligned}
S_{\mathrm{HH}} &= -\frac{1}{4}\frac{k^2}{q^2}(\varepsilon_\perp - 1 + \beta^2\Delta\varepsilon),\\
S_{\mathrm{VV}} &= \frac{1}{4}\Big((\varepsilon_\perp - 1 + \alpha^2\Delta\varepsilon) - \frac{K^2}{q^2}(\varepsilon_\perp - 1 + \gamma^2\Delta\varepsilon)\Big),\\
S_{\mathrm{HV}} &= -\frac{1}{4}\frac{k}{q}\Big(\alpha - \frac{K}{q}\gamma\Big)\beta\Delta\varepsilon,\\
S_{\mathrm{VH}} &= \frac{1}{4}\frac{k}{q}\Big(\alpha + \frac{K}{q}\gamma\Big)\beta\Delta\varepsilon.
\end{aligned}
\tag{4.72}
$$

It should be noted that here we used the approximations $\frac{1-\varepsilon_{xx}}{\varepsilon_{xx}} \approx 1-\varepsilon_{xx}$, $\frac{1-\varepsilon_{yy}}{\varepsilon_{yy}} \approx 1-\varepsilon_{yy}$, and $\frac{1-\varepsilon_{zz}}{\varepsilon_{zz}} \approx 1-\varepsilon_{zz}$ which are justified because thes diagonal entries of the permittivity matrix have values that are close to unity, making the numerators small.

4.2.4.5 Scattering off basal plane.

We start analyzing particular geometries by assuming that the interface between the vacuum and material is normal to the optical axis, in which case we say that it coincides with the so-called basal plane. Substituting $\alpha = 0$, $\beta = 0$, and $\gamma = 1$ (see Figure 4.1) into equations (4.72), we obtain the following expressions for the reflection coefficients:

$$
\begin{aligned}
&S_{\mathrm{HH}} = -\frac{1}{4}\frac{k^2}{q^2}(\varepsilon_\perp - 1),\\
&S_{\mathrm{VV}} = S_{\mathrm{HH}}Q, \quad \text{where} \quad Q = \frac{1}{k^2}\Big(K^2\frac{\varepsilon_\parallel - 1}{\varepsilon_\perp - 1} - q^2\Big),\\
&S_{\mathrm{VH}} = 0, \quad S_{\mathrm{HV}} = 0.
\end{aligned}
\tag{4.73}
$$

Comparing the values of Q in formulae (4.73) and (4.44), we see that unlike in the isotropic case (see Figure 4.2(a)), the ratio of the co-polarized reflection coefficients now depends on the material properties. Indeed, while the quantity Q in (4.44) depends only on the incident angle, in (4.73) it may assume any real value, depending on $(\varepsilon_\perp - 1)$ and $(\varepsilon_\parallel - 1)$. Therefore, this scattering configuration has two degrees of freedom rendered by the real-valued reflection coefficients S_{HH} and S_{VV}.

Once the co-polarized channels S_{HH} and S_{VV} have been defined according to (4.73), one can look into the possibility of reconstructing the material parameters $\varepsilon_\perp$ and $\varepsilon_\parallel$ while interpreting

S_{HH} and S_{VV} as the given data. It turns out that system (4.73) can be solved with respect to $\varepsilon_\perp$ and $\varepsilon_\parallel$ for any values of the observables S_{HH} and S_{VV}. However, not every choice of the input data results in a physically feasible solution. In particular, the value of $Q = S_{\mathrm{VV}}/S_{\mathrm{HH}}$ should satisfy the condition

$$Q + \frac{q^2}{k^2} > 0 \tag{4.74}$$

in order for the susceptibilities to be positive:

$$\varepsilon_\perp - 1 > 0 \quad \text{and} \quad \varepsilon_\parallel - 1 > 0. \tag{4.75}$$

If the condition (4.74) is not satisfied, then at least one of the requirements on the material parameters in (4.75) will not be met.

4.2.4.6 Arbitrary direction of the optical axis.

Analysis of the last two equations in (4.72) shows that the cross-polarized channels are nonzero if $\beta \neq 0$ and $\beta \neq 1$, i.e., when the optical axis is neither parallel nor perpendicular to the plane of incidence (note that the basal plane case considered in Section 4.2.4.5 corresponds to $\beta = 0$, i.e., optical axis is parallel to the incidence plane, and thus provides only co-polarized scattering channels, see (4.73)). The cross-polarized channels are also proportional to $\Delta\varepsilon$, which once again shows that they vanish in the isotropic case. The ratio of the two off-diagonal entries of the scattering matrix is given by

$$\frac{S_{\mathrm{HV}}}{S_{\mathrm{VH}}} = -\frac{q\alpha - K\gamma}{q\alpha + K\gamma}.$$

This expression can help identify the individual effects of α and γ. If $\alpha = 0$, then the off-diagonal entries are equal. If $\gamma = 0$, i.e., the optical axis is parallel to the interface, then the sum of the off-diagonal entries is zero. In either of these two cases, the overall number of degrees of freedom is three, otherwise, i.e., when $\alpha\beta\gamma \neq 0$, it is four.

The ratio Q of two co-polarized reflection coefficients for arbitrary direction of optical axis differs from that given in formula (4.73), but still depends on $\Delta\varepsilon$:

$$\begin{aligned} Q = \frac{S_{\mathrm{VV}}}{S_{\mathrm{HH}}} &= \frac{1}{k^2(\eta_{yy} - 1)}\Big(K^2(\eta_{zz} - 1) - q^2(\eta_{xx} - 1)\Big) \\ &= \frac{1}{k^2}\Big(K^2\frac{\varepsilon_\perp - 1 + \gamma^2\Delta\varepsilon}{\varepsilon_\perp - 1 + \beta^2\Delta\varepsilon} - q^2\frac{\varepsilon_\perp - 1 + \alpha^2\Delta\varepsilon}{\varepsilon_\perp - 1 + \beta^2\Delta\varepsilon}\Big). \end{aligned} \tag{4.76}$$

The plots in Figure 4.2(b) and (c) illustrate how Q depends on $\varepsilon_\perp$ and $\varepsilon_\parallel$ for $\theta_i = \pi/9$. The exact formulation is made according to [Che83]. Similarly to the reflection coefficients in Figure 4.2(a), the linearized and exact values are close if $|\varepsilon_\perp - 1| \ll 1$ and $|\varepsilon_\parallel - 1| \ll 1$.

4.2.4.7 Discussion of the lossless birefringent medium and Theorem 1.

Compared to the isotropic case characterized by the scalar dielectric coefficient ε (Section 4.2.3), the case of a perfect uniaxial dielectric is controlled by four parameters: $\varepsilon_\perp$, $\varepsilon_\parallel$, α, and γ (note that β is not an independent quantity due to relation (4.48)). Depending on the particular geometry, this case may provide two ($\gamma = 1$, Section 4.2.4.5), three ($\alpha = 0,\ \beta\gamma \neq 0$ or $\gamma = 0,\ \alpha\beta \neq 0$), or four ($\alpha\beta\gamma \neq 0$) degrees of freedom (Section 4.2.4.6). However, the mere availability of the correct number of degrees of freedom does not, generally speaking, guarantee that the problem of reconstructing the material properties from reflection coefficients has a solution for any angle of incidence and any input data (i.e., any arbitrary values of the observable quantities S_{HH}, S_{VV}, S_{HV}, and S_{VH}).

The issue of solvability of the aforementioned problem is addressed by the following

Theorem 1. Equations (4.72) can be solved with respect to $\varepsilon_\perp$, $\varepsilon_\parallel$, α, and γ for the given S_{HH}, S_{VV}, S_{HV}, S_{VH}, and θ_i if and only if

$$(S_{\mathrm{VV}} + VS_{\mathrm{HH}})^2 \geqslant 4VS_{\mathrm{HV}}S_{\mathrm{VH}}, \tag{4.77}$$

where

$$V = \frac{q^2 - K^2}{k^2} = \cos^2\theta_i - \sin^2\theta_i = \cos 2\theta_i,$$

and θ_i is the angle of incidence defined in (4.40).

Theorem 1 is proved in Appendix N. Theorem 1 shows, in particular, that for the linearized scattering off a plane interface between the vacuum and a lossless birefringent dielectric, the inverse problem does not have a solution for all possible combinations of reflection coefficients, see (4.77). It is not clear ahead of time what may be causing this limitation of solvability: whether it is the type of the material that we have chosen or the linearization itself. We address this question in Appendix O by conducting numerical simulations for the exact formulation of the direct scattering problem. It turns out that even with no linearization there are still regions in the space of reflection coefficients for which there is no solution. Moreover, if in the case of weak scattering (when the linearization applies) neither the linearized nor the original problem happen to have a solution, then the regions of no solution for both problems seem to coincide. Hence, the limitation of solvability of the linearized inverse problem shall be attributed to the type of the target material rather than to the first Born approximation.

4.2.5 Isotropic and anisotropic lossy dielectric

4.2.5.1 Modified permittivity tensor in the presence of a finite conductivity.

First, we consider the case of an isotropic lossy dielectric, i.e., $\boldsymbol{\varepsilon} = \varepsilon\mathcal{I}$, $\boldsymbol{\sigma} = \sigma\mathcal{I}$, where $\varepsilon > 0$ and $\sigma > 0$ are scalars. Then, the propagation is governed by equations (4.17) supplemented by

the material relations

$$\boldsymbol{D} = \varepsilon \boldsymbol{E} \quad \text{and} \quad \boldsymbol{j} = \sigma \boldsymbol{E}. \tag{4.78}$$

Given (4.78), the second equation of (4.17) transforms into

$$\nabla \times \boldsymbol{H} = -ik\tilde{\varepsilon}\boldsymbol{E},$$

where [cf. formula (4.10)]

$$\tilde{\varepsilon} = \varepsilon + i\frac{4\pi\sigma}{\omega} = 1 + (\varepsilon - 1) + i\frac{4\pi\sigma}{\omega}. \tag{4.79}$$

This is equivalent to the previously considered case of a perfect isotropic dielectric (Section 4.2.3) with a redefined dielectric constant. The applicability of the first Born approximation (see Section 4.2.3.1) requires that the conductivity term in expression (4.79) be small, or $4\pi\sigma/\omega \sim \varkappa \ll 1$, see (4.21). If this condition is satisfied, then all the formulae in Section 4.2.3 remain valid, with ε replaced by $\tilde{\varepsilon}$.

We will now extend this consideration to anisotropic permittivity and conductivity. For the latter, we assume a uniaxial model described by the parameters $\sigma_\perp$, $\sigma_\parallel$, α_σ, β_σ, and γ_σ, similarly to the model of the dielectric tensor described in Section 4.2.4.1. Hence, the representation of the conductivity tensor in the coordinates of Figure 4.1 will be given by formula (4.49) with $(\sigma_\perp, \sigma_\parallel)$ substituted for $(\varepsilon_\perp, \varepsilon_\parallel)$ and $(\alpha_\sigma, \beta_\sigma, \gamma_\sigma)$ substituted for (α, β, γ). Given this representation and the linearity of relations (4.78), we can derive the following tensor counterpart of the scalar formula (4.79):

$$\tilde{\boldsymbol{\varepsilon}} = \boldsymbol{\varepsilon} + i\frac{4\pi}{\omega}\boldsymbol{\sigma}. \tag{4.80}$$

Next, notice that the reflection coefficients in (4.72) are linear functions of susceptibilities $(\varepsilon_\parallel - 1)$ and $(\varepsilon_\perp - 1)$ [note that $\Delta\varepsilon \equiv (\varepsilon_\parallel - 1) - (\varepsilon_\perp - 1)$], which is in agreement with the first Born approximation being a linear perturbation method with the susceptibilities playing the role of small parameters. Therefore, with the conductivities taken into account, the new scattering amplitudes can be calculated by simple substitution rules:

$$\begin{gathered} S_{\mathrm{HH}} = -\frac{1}{4}\frac{k^2}{q^2}\Big((\varepsilon_\perp - 1) + \beta^2\Delta\varepsilon\Big) \\ \Downarrow \\ \tilde{S}_{\mathrm{HH}} = -\frac{1}{4}\frac{k^2}{q^2}\Big((\varepsilon_\perp - 1) + \beta^2\Delta\varepsilon + i\frac{4\pi}{\omega}(\sigma_\perp + \beta_\sigma^2\Delta\sigma)\Big), \end{gathered} \tag{4.81a}$$

$$S_{\mathrm{VV}} = \frac{1}{4}\left(\left(\varepsilon_\perp - 1 + \alpha^2\Delta\varepsilon\right) - \frac{K^2}{q^2}\left(\varepsilon_\perp - 1 + \gamma^2\Delta\varepsilon\right)\right)$$
$$\Downarrow$$
$$\tilde{S}_{\mathrm{VV}} = \frac{1}{4}\Bigg((\varepsilon_\perp - 1) + \alpha^2\Delta\varepsilon - \frac{K^2}{q^2}\left((\varepsilon_\perp - 1) + \gamma^2\Delta\varepsilon\right) + i\frac{4\pi}{\omega}\left(\sigma_\perp + \alpha_\sigma^2\Delta\sigma - \frac{K^2}{q^2}\left(\sigma_\perp + \gamma_\sigma^2\Delta\sigma\right)\right)\Bigg), \tag{4.81b}$$

$$S_{\mathrm{HV}} = -\frac{1}{4}\frac{k}{q}\left(\alpha - \frac{K}{q}\gamma\right)\beta\Delta\varepsilon$$
$$\Downarrow$$
$$\tilde{S}_{\mathrm{HV}} = -\frac{1}{4}\frac{k}{q}\left(\left(\alpha - \frac{K}{q}\gamma\right)\beta\Delta\varepsilon + i\frac{4\pi}{\omega}\left(\alpha_\sigma - \frac{K}{q}\gamma_\sigma\right)\beta_\sigma\Delta\sigma\right), \tag{4.81c}$$

and

$$S_{\mathrm{VH}} = \frac{1}{4}\frac{k}{q}\left(\alpha + \frac{K}{q}\gamma\right)\beta\Delta\varepsilon$$
$$\Downarrow$$
$$\tilde{S}_{\mathrm{VH}} = \frac{1}{4}\frac{k}{q}\left(\left(\alpha + \frac{K}{q}\gamma\right)\beta\Delta\varepsilon + i\frac{4\pi}{\omega}\left(\alpha_\sigma + \frac{K}{q}\gamma_\sigma\right)\beta_\sigma\Delta\sigma\right), \tag{4.81d}$$

where $\Delta\sigma = \sigma_\parallel - \sigma_\perp$.

4.2.5.2 Isotropic permittivity and isotropic conductivity.

The reflection coefficients (4.38) and (4.44) modified by the foregoing procedure, contain the factor of $(\tilde{\varepsilon} - 1)$, see (4.79), and thus become complex. Their complexity affects the phase of the reflected wave. However, the *ratio* of the reflection coefficients for the vertical and horizontal polarization is still equal to the same quantity Q defined in (4.44). Moreover, the phase difference between the two reflection coefficients, or CPD, remains unchanged, i.e., equal to zero. As such, despite the changes in the values of the reflection coefficients due to a finite conductivity, this case still has only one degree of freedom, the same as the case of a perfect isotropic dielectric (see Section 4.2.3.4).

4.2.5.3 Anisotropic permittivity and isotropic conductivity: reflection from basal plane.

We analyze the effect of conductivity on the scattering amplitudes obtained in Section 4.2.4.5 assuming that the conductivity is isotropic, i.e., $\sigma_\perp = \sigma_\parallel = \sigma$. In this case, the value of Q in (4.73) should be replaced by

$$Q = \frac{1}{k^2}\Big(K^2\frac{\varepsilon_\parallel - 1 + (i4\pi\sigma)/\omega}{\varepsilon_\perp - 1 + (i4\pi\sigma)/\omega} - q^2\Big). \tag{4.82}$$

The new quantity Q defined by (4.82) depends on σ provided that $\varepsilon_\perp \neq \varepsilon_\parallel$. This means that the conductivity σ brings along a new degree of freedom to the scattering matrix. Qualitatively, the difference compared to the lossless case (4.73) is that the ratio of the co-polarized scattering amplitudes becomes complex, which introduces a phase shift between the corresponding scattered waves (i.e., a nonzero CPD). In particular, if the incident wave is polarized linearly, then the scattered field will be polarized elliptically.

Similarly to the case of zero conductivity (Section 4.2.4.5), finite conductivity may also result in solutions that are not feasible from the standpoint of physics. For example, expression (4.82) can be rewritten as

$$Q_1 \stackrel{\text{def}}{=} \frac{k^2}{K^2}\Big(Q + \frac{q^2}{k^2}\Big) = \frac{\varepsilon_\parallel - 1 + (i4\pi\sigma)/\omega}{\varepsilon_\perp - 1 + (i4\pi\sigma)/\omega}. \tag{4.83}$$

If we assume that the conductivity and susceptibilities are positive, i.e., $\sigma > 0$, $\varepsilon_\perp - 1 > 0$, and $\varepsilon_\parallel - 1 > 0$, then both the real and imaginary part of the numerator and denominator in the last expression of (4.83) are positive. It means, in particular, that

$$\mathrm{Re}(Q_1) > 0. \tag{4.84a}$$

As the imaginary parts of the numerator and denominator are equal, by comparing the absolute values we get

$$\begin{cases} \mathrm{Im}(Q_1) < 0 & \text{if} \quad |Q_1| > 1, \\ \mathrm{Im}(Q_1) > 0 & \text{if} \quad |Q_1| < 1. \end{cases} \tag{4.84b}$$

Recall that Q (and, consequently, Q_1) is an observable: $Q = S_{\mathrm{VV}}/S_{\mathrm{HH}}$. If, however, the observed value of Q_1 does not satisfy (4.84), then the assumption that the conductivity and the two susceptibilities are positive is violated.

4.2.5.4 Anisotropic permittivity and isotropic conductivity.

Generalizing the scenario presented in Section 4.2.5.3 to any geometry, (4.82) becomes

$$Q = \frac{K^2\left((\varepsilon_\perp - 1) + \gamma^2\Delta\varepsilon\right) - q^2\left((\varepsilon_\perp - 1) + \alpha^2\Delta\varepsilon\right) + i\frac{4\pi}{\omega}\sigma\left(K^2 - q^2\right)}{k^2\left((\varepsilon_\perp - 1) + \beta^2\Delta\varepsilon + i\frac{4\pi}{\omega}\sigma\right)}. \tag{4.85}$$

Similarly, (4.83) can be generalized to

$$Q_1 \stackrel{\text{def}}{=} \frac{k^2}{K^2}\left(Q + \frac{q^2}{k^2}\right) = \frac{\varepsilon_\perp - 1 + \gamma^2\Delta\varepsilon + \frac{q^2}{K^2}\left(\beta^2 - \alpha^2\right)\Delta\varepsilon + i\frac{4\pi}{\omega}\sigma}{\varepsilon_\perp - 1 + \beta^2\Delta\varepsilon + i\frac{4\pi}{\omega}\sigma}. \tag{4.86}$$

4.2.5.5 Anisotropic permittivity and conductivity.

Let $\boldsymbol{P} = ((\varepsilon_\perp - 1), (\varepsilon_\parallel - 1), \alpha, \beta, \gamma)$ be a set of parameters defining the permittivity of the material (Section 4.2.4.1), and $\boldsymbol{C} = (\sigma_\perp, \sigma_\parallel, \alpha_\sigma, \beta_\sigma, \gamma_\sigma)$ be the parameters of the material conductivity (Section 4.2.5.1). As shown in Section 4.2.5.1, the effect of a finite "uniaxial" conductivity can be described by adding imaginary components to the reflection coefficients. For each coefficient, the functional dependence of the imaginary part on the parameters $\boldsymbol{C}$ is similar to that of the real part on $\boldsymbol{P}$ [as illustrated by formula (4.81a)]. For the entire matrix of reflection coefficients $\mathcal{S}$ (essentially equivalent to the scattering matrix $\mathcal{S}$ of (4.14), see Section 4.2.3.4), this functional dependence may be expressed as

$$\mathcal{S} = \mathcal{S}(\boldsymbol{P}, \boldsymbol{C}) = \begin{bmatrix} S_{\mathrm{HH}}(\boldsymbol{P}) & S_{\mathrm{HV}}(\boldsymbol{P}) \\ S_{\mathrm{VH}}(\boldsymbol{P}) & S_{\mathrm{VV}}(\boldsymbol{P}) \end{bmatrix} + i\frac{4\pi}{\omega} \begin{bmatrix} S_{\mathrm{HH}}(\boldsymbol{C}) & S_{\mathrm{HV}}(\boldsymbol{C}) \\ S_{\mathrm{VH}}(\boldsymbol{C}) & S_{\mathrm{VV}}(\boldsymbol{C}) \end{bmatrix}. \tag{4.87}$$

In the first term on the right-hand side of (4.87), the entries S_{HH}, S_{VH}, S_{HV}, and S_{VV} of the matrix are real-valued functions of $\boldsymbol{P}$ defined by (4.72). In the second term, the same functions are applied to $\boldsymbol{C}$.

It has been shown in Section 4.2.4.6 and Appendix N that for the lossless material the set of permittivity parameters $\boldsymbol{P}$ provides up to four degrees of freedom to the scattering matrix $\mathcal{S}$ of (4.87). Further, we notice that the real and imaginary parts of $\mathcal{S}$ depend on $\boldsymbol{P}$ and $\boldsymbol{C}$ the same way up to a multiplicative constant $4\pi/\omega$ in front of the imaginary part. Hence, the set of conductivity parameters $\boldsymbol{C}$ provides up to four additional degrees of freedom to the matrix $\mathcal{S}$. Altogether, the combination of $\boldsymbol{P}$ and $\boldsymbol{C}$ provides up to eight degrees of freedom to the complex-valued matrix $\mathcal{S}$.

The result of Theorem 1 naturally extends from the lossless material to the lossy material via the following

Corollary 1. The permittivity parameters $\boldsymbol{P}$ and the conductivity parameters $\boldsymbol{C}$ can be reconstructed from the given complex-valued entries of the scattering matrix $\mathcal{S}$ of (4.87) if and only if the inequalities

$$(\mathrm{Re}(S_{\mathrm{VV}}) + V\mathrm{Re}(S_{\mathrm{HH}}))^2 \geqslant 4V\mathrm{Re}(S_{\mathrm{HV}})\mathrm{Re}(S_{\mathrm{VH}}), \tag{4.88a}$$

$$(\mathrm{Im}(S_{\mathrm{VV}}) + V\mathrm{Im}(S_{\mathrm{HH}}))^2 \geqslant 4V\mathrm{Im}(S_{\mathrm{HV}})\mathrm{Im}(S_{\mathrm{VH}}), \tag{4.88b}$$

hold simultaneously.

Each of the inequalities (4.88a) and (4.88b) is similar to inequality (4.77) in Theorem 1. We can notice again that the functional dependence of $\mathrm{Re}(\mathcal{S})$ and $\mathrm{Im}(\mathcal{S})$ on $\boldsymbol{P}$ and $\boldsymbol{C}$, respectively, is the same up to a constant factor. Thus, the proof of Corollary 1 reduces to the proof of Theorem 1 applied independently to $\mathrm{Re}(\mathcal{S})$ and $\mathrm{Im}(\mathcal{S})$.

For this most general setting, it may also possible to formulate the criteria for a solution

to the inverse problem to be physical, i.e., to satisfy the conditions $\varepsilon_\perp > 1$, $\varepsilon_\parallel > 1$, $\sigma_\perp > 0$, and $\sigma_\parallel > 0$ (see Sections 4.2.3.4, 4.2.4.5, and 4.2.5.3 for particular cases). If so, however, the resulting expressions are cumbersome. They may be part of a future study.

4.2.5.6 Discussion of lossy materials.

Altogether, the case of anisotropic permittivity and conductivity has eight independent material parameters and may provide up to eight degrees of freedom to the scattering matrix. If the hypothesis of Corollary 1 holds, then the material parameters can be successfully reconstructed from the observables. At the same time, the particular cases of isotropic conductivity considered in Sections 4.2.5.2 and 4.2.5.3 illustrate that the introduction of a new physical effect that modifies the scattering mechanism does not necessarily lead to an increased number of the degrees of freedom. Some other simplifications may also reduce the number of degrees of freedom. For example, the assumption that the dielectric axis coincides with the conductivity axis will reduce the number of independent parameters from eight to six.

Similarly to Sections 4.1.2 and 4.2.3.2, the first Born approximation does not provide a physically viable solution in the material, which in the case of a finite conductivity would be a spatially decaying wave. Indeed, in order for the transmitted wave to decay as $z \to +\infty$, the component of its wavenumber normal to the interface should have an imaginary part. However, after the linearization, see equations (4.25) and (4.27), the only possible representation for the scattered field is given by (4.32), where the value of q is always real and is defined by the incident field. Thus, the effect of conductivity is restricted to the changes in the amplitude and phase of the reflected wave.

Let us also recall that even though the observed scattering matrix (4.14) or (4.87) has four complex-valued entries, in practice it may appear impossible to distinguish between the relative phase and the common phase that accounts for the travel distance. Hence, it is customary to keep the HH entry of the scattering matrix real, see the discussion around equations (4.15), which reduces the number of degrees of freedom to seven.

4.3 Convolution with the fundamental solution and surface potentials

Having discussed the linearized scattering off a half-space filled with various types of materials, we recall that in the context of SAR imaging the ground reflectivity function is taken in the form of a single layer, see formula (4.11), or in other words, the target material is considered concentrated only on the surface of the half-space. In this section, we show that for every material considered in Section 4.2, scattering off a material subspace can be equivalently reformulated as scattering off a layer of monopoles on its surface.

4.3.1 Lossless isotropic target

Let us return for the moment to the simplest case of a perfect isotropic dielectric. We will provide a somewhat different interpretation of the solutions obtained in Section 4.2.3 that will help us justify the use of the ground reflectivity function for SAR imaging in the form of a single layer on the interface $z = 0$, see formula (4.11).

For the operator $\hat{L}$ of (4.27), we first define its fundamental solution $\mathcal{E} = \mathcal{E}(z)$ as a solution to the inhomogeneous equation $\hat{L}\mathcal{E} = \delta(z)$ subject to the radiation conditions (4.28). The fundamental solution exists, is unique, and is given by

$$\mathcal{E}(z) = \frac{1}{2iq} e^{iq|z|}. \tag{4.89}$$

Recall that for the scattering solution in the form (4.32), we have $B = C$ (see (4.34)) for the "homogeneous" part of the solution, $u^{(\mathrm{h})}(z)$, see (4.29). Consequently, $u^{(\mathrm{h})}(z)$ can be represented in the form of a single layer potential:

$$u^{(\mathrm{h})}(z) = \mathcal{E}(z) * N\delta(z) = N\mathcal{E}(z). \tag{4.90}$$

The magnitude of the δ-function at the interface, i.e., the density N of the potential, is equal to the jump of its derivative at $z = 0$, i.e.,

$$N = \left[\frac{du^{(\mathrm{h})}}{dz}\right]_{z=0} = 2iqCu_0, \tag{4.91}$$

where we use the notation

$$\left[\frac{du}{dz}\right]_{z=0} \stackrel{\text{def}}{=} \left.\frac{du}{dz}\right|_{(M)} - \left.\frac{du}{dz}\right|_{(F)} \tag{4.92}$$

The quantity N in (4.91) depends on the polarization. For the horizontal polarization, the continuity of $\frac{du^{(\mathrm{sc})}}{dz}$ at $z = 0$, see (4.37), implies that the jump of $\frac{du^{(\mathrm{h})}}{dz}$ should be negative that of $\frac{du^{(\mathrm{p})}}{dz}$:

$$\left[\frac{du^{(\mathrm{h})}}{dz}\right]_{z=0} = -\left[\frac{du^{(\mathrm{p})}}{dz}\right]_{z=0},$$

Using (4.31), we get [cf. formula (4.38)]:

$$N_{\mathrm{HH}} = -\frac{iq}{2}\frac{k^2}{q^2}(\varepsilon - 1)u_0 \tag{4.93}$$

where u_0 is the amplitude of the incident wave for the horizontal polarization, i.e., $E_{0y}^{(\mathrm{inc})}$.

For the vertical polarization, formula (4.43) yields:

$$\left[\frac{du^{(\mathrm{h})}}{dz}\right]_{z=0} = -\left[\frac{du^{(\mathrm{p})}}{dz}\right]_{z=0} + (\varepsilon - 1)\frac{du^{(\mathrm{inc})}}{dz}\bigg|_{z=0},$$

where $u^{(\mathrm{inc})}$ is given by (4.24b). Consequently [cf. formula (4.44)],

$$N_{\mathrm{VV}} = -\frac{iq}{2}\frac{k^2}{q^2}(\varepsilon - 1)u_0 + iq(\varepsilon - 1)u_0 = QN_{\mathrm{HH}}. \tag{4.94}$$

Here, u_0 is the amplitude of the incident wave for the vertical polarization, i.e., $H_{0y}^{(\mathrm{inc})}$.

In either case, (4.93) or (4.94), the solution $u^{(\mathrm{h})}(z)$ of (4.90) coincides in the vacuum region $z < 0$ with the overall scattering solution $u^{(\mathrm{sc})}(z)$, see formulae (4.32) and (4.29). This means that the reflected field given by the first Born approximation for the scattering off a material half-space can be equivalently represented as the reflected field due to the linearized scattering off a specially chosen δ-layer at the boundary of the half-space. Moreover, for both horizontal and vertical polarization, the magnitude of the single layer is proportional to $(\varepsilon - 1)u_0$ or equivalently, to the scalar lossless ground reflectivity function (4.7) times the incident field at the interface:

$$N \propto (\varepsilon - 1)u_0 = \left(\frac{c^2}{v^2} - 1\right)u_0 = c^2\nu u_0.$$

This explains why for the analysis of the reflected field in the framework of the first Born approximation the ground reflectivity function can be chosen in the form of a single layer at the material interface, see formula (4.11). We also note that according to the electromagnetic equivalence theorem by Schelkunoff [Sch36], the field on a given region, regardless of its actual sources located outside of this region, can be reproduced as the field from the specially chosen auxiliary sources at the boundary of the region.

Given the representation (4.90) of the reflected field as a convolution with the fundamental solution, one can formulate a natural question of whether or not the entire scattering solution can be obtained as a convolution integral. In fact, equation (4.27) has been solved by convolution in [Ori85]. This approach, however, suffers from two limitations. First, the convolution of the fundamental solution (4.89) with the right-hand side $g(z)$ of (4.27) leads to a diverging improper integral over the interval $0 \leqslant z < \infty$, and the use of the limiting absorption principle in [Ori85] for "fixing" the divergence lacks mathematical rigor. But even disregarding that, the second limitation is more important. For a bounded continuous right-hand side $g(z)$ in (4.27), the convolution integral yields a C^1 smooth function. This implies, in particular, the continuity of the resulting solution and its first derivative at $z = 0$, which corresponds to the horizontal polarization only. In other words, a straightforward convolution-based approach cannot account for any boundary conditions other than (4.37) and hence cannot be used for studying other

polarizations. To analyze the vertical polarization, an additional singular term at $z = 0$ due to boundary condition (4.43) should be taken into account along with the right-hand side $g(z)$.

4.3.2 Anisotropic and lossy targets

The approach of Section 4.3.1 can be extended to include more complex cases considered in Table 4.2. The new effects to be described are the cross-polarized components in the scattered field and the phase shift due to a finite conductivity.

For an incident wave in one of the two basic polarizations, the presence of two components in the scattered field (co-polarized and cross-polarized) can be described by a two-dimensional vector δ-layer. In doing so, formula (4.90) applies to each component of the vector δ-layer separately. For a birefringent scatterer considered in Section 4.2.4, we can use relation (4.91) and express the components of the vector density using reflection coefficients defined by formulae (4.72):

$$\boldsymbol{M}_{\mathrm{H}} = \begin{bmatrix} N_{\mathrm{HH}} \\ N_{\mathrm{VH}} \end{bmatrix} = 2iqE_{0y}^{(\mathrm{inc})} \begin{bmatrix} S_{\mathrm{HH}} \\ S_{\mathrm{VH}} \end{bmatrix}, \quad \boldsymbol{M}_{\mathrm{V}} = \begin{bmatrix} N_{\mathrm{VV}} \\ N_{\mathrm{HV}} \end{bmatrix} = 2iqH_{0y}^{(\mathrm{inc})} \begin{bmatrix} S_{\mathrm{VV}} \\ S_{\mathrm{HV}} \end{bmatrix}. \tag{4.95}$$

A finite conductivity affects the density of the δ-layers given by formulae (4.93), (4.94), and (4.95) through the modified dielectric tensor $\tilde{\boldsymbol{\varepsilon}}$ of (4.80) and the corresponding changes in the reflection coefficients (see Section 4.2.5.1).

4.4 Application to polarimetric target decomposition

The polarimetric target decomposition [CP96, LP09] can be viewed as a heuristic method of solving the inverse scattering problem. Basically, the goal is to represent the scattering matrix[8] as a linear combination of the basis matrices:

$$\mathcal{S} = c_1\mathcal{S}_1 + c_2\mathcal{S}_2 + c_3\mathcal{S}_3 + c_4\mathcal{S}_4, \tag{4.96}$$

where each of $\mathcal{S}_i$, $i = 1, 2, 3, 4$, represents a particular scattering mechanism, and c_i, $i = 1, 2, 3, 4$, are complex-valued coefficients to be determined. For example, the Pauli matrices

$$\mathcal{S}_1 = \begin{bmatrix} 1 & 0 \\ 0 & 1 \end{bmatrix}, \quad \mathcal{S}_2 = \begin{bmatrix} 1 & 0 \\ 0 & -1 \end{bmatrix}, \quad \mathcal{S}_3 = \begin{bmatrix} 0 & 1 \\ 1 & 0 \end{bmatrix}, \quad \text{and} \quad \mathcal{S}_4 = \begin{bmatrix} 0 & -i \\ i & 0 \end{bmatrix}.$$

may be associated with single-bounce and double-bounce scattering off plane surfaces with different orientation, see [LP09, Chapter 6]. The choice of the basis $\mathcal{S}_i$ for decomposition spec-

[8] In practice, the decomposition is often applied to the coherency and covariance matrices, whose entries are second order moments of the particular combinations of entries of the Sinclair scattering matrix, see [LP09, Chapters 3, 6]. The decomposition considered here is called the "coherent decomposition."

ifies the range of admissible scattering mechanisms, whereas the decomposition coefficients c_i determine the (relative) weights for individual mechanisms.

If some a priori knowledge about the actual scattering process is available, then it may be beneficial to choose one (or more) of the matrices $\mathcal{S}_i$ as the matrix of reflection coefficients for a given scattering mechanism [see, e.g., formula (N.1)]. This choice allows one to estimate the role of a particular mechanism in the overall scattering, and makes it easier to interpret the results of decomposition. For example, some foliage penetration and terrain scattering models [CP96, Section VI] involve multiple scattering channels where one of the stages is the "mirror" reflection from the ground. The models developed in Section 4.2 may be used to represent this "mirror reflection" stage for sufficiently large radar wavelengths that allow one to neglect the roughness of the surface.

In the current work, we analyze the Sinclair scattering matrices built from physical principles. We can therefore expect that if an appropriate basis is chosen, then the polarimetric target decomposition will yield the corresponding material characteristics. For a lossless material, the matrix of reflection coefficients (4.72) can be equivalently represented as

$$\mathcal{S} = \begin{bmatrix} S_{\mathrm{HH}} & S_{\mathrm{HV}} \\ S_{\mathrm{VH}} & S_{\mathrm{VV}} \end{bmatrix} = -\frac{1}{4}\frac{k^2}{q^2}\Big((\varepsilon_\perp - 1)\mathcal{S}_1 + \Delta\varepsilon\mathcal{S}_2 + \frac{q}{k}\alpha\beta\Delta\varepsilon\mathcal{S}_3 - \frac{K}{k}\gamma\beta\Delta\varepsilon\mathcal{S}_4\Big), \tag{4.97}$$

where the matrices $\mathcal{S}_i$, $i = 1, 2, 3, 4$ are given by

$$\mathcal{S}_1 = \begin{bmatrix} 1 & 0 \\ 0 & \dfrac{K^2 - q^2}{k^2} \end{bmatrix}, \quad \mathcal{S}_2 = \begin{bmatrix} \beta^2 & 0 \\ 0 & \dfrac{K^2\gamma^2 - q^2\alpha^2}{k^2} \end{bmatrix}, \quad \mathcal{S}_3 = \begin{bmatrix} 0 & 1 \\ -1 & 0 \end{bmatrix}, \quad \text{and} \quad \mathcal{S}_4 = \begin{bmatrix} 0 & 1 \\ 1 & 0 \end{bmatrix}.$$

Hence, we can interpret formula (4.97) as a polarimetric target decomposition of type (4.96) with $c_1 = \varepsilon_\perp - 1$, $c_2 = \Delta\varepsilon$, $c_3 = q\alpha\beta\Delta\varepsilon/k$, and $c_4 = -K\gamma\beta\Delta\varepsilon/k$ (up to a common multiplicative factor of $-\frac{1}{4}\frac{k^2}{q^2}$, which can also be combined with the geometric attenuation coefficient). If we have the decomposition (4.97), then of the four material parameters to be reconstructed, the two permittivities are obtained directly from c_1 and c_2, while the relations for c_3 and c_4 provide two equations for two of the three directional cosines of the optical axis (with the third expressed via (4.48)). The problem however is that the entries of the matrix $\mathcal{S}_2$ depend on the material parameters (direction angles for the optical axis) and cannot be defined without having to solve the inverse problem first. It is possible though to break the loop by taking any diagonal matrix not proportional to $\mathcal{S}_1$ instead of $\mathcal{S}_2$. For example, the following set of matrices

$$\mathcal{S}_1 = \begin{bmatrix} 1 & 0 \\ 0 & \dfrac{K^2 - q^2}{k^2} \end{bmatrix}, \quad \mathcal{S}_2' = \begin{bmatrix} 0 & 0 \\ 0 & \dfrac{K^2}{k^2} \end{bmatrix} \quad \mathcal{S}_3 = \begin{bmatrix} 0 & -1 \\ 1 & 0 \end{bmatrix}, \quad \text{and} \quad \mathcal{S}_4 = \begin{bmatrix} 0 & 1 \\ 1 & 0 \end{bmatrix} \tag{4.98}$$

forms a basis in the space of 2x2 matrices with real entries, does not depend on the material

properties, and hence can be used for target decomposition. The disadvantage of this set is that the resulting value of c_2 will, generally speaking, differ from $\Delta\varepsilon$, and thus the values of ξ, α, and γ calculated from c_1, c_3, and c_4 will also be incorrect. Still, expansion (4.96) with respect to the basis (4.98) is capable of detecting several types of configurations (see Figure 4.1):

(i) Isotropy ($\zeta = 0$), by observing that $c_2 = c_3 = c_4 = 0$;

(ii) Optical axis being either parallel to the incidence plane ($\beta = 0$) or perpendicular to it ($\beta = 1$, $\alpha = \gamma = 0$), when $c_2 \neq 0$, $c_3 = c_4 = 0$;

(iii) Optical axis being horizontal, excluding the cases in item (ii), ($\alpha \neq 0$, $\beta \neq 0$, $\gamma = 0$) when $c_3 \neq 0$, $c_4 = 0$;

(iv) Optical axis lying in the plane normal to both the interface and the incidence plane, excluding the cases in item (ii), ($\alpha = 0$, $\beta \neq 0$, $\gamma \neq 0$) when $c_3 = 0$, $c_4 \neq 0$;

(v) Any of the "main diagonal" directions of the optical axis ($|\alpha| = |\beta| = |\gamma| = 1/\sqrt{3}$), when $c_2 = 0$, $c_3 \neq 0$, $c_4 \neq 0$, etc.

Thus, basis (4.98) appears suitable for the *qualitative classification* of birefringent targets, although exact determination of the material parameters still requires solving a nonlinear system (4.72) that consists of four equations. It is to be noted though that in practice, the equalities in criteria (i)–(v) shall be replaced by thresholds that would take into account the accuracy of the measurements and the noise levels. The questions related to noise and experimental accuracy will be addressed in a future publication.

Lossy targets can be identified by detecting a phase shift other than 0 or π between the channels. As the imaginary part of the matrix $\mathcal{S}$ is similar in structure to the real part [see formula (4.87)], a complex counterpart of the set of matrices (4.98) can be used for the decomposition of $\mathrm{Im}(\mathcal{S})$, which is equivalent to allowing the coefficients c_i to become complex.

4.5 Chapter summary

We have analyzed the linearized scattering of a plane transverse electromagnetic wave off a material half-space filled with a birefringent weakly conductive dielectric. Our main findings are as follows:

- We have shown that the first Born approximation correctly predicts the scattered field (both amplitude and phase for each polarization) in the vacuum region.
- We have demonstrated that with the polarization and anisotropy taken into account, the linearized scattering off a material half-space can still be equivalently reformulated in the

vacuum region as scattering off a specially chosen δ-layer at the interface. This justifies the choice of a ground reflectivity function in the form of a single layer at the surface of a target, which is common for SAR applications.

- The corresponding inverse scattering problem consists of reconstructing the material characteristics, i.e., the permittivities, conductivities, and direction angles at the target, from the observable quantities, i.e., from the four complex-valued entries of the Sinclair scattering matrix. We have provided a necessary and sufficient condition (see Theorem 1 and Corollary 1) for this inverse problem to have a solution in the linearized framework.

As of yet, our analysis is limited to "mirror" scattering off a flat surface, and does not account for backscattering. Hence, in the context of SAR it may be useful for bistatic rather than monostatic imaging, i.e., for the case where the transmitting and receiving antennas are two different antennas at two different locations. Another possible application of this "mirror reflection" mechanism is to be a ground reflection component in the composite foliage penetration and terrain scattering models [CP96, Section VI].

In this chapter, we have not formally considered any variation of material characteristics along the interface; that's why we could assume that all the waves have a common horizontal component K of the wavenumber, see Figure 4.1. It is obvious, however, that our analysis extends with no change to the case of slowly varying material characteristics. This means, in particular, that we can consider ground reflectivity functions that vary along the interface, but only if $\lambda \ll d$, where λ is the wavelength and d is the characteristic scale of material variations defined, e.g., as $d^{-1} \sim |\nabla\hat{\varepsilon}|/|\hat{\varepsilon}|$, where $\hat{\varepsilon}$ can stand for any of the actual physical quantities that we have taken into account. The constraint $\lambda \ll d$ should not present a major limitation for SAR applications, because the SAR resolution is typically much larger than the wavelength anyway, see (2.71). On the other hand, our current analysis does not apply to short-scale material variations, $d \sim \mathcal{O}(\lambda)$, and to include those it will need to be modified. This is related to accounting for backscattering.

Our motivation for analyzing the first Born approximation in the case of polarized waves and anisotropic targets was the possibility to build a polarimetric SAR ambiguity theory similarly to how it is done in the scalar case. This, in particular, may help extend the results of Chapter 2 from the case of scalar imaging to the case of polarimetric imaging that also involves the Faraday rotation in the magnetized ionosphere (Chapter 3). It may also appear useful for material identification (see Section 4.4). Our analysis shows that the polarimetric inverse problem as formulated in this chapter can be soved provided that the hypotheses of Theorem 1 and Corollary 1 hold. It is also to be noted that the limitation of solvability of the linearized inverse problem imposed by Theorem 1 is apparently due to the type of the material that we have chosen (a birefringent dielectric with weak anisotropic conductivity) rather than to the

linearization itself, see Appendix O. Giving a physical interpretation to inequality (4.77), as well as, perhaps, considering other materials and answering a related question of having non-physical solutions to the inverse problem, see Sections 4.2.3.4, 4.2.4.5, 4.2.5.3, and 4.2.5.5, will be a subject for the future study.

Chapter 5

Summary and Topics for the Future

5.1 Isotropic ionosphere

SAR images obtained from satellites are prone to deterioration due to the temporal dispersion of radio waves in the Earth's ionosphere. The deterioration is stronger for lower carrier frequencies and weaker for higher carrier frequencies. We have analyzed this phenomenon in the case of a scalar field (for which polarization of radar pulses is not taken into account) propagating in an inhomogeneous cold plasma. Our analysis shows that image deterioration is due to the mismatch between the actual signals scattered off the Earths' surface and received by the radar antenna and the matched filter (which is a signal processing tool) designed as if the propagation between the antenna and the ground was unobstructed.

To correct the filter, one needs to know the total electron content (per unit area) in the layer of ionospheric plasma between the satellite and the ground. This key characteristic needs to be known precisely at the time and place the image is taken. We have proposed to derive this quantity by probing the terrain, and hence the ionosphere, on two distinct carrier frequencies. We have also shown that within the accuracy of the TEC reconstruction, the resulting correction of the filter eliminates all the distortions of the image that are due to the deterministic part of the electron content in the ionosphere.

The correction, however, is not effective for removing the distortions due to the random part of the charged particle content, i.e., turbulent fluctuations of the electron number density. The reason is that the correction is essentially based on the information obtained from a single pass of the signal back and forth between the antenna and the target. For this single pass, the role of randomness is minimal because the effect of individual fluctuations averages out due to the ergodicity. Nonetheless, the stochastic part manifests itself as the contributions from multiple passes are added up along the synthetic array. Although we provide estimates for image distortions due to the stochastic part of ionospheric disturbances, mitigating them will

be a subject for the future study.

We have proposed to use the area-based image registration for improving the accuracy and robustness of the reconstructed TEC in the dual-carrier probing approach. In particular, we have related the error of the registration to that of the TEC reconstruction, and have also shown how the error of the TEC affects the final quality of the re-processed image. The proposed methodology leads to a multi-fold reduction of the image artifacts caused by the ionosphere in their part which is not due to the turbulence. An important advantage of the proposed methodology is that neither does it require the ground-based receivers (like GPS does) nor does it need a repeat satellite pass.

In addition, Chapter 2 exploits the true Kolmogorov-Obukhov spectrum of turbulence and includes a more accurate account of the effect of turbulent fluctuations on the image than that in [Tsy09a, ST11]. It also accounts for Ohmic losses in the ionospheric plasma and for the horizontal inhomogeneity of the ionosphere. In regard to the latter we note that whereas our description predicts that the sign of the azimuthal displacement S_A and that of the first moment $\mathcal{Q}$ will be the same, see (2.90), other descriptions in the literature may have those signs as opposite, see, e.g., [CZ12, LKI+03, GMS00]. We attribute this discrepancy to the difference in the definition of S_A.

In the case of an isotropic ionosphere, the issues to be addressed in the future may include:

- Studying the possibility of iterative application of registration/correction procedures. Even if the first correction is not perfect (say, because the images are blurry and cannot be registered well enough), the improvement of the image quality may result in a better registration of the two corrected images.

- A more thorough analysis of the stochastic component of ionospheric distortions using the turbulence structure function [RKT89b] rather than the correlation function. Development of appropriate strategies of how to additionally correct the matched filter in order to reduce the stochastic part of ionospheric distortions, assuming that the statistics of waves are known.

- An investigation of whether the stochastic component of distortions can be tackled by any of the general "black box" image sharpening and deblurring techniques [GW08] developed previously with no direct relation to spaceborne SAR. This may be warranted given that the current mitigation strategy based on dual carrier probing is effective mostly for the deterministic part of ionospheric distortions.

5.2 Anisotropic ionsphere

We have shown that for single-polarization SAR, the Faraday rotation is another factor that must be accounted for in a corrected matched filter. This can be done separately to the corrections for dispersive propagation, and the filter that accounts for the FR can have new corrections applied on top of the previous ones. We considered the case where the rotation is sufficiently large to not be neglected, but sufficiently small so that a linearization of the effect of rotation on the received signal could still be a valid approximation.

While it is another step towards a full-fledged SAR ambiguity theory, Chapter 3 is only the first stage in incorporating the presence of the Earth's magnetic field into the analysis. Future development may include investigation of the accuracy and robustness of the proposed algorithm for image improvement. Similarly to how we have looked into the issue of residual distortions when correcting for the effect of the scalar dispersive propagation (Section 2.9), this study will elucidate what kind of distortions one should still anticipate if the parameters characterizing the Faraday rotation are not known exactly but rather obtained with some error. The accuracy analysis will also include studying the sensitivity of the image ACF to the value of the shift h, and mitigating the effect of this sensitivity on the proposed correction procedure. In particular, the ACF of the image intensity can be employed instead of the ACF of the image itself, as one can expect a better robustness of the algorithm from incorporating the quadratic data [DJ13, JD13]. Yet another factor that contributes to the overall accuracy is the accuracy of the solution of equations (3.28) with respect to the Faraday rotation parameter (Section 3.5). It may also be investigated in the future.

For a radar operating on very low frequencies the case of a wide range of the Faraday rotation angle may become important (case (c) on page 74 that is not addressed in this dissertation, see also Figure 3.2(c)). It will require special attention in the future, because the linearization (3.8) does not apply. Therefore, this case should be treated differently on both the parameter estimation and filter correction stage. The sub-band processing approach (Section 3.4), if refined and made quantitative, might provide additional estimates of the FR parameters even in this wide-range case.

Another issue that may be the subject of future research is analysis of the Faraday rotation within the chirp for the fully polarimetric case.

Finally, a thorough investigation of the role of randomness for SAR imaging through a magnetized ionosphere is also warranted. To that end, one will need to distinguish between the randomness of the target, which we do not consider, and the randomness of the medium, i.e., the ionosphere itself. Randomness of the ionosphere is due to the turbulent fluctuations of the electron number density n_{e}, which, in turn, make the Langmuir frequency ω_{pe}, see formula (J.4), a random quantity (more precisely, a random field). In [Tsy09a] and Chapter 2, the effect of the

turbulent fluctuations of n_{e} on transionospheric SAR imaging in the scalar isotropic framework has been quantified under the assumption that the scale of inhomogeneities (fluctuations) is small. In particular, we have shown that the performance of a spaceborne SAR instrument in azimuth is affected by turbulence much stronger than its performance in range. An even more comprehensive study that allows for the large scale of turbulent inhomogeneities can be found in [GS13]. According to (3.7), the Faraday rotation angle is proportional to $\omega_{\mathrm{pe}}^2 \Omega \cos\beta$. In the presence of turbulence, the Langmuir frequency ω_{pe} becomes random. As far as the other two factors, Ω and $\cos\beta$, neither of them formally depends on n_{e}. On the other hand, the external magnetic field $\boldsymbol{H}_0$ may still fluctuate if it appears (partially) frozen into the plasma for the particular conditions of interest. Therefore, the behavior of both Ω and $\cos\beta$ in the presence of turbulence will need to be studied thoroughly so as to adequately represent the overall statistic of φ_F.

5.3 Anisotropic scattering

Chapter 4 presents an analysis of the effect of the target, possibly anisotropic, on the polarization signature. Specifically, we looked at a hierarchy of predominately dielectric scattering materials and, assuming the scattering was weak, we were able to show that the first Born approximation predicts the correct scattered field in a vacuum, even for a fully polarimetric imaging system. This has allowed us to present the results of the analysis in a relatively compact analytic form.

In a fully polarimetric imaging system, the return data can be characterized by four complex coefficients relating two inputs to two outputs. For convenience, these are traditionally represented by the Sinclair scattering matrix. If the scatterer is represented as a weakly conductive uniaxial crystal, then there is a necessary and sufficient condition under which all eight degrees of freedom of the scattering matrix can be reconstructed from the observed data. This is an important result; in the past, the scattering matrix has overwhelmingly been treated phenomenologically, but we have shown that within the linear framework of the Born approximation, its values reflect key physical properties of the scatterer such as the permittivity and conductivity. Furthermore, we have shown that the condition needed to establish this relation is not an artifact of the linearization process but inherent in the selection of a uniaxial crystal as the model for the target.

As stated in Section 4.5, the scattering study was limited to mirror scattering off a flat surface. More work will have to be done to fit this into a realistic SAR imaging scenario where a satellite is observing the Earth by exploiting the backscattering at oblique incidence angles. This, in particular, could include analysis of scattering of the polarized radio waves off rough surfaces, with the goal of relating SAR imaging to a physical mechanism of backscattering at the target.

Additionally, future research should incorporate dispersive targets. Dispersion of the target material is a key characteristic that may enable its identification [MPA02]. The goal is to build a mathematical model for SAR imaging that includes the dispersion of the target, with possible future applications to material identification, and with the potential of distinguishing between the target dispersion and the ionospheric dispersion.

5.4 Additional directions for future work

Additional directions for future study may include:

- Applying the proposed methodology to processing the actual experimental data.
- Approaches for reducing the noise that is always present, regardless of whether the imaging is done through the ionosphere or not, for example, instrument noise or rough terrain noise. As a minimum requirement, this noise may not be amplified by any of the techniques used for mitigating the ionospheric distortions.
- Optimization of interrogating waveforms for the ionosphere, beyond the standard linear upchirps.
- An in-depth investigation of the VHF SAR imaging through the ionosphere aimed at determining whether the VHF frequencies (very low in the SAR context yet still above the Langmuir frequency) may require a more comprehensive propagation model that would include, for example, kinetic considerations [Gin64].
- Combined analysis of the medium anisotropy and target anisotropy (Chapter 4).
- More comprehensive models for the ionosphere that take into account the ions.
- Incorporation of the improved ground reflectivity models that account for the dependence on the viewing direction [GT13] and target texture.

REFERENCES

[Abd99] Ikram E. Abdou. Practical approach to the registration of multiple frames of video images. In Kiyoharu Aizawa, Robert L. Stevenson, and Ya-Qin Zhang, editors, *Visual Communications and Image Processing '99 (Proceedings of SPIE)*, volume 3653, pages 371–382, San Jose, CA, USA, 1999. SPIE.

[Arm05] N. A. Armand. Limitations to the resolution of satellite based synthetic aperture radars due to the conditions of the propagation of radio waves in the ionosphere. *Exploration of Earth from Space*, (1):27–38, 2005. [in Russian].

[BE05] R. Bamler and M. Eineder. Accuracy of differential shift estimation by correlation and split-bandwidth interferometry for wideband and delta-k SAR systems. *IEEE Geoscience and Remote Sensing Letters*, 2(2):151–155, April 2005.

[Bel08] D. P. Belcher. Theoretical limits on SAR imposed by the ionosphere. *IET Radar, Sonar & Navigation*, 2(6):435–448, 2008.

[BFST93] Svetlana M. Bauer, Sergei B. Filippov, Andrei L. Smirnov, and Petr E. Tovstik. Asymptotic Methods in Mechanics with Applications to Thin Shells and Plates. In Remi Vaillancourt and Andrei L. Smirnov, editors, *Asymptotic Methods in Mechanics*, pages 3–142, 1993.

[BG88] Warren D. Brown and Dennis C. Ghiglia. Some methods for reducing propagation-induced phase errors in coherent imaging systems. I. Formalism. *J. Opt. Soc. Am. A — Opt. Image Sci.*, 5(6):924–941, June 1988.

[BPE+10] Ramon Brcic, Alessandro Parizzi, Michael Eineder, Richard Bamler, and Franz Meyer. Estimation and compensation of ionospheric delay for SAR interferometry. In *Proceedings of the 2010 IEEE International Geoscience and Remote Sensing Symposium (IGARSS 2010)*, pages 2908–2911, Honolulu, Hawaii, July 2010. IEEE.

[BPE+11] Ramon Brcic, Alessandro Parizzi, Michael Eineder, Richard Bamler, and Franz Meyer. Ionospheric effects in SAR interferometry: An analysis and comparison of methods for their estimation. In *Proceedings of the 2010 IEEE International Geoscience and Remote Sensing Symposium (IGARSS 2011)*, pages 1497–1500, Vancouver, Canada, July 2011. IEEE.

[Bud85] K. G. Budden. *The Propagation of Radio Waves.* Cambridge University Press, Cambridge, 1985. The theory of radio waves of low power in the ionosphere and magnetosphere.

[BW99] Max Born and Emil Wolf. *Principles of optics: Electromagnetic theory of propagation, interference and diffraction of light.* With contributions by A. B. Bhatia, P. C. Clemmow, D. Gabor, A. R. Stokes, A. M. Taylor, P. A. Wayman and W. L. Wilcock. Seventh (expanded) edition. Cambridge University Press, Cambridge, 1999.

[CB08] Margaret Cheney and Brett Borden. Imaging moving targets from scattered waves. *Inverse Problems*, 24(3):035005 (22pp), June 2008.

[CB09] Margaret Cheney and Brett Borden. *Fundamentals of Radar Imaging*, volume 79 of *CBMS-NSF Regional Conference Series in Applied Mathematics*. SIAM, Philadelphia, 2009.

[CGM95] W. G. Carrara, R. S. Goodman, and R. M. Majewski. *Spotlight Synthetic Aperture Radar. Signal Processing Algorithms*. Artech House, Inc., Boston, 1995.

[CH06] Alexandre J. Chorin and Ole H. Hald. *Stochastic Tools in Mathematics and Science*, volume 1 of *Surveys and Tutorials in the Applied Mathematical Sciences*. Springer, New York, 2006.

[Che83] Hollis C. Chen. *Theory of Electromagnetic Waves: A Coordinate-Free Approach*. McGraw Hill, 1983.

[Che01] Margaret Cheney. A mathematical tutorial on synthetic aperture radar. *SIAM Rev.*, 43(2):301–312 (electronic), 2001.

[CM91] John C. Curlander and Robert N. McDonough. *Synthetic Aperture Radar. Systems and Signal Processing*. Wiley series in remote sensing. John Wiley & Sons, New York, 1991.

[CN04] Margaret Cheney and Clifford J. Nolan. Synthetic-aperture imaging through a dispersive layer. *Inverse Problems*, 20(2):507–532, 2004.

[CP96] S.R. Cloude and E. Pottier. A review of target decomposition theorems in radar polarimetry. *IEEE Transactions on Geoscience and Remote Sensing*, 34(2):498–518, March 1996.

[Cut90] L. J. Cutrona. Synthetic aperture radar. In M. Skolnik, editor, *Radar Handbook*. McGraw-Hill, New-York, 2nd edition, 1990.

[CW05] Ian G. Cumming and Frank H. Wong. *Digital Processing of Synthetic Aperture Radar Data*. Artech House, Boston, 2005.

[CZ12] Jingyi Chen and Howad A. Zebker. Ionospheric artifacts in simulataneous L-band InSAR and GPS observations. *IEEE Transactions on Geoscience and Remote Sensing*, 50(4):1227–1239, April 2012.

[DJ13] Laurent Demanet and Vincent Jugnon. Convex recovery from interferometric measurements. Research preprint, MIT, July 2013.

[DS02] K. Davies and E. K. Smith. Ionospheric effects on satellite land mobile systems. *IEEE Antennas and Propagation Magazine*, 44(6):24–31, December 2002.

[Dul63] George A. Dulk. Faraday rotation near the transverse region of the ionosphere. *J. Geophys. Res.*, 68:6391–6400, 1963.

[EJJ89] P. H. Eichel and C. V. Jakowatz Jr. Phase-gradient algorithm as an optimal estimator of the phase derivative. *Optics Letters*, 14:1101–1103, 1989.

[Fed77] M. V. Fedoryuk. *The Saddle-Point Method [Metod perevala]*. Nauka, Moscow, 1977. [Russian].

[FL99] Giorgio Franceschetti and Riccardo Lanari. *Synthetic Aperture Radar Processing*. Electronic Engineering Systems Series. CRC Press, Boca Raton, FL, 1999.

[FS04] A. Freeman and S. S. Saatchi. On the detection of Faraday rotation in linearly polarized L-band SAR backscatter signatures. *IEEE Transactions on Geoscience and Remote Sensing*, 42(8):1607–1616, August 2004.

[FZB02] H. Foroosh, J. B. Zerubia, and M. Berthod. Extension of phase correlation to subpixel registration. *IEEE Transactions on Image Processing*, 11(3):188–200, March 2002.

[Gai98] William B. Gail. Effect of Faraday rotation on polarimetric SAR. *IEEE Transaction on Aerospace and Electronic Systems*, 34(1):301–308, January 1998.

[GB88] Dennis C. Ghiglia and Warren D. Brown. Some methods for reducing propagation-induced phase errors in coherent imaging systems. II. Numerical results. *J. Opt. Soc. Am. A — Opt. Image Sci.*, 5(6):942–957, June 1988.

[GG60] V. L. Ginzburg and A. V. Gurevich. Nonlinear phenomena in a plasma located in an alternating electromagnetic field. *Soviet Physics — Uspekhi*, 3(1):115–146, 1960.

[Gin64] V. L. Ginzburg. *The Propagation of Electromagnetic Waves in Plasmas*, volume 7 of *International Series of Monographs on Electromagnetic Waves*. Pergamon Press, Oxford, 1964.

[GMS00] A. Laurence Gray, Karim E. Mattar, and George Sofko. Influence of ionospheric electron density fluctuations on satellite radar interferometry. *Geophysical Research Letters*, 27(10):1451–1454, 2000.

[Gne97] B. V. Gnedenko. *Theory of Probability*. Gordon and Breach, Amsterdam, Sixth edition, 1997. Translated from the Russian.

[GS13] Josselin Garnier and Knut Sølna. A multiscale approach to synthetic aperture radar in dispersive random media. *Inverse Problems*, 29:054006 (18pp), 2013.

[GST12] Mikhail Gilman, Erick Smith, and Semyon Tsynkov. A linearized inverse scattering problem for the polarized waves and anisotropic targets. *Inverse Problems*, 28(8):085009 (38pp), 2012.

[GST13a] Mikhail Gilman, Erick Smith, and Semyon Tsynkov. Reduction of ionospheric distortions for spaceborne SAR with the help of image registration. *Inverse Problems*, 29(5):054005 (35pp), 2013.

[GST13b] Mikhail Gilman, Erick Smith, and Semyon Tsynkov. Single-polarization SAR imaging in the presence of Faraday rotation. 2013. [submitted to *Inverse Problems*].

[GSTF08] Manuel Guizar-Sicairos, Samuel T. Thurman, and James R. Fienup. Efficient subpixel image registration algorithms. *Opt. Lett.*, 33(2):156–158, January 2008.

[GT13] Mikhail Gilman and Semyon Tsynkov. On a physical approach to the SAR ambiguity function for distributed scatterers. 2013. [In progress].

[Gur78] A. V. Gurevich. *Nonlinear Phenomena in the Ionosphere*. Springer-Verlag, New York, 1978.

[Gur07] A. V. Gurevich. Nonlinear effects in the ionosphere. *Physics — Uspekhi (Advances in Physical Sciences)*, 50(11):1091–1121, 2007.

[GW08] R. C. Gonzalez and R. E. Woods. *Digital Image Processing*. Prentice-Hall, New York, 3rd edition, 2008.

[Huy70] J. R. Huynen. *Phenomenological theory of radar targets*. PhD thesis, University of Technology, Delft, The Netherlands, December 1970.

[IKL+99] Akira Ishimaru, Yasuo Kuga, Jun Liu, Yunjin Kim, and Tony Freeman. Ionospheric effects on synthetic aperture radar at 100MHz to 2GHz. *Radio Science*, 34(1):257–268, January-February 1999.

[Isa90] Victor Isakov. *Inverse Source Problems*, volume 34 of *Mathematical Surveys and Monographs*. American Mathematical Society, Providence, RI, 1990.

[JD13] Vincent Jugnon and Laurent Demanet. Interferometric inversion: a robust approach to linear inverse problems. In *Proceedings of the SEG International Exposition and 83rd Annual Meeting*, Houston, TX, September 2013.

[JFSM10] Michael Jehle, Othmar Frey, David Small, and Erich Meier. Measurement of ionospheric TEC in spaceborne SAR data. *IEEE Transactions on Geoscience and Remote Sensing*, 48(6):2460–2468, June 2010.

[JRZ+09] Michael Jehle, Maurice Rüegg, Lukas Zuberbühler, David Small, and Erich Meier. Measurement of ionospheric Faraday rotation in simulated and real spaceborne SAR data. *IEEE Transactions on Geoscience and Remote Sensing*, 47(5):1512–1523, 2009.

[JWE+96] Charles V. Jakowatz, Daniel E. Wahl, Paul H. Eichel, Dennis C. Ghiglia, and Paul A. Thompson. *Spotlight-Mode Synthetic Aperture Radar: A Signal Processing Approach*. Springer, 1996.

[KBP79] C. D. Kuglin, A. F. Blumenthal, and J. J. Pearson. Map-matching techniques for terminal guidance using Fourier phase information. In *Proceedings of SPIE: Digital Processing of Aerial Images*, volume 186, pages 21–29. SPIE, 1979.

[Kel99] C. T. Kelley. *Iterative methods for optimization*, volume 18 of *Frontiers in Applied Mathematics*. Society for Industrial and Applied Mathematics (SIAM), Philadelphia, PA, 1999.

[KH75] C. D. Kuglin and D. C. Hines. The phase correlation image alignment method. In *Proceedings of the IEEE 1975 International Conference on Cybernetics and Society*, pages 163–165. IEEE, 1975.

[Lek91] John Lekner. Reflection and refraction by uniaxial crystals. *J. Phys: Condens. Matter*, 3(32):6121–6133, 1991.

[LF92] F. C. Lin and M. A. Fiddy. The Born-Rytov controversy: I. Comparing analytical and approximate expressions for the one-dimensional deterministic case. *J. Opt. Soc. Am. A*, 9(7):1102–1110, July 1992.

[LFT+11] C. Lardeux, P.-L. Frison, C. Tison, J.-C. Souyris, B. Stoll, B. Fruneau, and J.-P. Rudant. Classification of tropical vegetation using multifrequency partial SAR polarimetry. *IEEE Geoscience and Remote Sensing Letters*, 8(1):133–137, January 2011.

[LKI+03] Jun Liu, Yasuo Kuga, Akira Ishimaru, Xiaoqing Pi, and Anthony Freeman. Ionospheric effects on SAR imaging: A numerical study. *IEEE Transaction on Geoscience and Remote Sensing*, 41(5):939–947, May 2003.

[LL75] L. D. Landau and E. M. Lifshitz. *Course of Theoretical Physics, Vol. 2, The Classical Theory of Fields*. Pergamon Press, Oxford, fourth edition, 1975. Translated from the Russian by Morton Hamermesh.

[LL84] L. D. Landau and E. M. Lifshitz. *Course of Theoretical Physics. Vol. 8, Electrodynamics of Continuous Media*. Pergamon International Library of Science, Technology, Engineering and Social Studies. Pergamon Press, Oxford, 1984. Translated from the second Russian edition by J. B. Sykes, J. S. Bell and M. J. Kearsley, Second Russian edition revised by Lifshitz and L. P. Pitaevskii.

[LL08] Lianlin Li and Fang Li. Ionosphere tomography based on spaceborne SAR. *Advances in Space Research*, 42(7):1187–1193, 2008.

[LP09] Jong-Sen Lee and Eric Pottier. *Polarimetric Radar Imaging from Basics to Applications*. CRC Press, Boca Raton, 2009.

[LS87] M. A. Lavrentiev and B. V. Shabat. *Methods of the Theory of Functions in a Complex Variable*. Nauka, Moscow, Fifth edition, 1987. [In Russian].

[Mar06] Daniel L. Marks. A family of approximations spanning the Born and Rytov scattering series. *Opt. Express*, 14(19):8837–8848, September 2006.

[MBJF06] Franz Meyer, Richard Bamler, Norbert Jakowski, and Thomas Fritz. The potential of low-frequency SAR systems for mapping ionospheric TEC distributions. *IEEE Geoscience and Remote Sensing Letters*, 3(4):560–564, 2006.

[Mes71] M. A. Messier. A standard ionosphere for the study of electromagnetic pulse propagation. EMP Technical Note 117, Air Force Weapons Laboratory, March 1971.

[Mey11] F. J. Meyer. Performance requirements for ionospheric correction of low-frequency SAR data. *IEEE Transactions on Geoscience and Remote Sensing*, 49(10):3694–3702, October 2011.

[MF53] Philip M. Morse and Herman Feshbach. *Methods of Theoretical Physics. 2 Volumes.* International Series in Pure and Applied Physics. McGraw-Hill Book Co., Inc., New York, 1953.

[MG02] K. E. Mattar and A. L. Gray. Reducing ionospheric electron density errors in satellite radar interferometry applications. *Canadian Journal of Remote Sensing*, 28(4):593–600, 2002.

[MM91] D. B. Melrose and R. C. McPhedran. *Electromagnetic Processes in Dispersive Media. A Treatment Based on the Dielectric Tensor.* Cambridge University Press, Cambridge, 1991.

[MM93] R. Manduchi and G. A. Mian. Accuracy analysis for correlation-based image registartion algorithms. In *Proceedings of the 1993 IEEE International Symposium on Circuits and Systems, Sheraton Chicago Hotel & Towers, Chicago, IL, May 3-6, 1993*, volume 1, pages 834–837, Piscataway, NJ, 1993. IEEE.

[MMP10] A. Merzouki, H. McNairn, and A. Pacheco. Potential of mapping soil moisture by combining radar backscatter modeling and PolSAR decomposition. In *2010 IEEE International Geoscience and Remote Sensing Symposium (IGARSS)*, pages 4419–4422, July 2010.

[MN08] F.J. Meyer and J.B. Nicoll. Prediction, detection, and correction of Faraday rotation in full-polarimetric L-band SAR data. *IEEE Transactions on Geoscience and Remote Sensing*, 46(10):3076–3086, October 2008.

[MNG09] M. Migliaccio, F. Nunziata, and A. Gambardella. On the co-polarized phase difference for oil spill observation. *Int. J. Remote Sens.*, 30:1587–1602, January 2009.

[Mot07] Harold Mott. *Remote Sensing with Polarimetric Radar.* Wiley-IEEE Press, Hoboken, 2007.

[MPA02] Richard Medina, John Penn, and Richard Albanese. Dielectric response data on materials of military consequence. Technical Report AFRL-HE-BR-TR-2002-0155, United States Air Force Research Laboratory, Human Effectiveness Directorate, Directed Energy Bioeffects Division, Biomechanics and Modeling Branch, Brooks AFB, San Antonio, TX, August 2002.

[MY71] A. S. Monin and A. M. Yaglom. *Statistical Fluid Mechanics: Mechanics of Turbulence. Volume 1.* The MIT Press, Cambridge, MA, 1971.

[MY75] A. S. Monin and A. M. Yaglom. *Statistical Fluid Mechanics: Mechanics of Turbulence. Volume 2.* The MIT Press, Cambridge, MA, 1975.

[NC04] Clifford J. Nolan and Margaret Cheney. Microlocal analysis of synthetic aperture radar imaging. *J. Fourier Anal. Appl.*, 10(2):133–148, 2004.

[OQ98] Chris Oliver and Shaun Quegan. *Understanding Synthetic Aperture Radar Images.* Artech House Remote Sensing Library. Artech House Publishers, 1998.

[Ora84] V. N. Oraevsky. Kinetic theory of waves. In A. A. Galeev and R. N. Sudan, editors, *Basic Plasma Physics: Selected Chapters, Handbook of Plasma Physics, Volume 1*, pages 243–278. North-Holland, Amsterdam; New York, 1984.

[Ori85] Michael L. Oristaglio. Accuracy of the Born and Rytov approximations for reflection and refraction at a plane interface. *J. Opt. Soc. Am. A*, 2(11):1987–1993, November 1985.

[Oug06] Kurt E. Oughstun. *Electromagnetic and optical pulse propagation 1. Spectral representations in temporally dispersive media*, volume 125 of *Springer Series in Optical Sciences.* Springer, New York, 2006.

[Par02] Sybil P. Parker, editor. *McGraw-Hill Dictionary of Scientific and Technical Terms.* McGraw-Hill Professional, New York, Sixth edition, September 2002.

[PFC+11] Xiaoqing Pi, Anthony Freeman, Bruce Chapman, Paul Rosen, and Zhenhong Li. Imaging ionospheric inhomogeneities using spaceborne synthetic aperture radar. *J. Geophys. Res.*, 116(A4):1–13, April 2011.

[QL86] S. Quegan and J. Lamont. Ionospheric and tropospheric effects on synthetic aperture radar performance. *Int. J. Remote Sensing*, 7(4):525–539, 1986.

[Que90] S. Quegan. Interpolation and sampling in SAR images. *Geoscience and Remote Sensing, IEEE Transactions on*, 28(4):641–646, July 1990.

[RES+11] P.A. Rosen, H. Eisen, Y. Shen, S. Hensley, S. Shaffer, L. Veilleux, R. Dubayah, K.J. Ranson, A. Dress, J.B. Blair, S. Luthcke, B.H. Hager, and I. Joughin. The proposed DESDynI mission — From science to implementation. In *2011 IEEE Radar Conference (RADAR)*, pages 1129–1131, May 2011.

[RHC10] Paul A. Rosen, Scott Hensley, and Curtis Chen. Measurement and mitigation of the ionosphere in L-band interferometric SAR data. In *Proceedings of the IEEE International Radar Conference*, pages 1459–1463, Arlington, VA, 2010.

[RKT89a] S. M. Rytov, Yu. A. Kravtsov, and V. I. Tatarskii. *Principles of Statistical Radiophysics. Volume 3. Elements of Random Fields.* Springer-Verlag, Berlin, 1989. Translated from the second Russian edition by Alexander P. Repyev.

[RKT89b] S. M. Rytov, Yu. A. Kravtsov, and V. I. Tatarskii. *Principles of Statistical Radiophysics. Volume 4. Wave Propagation Through Random Media.* Springer-Verlag, Berlin, 1989. Translated from the second Russian edition by Alexander P. Repyev.

[RT07] Victor S. Ryaben'kii and Semyon V. Tsynkov. *A Theoretical Introduction to Numerical Analysis*. Chapman & Hall/CRC, Boca Raton, FL, 2007.

[Sch36] S. A. Schelkunoff. Some equivalence problems of electromagnetics and their application to radiation problems. *Bell System Technical Journal*, 15(1):92–112, January 1936.

[Sin50] George Sinclair. Transmission and reception of elliptically polarized waves. In *Proceedings of the IRE, Volume 38*, pages 148–151, 1950.

[SLKP04] D. L. Schuler, J. S. Lee, D. Kasilingam, and E. Pottier. Measurement of ocean surface slopes and wave spectra using polarimetric SAR image data. *Remote Sensing of Environment*, 91(2):198–211, 2004.

[SOCM01] Harold S. Stone, Michael Orchard, Ee-Chien Chang, and Stephen Martucci. A fast direct Fourier-based algorithm for subpixel registration of images. *IEEE Transactions on Geoscience and Remote Sensing*, 39:2235–2243, 2001.

[ST11] E. M. Smith and S. V. Tsynkov. Dual carrier probing for spaceborne SAR imaging. *SIAM J. on Imaging Sciences*, 4(2):501–542, 2011.

[Tat68] V. I. Tatarskii. *Propagation of Waves in a Turbulent Medium*. Dover Publications Inc., New-York, 1968. Translated from the Russian by R. A. Silverman.

[TH86] Qi Tian and Michael N. Huhns. Algorithms for subpixel registration. *Computer Vision, Graphics, and Image Processing*, 35(2):220–233, 1986.

[Tsy09a] S. V. Tsynkov. On SAR imaging through the Earth's ionosphere. *SIAM J. Imaging Sci.*, 2(1):140–182, 2009.

[Tsy09b] S. V. Tsynkov. On the effect of start-stop approximation for spaceborne SAR imaging. *SIAM J. on Imaging Sciences*, 2(2):646–669, 2009.

[VCY13] Kaitlyn Voccola, Margaret Cheney, and Birsen Yazici. Polarimetric synthetic-aperture inversion for extended targets in clutter. *Inverse Problems*, 29:054003 (25pp), 2013.

[vdKCT09] Max van de Kamp, Paul S. Cannon, and Michael Terkildsen. Effect of the ionosphere on defocusing of space-based radars. *Radio Sci.*, 44(1):RS1003, January 2009.

[WEGJJ94] D. E. Wahl, P. H. Eichel, D. C. Ghiglia, and C. V. Jakowatz Jr. Phase gradient autofocus — A robust tool for high resolution SAR phase correction. *IEEE Trans. Aerosp. Electron. Syst.*, 30(3):827–835, 1994.

[WQWH03] Patricia A. Wright, Shaun Quegan, Nigel S. Wheadon, and C. David Hall. Faraday rotation effects on L-band spaceborne SAR data. *IEEE Transactions on Geoscience and Remote Sensing*, 41(12):2735–2744, 2003.

[XWW04] Zheng-Wen Xu, Jian Wu, and Zhen-Sen Wu. A survey of ionospheric effects on space-based radar. *Waves in Random Media*, 14(2):S189–S273, April 2004.

[ZF03] Barbara Zitová and Jan Flusser. Image registration methods: A survey. *Image and Vision Computing*, 21(11):977–1000, 2003.

APPENDICES

Appendix A

Factorization of the SAR ambiguity function

In this appendix, we analyze the error due to the factorization (2.34) of the GAF (2.30), (2.31).

Substituting expression (2.30) into (2.31), we can write

$$W(\boldsymbol{y},\boldsymbol{z}) = \sum_n \int_\chi \chi_\tau(t-t_{\boldsymbol{y}}^n) e^{-i\alpha(t-t_{\boldsymbol{y}}^n)^2} e^{-i\omega_0(t-t_{\boldsymbol{y}}^n)} \chi_\tau(t-t_{\boldsymbol{z}}^n) e^{i\alpha(t-t_{\boldsymbol{z}}^n)^2} e^{i\omega_0(t-t_{\boldsymbol{z}}^n)}\, dt, \tag{A.1}$$

where

$$t_{\boldsymbol{y}}^n \stackrel{\text{def}}{=} \frac{2R_{\boldsymbol{y}}^n}{c} = \frac{2|\boldsymbol{x}^n - \boldsymbol{y}|}{c} \quad \text{and} \quad t_{\boldsymbol{z}}^n \stackrel{\text{def}}{=} \frac{2R_{\boldsymbol{z}}^n}{c} = \frac{2|\boldsymbol{x}^n - \boldsymbol{z}|}{c}. \tag{A.2}$$

Then, we introduce a new integration variable u and new constants T^n:

$$u = t - \frac{t_{\boldsymbol{z}}^n + t_{\boldsymbol{y}}^n}{2}, \quad T^n = \frac{t_{\boldsymbol{y}}^n - t_{\boldsymbol{z}}^n}{2} \equiv \frac{R_{\boldsymbol{y}}^n - R_{\boldsymbol{z}}^n}{c}, \tag{A.3}$$

such that

$$t - t_{\boldsymbol{y}}^n = u - T^n \quad \text{and} \quad t - t_{\boldsymbol{z}}^n = u + T^n.$$

The travel time between $\boldsymbol{y}$ and $\boldsymbol{z}$ is of the order of $\Delta_R/c \ll \tau$. This is equivalent to $|T^n| \ll \tau$; hence, the two indicator functions χ_τ under the integral in (A.1) overlap on some interval. The center of this interval is $u = 0$ and the endpoints are $u = \tau/2 - |T^n|$ and $u = -\tau/2 + |T^n|$, so that its length is

$$\tau^n = \tau - 2|T^n|. \tag{A.4}$$

The phase of the integrand in (A.1) can be expressed as

$$\begin{aligned}
&-\alpha(t-t_{\boldsymbol{y}}^n)^2-\omega_0(t-t_{\boldsymbol{y}}^n)+\alpha(t-t_{\boldsymbol{z}}^n)^2+\omega_0(t-t_{\boldsymbol{z}}^n)\\
&=\alpha\Big[(u+T^n)^2-(u-T^n)^2\Big]+\omega_0(u+T^n-u+T^n)\\
&=\alpha\cdot 4uT^n+2\omega_0T^n,
\end{aligned}$$

so the integration can be carried out analytically:

$$\begin{aligned}
W(\boldsymbol{y},\boldsymbol{z}) &= \sum_n e^{2i\omega_0T^n}\int_{-\tau^n/2}^{\tau^n/2} e^{4i\alpha T^n u}du=\sum_n e^{2i\omega_0T^n}\frac{1}{4i\alpha T^n}(e^{i2\alpha\tau^nT^n}-e^{-i2\alpha\tau^nT^n})\\
&= \sum_n e^{2i\omega_0T^n}\frac{1}{4i\alpha T^n}2i\sin(2\alpha\tau^nT^n)=\sum_n e^{2i\omega_0T^n}\tau^n\operatorname{sinc}(2\alpha\tau^nT^n).
\end{aligned}\tag{A.5}$$

Similarly to (2.34)–(2.36), let us now introduce a new function

$$W_{(\mathrm{RA})}(\boldsymbol{y},\boldsymbol{z})\stackrel{\mathrm{def}}{=}W_R(\boldsymbol{y},\boldsymbol{z})\cdot W_A(\boldsymbol{y},\boldsymbol{z}),\tag{A.6}$$

where

$$W_A(\boldsymbol{y},\boldsymbol{z})=\sum_{n=-N/2}^{N/2}e^{2i\omega_0(R_{\boldsymbol{y}}^n-R_{\boldsymbol{z}}^n)/c}=\sum_n e^{2i\omega_0T^n}\tag{A.7}$$

and

$$W_R(\boldsymbol{y},\boldsymbol{z})=\int_\chi\overline{A(u_{\boldsymbol{y}}^0)}A(u_{\boldsymbol{z}}^0)\,dt=\tau^0\operatorname{sinc}(2\alpha\tau^0T^0).\tag{A.8}$$

In formula (A.8), τ^0 and T^0 denote τ^n and T^n, respectively, for $n=0$. Our goal is to determine how accurately this new function $W_{(\mathrm{RA})}(\boldsymbol{y},\boldsymbol{z})$ of (A.6)–(A.8) will approximate the GAF $W(\boldsymbol{y},\boldsymbol{z})$ of (A.1) or, equivalently, (A.5). To determine the accuracy of approximation, we will estimate the error

$$W-W_{(\mathrm{RA})}=\sum_n e^{2i\omega_0T^n}[\tau^n\operatorname{sinc}(2\alpha\tau^nT^n)-\tau^0\operatorname{sinc}(2\alpha\tau^0T^0)].\tag{A.9}$$

The Pythagorean theorem for $R_{\boldsymbol{y}}^n$ and $R_{\boldsymbol{z}}^n$ (see Figure 1.1) yields:

$$\begin{aligned}
(R_{\boldsymbol{z}}^n)^2=|\boldsymbol{z}-\boldsymbol{x}^n|^2 &= H^2+L^2+(x_1^n)^2=R^2+(x_1^n)^2\\
(R_{\boldsymbol{y}}^n)^2=|\boldsymbol{y}-\boldsymbol{x}^n|^2 &= H^2+(L+l)^2+(x_1^n-y_1)^2\\
&= R^2+2Ll+l^2+(x_1^n-y_1)^2,
\end{aligned}\tag{A.10}$$

where

$$L = z_2 = R\sin\theta \quad \text{and} \quad l = y_2 - z_2.$$

For the physical distances involved, we take

$$R \sim L \sim 10^6 m, \quad |x_1^n| \lesssim 10^4 m, \quad \text{and} \quad |y_1| \sim |l| \lesssim 10^2 m.$$

Then, using the Taylor formula $(1+\xi)^{1/2} \approx 1 + \frac{1}{2}\xi$ for $|\xi| \ll 1$ we get

$$\frac{R_{\boldsymbol{z}}^n}{R} \approx 1 + \frac{(x_1^n)^2}{2R^2} \quad \text{and} \quad \frac{R_{\boldsymbol{y}}^n}{R} \approx 1 + \frac{1}{2}\frac{l^2 + 2lL + (x_1^n)^2 - 2x_1^n y_1 + y_1^2}{R^2},$$

which, after keeping only the leading order term that does not depend on n and the leading term that depends on n, yields:

$$\frac{R_{\boldsymbol{y}}^n - R_{\boldsymbol{z}}^n}{R} \approx \frac{L}{R}\frac{l}{R} - \frac{x_1^n y_1}{R^2}. \tag{A.11}$$

Consequently, we have

$$T^n \approx \frac{1}{c}\Big(l\sin\theta - y_1\frac{x_1^n}{R}\Big) \stackrel{\text{def}}{=} T^0 - \mathbb{T}^n, \tag{A.12}$$

where, taking into account that $x_1^n = n\Delta x_1 = nL_{\text{SA}}/N$, we have introduced

$$T^0 = \frac{l\sin\theta}{c}, \quad \mathbb{T}^1 = \frac{y_1\Delta x_1}{cR} = \frac{y_1 L_{\text{SA}}}{NcR}, \quad \text{and} \quad \mathbb{T}^n = \frac{y_1 x_1^n}{cR} = n\mathbb{T}^1. \tag{A.13}$$

As $|T^0| \ll \tau$ and $|\mathbb{T}^n| \ll \tau$, we can write using the first-order Taylor formula:

$$\operatorname{sinc}(2\alpha\tau^n T^n) \approx \operatorname{sinc}(2\alpha\tau^0 T^0) - 2\alpha\tau^0\mathbb{T}^n \operatorname{sinc}'(2\alpha\tau^0 T^0), \tag{A.14}$$

so that the expression in the square brackets in (A.9) evaluates to

$$\tau^n \operatorname{sinc}(2\alpha\tau^n T^n) - \tau^0 \operatorname{sinc}(2\alpha\tau^0 T^0) \approx \mathbb{T}^n S = Sn\mathbb{T}^1,$$

where

$$S = \operatorname{sinc}(2\alpha\tau^0 T^0) - 2\alpha(\tau^0)^2 \operatorname{sinc}'(2\alpha\tau^0 T^0). \tag{A.15}$$

Hence, formula (A.9) transforms into

$$W - W_{(\text{RA})} \approx e^{i\Phi_0} S \sum_n e^{-2i\omega_0\mathbb{T}^n}\mathbb{T}^n = S\mathbb{T}^1 e^{i\Phi_0} \sum_{n=-N/2}^{N/2} n e^{in\varphi}, \tag{A.16}$$

where

$$\Phi_0 = 2\frac{\omega_0 l}{c}\sin\theta \quad \text{and} \quad \varphi = -2\omega_0 \mathbb{T}^1 = -2\frac{\omega_0 L_{\mathrm{SA}}}{NRc} y_1.$$

Note that Φ_0 defined above is not quite identical to the one in formula (2.37), but the discrepancy is small, on the order of those terms neglected when deriving (A.11).

To perform the summation in (A.16), we first use the standard summation of a geometric sequence:

$$\sum_{n=-N/2}^{N/2} e^{in\varphi} = \frac{\sin(\varphi(N+1)/2)}{\sin(\varphi/2)} \approx N \operatorname{sinc}\frac{N\varphi}{2}, \tag{A.17}$$

where the last approximate equality holds provided that $|\varphi| \ll 1$, i.e., $\pi y_1/(\Delta_A N) \ll 1$. Then, differentiating both sides of (A.17) w.r.t. φ we get

$$\sum_{n=-N/2}^{N/2} n e^{in\varphi} = \frac{1}{i}\frac{\partial}{\partial\varphi}\sum_{n=-N/2}^{N/2} e^{in\varphi} \approx \frac{1}{i}\frac{\partial}{\partial\varphi}\Big(N \operatorname{sinc}\frac{N\varphi}{2}\Big) = \frac{N^2}{2i}\operatorname{sinc}'\frac{N\varphi}{2}.$$

Therefore, the expression in (A.16) evaluates to

$$\begin{aligned} W - W_{(\mathrm{RA})} &\approx S\mathbb{T}^1 \frac{N^2}{2i} e^{i\Phi_0}\operatorname{sinc}'\frac{N\varphi}{2} = \frac{ie^{i\Phi_0}}{2\omega_0} N S Y_1 \operatorname{sinc}' Y_1 \\ &= \frac{ie^{i\Phi_0}}{2\omega_0} N\big(\operatorname{sinc}(2\alpha\tau^0 T^0) - 2\alpha(\tau^0)^2 \operatorname{sinc}'(2\alpha\tau^0 T^0)\big) Y_1 \operatorname{sinc}' Y_1, \end{aligned} \tag{A.18}$$

where $Y_1 = -N\varphi/2 = \pi y_1/\Delta_A$. Formula (A.18) provides an expression for the factorization error (A.9) that we will now estimate. Let us first assume that

$$|Y_1| \lesssim 1, \quad |\operatorname{sinc}' Y_1| \lesssim 1, \quad \text{and} \quad |\operatorname{sinc}'(2\alpha\tau^0 T^0)| \lesssim 1,$$

which is reasonable to expect. Then, let us notice that as $2\alpha(\tau^0)^2 \approx B\tau \gg 1$, the second term on the right-hand side of formula (A.15) is much greater than the first one (except for very small T^0, i.e., when $\boldsymbol{y}$ and $\boldsymbol{z}$ are nearly at the same range). Hence, we can keep only the second (dominant) term for S and obtain using (A.7), (A.8), and (A.18):

$$\frac{|\max(W - W_{(\mathrm{RA})})|}{|\max W_{(\mathrm{RA})}|} \sim \frac{1}{N\tau}\frac{N}{2\omega_0} 2\alpha\tau^2 = \frac{1}{2}\frac{B}{\omega_0}. \tag{A.19}$$

Formula (A.19) provides an estimate for the relative error due to the factorization (A.6)–(A.8) or, equivalently, (2.34)–(2.36). This error may be on the order of a few percent depending on the value of the relative bandwidth $\frac{B}{\omega_0}$. It is interesting to note that according to (A.18), the dominant term of this error vanishes if either $y_2 = z_2$ or $y_1 = 0$ (the latter is equivalent

to $y_1 = z_1$). The key to understanding this effect is the expression for T^n in (A.12)–(A.13). Physically, T^n is the difference between the pulse two-way travel time for the pairs $(\boldsymbol{x}^n, \boldsymbol{y})$ and $(\boldsymbol{x}^n, \boldsymbol{z})$. As a function of the satellite position n, T^n has a constant part T^0 and a part $\mathbb{T}^n$ which is linear in n. It is the variation of the range PSF $\mathrm{sinc}(2\alpha\tau^n T^n)$ with n in formula (A.5) that is responsible for the leading term of the factorization error. If $y_2 = z_2$, then the constant part of T^n vanishes and so does the PSF tangent slope given by $\mathrm{sinc}'(2\alpha\tau^0 T^0)$. Hence, the leading term of the variation of the PSF magnitude disappears. If, however, $y_1 = 0$ (or $y_1 = z_1$), then it is the leading term of the variation of T^n with n that vanishes [$\mathbb{T}^n \equiv 0$, see (A.13)], and so does the leading term of the variation of $\mathrm{sinc}(2\alpha\tau^n T^n)$ regardless of the value of $2\alpha\tau^0 T^0$. Only in the general "diagonal" configuration $y_1 \neq z_1$, $y_2 \neq z_2$ the coupling between the range and azimuthal terms is significant, yielding the error (A.18).

Appendix B

Propagation of SAR signals in a lossless homogeneous plasma

We are interested in obtaining a spherically symmetric solution similar to the retarded potential (2.21), but for the case of a dispersive propagation governed by the Klein-Gordon equation (2.8) with $\omega_{\mathrm{pe}} = \mathrm{const}$. Let $r = |\boldsymbol{z} - \boldsymbol{x}|$ denote the radial coordinate in the spherical system centered at $\boldsymbol{x} \in \mathbb{R}^3$, which is the location of the antenna (we are using the notations of Section 2.3), and let $\varphi = \varphi(t, r)$ be a spherically symmetric solution of equation (2.8). Introduce a new function $\phi = \phi(t, r)$, such that $\varphi(t, r) = \phi(t, r)/r$. Then, $\phi(t, r)$ satisfies the one-dimensional Klein-Gordon equation:

$$\frac{\partial^2 \phi}{\partial t^2} - c^2 \frac{\partial^2 \phi}{\partial r^2} + \omega_{\mathrm{pe}}^2 \phi = 0, \qquad r \geq 0. \tag{B.1}$$

Hence, we need to look into the propagation of pulses governed by equation (B.1).

Assume that a pulse of shape $P(t)$ is given at $r = 0$ (location of the antenna); for example, it can be the high-range resolution upchirp (2.18):

$$P(t) = \frac{1}{4\pi} \chi_\tau(t) e^{i\left(\omega_0 + \frac{Bt}{2\tau}\right)t}, \tag{B.2}$$

where ω_0 is the center carrier frequency, B is the angular bandwidth, and τ is the duration of the chirp. The factor $1/4\pi$ in (B.2) accounts for the difference between the one-dimensional and three-dimensional delta-functions $\delta(r)$ and $\delta(x_1, x_2, x_3)$ that excite the pulse at the origin.

A Fourier transform in time of the pulse (B.2) is expressed via the erf functions:

$$\begin{aligned}\hat{P}(\omega) &= \frac{1}{2\pi}\int\limits_{-\tau/2}^{\tau/2}\frac{1}{4\pi}e^{i\left(\omega_0+\frac{Bt}{2\tau}\right)t-i\omega t}dt = \frac{1}{8\pi^2}\int\limits_{-\tau/2}^{\tau/2}e^{i\alpha t^2+i\beta t}dt \\ &= -\frac{1}{8\pi^2}\frac{\sqrt{\pi}}{2\sqrt{\alpha}}e^{-i\frac{\beta^2}{4\alpha}+i\frac{\pi}{4}}\left[\operatorname{erf}\left(\frac{\sqrt{-i}(\beta-\alpha\tau)}{2\sqrt{\alpha}}\right)-\operatorname{erf}\left(\frac{\sqrt{-i}(\beta+\alpha\tau)}{2\sqrt{\alpha}}\right)\right],\end{aligned} \tag{B.3}$$

where $\alpha = \frac{B}{2\tau}$ is the chrip rate, and $\beta = \omega_0 - \omega$. To simplify expression (B.3), we need to analyze the arguments of the erf functions. Denote

$$\eta_\pm = \frac{\beta \pm \alpha\tau}{2\sqrt{\alpha}} = \frac{\omega_0 - \omega \pm B/2}{\sqrt{2B/\tau}} \tag{B.4}$$

and consider several cases. First, let $\omega \in [\omega_0 - B/2, \omega_0 + B/2]$ and in addition suppose that ω is not too close to either endpoint, $\omega_0 - B/2$ or $\omega_0 + B/2$. In other words, suppose that the numerator on the right-hand side of (B.4) is of the same order of magnitude as the bandwidth, i.e., $|\omega_0 - \omega \pm B/2| \sim B$. Then, $|\eta_\pm| \sim \sqrt{B\tau/2}$, and for the typical values of the parameters involved (see Table 1.1) this quantity is approximately 35.4. We can therefore evaluate the erf functions on the right-hand side of (B.3) by the stationary phase method. Indeed,

$$\operatorname{erf}(\sqrt{-i}\eta_\pm) = \frac{2}{\sqrt{\pi}}\int\limits_0^{\sqrt{-i}\eta_\pm} e^{-z^2}dz = \frac{2\sqrt{-i}}{\sqrt{\pi}}\eta_\pm\int\limits_0^1 e^{i\eta_\pm^2u^2}du = \frac{2\sqrt{-i}}{\sqrt{\pi}}\eta_\pm\left[\int\limits_0^1 f_\delta(u)e^{i\eta_\pm^2u^2}du + \mathcal{O}(\delta)\right],$$

where $f_\delta(u)$ is a specially chosen auxiliary function such that $f_\delta \in C^\infty[0,\,1]$, $f_\delta^{(k)}(1) = 0$ for all $k = 0, 1, 2, \ldots$, and $f_\delta(u) \equiv 1$ for $u \in [0, 1-\delta]$, where $\delta > 0$ can be arbitrarily small. Then, assuming that $\eta_\pm^2$ is sufficiently large, we can apply the Erdélyi lemma [Fed77], [BFST93, Chapter 1] to the last integral in the previous formula, and by dropping the $\mathcal{O}(\delta)$ term and choosing the branch of the square root such that $0 < arg\,(\sqrt{z}) \le \pi$, obtain:

$$\operatorname{erf}(\sqrt{-i}\eta_\pm) \approx \frac{2\sqrt{-i}}{\sqrt{\pi}}\eta_\pm\int\limits_0^1 f_\delta(u)e^{i\eta_\pm^2u^2}du \approx \frac{2\sqrt{-i}}{\sqrt{\pi}}\eta_\pm\frac{\Gamma(\frac{1}{2})}{2}e^{i\frac{\pi}{4}}\left(\eta_\pm^2\right)^{-1/2} = -\frac{\eta_\pm}{|\eta_\pm|}.$$

In doing so we note that in this particular case the asymptotic expansion given by the Erdélyi lemma actually converges because all of its terms except for the leading term happen to be exactly equal to zero. Altogether, if ω is inside the interval $[\omega_0 - B/2, \omega_0 + B/2]$ and not too

close to its endpoints, then we have:

$$\hat{P}(\omega) \approx -\frac{1}{8\pi^2}\frac{\sqrt{\pi}}{2\sqrt{\alpha}}e^{-i\frac{\beta^2}{4\alpha}+i\frac{\pi}{4}}\underbrace{\left[-\frac{\eta_-}{|\eta_-|}+\frac{\eta_+}{|\eta_+|}\right]}_{=2} = -\frac{1}{8\pi^2}\frac{\sqrt{\pi}}{\sqrt{\alpha}}e^{-i\frac{\beta^2}{4\alpha}+i\frac{\pi}{4}}, \tag{B.5}$$

since in this case η_- is always negative, and η_+ is always positive.

Next, let ω be outside the interval $[\omega_0 - B/2, \omega_0 + B/2]$ and again, not too close to either of its endpoints. Then, we can apply the exact same reasoning as before and obtain:

$$\hat{P}(\omega) \approx -\frac{1}{8\pi^2}\frac{\sqrt{\pi}}{2\sqrt{\alpha}}e^{-i\frac{\beta^2}{4\alpha}+i\frac{\pi}{4}}\underbrace{\left[-\frac{\eta_-}{|\eta_-|}+\frac{\eta_+}{|\eta_+|}\right]}_{=0} = 0, \tag{B.6}$$

because unlike in formula (B.5), now both η_- and η_+ have the same sign.

Finally, we need to consider the case when ω is close to one of the endpoints of the interval $[\omega_0 - B/2, \omega_0 + B/2]$, i.e., $|\omega_0 - \omega - B/2| \ll B$ or $|\omega_0 - \omega + B/2| \ll B$. For example, if ω is close to the left endpoint so that $|\omega_0 - \omega - B/2|$ is small, then $\mathrm{erf}(\sqrt{-i}\eta_-)$, see formulae (B.3) and (B.4), can be evaluated using the first order Taylor expansion for erf, whereas $\mathrm{erf}(\sqrt{-i}\eta_+)$ should still be computed with the help of the Erdélyi lemma, which altogether yields:

$$\hat{P}(\omega) = -\frac{1}{8\pi^2}\frac{\sqrt{\pi}}{2\sqrt{\alpha}}e^{-i\frac{\beta^2}{4\alpha}+i\frac{\pi}{4}}\left[\frac{\sqrt{-i}}{\sqrt{\pi}\sqrt{\alpha}}(\omega_0 - \omega - B/2) + 1\right]. \tag{B.7}$$

Expression (B.7) is valid not everywhere, but only when the term in the round brackets is small. Hereafter, we will leave out the foregoing transient case, $|\omega_0 - \omega - B/2| \ll B$ or $|\omega_0 - \omega + B/2| \ll B$, and evaluate the Fourier transform $\hat{P}(\omega)$ only by combining (B.5) and (B.6). Then the resulting transform $\hat{P}(\omega)$ approximately represents the chirp at $t = 0$ as a superposition of sinusoidal harmonics with different frequencies:

$$\hat{P}(\omega) \approx \begin{cases} -\frac{1}{8\pi^2}\frac{\sqrt{\pi}}{\sqrt{\alpha}}e^{-i\frac{\beta^2}{4\alpha}+i\frac{\pi}{4}}, & \text{if } \omega \in [\omega_0 - B/2, \omega_0 + B/2], \\ 0, & \text{if } \omega \notin [\omega_0 - B/2, \omega_0 + B/2]. \end{cases} \tag{B.8}$$

Each of the frequencies ω that compose the spectrum in (B.8), or, rather, each of the harmonics $e^{i\omega t}$, propagates with its own phase velocity of (2.44). Indeed, the propagating pulse $\phi(t, r)$ that has covered the distance r from the origin can be written as the inverse Fourier transform [BW99, Chapter I], which, according to (2.4), immediately leads to the introduction of the

phase velocity $v_{\rm ph} = \omega/k$ in the exponent:

$$\phi(t,r) = \int\limits_{\omega_0-B/2}^{\omega_0+B/2} \hat{P}(\omega) e^{i(\omega t - kr)} d\omega = \int\limits_{\omega_0-B/2}^{\omega_0+B/2} \hat{P}(\omega) e^{i\omega(t - r/v_{\rm ph})} d\omega. \tag{B.9}$$

In (B.9), the phase velocity $v_{\rm ph}$ and wavenumber k are assumed to be the functions of the frequency ω defined by the dispersion relation (2.3). Introducing

$$\frac{1}{v_{{\rm ph}_0}} = \left.\frac{k}{\omega}\right|_{\omega_0} \quad \text{and} \quad \frac{1}{v_{{\rm gr}_0}} = \left.\frac{dk}{d\omega}\right|_{\omega_0} \tag{B.10}$$

and using (2.3) and (2.44), we can approximately represent $(\omega t - kr)$ in (B.9) by means of the Taylor formula:

$$\begin{aligned} \omega t - kr &= \omega\Big(t - \frac{r}{v_{\rm ph}(\omega)}\Big) \approx (\omega_0 + \beta)\left[t - r\Big(\frac{1}{v_{\rm ph}} + \beta\frac{d}{d\omega}\frac{1}{v_{\rm ph}} + \frac{\beta^2}{2}\frac{d^2}{d\omega^2}\frac{1}{v_{\rm ph}}\Big)\Big|_{\omega_0}\right] \\ &= \omega_0\Big(t - \frac{r}{v_{{\rm ph}_0}}\Big) + b\beta - rb_2\beta^2, \end{aligned} \tag{B.11}$$

where

$$\begin{aligned} b &= t - \frac{r}{v_{{\rm ph}_0}} - \omega_0 r \left.\frac{d}{d\omega}\frac{1}{v_{\rm ph}}\right|_{\omega_0} = t - \frac{r}{v_{{\rm gr}_0}}, \\ b_2 &= \left.\frac{d}{d\omega}\frac{1}{v_{\rm ph}}\right|_{\omega_0} + \frac{\omega_0}{2}\left.\frac{d^2}{d\omega^2}\frac{1}{v_{\rm ph}}\right|_{\omega_0} \approx -\frac{1}{2c}\frac{\omega_{\rm pe}^2}{\omega_0^3}. \end{aligned} \tag{B.12}$$

Substituting (B.11) and (B.12) into (B.9) and changing the integral over ω to that over β, we get:

$$\begin{aligned} \phi(t,z) &= -\frac{1}{8\pi^2}\frac{\sqrt{\pi}}{\sqrt{\alpha}} e^{i\frac{\pi}{4}} \int\limits_{-B/2}^{B/2} e^{-i\frac{\tau}{2B}\beta^2} e^{i\omega_0(t - r/v_{{\rm ph}_0})} e^{ib\beta - irb_2\beta^2} d\beta \\ &= -\frac{1}{8\pi^2}\frac{\sqrt{\pi}}{\sqrt{\alpha}} e^{i\frac{\pi}{4}} e^{i\omega_0(t - r/v_{{\rm ph}_0})} \int\limits_{-B/2}^{B/2} e^{-ia\beta^2 + ib\beta} d\beta \\ &= -\frac{1}{8\pi^2}\frac{\sqrt{\pi}}{\sqrt{\alpha}} e^{i\frac{\pi}{4}} \frac{\sqrt{\pi}}{2\sqrt{a}} e^{i\frac{b^2}{4a}} e^{-i\frac{\pi}{4}} e^{i\omega_0(t - r/v_{{\rm ph}_0})} \left[\operatorname{erf}\left(\frac{\sqrt{i}(b + aB)}{2\sqrt{a}}\right) - \operatorname{erf}\left(\frac{\sqrt{i}(b - aB)}{2\sqrt{a}}\right)\right] \\ &= \frac{1}{16\pi\sqrt{\alpha}\sqrt{a}} e^{i\omega_0(t - r/v_{{\rm ph}_0})} e^{i\frac{b^2}{4a}} \left[\operatorname{erf}\left(\frac{\sqrt{i}(b - aB)}{2\sqrt{a}}\right) - \operatorname{erf}\left(\frac{\sqrt{i}(b + aB)}{2\sqrt{a}}\right)\right], \end{aligned} \tag{B.13}$$

where

$$a = \frac{\tau}{2B} + rb_2 \equiv \frac{\tau}{2B} - \frac{1}{2}\frac{r}{c}\frac{\omega_{\mathrm{pe}}^2}{\omega_0^3} \tag{B.14}$$

and the branch of the square root is chosen such that $|\arg(\cdot)| \leqslant \pi$.

Using a stationary phase argument one more time, it has been shown in [ST11, Appendix A] and (B.4)–(B.6) that the difference of the two erf functions in the last line of (B.13) is equal to 2 if the value of b is within the interval of $(-aB, aB)$, and zero otherwise.[1] Introducing

$$\eta_{\pm}^* = \frac{b \pm aB}{2\sqrt{a}}, \tag{B.15}$$

we can rewrite this difference as follows:

$$[\mathrm{erf}(\sqrt{i}\eta_-^*) - \mathrm{erf}(\sqrt{i}\eta_+^*)] = 2\chi_{\tau'}(b), \tag{B.16}$$

where χ is the indicator function defined in (2.18), and

$$\tau' \stackrel{\mathrm{def}}{=} 2aB = \tau - \frac{r}{c}\frac{\omega_{\mathrm{pe}}^2}{\omega_0^2}\frac{B}{\omega_0} = \tau - \delta\tau \tag{B.17}$$

is a new pulse length. Accordingly, the quantity

$$\alpha' \stackrel{\mathrm{def}}{=} \frac{1}{4a} = \frac{B}{2\tau'} \approx \frac{B}{2\tau}\Big(1 + \frac{\delta\tau}{\tau}\Big) = \alpha + \delta\alpha \tag{B.18}$$

becomes a new chirp rate [see the second exponent in the last line of (B.13)].

Altogether, combining formulae (B.13)–(B.18), using the notation of (2.18), and recalling that $\varphi(t,r) = \phi(t,r)/r$, we obtain the spherically symmetric propagating pulse in the form:

$$\begin{aligned}\varphi(t,r) &= \frac{1}{4\pi r} e^{i\omega_0(t - r/v_{\mathrm{ph}_0})} \chi_{\tau'}(t - r/v_{\mathrm{gr}_0}) e^{i\alpha'(t - r/v_{\mathrm{gr}_0})^2} \\ &\stackrel{\mathrm{def}}{=} \frac{1}{4\pi r} A'(t - r/v_{\mathrm{gr}_0}) e^{i\omega_0(t - r/v_{\mathrm{ph}_0})}.\end{aligned} \tag{B.19}$$

Remark. Leaving out the transients that correspond to the endpoints of the pulse and its spectrum when using the stationary phase method is equivalent to disregarding the so-called precursors, see [Gin64, Section 21] or [Oug06]. In other words, we are focusing on the propagation of the main body of the pulse because it is the main body of the pulse that is used for building the generalized ambiguity function in Section 2.4.

Remark. The observation that $\tau' < \tau$ (and, consequently, $\alpha' > \alpha$) for an upchirp [$\alpha > 0$,

[1] Although the integral in the second line of (B.13) is algebraically of the same type as that in (2.66), the analysis of Section 2.4 does not apply here because the QPE for (B.13) is not small: $\phi_{\mathrm{qB}} \approx B\tau/8 \gg 1$.

see (2.18)] agrees with the formula for the group velocity in (2.43). Indeed, for an upchirp the slower propagating low-frequency harmonics are emitted first and the faster propagating high-frequency harmonics are emitted last. Hence, the "tail" of the chirp travels faster than its "head," which results in the pulse compression. The situation for the downchirp ($\alpha < 0$) will be the opposite: it will get dilated rather than compressed, $\tau' > \tau$, while its absolute rate will become lower rather than higher, $|\alpha'| < |\alpha|$ (see also [JFSM10, Figure 1]).

Remark. Using expressions (B.9) and (2.35), one can represent the range factor of the GAF as a double integral in frequency ω and fast time t. In work [IKL$^+$99], the authors adopt this approach and consider Gaussian pulses, which allows them to express the integrals over t and ω in elementary functions. For the rectangular chirp (2.18), this method would still yield the erf functions at the first step (integration over t), and will thus have no advantage over the one used in the current work.

Appendix C

Travel times in the deterministic inhomogeneous ionosphere

In this section, the quantities $N_{\mathrm{e}} = N_{\mathrm{e}}(h)$ and $\omega_{\mathrm{pe}} = \omega_{\mathrm{pe}}(h)$ are assumed to have no random component.

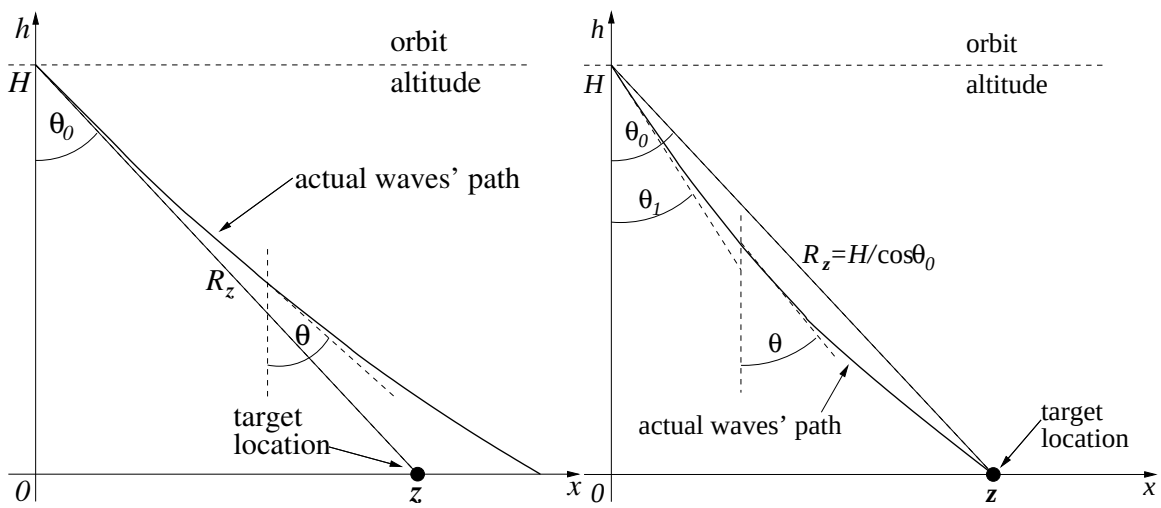

(a) With no correction of the look angle.

(b) With the correction of the look angle.

Figure C.1: Schematic waves' travel paths between the antenna and the target in the inhomogeneous ionosphere.

Suppose that the antenna is positioned at $x = 0$ and has altitude H above the Earth. It

sends a signal toward the target $\boldsymbol{z}$ on the ground, see Figure C.1(a), so that the look angle to the target is equal to θ_0 and as such, $R_{\boldsymbol{z}} = H/\cos\theta_0$. As the medium is lossless (collisionless dilute plasma with no Ohm conductivity, see Section 2.2), its electric permittivity is real:

$$\epsilon(h) = 1 - \frac{\omega_{\mathrm{pe}}^2(h)}{\omega^2}, \quad \text{where} \quad \omega_{\mathrm{pe}}^2(h) = \frac{4\pi e^2 N_{\mathrm{e}}(h)}{m_{\mathrm{e}}}, \tag{C.1}$$

and we can write Snell's law (for plane waves) in the continuous form [Gin64, Sec. 19] as follows:

$$n(h)\sin\theta(h) = n(H)\sin\theta_0, \tag{C.2}$$

where the refraction index is given by

$$n(h) = \sqrt{\epsilon(h)} = \sqrt{1 - \frac{\omega_{\mathrm{pe}}^2(h)}{\omega^2}}. \tag{C.3}$$

The angle $\theta(h)$ in formula (C.2) is the angle that the tangent to the wave trajectory at a given altitude h makes with the negative ordinate axis, see Figure C.1(a). Then, at every point on the trajectory we can write with the help of equation (C.2):

$$\frac{dx}{dh} = -\tan\theta(h) = -\frac{n(h)\sin\theta(h)}{n(h)\cos\theta(h)} = -\frac{n(H)\sin\theta_0}{n(h)\cos\theta(h)} = -\frac{n(H)\sin\theta_0}{\sqrt{n^2(h) - n^2(H)\sin^2\theta_0}}. \tag{C.4}$$

Hence, the actual trajectory can be obtained by integrating equality (C.4):

$$x(h) = \int_H^h \frac{dx}{dh}dh = \int_h^H \frac{n(H)\sin\theta_0}{\sqrt{n^2(h) - n^2(H)\sin^2\theta_0}}dh. \tag{C.5}$$

However, for the general dependence $N_{\mathrm{e}} = N_{\mathrm{e}}(h)$, the integration in (C.5) is not easy to perform. On the other hand, we can simplify formula (C.4) by taking into account that all the ionospheric corrections are small, and employing the first order Taylor expansion with respect to $\omega_{\mathrm{pe}}^2/\omega^2$:

$$\begin{aligned}
\frac{dx}{dh} &= -\frac{\sqrt{1 - \frac{\omega_{\mathrm{pe}}^2(H)}{\omega^2}}\sin\theta_0}{\sqrt{1 - \frac{\omega_{\mathrm{pe}}^2(h)}{\omega^2} - \left(1 - \frac{\omega_{\mathrm{pe}}^2(H)}{\omega^2}\right)\sin^2\theta_0}} \approx -\frac{\left(1 - \frac{1}{2}\frac{\omega_{\mathrm{pe}}^2(H)}{\omega^2}\right)\sin\theta_0}{\sqrt{\cos^2\theta_0 + \frac{\omega_{\mathrm{pe}}^2(H)\sin^2\theta_0 - \omega_{\mathrm{pe}}^2(h)}{\omega^2}}} \\
&\approx -\tan\theta_0\left(1 - \frac{1}{2}\frac{\omega_{\mathrm{pe}}^2(H)}{\omega^2}\right)\left(1 - \frac{1}{2}\frac{\omega_{\mathrm{pe}}^2(H)\sin^2\theta_0 - \omega_{\mathrm{pe}}^2(h)}{\omega^2\cos^2\theta_0}\right) \\
&\approx -\tan\theta_0\left(1 - \frac{1}{2}\frac{\omega_{\mathrm{pe}}^2(H) - \omega_{\mathrm{pe}}^2(h)}{\omega^2\cos^2\theta_0}\right).
\end{aligned} \tag{C.6}$$

The integration of equation (C.5) yields:

$$
\begin{aligned}
x(h,\theta_0) &= \int\limits_H^h -\tan\theta_0 \left(1 - \frac{1}{2}\frac{\omega_{\rm pe}^2(H) - \omega_{\rm pe}^2(h)}{\omega^2\cos^2\theta_0}\right) dh \\
&= (H-h)\tan\theta_0 + \frac{1}{2}\frac{4\pi e^2}{m_{\rm e}}\frac{\tan\theta_0}{\omega^2\cos^2\theta_0}\left(\int\limits_h^H N_{\rm e}(h)dh - (H-h)N_{\rm e}(H)\right).
\end{aligned}
\tag{C.7}
$$

The shape of the curve (C.7) is determined by the profile of the electron number density $N_{\rm e} = N_{\rm e}(h)$. The curve is also parameterized by the look angle θ_0 at the location of the antenna. With no variation in the electron number density, $N_{\rm e}(h) \equiv N_{\rm e}(H)$, formula (C.7) yields a straight line between the antenna and the target:

$$
x(h) = (H-h)\tan\theta_0. \tag{C.8}
$$

As, however, $N_{\rm e}(h)$ is not constant, the ray that originates at the antenna under the look angle θ_0 will not, generally speaking, come to the target, see Figure C.1(a). To have this ray come to the target, we need to correct the look angle, see Figure C.1(b).

Let θ_1 be the new look angle. We substitute it into formula (C.7) instead of θ_0, and require that $x(0,\theta_1) = H\tan\theta_0$. In other words, we require that the wave trajectory that originates at the antenna under the new look angle θ_1 terminate precisely at the target $\boldsymbol{z}$ on the ground, see Figure C.1(b). We have:[1]

$$
x(0,\theta_1) = H\tan\theta_1 + \frac{1}{2}\frac{4\pi e^2}{m_{\rm e}}\frac{N_H - N_{\rm e}(H)H}{\omega^2\cos^2\theta_1}\tan\theta_1 = H\tan\theta_0, \tag{C.9}
$$

where N_H is an important characteristic of the ionosphere — the integral of its electron number density across the layer of thickness H, as defined in (2.54):

$$
N_H \stackrel{\rm def}{=} \int\limits_0^H N_{\rm e}(h)dh.
$$

Formula (C.9) is an equation for θ_1. Let us now introduce a new notation K for brevity:

$$
K = \frac{1}{2}\frac{4\pi e^2}{m_{\rm e}}\frac{N_H - N_{\rm e}(H)H}{\omega^2} \tag{C.10}
$$

[1]Formula (C.9) corrects formula (D.2) from the previous publication on the subject [Tsy09a] (page 177), in which there was an arithmetic error.

and recast equation (C.9) as

$$H \tan\theta_1 + \frac{K}{\cos^2\theta_1}\tan\theta_1 = H\tan\theta_0. \tag{C.11}$$

Then, assuming that $\theta_1 = \theta_0 + \delta_\theta$, where $\delta\theta \ll \theta_0$, we can use the first order Taylor formula and write:

$$\tan\theta_1 \approx \tan\theta_0 + \frac{\delta\theta}{\cos^2\theta_0} \quad \text{and} \quad \frac{1}{\cos^2\theta_1} \approx \frac{1}{\cos^2\theta_0}(1 + 2\tan\theta_0\delta\theta).$$

Substituting these expressions into equation (C.11), we arrive at

$$H\frac{\delta\theta}{\cos^2\theta_0} + \frac{K}{\cos^2\theta_0}(1 + 2\tan\theta_0\delta\theta)\left(\tan\theta_0 + \frac{\delta\theta}{\cos^2\theta_0}\right) = 0.$$

In the previous equation, we keep only linear terms with respect to $\delta\theta$:

$$H\delta\theta + K\tan\theta_0 + K\frac{2\sin^2\theta_0 + 1}{\cos^2\theta_0}\delta\theta = 0,$$

which yields:

$$\delta\theta = -\frac{K\tan\theta_0}{H + K\frac{2\sin^2\theta_0+1}{\cos^2\theta_0}} = -\frac{K\tan\theta_0}{H}\frac{1}{1 + \frac{K}{H}\frac{2\sin^2\theta_0+1}{\cos^2\theta_0}} \approx -\frac{K\tan\theta_0}{H}\left(1 - \frac{K}{H}\frac{2\sin^2\theta_0+1}{\cos^2\theta_0}\right), \tag{C.12}$$

because according to formula (C.10), the quotient K/H is small, $K/H \sim \omega_{\rm pe}^2/\omega^2 \ll 1$. Our subsequent analysis shows that the second term in parentheses on the right-hand side of (C.12) can be disregarded.

Let s denote the arc length of the pulse trajectory. Then, using formula (C.4) and keeping only first order terms in the Taylor expansion, we can write:

$$\frac{ds}{dh} = \sqrt{1 + \left(\frac{dx}{dh}\right)^2} = \sqrt{\frac{n^2(h)}{n^2(h) - n^2(H)\sin^2\theta_0}} \approx \frac{1}{\cos\theta_0}\left(1 + \frac{1}{2}\frac{\omega_{\rm pe}^2(h) - \omega_{\rm pe}^2(H)}{\omega^2}\tan^2\theta_0\right). \tag{C.13}$$

Consequently, the total length of the trajectory which originates at the angle θ_1 and is shown in Figure C.1(b) is given by

$$S = \int_0^H \frac{ds(\theta_1)}{dh}dh = \frac{1}{\cos\theta_1}\left(H + \frac{1}{2}\frac{4\pi e^2}{m_{\rm e}}\frac{N_H - \omega_{\rm pe}^2(H)H}{\omega^2}\tan^2\theta_1\right) = \frac{H}{\cos\theta_1}\left(1 + \frac{K}{H}\tan^2\theta_1\right). \tag{C.14}$$

For the trigonometric functions in formula (C.14), we can use (C.12) and write:

$$\frac{1}{\cos\theta_1} \approx \frac{1}{\cos\theta_0}(1+\tan\theta_0\delta\theta) \approx \frac{1}{\cos\theta_0}\left[1-\frac{K\tan^2\theta_0}{H}\left(1-\frac{K}{H}\frac{2\sin^2\theta_0+1}{\cos^2\theta_0}\right)\right] \approx \frac{1}{\cos\theta_0}\left[1-\frac{K\tan^2\theta_0}{H}\right]$$

and

$$\tan^2\theta_1 \approx \tan^2\theta_0 + \frac{2\tan\theta_0}{\cos^2\theta_0}\delta\theta \approx \tan^2\theta_0 - \frac{K}{H}\frac{2\tan^2\theta_0}{\cos^2\theta_0}\left(1-\frac{K}{H}\frac{2\sin^2\theta_0+1}{\cos^2\theta_0}\right) \approx \tan^2\theta_0 - \frac{K}{H}\frac{2\tan^2\theta_0}{\cos^2\theta_0}.$$

On the right-hand side of the previous equalities, we have dropped the terms of order K^2/H^2, because $K/H \ll 1$, and hence the quantities quadratic with respect to K/H are negligible. We could have arrived at the same result if we dropped the second term in parentheses on the right-hand side of the last equality in formula (C.12) ahead of time. Substituting the previous two expressions back into formula (C.14), we have:

$$S = \frac{H}{\cos\theta_0}\left[1-\frac{K}{H}\tan^2\theta_0\right]\cdot\left[1+\frac{K}{H}\left(\tan^2\theta_0-\frac{K}{H}\frac{2\tan^2\theta_0}{\cos^2\theta_0}\right)\right] = \frac{H}{\cos\theta_0}\left[1+\mathcal{O}\left(\frac{K^2}{H^2}\right)\right]. \tag{C.15}$$

Formula (C.15) implies that up to the negligibly small additive terms of order K^2/H^2, the length of the pulse trajectory between the antenna $\boldsymbol{x}$ and the target $\boldsymbol{z}$, see Figure C.1(b), is equal to the length of a straight line that connects the antenna and the target:

$$S \approx \frac{H}{\cos\theta_0} = |\boldsymbol{z}-\boldsymbol{x}| = R_{\boldsymbol{z}}. \tag{C.16}$$

The travel time along the trajectory (C.5) is given by the integral

$$T = \int_0^H \frac{dt}{dh}dh = \int_0^H \frac{1}{v(h)}\frac{ds}{dh}dh, \tag{C.17}$$

where $v(h) = v(\omega, \omega_{\mathrm{pe}}(h))$ can be either the group velocity (2.43) or the phase velocity (2.44), and the quantity $\frac{ds}{dh}$ is given by equation (C.13). For the case of group velocity, formula (C.17) yields:

$$\begin{aligned} T_{\mathrm{gr}}(\boldsymbol{x},\boldsymbol{z},\omega) &\approx \int_0^H \frac{1}{c}\left(1-\frac{1}{2}\frac{\omega_{\mathrm{pe}}^2(h)}{\omega^2}\right)^{-1}\frac{1}{\cos\theta_1}\left(1+\frac{1}{2}\frac{\omega_{\mathrm{pe}}^2(h)-\omega_{\mathrm{pe}}^2(H)}{\omega^2}\tan^2\theta_1\right)dh \\ &\approx \frac{1}{c\cdot\cos\theta_1}\int_0^H\left(1+\frac{1}{2}\frac{\omega_{\mathrm{pe}}^2(h)}{\omega^2}+\frac{1}{2}\frac{\omega_{\mathrm{pe}}^2(h)-\omega_{\mathrm{pe}}^2(H)}{\omega^2}\tan^2\theta_1\right)dh, \end{aligned} \tag{C.18}$$

because we are disregarding all the terms of higher order than linear with respect to $\omega_{\rm pe}^2/\omega^2$. Formula (C.18), along with formulae (C.14) and (C.16), imply that

$$\begin{aligned} T_{\rm gr}(\boldsymbol{x},\boldsymbol{z},\omega) &\approx \frac{S}{c} + \frac{1}{c\cdot\cos\theta_1}\int\limits_0^H \frac{1}{2}\frac{\omega_{\rm pe}^2(h)}{\omega^2}dh \\ &= \frac{H}{c\cdot\cos\theta_0} + \frac{1}{c\cdot\cos\theta_0}\left[1-\frac{K\tan^2\theta_0}{H}\right]\frac{1}{2}\frac{4\pi e^2}{m_{\rm e}}\frac{N_H}{\omega^2} \\ &\approx \frac{H}{c\cdot\cos\theta_0}\left(1+\frac{1}{2}\frac{4\pi e^2}{m_{\rm e}\omega^2}\frac{N_H}{H}\right) = \frac{R_{\boldsymbol{z}}}{c}\left(1+\frac{1}{2}\frac{4\pi e^2}{m_{\rm e}\omega^2}\frac{N_H}{H}\right), \end{aligned} \tag{C.19}$$

where we have again dropped the terms higher than first order with respect to $K/H \sim \omega_{\rm pe}^2/\omega^2$. Formula (C.19) yields a final expression for the group travel time of a high frequency, $\omega \gg \omega_{\rm pe}$, radar pulse between the antenna and the target in an inhomogeneous deterministic ionosphere. Let us also recall that in our linearized framework the length of the pulse trajectory is equal to that of a straight segment between the antenna and the target, $S = R_{\boldsymbol{z}}$, because all the corrections are quadratic, see formulae (C.15) and (C.16). Hence, formula (C.19) could have been obtained merely as [cf. formula (C.17)]

$$\begin{aligned} T_{\rm gr}(\boldsymbol{x},\boldsymbol{z},\omega) &= \int\limits_0^{R_{\boldsymbol{z}}} \frac{ds}{v_{\rm gr}(h)} = \frac{1}{\cos\theta_0}\int\limits_0^H \frac{dh}{v_{\rm gr}(h)} \\ &\approx \frac{1}{c\cdot\cos\theta_0}\int\limits_0^H \left(1+\frac{1}{2}\frac{\omega_{\rm pe}^2(h)}{\omega^2}\right)dh = \frac{R_{\boldsymbol{z}}}{c}\left(1+\frac{1}{2}\frac{4\pi e^2}{m_{\rm e}\omega^2}\frac{N_H}{H}\right). \end{aligned} \tag{C.20}$$

Formula (C.20) can be interpreted in the context of the perturbation theory. Namely, the unperturbed pulse trajectory is a straight line. To get the first order perturbation for the group travel time, we integrate the reciprocal of the perturbed group velocity along the unperturbed trajectory.

As concerns the phase travel time, we just need to notice that the linearized group and phase velocities differ only by the sign of the $\sim \omega_{\rm pe}^2/\omega^2$ correction, see formulae (2.43) and (2.44). Hence, we have:

$$T_{\rm ph}(\boldsymbol{x},\boldsymbol{z},\omega) \approx \frac{R_{\boldsymbol{z}}}{c}\left(1-\frac{1}{2}\frac{4\pi e^2}{m_{\rm e}\omega^2}\frac{N_H}{H}\right). \tag{C.21}$$

Appendix D

Travel times in the stochastic ionosphere

The analysis of Appendix C indicates that we can use the geometrical optics perturbation method (see [RKT89b, Ch. I] for more detail) to derive the travel times of radar pulses in the turbulent ionosphere as well. In this case, the electron number density is a quasi-homogeneous random field [see formula (2.9)]:

$$N_{\mathrm{e}} = \langle N_{\mathrm{e}}(h) \rangle + \mu(\boldsymbol{x}), \tag{D.1}$$

and the dependence of μ on $\boldsymbol{x}$ in formula (D.1) means that μ depends on all spatial coordinates, $\boldsymbol{x} \in \mathbb{R}^3$.

Next, with no loss of generality, we can assume that the propagation plane (x, h) is fixed, see Figure C.1, and consider only two independent spatial variables. Moreover, recall that the random contribution to the electron number density is generally small compared to the deterministic part, because the quantity $M = \sqrt{\langle \mu^2 \rangle}/\langle N_{\mathrm{e}} \rangle$ introduced by formula (2.11) is small, see [Arm05]. Consequently, we can still linearize with respect to the terms of order $\omega_{\mathrm{pe}}^2/\omega^2$ as done in Appendix C (high frequency regime), and write down the equation for the pulse trajectory similar to equation (C.6), but with $\mu = \mu(x, h)$ taken into account:

$$\frac{dx}{dh} \approx -\tan\theta_0 \left(1 - \frac{1}{2} \frac{4\pi e^2}{m_{\mathrm{e}}} \frac{(\langle N_{\mathrm{e}}(H) \rangle - \langle N_{\mathrm{e}}(h) \rangle) + (\mu(0, H) - \mu(x, h))}{\omega^2 \cos^2\theta_0} \right). \tag{D.2}$$

Equation (D.2) is a first order ordinary differential equation that will be solved (approximately) by the perturbation method. First, we represent the solution in the form of a series:

$$x(h) = x^{(0)}(h) + x^{(1)}(h) + \ldots,$$

assuming that $x^{(0)} \sim 1$ and $x^{(1)} \sim \omega_{\rm pe}^2/\omega^2$, where $\omega_{\rm pe}^2/\omega^2$ is the small parameter for the asymptotic expansion.[1] Then, from equation (D.2) we immediately obtain the zeroth order contribution to the solution:

$$x^{(0)}(h) = \int_H^h -\tan\theta_0 dh = (H-h)\tan\theta_0, \tag{D.3}$$

which is a straight line between the antenna and the target, see Figure C.1 [also see formula (C.8)]. For the first order correction, equation (D.2) yields:

$$\frac{dx^{(1)}}{dh} = \tan\theta_0 \frac{1}{2}\frac{4\pi e^2}{m_{\rm e}} \frac{(\langle N_{\rm e}(H)\rangle - \langle N_{\rm e}(h)\rangle) + (\mu(0,H) - \mu(x^{(0)}(h),h))}{\omega^2\cos^2\theta_0}. \tag{D.4}$$

Integrating equation (D.4) between H and h, we obtain:

$$\begin{aligned} x^{(1)}(h) = \frac{1}{2}\frac{4\pi e^2}{m_{\rm e}}\frac{\tan\theta_0}{\omega^2\cos^2\theta_0}\Bigg[&\left(\int_h^H \langle N_{\rm e}(h)\rangle dh - (H-h)\langle N_{\rm e}(H)\rangle\right) \\ &+ \left(\int_h^H \mu(x^{(0)}(h),h)dh - (H-h)\mu(0,H)\right)\Bigg]. \end{aligned} \tag{D.5}$$

If $\mu = 0$, then combining the zeroth order contribution (D.3) with the first order correction (D.5), we arrive at the previously obtained deterministic solution (C.7). Otherwise, for the solution $x(h) = x^{(0)}(h) + x^{(1)}(h)$ given by (D.3), (D.5) but with the adjusted look angle θ_1 we can write similarly to (C.9) and (C.11):

$$x(0,\theta_1) = H\tan\theta_1 + \frac{K}{\cos^2\theta_1}\tan\theta_1 = H\tan\theta_0, \tag{D.6}$$

where the quantities K of (C.10) and N_H of (C.9) are redefined as follows:

$$K = \frac{1}{2}\frac{4\pi e^2}{m_{\rm e}\omega^2}\Bigg[\underbrace{(N_H - \langle N_{\rm e}(H)\rangle H)}_{\text{deterministic part}} + \underbrace{\left(\int_0^H \mu(x^{(0)}(h),h))dh - \mu(0,H)H\right)}_{\text{stochastic part}}\Bigg] = \langle K\rangle + \eta \tag{D.7}$$

[1] We do not formally introduce the second perturbation parameter, which would be of the order $\frac{4\pi e^2}{m_{\rm e}}\frac{\sqrt{\langle\mu^2\rangle}}{\omega^2} \ll \frac{\omega_{\rm pe}^2}{\omega^2}$, because the quantity M of (2.11) is an altitude-independent constant, and hence the two parameters would be related to one another.

and

$$N_H \stackrel{\text{def}}{=} \int_0^H \langle N_{\mathrm{e}}(h)\rangle dh. \tag{D.8}$$

Since $\sqrt{\langle\eta^2\rangle} < \langle K\rangle$ or even $\sqrt{\langle\eta^2\rangle} \ll \langle K\rangle$ [see the discussion right after equation (2.11)], and $\langle K\rangle/H \ll 1$, we can employ the same argument as in Appendix C and show using equation (D.6) that for any particular realization of μ the look angle increment $\delta\theta = \theta_1 - \theta_0$ will be given by the same expression (C.12), but with K and $N_{\mathrm{e}}^{(H)}$ defined by (D.7) and (D.8), respectively.

The arc length along the pulse trajectory with the look angle θ_1 can be found by integrating the differential equation [cf. formulae (C.13), (C.14)]:

$$\frac{ds}{dh} = \frac{1}{\cos\theta_1}\left(1 + \frac{1}{2}\frac{4\pi e^2}{m_{\mathrm{e}}}\frac{(\langle N_{\mathrm{e}}(H)\rangle - \langle N_{\mathrm{e}}(h)\rangle) + (\mu(0,H) - \mu(x,h))}{\omega^2}\tan^2\theta_1\right). \tag{D.9}$$

To integrate equation (D.9) we can again use the perturbation method. Representing $s(h)$ in the form

$$s(h) = s^{(0)}(h) + s^{(1)}(h) + \ldots,$$

we have the zeroth order term:

$$s^{(0)}(h) = \frac{H-h}{\cos\theta_1} \tag{D.10}$$

and the first order term:

$$\begin{aligned} s^{(1)}(h) = \frac{1}{2}\frac{4\pi e^2}{m_{\mathrm{e}}}\frac{\tan^2\theta_1}{\omega^2\cos\theta_1}\Bigg[&\left(\int_h^H \langle N_{\mathrm{e}}(h)\rangle dh - (H-h)\langle N_{\mathrm{e}}(H)\rangle\right) \\ &+ \left(\int_h^H \mu(x^{(0)}(h),h)dh - (H-h)\mu(0,H)\right)\Bigg]. \end{aligned} \tag{D.11}$$

To obtain the full length of the trajectory we substitute $h = 0$ into formulae (D.10) and (D.11), and also use formula (D.7), which yields:

$$S = s^{(0)}(0) + s^{(1)}(0) = \frac{H}{\cos\theta_1}\left(1 + \frac{K}{H}\tan^2\theta_1\right). \tag{D.12}$$

Expression (D.12) formally coincides with (C.14), only the definition of K is different. Consequently, we can repeat the argument from Appendix C and show that for every particular realization of μ the total length S of the pulse trajectory will be equal to that of a straight line between the antenna and the target, up to the terms of order $\langle K\rangle^2/H^2$ that are negligible, see

formulae (C.15) and (C.16):

$$S = \frac{H}{\cos\theta_0}\left[1 + \mathcal{O}\left(\frac{\langle K\rangle^2}{H^2}\right)\right] \approx \frac{H}{\cos\theta_0} = R_{\boldsymbol{z}}. \tag{D.13}$$

Finally, to obtain the group travel time, we need to integrate the following ordinary differential equation:

$$\begin{aligned}\frac{dt}{dh} &= \frac{1}{v_{\mathrm{gr}}(x,h)}\frac{ds}{dh} = \frac{1}{c}\left(1 - \frac{1}{2}\frac{4\pi e^2}{m_{\mathrm{e}}}\frac{\langle N_{\mathrm{e}}(h)\rangle + \mu(x,h)}{\omega^2}\right)^{-1} \\ &\cdot \frac{1}{\cos\theta_1}\left(1 + \frac{1}{2}\frac{4\pi e^2}{m_{\mathrm{e}}}\frac{(\langle N_{\mathrm{e}}(H)\rangle - \langle N_{\mathrm{e}}(h)\rangle) + (\mu(0,H) - \mu(x,h))}{\omega^2}\tan^2\theta_1\right) \\ &\approx \frac{1}{c\cdot\cos\theta_1}\left(1 + \frac{1}{2}\frac{4\pi e^2}{m_{\mathrm{e}}}\frac{\langle N_{\mathrm{e}}(h)\rangle + \mu(x,h)}{\omega^2} + \frac{1}{2}\frac{4\pi e^2}{m_{\mathrm{e}}}\frac{(\langle N_{\mathrm{e}}(H)\rangle - \langle N_{\mathrm{e}}(h)\rangle) + (\mu(0,H) - \mu(x,h))}{\omega^2}\tan^2\theta_1\right).\end{aligned} \tag{D.14}$$

As according to formula (D.13) the shape of the trajectory will not contribute to the travel time in the linearized framework, the integration of equation (D.14) by means of the perturbation method yields:

$$\begin{aligned}T_{\mathrm{gr}}(\boldsymbol{x},\boldsymbol{z},\omega) &= \frac{H}{c\cdot\cos\theta_0}\left[1 + \frac{1}{2}\frac{4\pi e^2}{m_{\mathrm{e}}\omega^2}\left(\frac{N_H}{H} + \frac{1}{H}\int_0^H \mu(x^{(0)}(h),h)dh\right)\right] \\ &= \frac{R_{\boldsymbol{z}}}{c}\left[1 + \frac{1}{2}\frac{4\pi e^2}{m_{\mathrm{e}}\omega^2}\left(\frac{N_H}{H} + \frac{1}{R_{\boldsymbol{z}}}\int_0^{R_{\boldsymbol{z}}} \mu(s)ds\right)\right].\end{aligned} \tag{D.15}$$

When deriving formula (D.15), we took into account that the look angle increment is small, $\delta\theta \sim \langle K\rangle/H$, as we did when deriving formula (C.19). We also note that the last integral in formula (D.15) shall be interpreted as taken along the unperturbed straight trajectory.

The phase travel time, as before, is obtained by changing the sign [cf. formula (C.21)]:

$$T_{\mathrm{ph}}(\boldsymbol{x},\boldsymbol{z},\omega) = \frac{R_{\boldsymbol{z}}}{c}\left[1 - \frac{1}{2}\frac{4\pi e^2}{m_{\mathrm{e}}\omega^2}\left(\frac{N_H}{H} + \frac{1}{R_{\boldsymbol{z}}}\int_0^{R_{\boldsymbol{z}}} \mu(s)ds\right)\right]. \tag{D.16}$$

Appendix E

Propagation of SAR signals in a plasma with losses

Ohmic losses in the ionosphere are due to the collisions of particles. Let $\nu_e > 0$ denote the effective collision frequency [Gin64]. Then, the dielectric constant of the ionospheric plasma is given by the following expression [cf. formula (2.7)]:

$$\frac{k^2c^2}{\omega^2} = \varepsilon' = 1 - \frac{\omega_{\mathrm{pe}}^2}{\omega(\omega - i\nu_e)}. \tag{E.1}$$

The value of ν_e in the ionosphere depends on the altitude, solar activity, and the time of the day, but generally it does not exceed $10^5 Hz$ [Mes71, Gin64], i.e., $\nu_e \ll \omega$. Under this condition, the solution $k^* = k^*(\omega)$ to equation (E.1) will have a small imaginary part:[1]

$$k^* = \frac{\omega}{c}\left(1 - \frac{1}{2}\frac{\omega_{\mathrm{pe}}^2}{\omega^2} - \frac{i}{2}\frac{\omega_{\mathrm{pe}}^2}{\omega^2}\frac{\nu_e}{\omega}\right).$$

Similarly, the expressions in (B.10), (B.12), and (B.14) will all acquire small imaginary parts proportional to ν_e:

$$\begin{aligned}
\frac{1}{v_{\mathrm{ph}_0}^*} &= \frac{1}{v_{\mathrm{ph}_0}} - \frac{i}{2}\frac{1}{c}\frac{\nu_e\omega_{\mathrm{pe}}^2}{\omega_0^3}, \\
b^* &= b - i\frac{r}{c}\frac{\nu_e\omega_{\mathrm{pe}}^2}{2\omega_0^3}, \\
b_2^* &= b_2 - i\frac{3}{2}\frac{\nu_e\omega_{\mathrm{pe}}^2}{c\omega_0^4}, \\
a^* &= \frac{\tau}{2B} + rb_2^* = a - i\frac{3}{2}\frac{\nu_e r}{c}\frac{\omega_{\mathrm{pe}}^2}{\omega_0^4}.
\end{aligned} \tag{E.2}$$

[1] In this Appendix, the asterisk superscript will denote the quantities that pertain to the lossy case.

The reasoning in Appendix B that leads to formula (B.13) will hold in the lossy case with the replacement of the variables $(a, b, b_2, v_{\mathrm{ph}_0})$ by $(a^*, b^*, b_2^*, v_{\mathrm{ph}_0}^*)$ given by (E.2). The overall effect of complexity in (E.2) is as follows. First, it causes a gradual exponential attenuation of the propagating wave:

$$e^{i\omega_0(t-r/v_{\mathrm{ph}_0}^*)} = e^{i\omega_0(t-r/v_{\mathrm{ph}_0})} e^{-\frac{1}{2}\frac{r}{c}\frac{\nu_e\omega_{\mathrm{pe}}^2}{\omega_0^2}}. \tag{E.3}$$

Other than that, we can write:

$$e^{i\frac{(b^*)^2}{4a^*}} = e^{i\frac{b^2}{4a}} e^{i\left(\frac{(b^*)^2}{4a^*}-\frac{b^2}{4a}\right)} \approx e^{i\frac{b^2}{4a}} e^{i\left(-\frac{2ib}{4a}\frac{r}{c}\frac{\nu_e\omega_{\mathrm{pe}}^2}{2\omega_0^3}\right)} = e^{i\frac{b^2}{4a}} e^{\frac{b}{2a}\frac{r}{c}\frac{\nu_e\omega_{\mathrm{pe}}^2}{2\omega_0^3}},$$

and using (B.16), (B.17): $|b| \le \tau'/2 = aB$, conclude that the second exponent in the previous equality satisfies:

$$\left|\frac{b}{2a}\frac{r}{c}\frac{\nu_e\omega_{\mathrm{pe}}^2}{2\omega_0^3}\right| \le \frac{1}{4}\frac{r}{c}\frac{\nu_e\omega_{\mathrm{pe}}^2}{\omega_0^2}\frac{B}{\omega_0}.$$

The corresponding exponential function may be either decreasing or increasing, but either way the rate of its amplitude change will be much slower than that in (E.3) because of an additional small factor $\frac{B}{\omega_0} \ll 1$ in the exponent.

Using (B.4), we can also introduce $\eta_\pm^*$ by substituting the corresponding complex quantities from (E.2), and define $\delta\eta_\pm \stackrel{\mathrm{def}}{=} \eta_\pm^* - \eta_\pm$, where

$$|\delta\eta_\pm| \sim \frac{1}{2}\sqrt{\frac{2B}{\tau}}\frac{r}{c}\frac{\nu_e\omega_{\mathrm{pe}}^2}{2\omega^3} \ll 1.$$

Then, for the difference between the erf functions of the complex argument $\eta_\pm^*$ and the real argument $\eta_\pm$ we have:

$$\left|\mathrm{erf}\big(\sqrt{i}(\eta_\pm + \delta\eta_\pm)\big) - \mathrm{erf}\big(\sqrt{i}\eta_\pm\big)\right| \approx \left|\frac{2}{\sqrt{\pi}}e^{-i\eta_\pm^2}\cdot\sqrt{i}\delta\eta_\pm\right| = \frac{2}{\sqrt{\pi}}|\delta\eta_\pm|.$$

Consequently, the total variation of the quantity $[\mathrm{erf}(\sqrt{i}\eta_-^*) - \mathrm{erf}(\sqrt{i}\eta_+^*)]$ that appears in the "lossy" counterpart of (B.13) will not exceed $\frac{4}{\sqrt{\pi}}|\delta\eta_\pm|$ by absolute value, which is a negligible contribution compared to the value of 2 in the lossless case.

Altogether, using (E.3) and disregarding other effects of complexity, we obtain the following form of the propagating signal in the case of a lossy plasma [cf. formula (B.19)]:

$$\varphi(t,r) \approx \frac{1}{4\pi r}A'(t-r/v_{\mathrm{gr}_0})e^{i\omega_0(t-r/v_{\mathrm{ph}_0})}e^{-\frac{1}{2}\frac{r}{c}\frac{\nu_e\omega_{\mathrm{pe}}^2}{\omega_0^2}}. \tag{E.4}$$

Appendix F

Time integration for the range component of the ambiguity function

When calculating the range component of the ambiguity function, one deals with the integrals of the following type (see (2.35))

$$W_R(\boldsymbol{y}, \boldsymbol{z}) = \int \overline{A(t - 2|\boldsymbol{y} - \boldsymbol{x}^0|/c)} A(t - 2|\boldsymbol{z} - \boldsymbol{x}^0|/c) dt. \tag{F.1}$$

Here we provide a detailed account of how this integration is done and the corresponding resolution obtained. We first do it in the non-dispersive case, and then in the dispersive case.

F.1 Non-dispersive case

Introduce

$$t_{\boldsymbol{y}} = \frac{2|\boldsymbol{y} - \boldsymbol{x}^0|}{c}; \quad t_{\boldsymbol{z}} = \frac{2|\boldsymbol{z} - \boldsymbol{x}^0|}{c} \tag{F.2}$$

and rewrite (F.1) with the help of (2.18) as

$$W_R(\boldsymbol{y}, \boldsymbol{z}) = \int e^{-i\alpha(t-t_{\boldsymbol{y}})^2} \chi_\tau(t - t_{\boldsymbol{y}}) e^{i\alpha(t-t_{\boldsymbol{z}})^2} \chi_\tau(t - t_{\boldsymbol{z}})\, dt. \tag{F.3}$$

The integration interval in (F.3) is determined by the intersection of the supports of the two χ_τ functions in the integrand. Assume, for definiteness, that $t_{\boldsymbol{y}} > t_{\boldsymbol{z}}$ and introduce new constants and a new integration variable

$$t_M = \frac{t_{\boldsymbol{y}} + t_{\boldsymbol{z}}}{2}; \quad T = \frac{t_{\boldsymbol{y}} - t_{\boldsymbol{z}}}{2} > 0; \quad u = t - t_M \tag{F.4}$$

such that the integration limits in (F.3) become symmetric about zero:

$$W_R(\boldsymbol{y}, \boldsymbol{z}) = \int_{-\tau_T/2}^{\tau_T/2} e^{ibu} du \tag{F.5}$$

where

$$\tau_T = \tau - 2T; \quad b = 4T\alpha. \tag{F.6}$$

It should be noted that (F.5) is, accurate to notation differences, a special case of the integral appearing in (A.5) for $n = 0$. Performing integration in (F.5) we get [1]

$$W_R(\boldsymbol{y}, \boldsymbol{z}) = \tau_T \operatorname{sinc}\Big(\frac{b\tau_T}{2}\Big). \tag{F.7}$$

In order to determine the resolution, we find the first positive root of W_R, which corresponds to

$$\frac{b\tau_T}{2} = \frac{4T\alpha(\tau - 2T)}{2} = \pi. \tag{F.8}$$

We will determine T from (F.8). Although this is only a quadratic equation in T, we will solve it by iterations assuming that $T \ll \tau$ (the solution $T \approx \frac{\tau}{2}$ is not relevant). So,

$$T = T_1 + T_2.$$

In order to find T_1 we disregard $2T$ in the brackets in (F.8) to get

$$T_1 = \frac{2\pi}{4\alpha\tau} = \frac{\pi}{B},$$

and, indeed, $|T_1| \ll \tau$. This same relation can also be written as

$$\frac{\pi}{B} \approx T = \frac{t_{\boldsymbol{y}} - t_{\boldsymbol{z}}}{2} = \frac{R_{\boldsymbol{y}} - R_{\boldsymbol{z}}}{c} \Longrightarrow R_{\boldsymbol{y}} - R_{\boldsymbol{z}} \approx \frac{\pi c}{B} = \Delta_R$$

which also corresponds to [Che01, Equation(46)]. The second iteration is

$$2\alpha\Big(\frac{\pi}{B} + T_2\Big)\Big(\tau - 2\frac{\pi}{B}\Big) = \pi$$

if the T_2^2 term is dropped which gives

$$T_2 = \frac{2\pi^2}{\tau\,(B^2 - 4\alpha\pi)} \approx \frac{1}{\tau} 2\frac{\pi^2}{B^2} = \frac{\pi}{B}\frac{2\pi}{B\tau} = T_1\frac{2\pi}{B\tau} \tag{F.9}$$

[1] Formula (F.7) corrects [Che01, Equations (45–46)] in that it eliminates a bogus phase multiplier $e^{i\alpha(R_z^2 - R_y^2)/c^2}$ (for $|R_y - R_z| \sim c/B$, this phase is about $R/(c\tau) \gg 1$ by absolute value) and replaces τ with τ_T. The latter of these corrections can be disregarded, as the subsequent analysis shows that $|T| \ll \tau$.

and demonstrates that $|T_2| \ll |T_1|$ because $B\tau \gg 1$.

We see that in the non-dispersive case, setting the integration interval in (F.5) to $(-\frac{\tau}{2}, \frac{\tau}{2})$ results in a "standard" expression for the the width of the main lobe of the ambiguity function, while introducing a relative error of about $2\pi/(B\tau)$ compared to the more accurate calculations with the $(-\frac{\tau_T}{2}, \frac{\tau_T}{2})$ interval.

F.2 Dispersive case

The dispersive case differs from the non-dispersive case of (F.3) in the following:

1. The propagation speed is different from c;
2. The chirp rate of the incoming chirp is different from that of emitted, and
3. The incoming chirp duration is different from that of emitted.

These differences are expressed by the equation (2.60):

$$W'_R(\boldsymbol{y}, \boldsymbol{z}) = \int \overline{A(t - 2|\boldsymbol{y} - \boldsymbol{x}^0|/c)} A'_{2\delta}(t - 2|\boldsymbol{z} - \boldsymbol{x}^0|/\bar{v}_{\mathrm{gr}}) dt \tag{F.10}$$

where the group velocity is taken at $\omega = \omega_0$. Accordingly, equations (F.2)–(F.4) turn into:

$$\begin{aligned} t_{\boldsymbol{y}} &= \frac{2|\boldsymbol{y} - \boldsymbol{x}^0|}{c}; \quad t'_{\boldsymbol{z}} = \frac{2|\boldsymbol{z} - \boldsymbol{x}^0|}{\bar{v}_{\mathrm{gr}}(\omega_0)} \\ t'_M &= \frac{t_{\boldsymbol{y}} + t'_{\boldsymbol{z}}}{2}; \quad T' = \frac{t_{\boldsymbol{y}} - t'_{\boldsymbol{z}}}{2}; \quad u' = t - t'_M \end{aligned} \tag{F.11}$$

and

$$\begin{aligned} W'_R(\boldsymbol{y}, \boldsymbol{z}) &= \int e^{-i\alpha(t-t_{\boldsymbol{y}})^2} \chi_\tau(t - t_{\boldsymbol{y}}) e^{i\alpha''(t-t'_{\boldsymbol{z}})^2} \chi_{\tau''}(t - t'_{\boldsymbol{z}})\, dt \\ &= \int_{\max\{-\tau/2+t_{\boldsymbol{y}},\, -\tau''/2+t'_{\boldsymbol{z}}\}}^{\min\{\tau/2+t_{\boldsymbol{y}},\, \tau''/2+t'_{\boldsymbol{z}}\}} e^{-i\alpha(t-t_{\boldsymbol{y}})^2} e^{i\alpha''(t-t'_{\boldsymbol{z}})^2}\, dt \end{aligned} \tag{F.12}$$

(see (2.63)). The dispersive version of (F.5) is thus

$$W'_R(\boldsymbol{y}, \boldsymbol{z}) \int_{\max\{-\tau/2+T',\, -\tau''/2-T'\}}^{\min\{\tau/2+T',\, \tau''/2-T'\}} e^{i(\alpha''-\alpha)(u')^2} e^{i2T'(\alpha''+\alpha)u'} e^{i(\alpha''-\alpha)(T')^2} du'. \tag{F.13}$$

Before proceeding with (F.13) we make a remark about the integration limits, in other words — about the relation between the ends of the support intervals of $\chi_\tau(t-t_{\boldsymbol{y}})$ and $\chi_{\tau''}(t-t'_{\boldsymbol{z}})$ in (F.12). In the non-dispersive case, see (F.3), the two intervals have equal lengths, so one interval can contain the second only if these two intervals coincide, i.e., $t_{\boldsymbol{y}} = t_{\boldsymbol{z}}$. In the dispersive

case, as the chirps have different lengths, one chirp may contain the other for some $t_{\boldsymbol{y}} \neq t'_{\boldsymbol{z}}$. The condition for this is

$$|t_{\boldsymbol{y}} - t'_{\boldsymbol{z}}| < \frac{|\tau - \tau''|}{2} = |\delta\tau|.$$

In distance terms, it corresponds to

$$\Delta R \approx \frac{1}{2} c\delta\tau \sim 10m \sim \Delta_R$$

so, technically, in the analysis of resolution, this may lead to several different sets of expressions for the ends of the integration interval:

(i) $-\frac{\tau''}{2} + t'_{\boldsymbol{z}} < -\frac{\tau}{2} + t_{\boldsymbol{y}} < \frac{\tau}{2} + t_{\boldsymbol{y}} < \frac{\tau''}{2} + t'_{\boldsymbol{z}}$

(ii) $-\frac{\tau}{2} + t_{\boldsymbol{y}} < -\frac{\tau''}{2} + t'_{\boldsymbol{z}} < \frac{\tau}{2} + t_{\boldsymbol{y}} < \frac{\tau''}{2} + t'_{\boldsymbol{z}}$

(iii) $-\frac{\tau''}{2} + t'_{\boldsymbol{z}} < -\frac{\tau}{2} + t_{\boldsymbol{y}} < \frac{\tau''}{2} + t'_{\boldsymbol{z}} < \frac{\tau}{2} + t_{\boldsymbol{y}}$

(iv) $-\frac{\tau}{2} + t_{\boldsymbol{y}} < -\frac{\tau''}{2} + t'_{\boldsymbol{z}} < \frac{\tau''}{2} + t'_{\boldsymbol{z}} < \frac{\tau}{2} + t_{\boldsymbol{y}}$.

We avoid considering these cases separately by analyzing the error due to the "symmetrization" of the integration interval. In this symmetrization, we assume that the length of the received chirp is τ rather than τ'' (as in the non-dispersive case). In so doing, we shift the limit(s) of integration by no more than $\left|\frac{\tau''-\tau}{2}\right| = |\delta\tau|$. As the integrand in (F.12) is one by absolute value, the change of the value of the integral due to these shifts does not exceed $2|\delta\tau|$. This is negligible compared to the height of the main lobe in (F.7), which is about $\tau \gg 2|\delta\tau|$; the relative error is

$$e_R = \frac{2\delta\tau}{\tau} \approx 0.3\% \tag{F.14}$$

for the parameter values given in Table 1.1. It turns out that this relative error is also small compared to the parameters used to evaluate smearing of the main lobe in (2.72):

$$e_R \left(\frac{|w_1|_{\frac{b\tau}{2}=\pi}}{|w_0|_{\frac{b\tau}{2}=0}} \right)^{-1} \approx \frac{2\delta\tau}{\tau} \frac{2\pi^2}{\tau^2\delta\alpha} = \frac{2\delta\alpha}{\alpha} \frac{2\pi^2}{\tau^2\delta\alpha} = \frac{8\pi^2}{B\tau} \ll 1$$

so, for the analysis in this dissertation, the integration limits can be made symmetric as in (F.5). Thus, the integral in (F.13) simplifies to

$$W'_R(\boldsymbol{y}, \boldsymbol{z}) = \int_{-\tau'_T/2}^{\tau'_T/2} e^{i(\alpha''-\alpha)(u')^2} e^{ib'u'} e^{i(\alpha''-\alpha)(T')^2} du' \tag{F.15}$$

where we have assumed once again that $T' > 0$ and

$$\tau'_T = \tau - 2T'; \quad b' = 2T'(\alpha + \alpha'') \tag{F.16}$$

[cf. (2.65–2.66)].

The first exponent in the integrand in (F.15) contains a quadratic in u' phase; this term results in the smearing of the main lobe of W'_R, see Section 2.4. The phase in the third exponent is independent of u'; assuming $|T'| \sim 1/B$, this phase is about

$$2\delta\alpha|T'|^2 = 2\frac{\delta\alpha}{B^2} = 2\frac{\delta\alpha}{\alpha}\frac{\alpha}{B^2} = 2\frac{\delta\tau}{\tau}\frac{B/2\tau}{B^2} = \frac{\delta\tau}{\tau}\frac{1}{B\tau} \ll 1$$

i.e., infinitisemal. With the first and third exponents in (F.15) dropped, the form of equations (F.15–F.16) is similar to that of (F.5–F.6), so the analysis of resolution may follow the same pattern as that in the non-dispersive case. In particular, the maximum of W'_R is achieved at $T' = 0$, which corresponds to (see (F.11))

$$\frac{R_{\boldsymbol{y}}}{c} - \frac{R_{\boldsymbol{z}}}{\bar{v}_{\mathrm{gr}}} = 0 \Longrightarrow R_{\boldsymbol{y}} = R_{\boldsymbol{z}}\frac{c}{\bar{v}_{\mathrm{gr}}} \approx R_{\boldsymbol{z}}\Big(1 + \frac{\bar{\omega}_{\mathrm{pe}}^2}{2\omega_0^2}\Big)$$

thus giving a shift in range, see (2.73).

To analyze resolution in the dispersive case, we solve

$$\frac{b'\tau'_T}{2} = T'(\alpha + \alpha'')(\tau - 2T') = \pi \tag{F.17}$$

[cf. (F.8)] with respect to $T' = T'_1 + T'_2$ by iterations. First, we get

$$T'_1 = \frac{\pi}{B} = T_1$$

and then,

$$\Big(\frac{\pi}{B} + T'_2\Big)(\alpha + \alpha'')\Big(\tau - 2\frac{\pi}{B}\Big) = \pi.$$

Using $\alpha'' = \alpha + 2\delta\alpha$ we get

$$T'_2\alpha\tau + \frac{\pi}{B}\tau\delta\alpha - 2\alpha\Big(\frac{\pi}{B}\Big)^2 = 0$$

which gives

$$T'_2 = \frac{2}{\tau}\frac{\pi^2}{B^2} - \frac{\pi}{B}\frac{\delta\alpha}{\alpha} = T_1\Big(\frac{2\pi}{B\tau} - \frac{\delta\tau}{\tau}\Big). \tag{F.18}$$

Notice that the first term in (F.18) is equal to T_2 in the non-dispersive case, see (F.9), so

$$T'_2 = T_2 - T_1\frac{\delta\tau}{\tau}. \tag{F.19}$$

Thus, the second term in (F.19) could be considered as the effect of dispersion on range resolution; this term also coincides with that in (2.71). This second term however is of the same order as those ignored at the symmetrization of the integration limits in (F.13), see (F.14), and is also not bigger than T_2. Note that T_2 is usually ignored in the expression for range resolution. Therefore the choice of integration limits for (2.63) is inconsequential to our analysis.

Remark. As it turns out, the case (i) on page 181 that is used in the main body of the dissertation is invalid for the linear upchirps that we use. This can be easily proven: We know from (2.64) that $\tau'' < \tau$. Now suppose that $\frac{\tau}{2} + t_{\boldsymbol{y}} < \frac{\tau''}{2} + t'_{\boldsymbol{z}}$. Then

$$-\frac{\tau}{2} + t_{\boldsymbol{y}} < -\frac{\tau}{2} + \frac{\tau''}{2} - \frac{\tau}{2} + t'_{\boldsymbol{z}} < -\frac{\tau}{2} + t'_{\boldsymbol{z}} < -\frac{\tau''}{2} + t'_{\boldsymbol{z}}.$$

However, as we have demonstrated, it is acceptable for our purposes. We choose to use it because it results in the least cumbersome expressions.

Appendix G

Conditioning of the TEC found by dual carrier probing

In this appendix, we investigate conditioning of formula (2.94). If the quantity f depends on x, then the conditioning of $f(x)$, i.e., the sensitivity of f to the perturbations of x, is naturally defined as the maximum ratio of the relative error in f over the corresponding relative error in the input x, see [RT07, Chapter 1]:

$$\sup_{\delta x} \frac{|\delta f/f|}{|\delta x/x|} \approx |f'(x)| \frac{|x|}{|f|}.$$

In formula (2.94), the dependent quantity f is $\bar{\omega}_{\mathrm{pe}}^2$, and the input data are $R_{\boldsymbol{y}}^{(1)}$ and $R_{\boldsymbol{y}}^{(2)}$. Due to the obvious symmetry, it is sufficient to estimate the conditioning with respect to either of the two, and hereafter we will interpret $R_{\boldsymbol{y}}^{(1)}$ as the independent variable x. Then,

$$\frac{\partial \bar{\omega}_{\mathrm{pe}}^2}{\partial R_{\boldsymbol{y}}^{(1)}} = \frac{2\omega_1^2\omega_2^2}{\omega_2^2 R_{\boldsymbol{y}}^{(2)} - \omega_1^2 R_{\boldsymbol{y}}^{(1)}} \left(1 + \frac{\omega_1^2 (R_{\boldsymbol{y}}^{(1)} - R_{\boldsymbol{y}}^{(2)})}{\omega_2^2 R_{\boldsymbol{y}}^{(2)} - \omega_1^2 R_{\boldsymbol{y}}^{(1)}}\right),$$

and hence the condition number of $\bar{\omega}_{\mathrm{pe}}^2$ with respect to $R_{\boldsymbol{y}}^{(1)}$ is given by

$$\begin{aligned} \left| \frac{\partial \bar{\omega}_{\mathrm{pe}}^2}{\partial R_{\boldsymbol{y}}^{(1)}} \frac{R_{\boldsymbol{y}}^{(1)}}{\bar{\omega}_{\mathrm{pe}}^2} \right| &= \left| \frac{R_{\boldsymbol{y}}^{(1)}}{R_{\boldsymbol{y}}^{(1)} - R_{\boldsymbol{y}}^{(2)}} + \frac{\omega_1^2 R_{\boldsymbol{y}}^{(1)}}{\omega_2^2 R_{\boldsymbol{y}}^{(2)} - \omega_1^2 R_{\boldsymbol{y}}^{(1)}} \right| \\ &\leqslant \frac{R_{\boldsymbol{y}}^{(1)}}{|R_{\boldsymbol{y}}^{(1)} - R_{\boldsymbol{y}}^{(2)}|} + \frac{\omega_1^2 R_{\boldsymbol{y}}^{(1)}}{|\omega_2^2 R_{\boldsymbol{y}}^{(2)} - \omega_1^2 R_{\boldsymbol{y}}^{(1)}|}. \end{aligned} \tag{G.1}$$

The first term on the right hand of (G.1) is large, because the ranges $R_{\boldsymbol{y}}^{(1)}$ and $R_{\boldsymbol{y}}^{(2)}$ are close to one another and the difference between the two is much smaller than each of them. The

second term is not too large, because according to (2.93), the denominator $\omega_2^2 R_{\boldsymbol{y}}^{(2)} - \omega_1^2 R_{\boldsymbol{y}}^{(1)} = R_{\boldsymbol{z}}(\omega_2^2 - \omega_1^2)$, and consequently, the entire fraction is of the order $\omega_1^2/(\omega_2^2 - \omega_1^2)$, which is about 5 when the difference between ω_2 and ω_1 is 10%.

To improve the overall conditioning of $\bar{\omega}_{\mathrm{pe}}^2$, one can use several reference locations: $\boldsymbol{y}_1$, $\boldsymbol{y}_2$, $\boldsymbol{y}_3, \ldots$, or features, instead of only one. Assume that we have computed $\bar{\omega}_{\mathrm{pe}}^2(\boldsymbol{y}_1)$, $\bar{\omega}_{\mathrm{pe}}^2(\boldsymbol{y}_2)$, ..., $\bar{\omega}_{\mathrm{pe}}^2(\boldsymbol{y}_K)$ for K different reference locations according to formula (2.94), and that we evaluate $\bar{\omega}_{\mathrm{pe}}^2$ by plain averaging:

$$\bar{\omega}_{\mathrm{pe}}^2 = \frac{1}{K} \sum_{k=1}^{K} \bar{\omega}_{\mathrm{pe}}^2(\boldsymbol{y}_k). \tag{G.2}$$

Note that as $\bar{\omega}_{\mathrm{pe}}^2$ is a scalar quantity, formula (G.2) is equivalent to the least squares fit, see [RT07, Chapter 7].

Let us now interpret $\bar{\omega}_{\mathrm{pe}}^2(\boldsymbol{y}_k)$ as independent random variables with means $\langle \bar{\omega}_{\mathrm{pe}}^2(\boldsymbol{y}_k) \rangle$ and variances $\sigma^2(\bar{\omega}_{\mathrm{pe}}^2(\boldsymbol{y}_k))$, $k = 1, 2, \ldots, K$. Then (see, e.g., [CH06, Chapter 2]),

$$\langle \bar{\omega}_{\mathrm{pe}}^2 \rangle = \frac{1}{K} \sum_{k=1}^{K} \langle \bar{\omega}_{\mathrm{pe}}^2(\boldsymbol{y}_k) \rangle \quad \text{and} \quad \sigma^2(\bar{\omega}_{\mathrm{pe}}^2) = \frac{1}{K^2} \sum_{k=1}^{K} \sigma^2(\bar{\omega}_{\mathrm{pe}}^2(\boldsymbol{y}_k)). \tag{G.3}$$

Assume in addition, and with no loss of generality, that the errors associated with computing the individual $\bar{\omega}_{\mathrm{pe}}^2(\boldsymbol{y}_k)$ are approximately equal to the corresponding standard deviations $\sigma(\bar{\omega}_{\mathrm{pe}}^2(\boldsymbol{y}_k)$, and that these errors are roughly the same for all $k = 1, 2, \ldots, K$. Then, the second equality in formula (G.3) indicates that the overall error of evaluating $\bar{\omega}_{\mathrm{pe}}^2$ according to (G.2) will decrease proportionally to $K^{-1/2}$ as K increases.

Appendix H

Accuracy analysis of area-based image registration

In this Appendix, we show how one can reduce the error of the area-based image registration due to the discrete Fourier transform and due to noise. Possible misregistration due to different terrain reflectivity on two different carrier frequencies belongs to neither of these two categories and is not discussed hereafter. Note also that while we are proposing to use the area-based image registration for correcting the matched filter in SAR signal processing, it is otherwise used routinely for SAR interferometry, see, e.g., [BE05]. Our subsequent discussion focuses on one-dimensional signals for simplicity; the extension to two dimensions can be found, e.g., in [FZB02, SOCM01].

The phase correlation method is based on formula (2.111), which is written for two continuous one-dimensional signals $u(x)$ and $v(x)$ defined on $-\infty < x < \infty$. In practice, however, the signals are discrete rather than continuous, and their length is finite. Let us therefore introduce two sequences of length L: $\{u_l\}_{l=0}^{L-1}$ and $\{v_l\}_{l=0}^{L-1}$, and interpret them as traces of two continuous functions, $u(x)$ and $v(x) = u(x-s)$, assuming $s > 0$, on a uniform grid of size T:[1] $u_l \equiv u(x_l)$ and $v_l \equiv v(x_l)$, where $x_l = lT$ and $l = 0, 1, \ldots, L-1$. Clearly, the lower bound for T is the pixel size, whereas the upper bound for L is the total number of pixels in those fragments of each image that are employed for registration. Instead of (2.111), we will use the discrete Fourier transform (see, e.g., [RT07, Section 5.7]) of u_l and v_l (which assumes, in particular, that both sequences are L-periodic):

$$\hat{u}_k = \frac{1}{\sqrt{L}} \sum_{l=0}^{L-1} u_l e^{-ik\frac{2\pi}{LT}x_l} = \frac{1}{\sqrt{L}} \sum_{l=0}^{L-1} u_l e^{-ik\frac{2\pi}{L}l} \tag{H.1a}$$

[1] In the image registration literature, the grid size T is often called the sampling rate, and accordingly, the grid dimension (length of sequence) L is referred to as the number of samples, see, e.g., [MM93].

and

$$\hat{v}_k = \frac{1}{\sqrt{L}} \sum_{l=0}^{L-1} v_l e^{-ik\frac{2\pi}{LT}x_l} = \frac{1}{\sqrt{L}} \sum_{l=0}^{L-1} u(x_l - s) e^{-ik\frac{2\pi}{LT}x_l}$$
$$= \frac{1}{\sqrt{L}} \sum_{l=0}^{L-1} u(x_l - s) e^{-ik\frac{2\pi}{LT}(x_l - s)} \cdot e^{-ik\frac{2\pi}{LT}s} \approx \hat{u}_k e^{-ik\frac{2\pi}{LT}s}. \tag{H.1b}$$

Note that the last equality of (H.1b) is only approximate rather than exact because of the error that may appear if the shift s is not a multiple of the grid size T. For smooth periodic functions though, this error can be shown to decay rapidly as L increases (see, e.g., the analysis in [RT07, Sections 3.1 and 4.1]), and we therefore disregard it hereafter.

Next, we build a discrete function similar to that of (2.112):

$$\tilde{\delta}_l \stackrel{\text{def}}{=} \frac{1}{\sqrt{L}} \sum_{k=0}^{L-1} \frac{\hat{u}_k^* \hat{v}_k}{|\hat{u}_k^* \hat{v}_k|} e^{ik\frac{2\pi}{LT}x_l} = \frac{1}{\sqrt{L}} \sum_{k=0}^{L-1} e^{-ik\frac{2\pi}{LT}s} e^{ik\frac{2\pi}{LT}x_l} = \frac{1}{\sqrt{L}} \sum_{k=0}^{L-1} e^{ik\frac{2\pi}{L}\left(l - \frac{s}{T}\right)}. \tag{H.2}$$

To analyze $\tilde{\delta}_l$ of (H.2), we consider two cases: $\frac{s}{T}$ is an integer and $\frac{s}{T}$ is not an integer. First, let $\frac{s}{T} = m \in \mathbb{N}$. Then, from (H.2) we can derive:

$$\tilde{\delta}_l = \frac{1}{\sqrt{L}} \sum_{k=0}^{L-1} e^{ik\frac{2\pi}{L}(l-m)} = \begin{cases} \sqrt{L}, & \text{if } \ l = m, \\ \frac{1}{\sqrt{L}} \frac{1 - e^{i2\pi(l-m)}}{1 - e^{i\frac{2\pi}{L}(l-m)}} = 0, & \text{if } \ l \neq m. \end{cases}$$

In other words, if the shift s happens to be a shift by the integer number m of grid cells, then the function $\tilde{\delta}_l$ of (H.2) has a peak value of $\sqrt{L}$ precisely at $l = m$, and is equal to zero everywhere else on the grid. Hence, in this case the discrete version of phase correlation will yield the value of the shift exactly.

If $\frac{s}{T}$ is not an integer, then using (H.2) and assuming that l is close to $\frac{s}{T}$ we obtain:

$$\tilde{\delta}_l = \frac{1}{\sqrt{L}} \frac{1 - e^{i2\pi\left(l - \frac{s}{T}\right)}}{1 - e^{i\frac{2\pi}{L}\left(l - \frac{s}{T}\right)}}$$
$$\approx \frac{\sqrt{L}}{2} e^{i\pi\left(l - \frac{s}{T}\right)} \frac{e^{-i\pi\left(l - \frac{s}{T}\right)} - e^{i\pi\left(l - \frac{s}{T}\right)}}{-i\pi\left(l - \frac{s}{T}\right)} = \sqrt{L} e^{i\pi\left(l - \frac{s}{T}\right)} \frac{\sin \pi\left(l - \frac{s}{T}\right)}{\pi\left(l - \frac{s}{T}\right)},$$

which means that the maximum absolute value of $\tilde{\delta}_l$ is $\sim \sqrt{L}$, and it is attained at the grid node l closest to $\frac{s}{T}$. At all other grid nodes, generally speaking, $\tilde{\delta}_l \neq 0$. Therefore, if $\frac{s}{T}$ is not an integer, the best accuracy of reconstructing the shift s that one can achieve by looking for the maximum of $\tilde{\delta}_l$ of (H.2) is roughly $T/2$, i.e., at most half size of the pixel. Extension of this method to the accuracies on the order of a fraction of one pixel may involve a certain

interpolation procedure, see, e.g., [Abd99], and also [MM93, GSTF08]. The effects of aliasing and aperiodicity can be reduced by filtering, see [FZB02, SOCM01].

Another approach to further improving the accuracy of phase correlation is based on analyzing the phase of $\hat{u}_k$ and $\hat{v}_k$ of (H.1). Namely, it is easy to see from (H.1b) that

$$\arg \hat{u}_k - \arg \hat{v}_k = k\frac{2\pi}{LT}s. \tag{H.3}$$

Speaking formally, the value of s can be obtained from (H.3) by merely dividing the left-hand side of the equality by $k\frac{2\pi}{LT}$ for any non-zero k:

$$s = \frac{LT}{2\pi}\frac{\arg \hat{u}_k - \arg \hat{v}_k}{k}. \tag{H.4}$$

This formula, however, is prone to inaccuracies due to errors in the data $\arg \hat{u}_k - \arg \hat{v}_k$. The way to improve the accuracy is to obtain s by the method of least squares using all k's rather than only one as in (H.4), see [SOCM01, MM93]. Namely, s shall be sought for as a solution to the following quadratic minimization problem (see, e.g., [RT07, Chapter 7]):

$$\min_s \sum_{k=1}^{L-1} \left[k\frac{2\pi}{LT}s - (\arg \hat{u}_k - \arg \hat{v}_k) \right]^2. \tag{H.5}$$

The stationary point of the functional in (H.5) can be found by requiring that its first derivative with respect to s be equal to zero, which yields:

$$s = \frac{LT}{2\pi}\frac{\sum_{k=1}^{L-1} k(\arg \hat{u}_k - \arg \hat{v}_k)}{\sum_{k=1}^{L-1} k^2}. \tag{H.6}$$

Let us now interpret the data $\{\arg \hat{u}_k - \arg \hat{v}_k\}$, $k = 1, 2, \ldots, L-1$, as independent identically distributed random variables[2] with variances

$$\mathrm{Var}(\arg \hat{u}_k - \arg \hat{v}_k) \stackrel{\text{def}}{=} \langle (\arg \hat{u}_k - \arg \hat{v}_k - \langle \arg \hat{u}_k - \arg \hat{v}_k \rangle)^2 \rangle = \sigma^2.$$

The actual errors in the data may be due to the terrain noise, as well as measurement errors, instrument noise, etc. In all those cases, it is convenient to use the description in the form of random variables. Then, $\mathrm{Var}(k(\arg \hat{u}_k - \arg \hat{v}_k)) = k^2\sigma^2$, and according to (H.6) we can write

[2] The requirement of independence is important. However, the requirement that all random variables be identically distributed can be alleviated.

(see, e.g., [CH06, Chapter 2]):

$$\begin{aligned}\mathrm{Var}(s) &= \left(\frac{LT}{2\pi}\right)^2 \frac{\sum_{k=1}^{L-1} k^2\sigma^2}{(\sum_{k=1}^{L-1} k^2)^2} \\ &= \left(\frac{LT}{2\pi}\right)^2 \frac{\sigma^2}{\sum_{k=1}^{L-1} k^2} = \left(\frac{LT}{2\pi}\right)^2 \frac{6\sigma^2}{(L-1)L(2L-1)}.\end{aligned} \tag{H.7}$$

From formula (H.7), one can easily deduce that for sufficiently large L the standard deviation of the shift s determined by the least squares fit according to (H.6) is

$$\sigma(s) = \sqrt{\mathrm{Var}(s)} \sim \frac{\sigma}{\sqrt{L}}. \tag{H.8}$$

In other words, the error of obtaining the shift by phase correlation scales as the inverse square root of the number of samples L. While formula (H.8) describes the asymptotic behavior of the error, the practical values of the registration accuracy can be as low as only a few percent of a pixel, see [TH86, SOCM01, GSTF08, FZB02, Abd99], i.e., a few percent of the resolution cell.

Appendix I

Split bandwidth setup for dual carrier probing

Linear chirps of Section 2.3 represent a natural waveform for the split bandwidth approach. Indeed, partitioning such a chirp in time causes a proportional partition in frequency, and the other way around. For example, the chirp (2.18) given by $P(t) = e^{i\alpha t^2} e^{i\omega_0 t}$ on the interval $[-\tau/2, \tau/2]$ with the rate $\alpha = \frac{B}{2\tau}$ and angular bandwidth B centered around ω_0 can be considered as a combination of two successive sub-chirps:

$$P^{(1)}(t) = e^{i\alpha t^2} e^{i\omega_0 t} \text{ for } t \in [-\tau/2, 0] \quad \text{and} \quad P^{(2)}(t) = e^{i\alpha t^2} e^{i\omega_0 t} \text{ for } t \in [0, \tau/2].$$

Obviously, the frequency intervals for sub-chirps $P^{(1)}(t)$ and $P^{(2)}(t)$ are $[\omega_0 - B/2, \omega_0]$ and $[\omega_0, \omega_0 + B/2]$, respectively. Next, consider a new half-length envelope:

$$A_{\tau/2}(t) \stackrel{\text{def}}{=} \chi_{\tau/2}(t) e^{i\alpha t^2}, \quad \text{where} \quad \chi_{\tau/2}(t) = \begin{cases} 1, & t \in [-\tau/4, \tau/4], \\ 0, & \text{otherwise.} \end{cases}$$

Then, it is easy to show that

$$\begin{aligned} P^{(1)}(t) &= e^{i\alpha \frac{\tau^2}{16} - i\omega_0 \frac{\tau}{4}} P_1(t + \tau/4), \\ P^{(2)}(t) &= e^{i\alpha \frac{\tau^2}{16} + i\omega_0 \frac{\tau}{4}} P_2(t - \tau/4), \end{aligned} \tag{I.1}$$

where

$$P_{1,2}(t) \stackrel{\text{def}}{=} A_{\tau/2}(t) e^{i\omega_{1,2} t}, \quad \omega_{1,2} = \omega_0 \mp \frac{B}{4}, \quad \text{and} \quad t \in [-\tau/4, \tau/4]. \tag{I.2}$$

In other words, up to a constant factor of magnitude one, the sub-chirps $P^{(1)}(t)$ and $P^{(2)}(t)$ are equivalent to time-shifted half-length half-bandwidth linear chirps P_1 and P_2 of (I.2) that

are centered around ω_1 and ω_2, respectively, and have the same rate $\alpha = \frac{B}{2\tau}$. Consequently, by processing the same raw data first by means of the filter $\overline{P_1(t + \tau/4 - |\boldsymbol{x} - \boldsymbol{y}|/c)}$ and then by means of $\overline{P_2(t - \tau/4 - |\boldsymbol{x} - \boldsymbol{y}|/c)}$ we will obtain two images on two frequencies, ω_1 and ω_2. Due to the ionosphere, these images will be shifted with respect to one another. Hence, they can be used for reconstructing the TEC N_H and its first moment $\mathcal{Q}$ according to the methodology of Section 2.8.

Of course, it is also possible to define sub-chirps with the sub-bandwidth b taking any value in the interval $(0, B)$ other than $b = B/2$. The expression for sub-chirp central frequencies is then $\omega_{1,2} = \omega_0 \mp (B-b)/2$. If $b < B/2$, then the central part of the received signal and the central frequencies of the main chirp bandwidth will not be used for any of the sub-images, whereas if $b > B/2$, then those central parts will be used for both sub-images.[1] The accuracy of the TEC reconstruction by means of image registration (Sections 2.8 and 2.9.2) is affected by the choice of b in two ways. First, as the residual image displacement given by (2.122) (where b should be substituted instead of B) are proportional to the sub-image resolution $\frac{\pi c}{b}$, the increase of b reduces the distortions. Second, as the sub-bands are limited by the bandwidth of the original chirp, the frequency separation factor given by (2.121) with (I.2) decreases as b increases:

$$Z(b) = \frac{|\omega_1 - \omega_2|}{\omega_0} = \frac{B - b}{\omega_0}. \tag{I.3}$$

This, in turn, increases the distortions. The value of b minimizing the residual shift given by (2.122) in the split bandwidth setting is therefore

$$b^* = \arg\min_b \tilde{S}_R(b) = \arg\min_b \frac{\pi c}{b} \frac{\zeta_R}{2Z(b)} = \arg\min_b \frac{1}{b(B-b)} = \frac{B}{2}.$$

In other words, it corresponds exactly to the partition of the original chirp into two half-bandwidth chirps P_1 and P_2 given by (I.1).[2] The actual minimum value is given by formula (2.122) with the substituted bandwidth $b^* = B/2$ and the frequency separation factor $Z(b^*) = B/(2\omega_0)$, see (I.3):

$$\tilde{S}_R = \frac{2\pi c \zeta_R \omega_0}{B^2} \tag{I.4}$$

Similarly to (2.122), expression (I.4) does not depend on the ionospheric parameters.

By matching the residual range shift of (I.4) and the original range shift of (2.73) we get the sensitivity threshold of the split band implementation to the ionospheric TEC:

$$N_H = \frac{H}{R} \frac{m_e c}{e^2} \zeta_R \frac{\omega_0^3}{B^2}. \tag{I.5}$$

[1] It is also possible to use sub-bands with different bandwidths, as suggested in [RES+11].

[2] A similar yet not equivalent optimization formulation is analyzed in [BE05].

Formula (I.5) yields about $8\,TECU$ for the parameters in Table 1.1 and, according to (I.4), corresponds to $\tilde{S}_R \approx 70m$. When the background value of the TEC is lower than that given by formula (I.5), it is not practical to use the split band version of dual carrier correction described in this appendix. This limitation, however, does not apply to the full-fledged version of the algorithm that employs two independent carrier frequencies with their respective bandwidths.

Appendix J

Faraday rotation for a chirped signal

Linear time-harmonic waves

$$(\boldsymbol{E}, \boldsymbol{H}) \sim e^{i(\omega t - \boldsymbol{k}\boldsymbol{r})}$$

in a cold magnetized plasma are governed by the following equation (see, e.g., [Gin64, Ora84]):

$$\Lambda_{ij} E_j \equiv \Big[\frac{k^2 c^2}{\omega^2}\Big(\frac{k_i k_j}{k^2} - \delta_{ij}\Big) + \varepsilon_{ij}\Big] E_j = 0. \tag{J.1}$$

Let the constant external magnetic field $\boldsymbol{H}_0$ be aligned with the z-axis.[1] Then, the dielectric tensor has the form

$$\varepsilon = \begin{pmatrix} \varepsilon_\perp & -ig & 0 \\ ig & \varepsilon_\perp & 0 \\ 0 & 0 & \varepsilon_\parallel \end{pmatrix}, \tag{J.2}$$

where

$$\varepsilon_\perp = 1 - \frac{\omega_{\mathrm{pe}}^2}{\omega^2 - \Omega^2}, \quad \varepsilon_\parallel = 1 - \frac{\omega_{\mathrm{pe}}^2}{\omega^2}, \quad \text{and} \quad g = \frac{\omega_{\mathrm{pe}}^2 \Omega}{\omega(\omega^2 - \Omega^2)}. \tag{J.3}$$

In (J.3), ω_{pe} and Ω denote the Langmuir and Larmor frequency:

$$\omega_{\mathrm{pe}} = \Big(\frac{4\pi n_{\mathrm{e}} e^2}{m_{\mathrm{e}}}\Big)^{1/2} \quad \text{and} \quad \Omega = \frac{e H_{0z}}{m_{\mathrm{e}} c}, \tag{J.4}$$

respectively, n_{e} is the electron number density, and m_{e} is the electron mass. With this definition, the sign of Ω is determined by the direction of the magnetic field. We are assuming that

$$\omega \gg \omega_{\mathrm{pe}} \gg |\Omega|, \tag{J.5}$$

which allows us to neglect the contribution of the ion motion to (J.3).

[1] In this appendix, we use the xyz-notation for the coordinates.

The dispersion relation for the waves governed by (J.1) is

$$\det \Lambda = 0, \tag{J.6}$$

and the corresponding non-trivial solutions $\boldsymbol{E}$ are called the polarization vectors. For simplicity, we first consider the case of a parallel propagation:

$$|\boldsymbol{k}| = |k_z|, \quad k_x = k_y = 0. \tag{J.7}$$

If there is no magnetic field, then $\Omega = 0$, the matrices ε and Λ are diagonal, and there are two types of polarization: longitudinal, $\boldsymbol{E} = (0, 0, E_z)$, and transverse, $\boldsymbol{E} = (E_x, E_y, 0)$. For the latter, one of the transverse polarization vectors can be chosen with $E_x = 0$ and the other with $E_y = 0$, which corresponds to two linear polarizations. When $\Omega \neq 0$, (J.6) yields the following dispersion relation for transverse waves ($E_z = 0$):

$$\frac{(k^{\pm})^2 c^2}{\omega^2} = 1 - \frac{\omega_{\rm pe}^2}{\omega^2} \pm \frac{\omega_{\rm pe}^2 \Omega}{\omega^3}, = 1 - f_1 \pm f_2, \tag{J.8}$$

where we have introduced the notations

$$f_1 \equiv f_1(\omega) = \frac{\omega_{\rm pe}^2}{\omega^2}, \quad f_2 \equiv f_2(\omega) = \frac{\omega_{\rm pe}^2 \Omega}{\omega^3}, \quad \text{and} \quad 1 \gg f_1 \gg |f_2|. \tag{J.9}$$

Solutions to equation (J.8) correspond to two polarization vectors:

$$\begin{pmatrix} E_x \\ E_y \end{pmatrix} \sim \begin{pmatrix} 1 \\ \pm i \end{pmatrix}, \tag{J.10}$$

that represent two circular polarizations with opposite direction of rotation. The phase and group velocities for these two circularly polarized waves are given by

$$v_{\rm ph}^{\pm} \stackrel{\rm def}{=} \frac{\omega}{k^{\pm}} = c(1 - f_1 \pm f_2)^{-1/2}, \tag{J.11a}$$

$$v_{\rm gr}^{\pm} \stackrel{\rm def}{=} \left(\frac{d\omega}{dk}\right)^{\pm} = \frac{2c\sqrt{1 - f_1 \pm f_2}}{2 \mp f_2}. \tag{J.11b}$$

Formulae (J.11) along with (J.5) and (J.9) indicate that the terms due to the magnetic field $\boldsymbol{H}_0$ (i.e., proportional to f_2) have a very small effect on $v_{\rm gr}$ and $v_{\rm ph}$. The only situation where this effect can be seen is when the terms of order 1 and f_1 cancel, which happens when one evaluates the difference between the propagation speeds for two circular polarizations: $(v_{\rm gr}^{+} - v_{\rm gr}^{-})$ or $(v_{\rm ph}^{+} - v_{\rm ph}^{-})$. It is the phase speed difference that is responsible for the Faraday rotation.

The expression for the chirp (2.18)–(2.19) traveling through an isotropic ionosphere (no

external magnetic field and no FR) has been obtained in Appendix B by Fourier transforming the initial pulse in time, propagating each harmonic in space with the corresponding phase velocity, and finally making the inverse Fourier transform:

$$\begin{aligned}\varphi(t,r) &= \frac{1}{4\pi r} e^{i\omega_0(t-r/v_{\mathrm{ph}_0})} \chi_{\tau'}(t-r/v_{\mathrm{gr}_0}) e^{i\alpha'(t-r/v_{\mathrm{gr}_0})^2} \\ &\stackrel{\mathrm{def}}{=} \frac{1}{4\pi r} A'(t-r/v_{\mathrm{gr}_0}) e^{i\omega_0(t-r/v_{\mathrm{ph}_0})},\end{aligned} \tag{J.12}$$

where

$$\tau' = \tau - \delta\tau = \tau - \frac{r}{c}\frac{\omega_{\mathrm{pe}}^2}{\omega_0^2}\frac{B}{\omega_0} \quad \text{and} \quad \alpha' = \alpha + \delta\alpha = \frac{B}{2\tau}\Big(1 + \frac{\delta\tau}{\tau}\Big) \tag{J.13}$$

are the modified chirp parameters that account for the temporal dispersion. Hereafter, v_{ph_0}, v_{gr_0}, and k_0 refer to the phase and group velocities and the wavenumber for the isotropic plasma, i.e., calculated according to (J.8) and (J.11) at $\omega = \omega_0$ with $f_2 = 0$.

For the case of a magnetized plasma, formula (J.12) can be extended to the circularly polarized waves. Considering the form of the polarization vectors in (J.10), the expressions for the propagating circular harmonics are

$$\begin{pmatrix} E_x \\ E_y \end{pmatrix}(t,r) = \begin{pmatrix} 1 \\ \pm i \end{pmatrix} \frac{1}{4\pi r} A'(t-r/v_{\mathrm{gr}_0}^{\pm}) e^{i\omega_0(t-r/v_{\mathrm{ph}_0}^{\pm})}$$

where $v_{\mathrm{gr}_0}^{\pm}$ and $v_{\mathrm{ph}_0}^{\pm}$ are $v_{\mathrm{gr}}^{\pm}$ and $v_{\mathrm{ph}}^{\pm}$, respectively, with ω_0 substituted for ω. The total propagating field is a linear combination of these circular harmonics:

$$\begin{aligned}\begin{pmatrix} E_x \\ E_y \end{pmatrix}(t,r) &\propto \frac{1}{4\pi r}\sum_{\pm}\begin{pmatrix} 1 \\ \pm i \end{pmatrix} C_{\pm} A'(t-r/v_{\mathrm{gr}_0}^{\pm}) e^{i\omega_0(t-r/v_{\mathrm{ph}_0}^{\pm})} \\ &= \frac{1}{4\pi r}\sum_{\pm}\begin{pmatrix} 1 \\ \pm i \end{pmatrix} C_{\pm} \chi_{\tau'}(t-r/v_{\mathrm{gr}_0}^{\pm}) e^{i\alpha'(t-r/v_{\mathrm{gr}_0}^{\pm})^2} e^{i\omega_0(t-r/v_{\mathrm{ph}_0}^{\pm})},\end{aligned} \tag{J.14}$$

where $C_{\pm}$ are the amplitudes. To make the emitted field ($r = 0$) linearly polarized in the xz-plane, we set $C_+ = C_- = 1$. Per our earlier discussion, in the argument of $\chi_{\tau'}$ on the second line of (J.14) we leave out the effect of polarization on the chirp boundaries.

Introduce the "chirp time" variable

$$u \stackrel{\mathrm{def}}{=} t - \frac{r}{v_{\mathrm{gr}_0}} \quad \text{so that} \quad -\frac{\tau'}{2} < u < \frac{\tau'}{2}.$$

For the retarded group travel time in (J.14), we have:

$$
\begin{aligned}
t_{\mathrm{gr}}^{\pm} \stackrel{\mathrm{def}}{=} t - \frac{r}{v_{\mathrm{gr}_0}^{\pm}} &= u + r\Big(\frac{1}{v_{\mathrm{gr}_0}} - \frac{1}{v_{\mathrm{gr}_0}^{\pm}}\Big) = u + r\left(\frac{1}{c\sqrt{1-f_1}} - \frac{2 \mp f_2}{2c\sqrt{1-f_1 \pm f_2}}\right) \\
&\approx u + r\left(\frac{1}{c\sqrt{1-f_1}} - \frac{1}{c\sqrt{1-f_1}} - \frac{d}{df_2}\left(\frac{2 \mp f_2}{2c\sqrt{1-f_1 \pm f_2}}\right)\Big|_{f_2=0} f_2\right) \\
&= u \pm r\left(\frac{2-f_1}{2c\,(1-f_1)^{\frac{3}{2}}} f_2\right).
\end{aligned}
$$

From (J.9), we know $1 \gg f_1$, and therefore

$$
t_{\mathrm{gr}}^{\pm} \approx u \pm \frac{r}{c} f_2. \tag{J.15a}
$$

For the retarded phase travel time, we can write:

$$
\begin{aligned}
t_{\mathrm{ph}}^{\pm} \stackrel{\mathrm{def}}{=} t - \frac{r}{v_{\mathrm{ph}_0}^{\pm}} &= u + r\left(\frac{1}{v_{\mathrm{gr}_0}} - \frac{1}{v_{\mathrm{ph}_0}^{\pm}}\right) = u + r\left(\frac{1}{v_{\mathrm{gr}_0}} - \frac{1}{v_{\mathrm{ph}_0}}\right) + r\left(\frac{1}{v_{\mathrm{ph}_0}} - \frac{1}{v_{\mathrm{ph}_0}^{\pm}}\right) \\
&\approx u + r s_0 \mp \frac{r}{2c} f_2,
\end{aligned} \tag{J.15b}
$$

where the dispersive term

$$
s_0 \stackrel{\mathrm{def}}{=} \frac{1}{v_{\mathrm{gr}_0}} - \frac{1}{v_{\mathrm{ph}_0}}
$$

is the same for both polarizations and $v_{\mathrm{ph}_0}^{\pm}$ is defined similarly to $v_{\mathrm{gr}_0}^{\pm}$. Substituting (J.15) into (J.14), we get

$$
\begin{aligned}
\begin{pmatrix} E_x \\ E_y \end{pmatrix}(t,r) &\propto \chi_{\tau'}(u) \sum_{\pm} \begin{pmatrix} 1 \\ \pm i \end{pmatrix} e^{i\alpha'(u^2 \pm 2u\frac{r}{c}f_2)} e^{i\omega_0(u + r s_0 \mp \frac{r}{2c} f_2)} \\
&= \chi_{\tau'}(u) \sum_{\pm} \begin{pmatrix} 1 \\ \pm i \end{pmatrix} e^{i\omega_0(u + r s_0) + i\alpha' u^2} e^{\mp i \varphi_F},
\end{aligned} \tag{J.16}
$$

where

$$
\varphi_F = \frac{\omega_0 r}{2c} f_2 - 2\alpha' u \frac{r}{c} f_2 = \frac{r}{2c}\omega_{\mathrm{pe}}^2 \Omega \left[\frac{1}{\omega_0^2} + 2\alpha' u \cdot \left(\frac{d}{d\omega}\frac{1}{\omega^2}\right)\Big|_{\omega=\omega_0}\right]. \tag{J.17}
$$

Per our definitions of u and s_0, we see that the phase in the first exponent of (J.16) is equivalent

to the one in the isotropic dispersive propagator (J.12):

$$\begin{aligned}\omega_0(u+rs_0)+\alpha' u^2 &= \omega_0\Big[t-\frac{r}{v_{\mathrm{gr}0}}+r\Big(\frac{1}{v_{\mathrm{gr}0}}-\frac{1}{v_{\mathrm{ph}0}}\Big)\Big]+\alpha'\Big(t-\frac{r}{v_{\mathrm{gr}0}}\Big)^2\\ &= \omega_0\Big(t-\frac{r}{v_{\mathrm{ph}0}}\Big)+\alpha'\Big(t-\frac{r}{v_{\mathrm{gr}0}}\Big)^2.\end{aligned}$$

The quantity φ_F in the last exponent of (J.16) is the Faraday rotation angle which is equal to one half of the difference between the phases of the helical harmonics:

$$\begin{pmatrix}E_x\\E_y\end{pmatrix}(t,r)\sim\begin{pmatrix}\cos\varphi_F\\ \sin\varphi_F\end{pmatrix}A'(t-r/v_{\mathrm{gr}0})e^{i\omega_0(t-r/v_{\mathrm{ph}0})}. \tag{J.18}$$

Note that this shows that when the propagation is parallel to the external magnetic field, Faraday rotation occurs clockwise [Dul63]. The expression in the square brackets in (J.17) may be interpreted as the function $f(\omega)=\frac{1}{\omega^2}$ evaluated at the instantaneous frequency $\omega=\omega_0+2\alpha' u$, cf. formula (2.20), by means of a first order Taylor formula. Except for the small difference between α' and α, the expression for the Faraday rotation as a function of the instantaneous frequency in (J.17) coincides with the intuitive formula (3.7) for $r=2R$ and $\beta=0$.

For oblique propagation, i.e., when $|k_z|<|\boldsymbol{k}|$ and $\beta\neq 0$, a careful analysis shows (see [Gin64]) that except in a very narrow range of nearly transverse propagation angles β, viz. $|\cos\beta|\lesssim\frac{|\Omega|}{\omega_0}$, the results obtained for the parallel case (J.7) extend to the oblique case once Ω is replaced by $\Omega\cos\beta$, which, again, transforms (J.17) into (3.7). Thus,

$$\varphi_F(\omega)=\frac{r}{2c}\frac{\omega_{\mathrm{pe}}^2\Omega\cos\beta}{\omega^2} \tag{J.19}$$

is an expression for the Faraday rotation angle of different parts of a linear chirp parameterized by the instantaneous frequency ω.

Appendix K

Faraday rotation and dispersion-compensated matched filter

In this appendix, we show that the effect of dispersive propagation on SAR imaging analyzed in [Tsy09a] and Chapter 2 can be separated from that of the Faraday rotation. Given the form (J.12)–(J.13) of the radar pulse propagating in an isotropic plasma, the matched filter focused at the reference point $\boldsymbol{y}$ and corrected for dispersion (but not the Faraday rotation) should be taken as

$$\begin{aligned}&\overline{A_{\tau'}(t-2R_{\boldsymbol{y}}/v_{\mathrm{gr}_0})e^{i\omega_0(t-2R_{\boldsymbol{y}}/v_{\mathrm{ph}_0})}}\\&=\chi_{\tau'}(t-2R_{\boldsymbol{y}}/v_{\mathrm{gr}_0})e^{-i\alpha'(t-2R_{\boldsymbol{y}}/v_{\mathrm{gr}_0})^2}e^{-i\omega_0(t-2R_{\boldsymbol{y}}/v_{\mathrm{ph}_0})},\end{aligned} \tag{K.1}$$

where the travel distance $2R_{\boldsymbol{y}}$ accounts for the round-trip. Let us also introduce the following "dispersive" quantities that replace those of (A.2), (A.3), and (A.4):

$$\begin{aligned}t_{\boldsymbol{y}}^{n\,\prime}=\frac{2R_{\boldsymbol{y}}^n}{v_{\mathrm{gr}_0}},\quad t_{\boldsymbol{z}}^{n\,\prime}=\frac{2R_{\boldsymbol{z}}^n}{v_{\mathrm{gr}_0}},\quad u'=t-\frac{t_{\boldsymbol{z}}^{n\,\prime}+t_{\boldsymbol{y}}^{n\,\prime}}{2},\\T^{n\,\prime}=\frac{t_{\boldsymbol{y}}^{n\,\prime}-t_{\boldsymbol{z}}^{n\,\prime}}{2},\quad \tau^{n\,\prime}=\tau-2|T^{n\,\prime}|,\quad \omega_0'=\frac{v_{\mathrm{gr}_0}}{v_{\mathrm{ph}_0}}\omega_0.\end{aligned} \tag{K.2}$$

Applying the filter (K.1) to the dispersive propagator (J.12)–(J.13), and using the primed variables of (K.2) and (J.13) instead of their non-primed counterparts, we will arrive at a primed equivalent of (A.1). Then, performing the integration we obtain the same functional expression for the generalized ambiguity function as given by (A.5) in the non-dispersive case:

$$W'(\boldsymbol{y},\boldsymbol{z})=\sum_n e^{2i\omega_0'T^{n\,\prime}}\sum_n\int_{-\tau^{n\,\prime}/2}^{\tau^{n\,\prime}/2}e^{4i\alpha'T^{n\,\prime}u'}du'.$$

Hence, in the case of a dispersive isotropic medium and the filter corrected accordingly, one can drop the primes and use the non-dispersive expressions for the GAF, see (2.30)–(2.31). Factorization (3.1)–(2.35) can also be used, because the reasoning of the rest of Appendix A applies with no changes. There will only be minute numerical discrepancies in the final results (e.g., the resolution) between the dispersive (primed) and non-dispersive (non-primed) case that are due to different values of the parameters in (J.13), (K.2) and in (2.18), (2.19), (A.2), (A.3). Those discrepancies are referred to as the residual image distortions when the matched filter has been fully corrected for the ionosphere ([Tsy09a] and Chapter 2).

Let us now see how the filter corrected for dispersion acts on a linearly polarized chirp that propagates in a medium that is both dispersive and gyrotropic, see Appendix J. From (J.18), we get the following relation between the actual signal $\psi_F(t, \boldsymbol{x})$ and the hypothetical signal $\psi(t, \boldsymbol{x})$ obtained if there were no Faraday rotation:

$$\psi_F(t, \boldsymbol{x}) = \psi(t, \boldsymbol{x}) \cos \varphi_F. \tag{K.3}$$

If the reflected field in (K.3) is due to a scatterer at $\boldsymbol{z}$, then the application of the filter (K.1) yields the following expression instead of (A.1):

$$W_F = \sum_n \int_\chi \overline{A_{\tau'}(t - t_{\boldsymbol{y}}^{n\,\prime}) e^{i\omega_0'(t' - t_{\boldsymbol{y}}^{n\,\prime})}} A_{\tau'}(t - t_{\boldsymbol{z}}^{n\,\prime}) e^{i\omega_0'(t' - t_{\boldsymbol{z}}^{n\,\prime})} \cos \varphi_F(t - t_{\boldsymbol{z}}^{n\,\prime})\, dt, \tag{K.4}$$

where $t' = t v_{\mathrm{ph}_0}/v_{\mathrm{gr}_0}$ and φ_F is given by (J.17) with $r = 2R_{\boldsymbol{z}}$. The terms $\omega_0' t'$ in the exponents in (K.4) cancel out. Apart from those, the difference between (K.4) and (A.1) is two-fold: equation (K.4) involves the primed constants of (J.13) and (K.2), and it also involves the amplitude factor $\cos \varphi_F$ that varies over the chirp. As far as the primed vs. non-primed constants, we have indicated that all the functional dependencies in the GAF remain exactly the same, and there may only be a small numerical difference between the two cases. Therefore, we can drop the primes in (K.4), which yields equation (3.13), and henceforth focus only on the effect of the FR on imaging, which manifests itself through the magnitude variation $\cos \varphi_F$. This is basically equivalent to thinking that the FR goes together with the otherwise undistorted, i.e., non-dispersive, propagation.

Appendix L

Factorization of the SAR ambiguity function in the presence of the Faraday rotation

Our goal here is to perform the analysis similar to that in Appendix A, but taking into account the FR, i.e., evaluate the error due to the factorization (3.15) of the GAF (3.13)-(3.14). In (K.4), we drop the primes and linearize $\cos\varphi_F(u)$ around $u = 0$ [cf. (3.8)]:

$$\cos\varphi_F(u_{\boldsymbol{z}}^n) \approx p + \frac{2q}{\tau} u_{\boldsymbol{z}}^n, \tag{L.1}$$

where p and q are defined in (3.9). This yields the GAF (3.13)-(3.14), which we write as

$$W_F(\boldsymbol{y}, \boldsymbol{z}) = pW(\boldsymbol{y}, \boldsymbol{z}) + q\frac{2}{\tau} W_q(\boldsymbol{y}, \boldsymbol{z}),$$

where $W(\boldsymbol{y}, \boldsymbol{z})$ is given by (A.1), and

$$W_q(\boldsymbol{y}, \boldsymbol{z}) = \sum_n \int_\chi \chi_\tau(t - t_{\boldsymbol{y}}^n) e^{-i\alpha(t-t_{\boldsymbol{y}}^n)^2} e^{-i\omega_0(t-t_{\boldsymbol{y}}^n)} \chi_\tau(t - t_{\boldsymbol{z}}^n) e^{i\alpha(t-t_{\boldsymbol{z}}^n)^2} e^{i\omega_0(t-t_{\boldsymbol{z}}^n)} (t - t_{\boldsymbol{z}}^n)\, dt. \tag{L.2}$$

It is the last factor $(t - t_{\boldsymbol{z}}^n)$ under the integral that distinguishes W_q of (L.2) from W of (A.1). Using the substitutions from (A.2) and (A.3), we transform (L.2) into [cf. (A.5)]

$$W_q = \sum_n e^{2i\omega_0 T^n} \int_{-\tau^n/2}^{\tau^n/2} e^{4i\alpha T^n u} (u + T^n)\, du = W_{q1} + W_{q2}, \tag{L.3}$$

where the terms W_{q1} and W_{q2} originate from u and T^n in the round brackets, respectively.

The term W_{q1} can be evaluated as follows:

$$\begin{aligned} W_{q1} &= \sum_n e^{2i\omega_0 T^n} \int_{-\tau^n/2}^{\tau^n/2} e^{4i\alpha T^n u} u \, du = \sum_n e^{2i\omega_0 T^n} \frac{1}{4iT^n} \frac{\partial}{\partial \alpha} \int_{-\tau^n/2}^{\tau^n/2} e^{4i\alpha T^n u} \, du \\ &= \sum_n e^{2i\omega_0 T^n} \frac{1}{4iT^n} \frac{\partial}{\partial \alpha} \left[\tau^n \operatorname{sinc}(2\alpha \tau^n T^n) \right] = \frac{1}{2i} \sum_n e^{2i\omega_0 T^n} (\tau^n)^2 \operatorname{sinc}'(2\alpha \tau^n T^n), \end{aligned}$$

so that $|W_{q1}| \sim \frac{N\tau^2}{2}$. The second term in (L.3) is estimated similarly to (A.16)–(A.18):

$$\begin{aligned} |W_{q2}| &= \left| \sum_n e^{2i\omega_0 T^n} T^n \int_{-\tau^n/2}^{\tau^n/2} e^{4i\alpha T^n u} \, du \right| = \left| \sum_n e^{2i\omega_0 T^n} T^n \tau^n \operatorname{sinc}(2\alpha \tau^n T^n) \right| \\ &\approx \tau^0 \operatorname{sinc}(2\alpha \tau^0 T^0) \left| \sum_n T^n e^{-2i\omega_0 \mathbb{T}^n} \right| \lesssim \tau^0 N |\max(T^n)| \ll |W_{q1}|, \end{aligned}$$

and we see that it is negligible compared to the first term because $|T^n| \ll \tau$.

Thus, we will compare $W_q \approx W_{q1}$ against the expression [cf. (A.6)]

$$W_{q(\mathrm{RA})}(\boldsymbol{y}, \boldsymbol{z}) \stackrel{\text{def}}{=} W_A(\boldsymbol{y}, \boldsymbol{z}) \cdot W_{qR}(\boldsymbol{y}, \boldsymbol{z}),$$

where $W_A(\boldsymbol{y}, \boldsymbol{z})$ is given by (2.36), and for the factor $W_{qR}(\boldsymbol{y}, \boldsymbol{z})$ we have [cf. (3.17), (3.18)]:

$$W_{qR}(\boldsymbol{y}, \boldsymbol{z}) = \int_\chi \overline{A(u_{\boldsymbol{y}}^0)} u_{\boldsymbol{z}}^0 A(u_{\boldsymbol{z}}^0) \, dt = \frac{(\tau^0)^2}{2i} w_p'(2\alpha \tau^0 T^0) = \frac{(\tau^0)^2}{2i} \operatorname{sinc}'(2\alpha \tau^0 T^0). \tag{L.4}$$

Similarly to (A.9), we write

$$2i(W_q - W_{q(\mathrm{RA})}) = \sum_n e^{2i\omega_0 T^n} [(\tau^n)^2 \operatorname{sinc}'(2\alpha \tau^n T^n) - (\tau^0)^2 \operatorname{sinc}'(2\alpha \tau^0 T^0)].$$

Then, using the Taylor formula to approximate $\operatorname{sinc}'(2\alpha \tau^n T^n)$ [cf. (A.14)]:

$$\operatorname{sinc}'(2\alpha \tau^n T^n) \approx \operatorname{sinc}'(2\alpha \tau^0 T^0) - 2\alpha \tau^0 \mathbb{T}^n \operatorname{sinc}''(2\alpha \tau^0 T^0),$$

we obtain

$$i(W_q - W_{q(\mathrm{RA})}) = e^{i\Phi_0}(-2\tau^0 S_q) \sum_n T^n e^{-2i\omega_0 \mathbb{T}^n} = -2\tau^0 S_q e^{i\Phi_0} \frac{iN}{2\omega_0} Y_1 \operatorname{sinc}' Y_1,$$

where Y_1 is introduced right after equation (A.18), and

$$S_q = \operatorname{sinc}'(2\alpha \tau^0 T^0) + \alpha (\tau^0)^2 \operatorname{sinc}''(2\alpha \tau^0 T^0).$$

The second term in the expression for S_q dominates because $\alpha\tau^2 \gg 1$. Then, the error due to the factorization of W_q can be estimated similarly to (A.19):

$$\frac{|\max(W_q - W_{q(\mathrm{RA})})|}{|\max W_{q(\mathrm{RA})}|} \sim \frac{2}{\omega_0\tau^0} Y_1 S_q \approx \frac{2}{\omega_0\tau^0} Y_1 \frac{B}{2\tau}\tau^2 \sim \frac{B}{\omega_0} \tag{L.5}$$

which is of the same order of magnitude as the error of the factorization of W, see (A.19). Hence, for the overall factorization error in (3.15) we have the same estimate: $\mathcal{O}\big(\frac{B}{\omega_0}\big)$.

Appendix M

Governing equations for scattered fields and the first Born approximation

By subtracting equations (4.4) from respective equations (4.1) and using (4.3), we obtain the following governing equations for the scattered fields:

$$\begin{aligned} &\frac{1}{c}\frac{\partial \boldsymbol{H}^{(\mathrm{sc})}}{\partial t} + \nabla \times \boldsymbol{E}^{(\mathrm{sc})} = \boldsymbol{0}, && \nabla \cdot \boldsymbol{H}^{(\mathrm{sc})} = 0, \\ &\frac{1}{c}\frac{\partial \boldsymbol{E}^{(\mathrm{sc})}}{\partial t} - \nabla \times \boldsymbol{H}^{(\mathrm{sc})} = -\frac{1}{c}\left[(\boldsymbol{\varepsilon} - \mathcal{I}) \cdot \frac{\partial \boldsymbol{E}}{\partial t} + 4\pi \boldsymbol{\sigma} \cdot \boldsymbol{E}\right], && \nabla \cdot \boldsymbol{E}^{(\mathrm{sc})} = -\nabla \cdot (\boldsymbol{D} - \boldsymbol{E}). \end{aligned} \tag{M.1}$$

Note that the scattered field $\boldsymbol{E}^{(\mathrm{sc})}$ appears both on the left-hand side and on the right-hand side of the second pair of equations of (M.1). Differentiating the Ampère law in (M.1) with respect to time, we have:

$$\frac{1}{c}\frac{\partial^2 \boldsymbol{E}^{(\mathrm{sc})}}{\partial t^2} - \frac{\partial}{\partial t}\nabla \times \boldsymbol{H}^{(\mathrm{sc})} = -\frac{1}{c}\left[(\boldsymbol{\varepsilon} - \mathcal{I}) \cdot \frac{\partial^2 \boldsymbol{E}}{\partial t^2} + 4\pi \boldsymbol{\sigma} \cdot \frac{\partial \boldsymbol{E}}{\partial t}\right], \tag{M.2}$$

and taking the curl (i.e., $\nabla\times$) of the Faraday law in (M.1), we obtain:

$$\begin{aligned} &\frac{1}{c}\frac{\partial}{\partial t}\nabla \times \boldsymbol{H}^{(\mathrm{sc})} + \nabla \times \nabla \times \boldsymbol{E}^{(\mathrm{sc})} \\ &\qquad = \frac{1}{c}\frac{\partial}{\partial t}\nabla \times \boldsymbol{H}^{(\mathrm{sc})} - \Delta \boldsymbol{E}^{(\mathrm{sc})} + \nabla\nabla \cdot \boldsymbol{E}^{(\mathrm{sc})} = \boldsymbol{0}. \end{aligned} \tag{M.3}$$

The operation $\nabla\nabla\cdot$ on the right hand side of equation (M.3), see also (M.4) and (M.6), means gradient of the divergence of the corresponding vector. Substituting the time derivative of

$\nabla \times \boldsymbol{H}^{(\mathrm{sc})}$ from equation (M.3) into equation (M.2), and also taking into account the Gauss law of electricity in (M.1), we arrive at

$$\frac{1}{c^2}\frac{\partial^2 \boldsymbol{E}^{(\mathrm{sc})}}{\partial t^2} - \Delta \boldsymbol{E}^{(\mathrm{sc})} = -\frac{\boldsymbol{\varepsilon} - \mathcal{I}}{c^2} \cdot \frac{\partial^2 \boldsymbol{E}}{\partial t^2} - \frac{4\pi \boldsymbol{\sigma}}{c^2} \cdot \frac{\partial \boldsymbol{E}}{\partial t} + \nabla\nabla \cdot (\boldsymbol{D} - \boldsymbol{E}), \tag{M.4}$$

where on the left-hand side we have the standard constant coefficient d'Alembert operator acting on $\boldsymbol{E}^{(\mathrm{sc})}$, and on the right-hand side we have additional occurrences of the scattered field via equations (4.2) and (4.5). Similarly, the incident electric field that provides the the source terms for (M.4) is governed by the d'Alembert equation:

$$\frac{1}{c^2}\frac{\partial^2 \boldsymbol{E}^{(\mathrm{inc})}}{\partial t^2} - \Delta \boldsymbol{E}^{(\mathrm{inc})} = -\frac{4\pi}{c^2}\frac{\partial \boldsymbol{j}^{(\mathrm{ex})}}{\partial t}. \tag{M.5}$$

If the target material is isotropic, i.e., if $\boldsymbol{\varepsilon} = \frac{c^2}{v^2}\mathcal{I}$, where $v = v(\boldsymbol{x})$ is the local propagation speed, and $\boldsymbol{\sigma} = \sigma\mathcal{I}$, then equation (M.4) simplifies, and we have:

$$\frac{1}{c^2}\frac{\partial^2 \boldsymbol{E}^{(\mathrm{sc})}}{\partial t^2} - \Delta \boldsymbol{E}^{(\mathrm{sc})} = \nu(\boldsymbol{x})\frac{\partial^2 \boldsymbol{E}}{\partial t^2} - \frac{4\pi\sigma}{c^2}\frac{\partial \boldsymbol{E}}{\partial t} + \nabla\nabla \cdot \left(\frac{c^2}{v^2} - 1\right)\boldsymbol{E}, \tag{M.6}$$

where the scalar quantity

$$\nu(\boldsymbol{x}) \stackrel{\mathrm{def}}{=} \frac{1}{c^2} - \frac{1}{v(\boldsymbol{x})^2} \tag{M.7}$$

is known as the (target) reflectivity function, see, e.g., [CB09, Chapter 6].

In the context of inverse scattering, equation (M.6) shall be interpreted as an equation for ν and σ, whereas $\boldsymbol{E}^{(\mathrm{sc})}$ provides the data. A key difficulty, however, is that the scattered field is not known at the target. For example, for the SAR applications, $\boldsymbol{E}^{(\mathrm{sc})}$ is known at the receiving antenna, which is airborne or spaceborne, whereas at the target, i.e., on the ground, it is not known. This makes the inverse problem nonlinear, because the unknown material characteristics ν and σ are multiplied on the right-hand side of (M.6) with the unknown scattered field.

A well-known remedy is to assume that the scattering is weak, and employ the first Born approximation, see [BW99, Chapter XIII]. Under this assumption, the total field $\boldsymbol{E}$ on the right-hand side of equation (M.6) is replaced with the incident field $\boldsymbol{E}^{(\mathrm{inc})}$ only, which makes the inverse problem linear. The rationale is that in the case of weak scattering both the deviations of the material parameters from the vacuum values are small, and the scattered field $\boldsymbol{E}^{(\mathrm{sc})}$ is also small, so their products on the right hand side of equation (M.6) can be neglected. Moreover, the last term on the right-hand side of (M.6) drops as well because we first invoke the Gauss law of electricity from system (4.1) in the form $\nabla \cdot \frac{c^2}{v^2}\boldsymbol{E} = 0$ and then the Gauss law of electricity

for the incident field from system (4.4). Altogether this yields:

$$\frac{1}{c^2}\frac{\partial^2 \boldsymbol{E}^{(\mathrm{sc})}}{\partial t^2} - \Delta \boldsymbol{E}^{(\mathrm{sc})} = \nu \frac{\partial^2 \boldsymbol{E}^{(\mathrm{inc})}}{\partial t^2} - \frac{4\pi\sigma}{c^2}\frac{\partial \boldsymbol{E}^{(\mathrm{inc})}}{\partial t}. \tag{M.8}$$

The first Born approximation can also be given another equivalent interpretation based on perturbation theory. In this framework, the zeroth order solution is the incident field governed by equation (M.5), and the equation for the first order perturbation is obtained from equation (M.6) by replacing the total solution on its right-hand side by the zeroth order solution, which yields equation (M.8). Again, considering no more than first order perturbations is justified only if the scattering is weak, i.e., if $|\nu| \ll 1/c^2$ and $\sigma/\omega \ll 1$, where ω is the typical frequency. These two requirements are equivalent to treating the difference between the complex electric permittivity and one as a small parameter; it is used for deriving the first Born approximation for a hierarchy of scattering problems in Section 4.2, see formulae (4.21) and (4.24).

Appendix N

Proof of Theorem 1

Reflection coefficients obtained with the help of the first Born approximation for a lossless birefringent target are given by formulae (4.72). Introducing the new variable $\xi = \varepsilon_\perp - 1$ and denoting $\zeta = \Delta\varepsilon$, we rewrite these formulae as follows:

$$
\begin{aligned}
S_{\mathrm{HH}} &= -\frac{1}{4}\frac{k^2}{q^2}(\xi + \beta^2\zeta),\\
S_{\mathrm{VV}} &= \frac{1}{4}\Big((\xi + \alpha^2\zeta) - \frac{K^2}{q^2}(\xi + \gamma^2\zeta)\Big),\\
S_{\mathrm{HV}} &= -\frac{1}{4}\frac{k}{q}\Big(\alpha - \frac{K}{q}\gamma\Big)\zeta\beta,\\
S_{\mathrm{VH}} &= \frac{1}{4}\frac{k}{q}\Big(\alpha + \frac{K}{q}\gamma\Big)\zeta\beta.
\end{aligned}
\tag{N.1}
$$

These expressions can also be obtained by linearization of the exact reflection coefficients given in [Che83]; for a special case of $\gamma = 0$, formulae (N.1) can be obtained by linearization of the results of [Lek91] as well.

Formulae (N.1) define four functions of the arguments ξ, ζ, α, and γ (with β expressed via (4.48)). Therefore, we can introduce the Jacobian:

$$
\left|\frac{\partial(S_{\mathrm{HH}}, S_{\mathrm{VV}}, S_{\mathrm{HV}}, S_{\mathrm{VH}})}{\partial(\xi, \zeta, \alpha, \gamma)}\right| = \left|\frac{Kk^4(K^2(\alpha^2 - 1) - q^2(\gamma^2 - 1))\zeta^2}{128q^7}\right|. \tag{N.2}
$$

One can see that the right-hand side of (N.2) is nonzero at least for some values of the arguments. Indeed, if $\zeta \neq 0$ (i.e., if the material is anisotropic), then we can choose independent directional cosines α and γ so that the numerator on the right-hand side of (N.2) is nonzero.

Thus, in the vicinity of such points in the parameter space, the transformation from $(\xi, \zeta, \alpha, \gamma)$ to $(S_{\mathrm{HH}}, S_{\mathrm{VV}}, S_{\mathrm{HV}}, S_{\mathrm{VH}})$ is locally non-degenerate, and preserves the number of degrees of freedom. This local non-degeneracy, however, does not guarantee that system (N.1) can be resolved for $(\xi, \zeta, \alpha, \gamma)$ given arbitrary scattering data (i.e., the left-hand side of system (N.1)).

To find out when system (N.1) has a solution, we denote $Z = K/q = \tan\theta_i$, and transform the last two equations of the system to:

$$S^+ = \gamma\zeta\beta, \quad S^- = \alpha\zeta\beta, \tag{N.3}$$

where

$$S^+ = \frac{2}{Z\sqrt{1+Z^2}}(S_{\mathrm{VH}} + S_{\mathrm{HV}}) \quad \text{and} \quad S^- = \frac{2}{\sqrt{1+Z^2}}(S_{\mathrm{VH}} - S_{\mathrm{HV}}).$$

Next, we introduce

$$D = \frac{S^-}{S^+} = \frac{\alpha}{\gamma}, \tag{N.4}$$

which, together with (4.48), yields:

$$\beta^2 = 1 - \gamma^2(1 + D^2). \tag{N.5}$$

We can eliminate ξ from the first two equations of (N.1) to get

$$\tilde{S} = \zeta W, \tag{N.6}$$

where

$$\begin{aligned} \tilde{S} &= 4\Big(S_{\mathrm{VV}} + S_{\mathrm{HH}}\frac{1-Z^2}{1+Z^2}\Big), \\ W &= (Z^2 - 1) + \gamma^2\Big(D^2 - Z^2 + (1-Z^2)(1+D^2)\Big). \end{aligned} \tag{N.7}$$

Using equations (N.5), (N.6), and the second equation of (N.3), we arrive at

$$P^2\gamma^2 D^2\big(1 - \gamma^2(1+D^2)\big) = W^2, \tag{N.8}$$

where $P = \tilde{S}/S^-$. As W in formula (N.7) is linear w.r.t. γ^2, equation (N.8) is biquadratic w.r.t. γ. A solution for γ^2 exists if and only if the corresponding discriminant is nonnegative, which can be shown to be equivalent to

$$P^2 \geqslant 4\frac{(D^2 - Z^2)(Z^2 - 1)}{D^2}. \tag{N.9}$$

Condition (N.9) can be transformed into (4.77) using equations (N.3), (N.7), and (N.8).

It should also be noted that whereas the right-hand side of (N.8) is always nonnegative, the

left-hand is nonnegative only if

$$0 \leqslant \gamma^2 \leqslant \frac{1}{1+D^2}. \tag{N.10}$$

This means that if condition (N.9) for the existence of a solution to (N.8) with respect to γ^2 is satisfied, then this solution, i.e., γ^2, satisfies (N.10). If (N.9) has two solutions, then both should satisfy (N.10). The second inequality in (N.10), together with equations (N.4) and (N.5), also ensures that $0 \leqslant \alpha^2 \leqslant 1$ and $0 \leqslant \beta^2 \leqslant 1$ (see (4.48)).

If condition (N.9) (or its equivalent (4.77)) is satisfied, then γ^2 can be found by solving (N.8), and the sign of γ can be chosen arbitrarily because the system (N.1) is invariant w.r.t. the transformation $(\alpha, \beta, \gamma) \longrightarrow (-\alpha, -\beta, -\gamma)$. Then, the value of α is obtained from (N.4), ζ from (N.6), β from any of the equations (N.3), and ξ from the first equation of system (N.1). With that, all the material parameters are determined, which completes the proof of Theorem 1.

Appendix O

Numerical study of the exact formulation for the problem of scattering off an interface of a half-space

Theorem 1 indicates that the linearized inverse problem has a solution only for certain combinations of the reflection coefficients S_{HH}, S_{VV}, S_{HV}, S_{VH}, and the incidence angle θ_i. For example, if $\alpha = 0$ then $S_{\mathrm{HV}} = S_{\mathrm{VH}}$, see formulae (N.1), and the right-hand side of inequality (4.77) is negative provided that $\theta_i > \pi/4$. Hence, inequality (4.77) holds automatically, and the linearized inverse problem always has a solution for $\theta_i > \pi/4$. On the other hand, for $\theta_i < \pi/4$ inequality (4.77) puts an additional constraint on the values of the reflection coefficients and thus implies a limitation of solvability of the linearized inverse problem.

While inequality (4.77) may be given a physical interpretation later on, currently we would like to try and answer the question of whether the foregoing limitation of solvability (Theorem 1) is due to the type of the target material that we have chosen (a birefringent dielectric with weak anisotropic conductivity) or to the linearization itself. Expressions for the exact (i.e., not linearized) reflection coefficients can be found, e.g., in [Che83, equation (6.61)]. However, that system [unlike the linearized system (N.1)] has proven too complicated for analytical inversion. Instead, we employ a numerical approach. First, we sample the domain of feasible material parameters (typically, $\varepsilon_{\|}$ and $\varepsilon_{\perp}$ are taken between 1 and 5) with a sufficiently high rate, and calculate the exact reflection coefficients for every sample, i.e., solve the direct problem exactly with the help of [Che83]. In doing so, we obtain a cloud of points in the three-dimensional space of coefficients S_{HH}, S_{VV}, and $S_{\mathrm{HV}} = S_{\mathrm{VH}}$. Areas of no solution would correspond to the regions

with no points inside the cloud, i.e., to the voids. To see whether or not there are any voids we plot several cross-sections of the cloud normal to the S_{VH} axis. As, however, the cloud consists of discrete points, we rather take slices of finite thickness in S_{VH} and collapse all the points inside each slice onto the $(S_{\mathrm{HH}}, S_{\mathrm{VV}})$ plane for plotting.

The visualization we have described reveals distinct voids in the cloud of the results for the exact formulation of the direct scattering problem. Those voids can, in particular, be clearly seen in Figure O.1, where we are showing the values of $\varepsilon_{\|}$ as they depend on S_{HH}, S_{VV}, and S_{VH}. Inside the voids the solution to the original (i.e., not linearized) inverse problem does not exist, because the corresponding values of the reflection coefficients cannot be obtained using any choice of the material parameters.

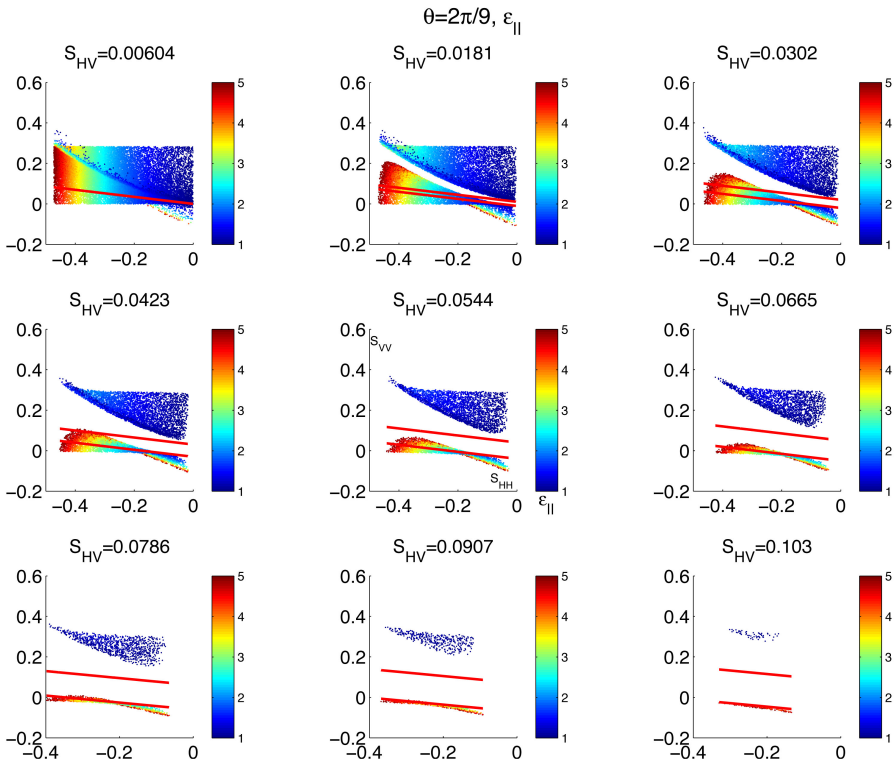

Figure O.1: $\varepsilon_{\|}$ as a function of the exact reflection coefficients for $\alpha = 0$ and $\theta_i = 2\pi/9$. The value of $\varepsilon_{\|}$ is indicated by color. The horizontal axis is S_{HH} and the vertical axis is S_{VV}, as indicated in the middle plot. The approximate ranges for the cloud of the results are $-0.5 \leqslant S_{\mathrm{HH}} \leqslant 0$, $-0.2 \leqslant S_{\mathrm{VV}} \leqslant 0.6$, and $0 \leqslant |S_{\mathrm{VH}}| \leqslant 0.11$. The gap between two red lines corresponds to the region for which inequality (4.77) does not hold, i.e., for which the linearized inverse problem has no solution.

Moreover, as $\theta_i = 2\pi/9 \leqslant \pi/4$ in Figure O.1, the linearized problem may have no solution according to Theorem 1. The region where the linearized solution does not exist [see inequality (4.77)] is bounded by two straight red lines on each of the plots in Figure O.1. We see that when the scattering is weak, i.e., when all the reflection coefficients S_{HH}, S_{VV}, and S_{VH} are small, those red lines appear tangential to the apparent boundaries of a given void that corresponds to the exact formulation. This is precisely the behavior that would be natural to expect in the case when both the linearized and the original inverse problem have regions with no solution. This tangential behavior can be observed more clearly in Figure O.2, which is a zoom-in of the middle plot in the top row of Figure O.1.

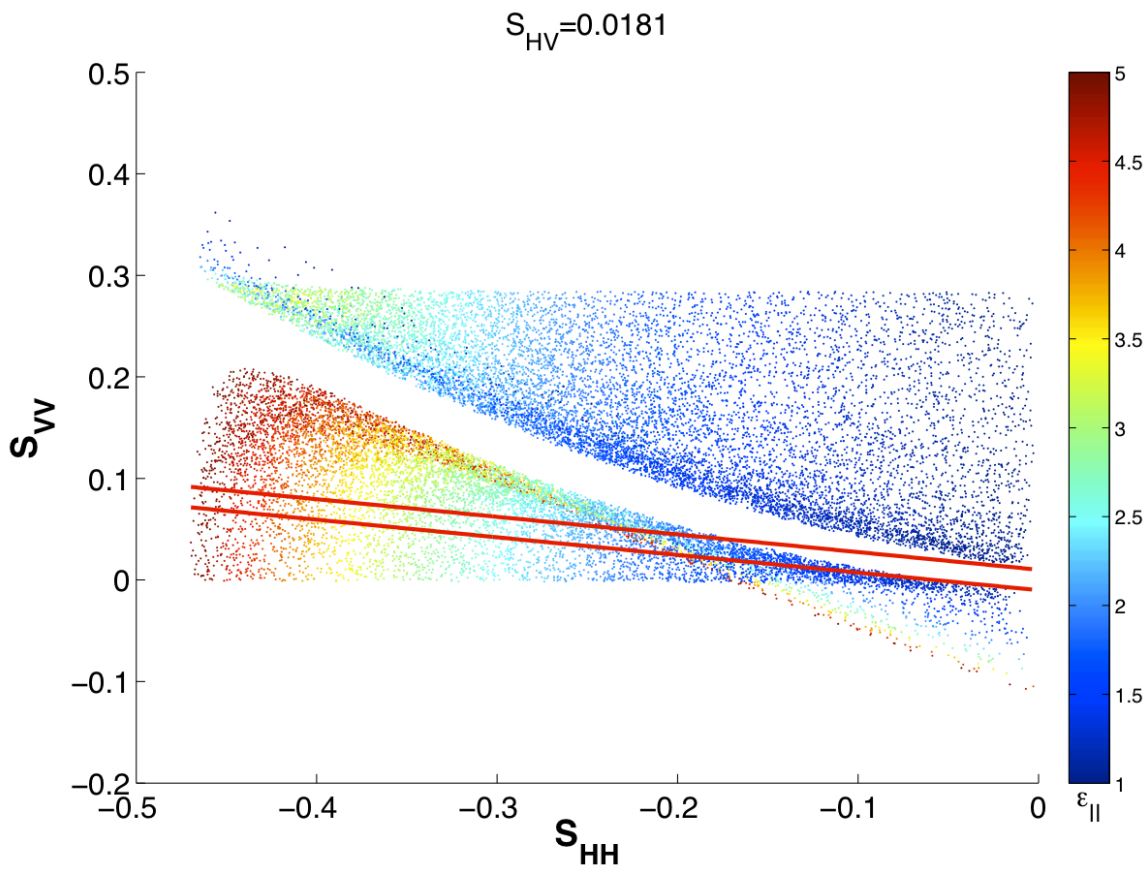

Figure O.2: Zoom-in of the middle plot in the top row of Figure O.1.

Let us also note that whereas for larger values of the incidence angle, $\theta_i > \pi/4$, the linearized inverse problem has a solution, the original, i.e., not linearized, inverse problem may still have no

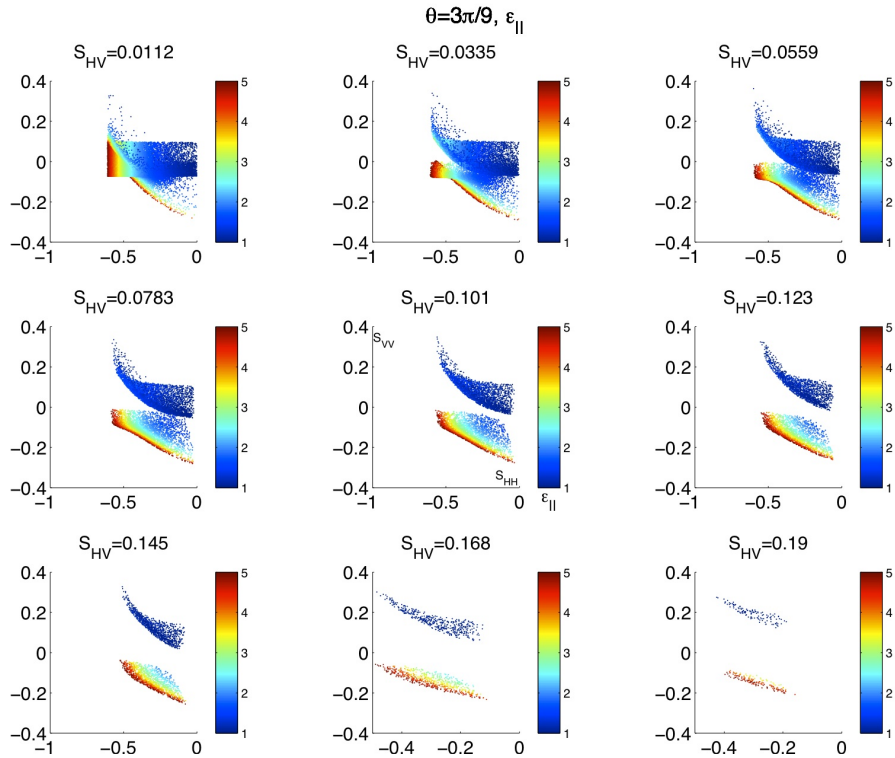

Figure O.3: $\varepsilon_{\|}$ as a function of the exact reflection coefficients for $\alpha = 0$ and $\theta_i = \pi/3$. The value of $\varepsilon_{\|}$ is indicated by color. The horizontal axis is S_{HH} and the vertical axis is S_{VV}, as indicated in the middle plot. The approximate ranges for the cloud of the results are $-1 \leqslant S_{\mathrm{HH}} \leqslant 0$, $-0.4 \leqslant S_{\mathrm{VV}} \leqslant 0.4$, and $0 \leqslant |S_{\mathrm{VH}}| \leqslant 0.2$.

solutions. We illustrate that in Figure O.3, which is similar to Figure O.1 in every respect except that $\theta_i = \pi/3$ and the computed ranges for S_{HH}, S_{VV}, and S_{VH} appear somewhat different. From Figure O.3 it is apparent that when all three coefficients S_{HH}, S_{VV}, and S_{VH} are small, which is basically equivalent to the linear regime (weak scattering), there are no voids in the cloud of the results and the solution exists, as expected. As, however, the scattering becomes stronger so that S_{VH} increases, a void appears again indicating a limitation of solvability.[1]

Altogether, our rigorous analysis of the first Born approximation along with the simulations conducted for the unabridged formulation indicate that for the weak scattering regime when the two formulations are supposed to be close, the linear and nonlinear problems indeed have or do not have a solution simultaneously. In particular, the full nonlinear problem will have no solution for the same combinations of parameters for which the linearized problem has no solution. This means that the linearization is apparently not the reason for the loss of solvability, and that the

[1]The voids we discuss here provide additional constraints, beyond the general limitations on the solvability of the inverse problem that come, e.g., from the conservation of energy.

result of Theorem 1 should most likely be attributed to the properties of the target material that we have taken for our analysis rather than "blamed" on the first Born approximation.

Appendix P

Instruction manual for Matlab code used in Chapter 4 and Appendix O

This purpose of this appendix is to allow the reader to reproduce the results given in Figures 4.2, O.1, O.2, and O.3. We give a description of how to use the Matlab programs used to generate the figures and describe what these programs were designed to do in general. While the main focus is on the plots in Appendix O due to their complexity, other smaller programs used during the development are covered, as well. It is presented in an outline format to make it easier to find specific information than if this was written as paragraphs or even as comments in the code.

1. **What you need to get started:** To generate the plots seen in Appendix O, you need the following:
   (a) Matlab
   (b) Files:
      i. scatterer4.m
      ii. ourlin.m
      iii. ourlinn.m
      iv. refcoef.m
      v. refcoefn.m
      vi. lin.m (not used in the appendix, but does generate Figure 4.2 — see 7h)
2. **Useful terminology**
   (a) Optical Axis: This is the axis that the optical properties of the uniaxial material are symmetric around. A unit vector along this axis is represented by (α, β, γ).

(b) θ_i: the incidence angle (in radians).

(c) $\varepsilon_\perp$: the perpendicular permittivity (associated with the ordinary wave).

(d) $\varepsilon_\parallel$: the parallel permittivity (associated with the extraordinary wave).

(e) k: the wave number.

(f) $S_{\mathrm{HH}}, S_{\mathrm{HV}}, S_{\mathrm{VH}}, S_{\mathrm{VV}}$: the four elements of the scattering matrix. In the subscript the first letter stands for the polarization of the transmitted wave, and the second stands for the polarization of the received wave (This is different than the notation used in Chapter 4). It should be noted that in the code G is used instead of S.

3. **Purpose of the functions**

(a) ourlin.m

i. Compute the four reflection coefficients off a uniaxial crystal within a linearized framework.

ii. Assumption: $\beta \geq 0$.

(b) ourlinn.m

i. Compute the four reflection coefficients off a uniaxial crystal within a linearized framework.

ii. Assumption: $\beta \leq 0$.

(c) refcoef.m

i. Compute the four reflection coefficients off a uniaxial crystal using the general formulas as seen in [Che83].

ii. Assumption: $\beta \geq 0$.

(d) refcoefn.m

i. Compute the four reflection coefficients off a uniaxial crystal using the general formulas as seen in [Che83].

ii. Assumption: $\beta \leq 0$.

(e) scatterer4.m

i. Assuming $\alpha = 0$, plot the scattering coefficients generated by the other functions for a specified range of values of $\varepsilon_\perp$, $\varepsilon_\parallel$, and γ.

ii. Optionally, plot the asymptotes seen when the cross-polarized scattering coefficient is zero, projecting it along all of the values of that coefficient for comparative purposes.

iii. Optionally, plot the diagonal swath of points where the parallel permittivity is low when the cross-polarized coefficient is zero.

iv. Save certain predetermined figures as eps files. This will be elaborated upon when discussing the example used in Appendix O.

4. **Function syntax:** Using Matlab's syntax of [output]=functionname(input), the I/O parameters are as follows, in the order that they are given.

   (a) ourlin and ourlinn

      i. Input

         A. θ_i

         B. $\varepsilon_\perp$

         C. $\varepsilon_\parallel$

         D. α

         E. γ

         F. k

      ii. Output

         A. S_{HH}

         B. S_{HV}

         C. S_{VH}

         D. S_{VV}

   (b) refcoef and refcoefn

      i. Input: The input to these functions is in the form of two structures. The first is called material while the second is called wave. While the variables used for the individual elements inside the structures can be arbitrary, it is important that each field be verbatim what is given here (typed in Matlab inside single quotes).

         A. material

            - 'pe': this represents $\varepsilon_\perp$.
            - 'pa': this represents $\varepsilon_\parallel$.
            - 'alpha': this represents α.
            - 'gamma': this represents γ.

         B. wave

            - 'k': this represents k, the value of which is arbitrary.
            - 'theta': this represents θ_i.

      ii. Output

         A. S_{HH}

         B. S_{HV}

C. S_{VH}

D. S_{VV}

(c) scatterer4

i. Input

A. $\left[\varepsilon_{\perp}^{\min}\ \varepsilon_{\perp}^{\max}\right]$

- $\varepsilon_{\perp}^{\min}$ is the minimum value of $\varepsilon_{\perp}$ to be used, usually 1.
- $\varepsilon_{\perp}^{\max}$ is the maximum value of $\varepsilon_{\perp}$ to be used.

B. $\left[\varepsilon_{\parallel}^{\min}\ \varepsilon_{\parallel}^{\max}\right]$

- $\varepsilon_{\parallel}^{\min}$ is the minimum value of $\varepsilon_{\parallel}$ to be used, usually 1.
- $\varepsilon_{\parallel}^{\max}$ is the maximum value of $\varepsilon_{\parallel}$ to be used.

C. $\left[\gamma^{\min}, \gamma^{\max}\right]$

- $\gamma^{\min}$ is the minimum value of γ to be used.
- $\gamma^{\max}$ is the maximum value of γ to be used.
- $[-1, 1]$ is the maximum range this parameter can be set at for it to make physical sense.

D. p: this can be one of three things:

- 'pe' means that the color in the plots will vary over $\varepsilon_{\perp}$.
- 'pa' means that the color in the plots will vary over $\varepsilon_{\parallel}$.
- 'norm' means that the color in the plots will vary over $\sqrt{\varepsilon_{\perp}\varepsilon_{\parallel}}$.

E. func: this can be one of two things:

- @ourlin means that the scattering coefficients in the linearized framework will be computed and plotted.
- @refcoef means that the scattering coefficients according to [Che83] will be computed and plotted.

ii. Output

A. N/A since the only outputs are plots.

B. The function will generate a certain number of figures, specifically $2\left\lfloor \frac{d}{2} \right\rfloor$, where d is defined in the code.

C. Half of these figures will contain nine subplots whereas the other half will only contain one plot. For each angle the entire range of S_{HV} is represented in the nine subplots.

iii. Example used in Appendix O

- To get the results seen in Figures O.1, O.2, and O.3, the following command should be typed in the command line:

- scatterer4([1 5],[1 5],[-1,1],'pa',@refcoef)
- Note that this generates five additional plots that were not used in Appendix O.

5. **Options within the code:** There are several options within the scatterer4 code that must be manually turned on and off by adding and removing the % symbols. Most of these are easily identifiable in the code from the lines of code that are commented out (as opposed to actual comments).

   (a) The variable *sorp* can be changed to whatever letter represents the scattering matrix. The default is S.

   (b) d determines the incidence angle(s) that the function will look at when plotting. It is best to let d be an odd number.

      i. Angles plotted will be $\frac{n\pi}{d}$, where $n = 1, 2, 3, \ldots \left\lfloor \frac{d}{2} \right\rfloor$.

      ii. For Appendix O, $d = 9$.

   (c) The wave number can be completely arbitrary. The default is 3.

   (d) Given the minimum and maximum values of the permittivities, $100,000$ different permittivities are chosen within this range. They can either be evenly spaced or logarithmically spaced. The latter is the default.

   (e) The points that are generated are symmetric with respect to $S_{\mathrm{HV}} = S_{\mathrm{VH}}$. The default is to disregard the points with negative cross-polarization amplitudes when plotting. Thus it is the default to only be concerned with one of the extrema: the maximum. However, if the negative points are also accounted for, the code can keep track of the minimum and use it when needed.

   (f) There was a strange glitch for the example in Appendix O when saving figures to eps files. Thus several dimensions of figure windows were tested. The default setting produces the best results, but the other dimensions are left in the code as options.

   (g) The default for the actual plotting part of the code is to plot the points generated by the other functions and two thick red lines representing the boundaries of the area of nonexistence in the linearized framework. This can be used to compare the linearized framework to that of the general formulas. There are two additional things that can be plotted:

      i. A thick blue dashed line can be used to represent the main asymptotes seen in the plots. These lines produce a "box" that contains almost all of the points when $S_{\mathrm{HV}} = 0$. It is visible in all plots for comparison on how those points relate to those at the "base."

ii. A thick yellow dashed curve represents what initially appeared to be anomalous behavior of some points with low values of $\varepsilon_{\|}$. This was used to corroborate some analysis and thus is turned off by default. Like the previous "box", it is projected onto all subplots for comparison purposes.

(h) In order to avoid clutter, in the figures that contain nine subplots only the middle subplot is properly labeled. Late in the development of the code it was decided that the axis labels looked nicer as text boxes than by using Matlab's *xlabel* and *ylabel* commands. If those commands are desired, however, the option is still there.

i. The default positions for these text boxes are specified to the example used in the paper. Another option is to have them appear at the axis extrema.

(i) There are a few different options for the amount of information given in the figure titles. The default is minimal information.

(j) In the figures with one plot, the *xlabel* and *ylabel* commands work the best. If consistency is desired, however, the option to use text boxes remains.

6. **The example used in Appendix O:** Many of the default settings in the code are specifically set for the example used in Appendix O. As described at the end of the section on function syntax, this example considered permittivity values from one to five with the full range of gamma. It also uses the color axis to measure $\varepsilon_{\|}$ and uses the general formulas for the computation. Again, to run the code

$$scatterer4([15],[15],[-1,1],'pa',@refcoef);$$

must be typed in the command line. The function will not produce any output variables, but it will display eight figure windows. In addition to this, the third, fourth, and fifth figure windows will be saved as eps files named paggap9c.eps, paggap1c.eps, and pagno9c.eps, respectively. If run correctly, the figures that are saved should look like Figure O.1, Figure O.2, and Figure O.3 As noted in Appendix O, Figure O.2 (Figure 4 of Matlab's output) is the top middle subplot of Figure O.1 (Figure 3 of Matlab's output).

Although the code can easily be used for other applications without many changes, it should be noted, as described above, that some changes will have to be made for different applications. The computations will all still be done correctly, but the output will not work out as nice.

7. **Other functions:** In order to ensure that the coded versions of the scattering coefficient formulas (both linearized and general) were correct, several other programs were created to test various aspects of them. These will be listed here.

(a) fresnel.m

i. Input: a known permittivity [optional]. If no input is given, the default is set at 1.7

ii. Output: a figure with a plot showing the Fresnel curves for that permittivity. The Fresnel curves are S_{HH} and S_{VV} plotted with respect to the incidence angle (in degrees). The Brewster angle is also computed and represented on the graph as well as given numerically.

(b) basal.m

i. Input: The inputs are in the form of structures again.

- material
  - 'pe': this represents $\varepsilon_{\perp}$.
  - 'pa': this represents $\varepsilon_{\parallel}$.
  - 'alpha': this represents α. IT MUST BE 0.
  - 'gamma': this represents γ. IT MUST BE 1.
- wave
  - 'k': this represents k, the value of which is arbitrary.
  - 'theta': this represents θ_i.
- variable: 'pe', 'pa', or 'theta': this is the variable that will serve as the x-axis in the plot output. Note that the value given in the material structure for the variable chosen here will be ignored.

ii. Output:

- S_{HH}
- S_{HV} (should always be zero)
- S_{VH} (should always be zero)
- S_{VV}
- r_{ss}: the reflection coefficient of the same name given in (51) of [Lek91]
- r_{pp} the reflection coefficient of the same name given in (51) of [Lek91]

iii. This function generates a plot in a figure comparing the reflection coefficients off a basal plane given by the code based on [Che83] and those found in [Lek91]. The code for them is given in rppcheck.m.

iv. It should be noted that [Lek91] uses a different convention for the direction of the z-axis than [Che83], and this difference is accounted for in the plot.

(c) par.m

i. Input: same as basal.m except a new fourth option for the variable is 'alpha'. Also, the only requirement for the value of the material parameters is that now γ MUST BE 0.

ii. Output:

- S_{HH}
- S_{HV}
- S_{VH}
- S_{VV}
- r_{ss}: see Section 5.2 in [Lek91] for this and the following three
- r_{sp}
- r_{ps}
- r_{pp}

iii. This function does the same thing as basal.m except for the special case where the reflecting plane is parallel to the optic axis. It uses the file Lekpar.m for the formulas given by [Lek91].

iv. Due to the different convention used in [Lek91], two of the reflection coefficients had to be slightly modified to match the results from [Che83]. This affects the figure and not the actual computation.

(d) rppcheck.m (used in basal.m)

i. Input:

- θ_i
- $\varepsilon_\perp$
- $\varepsilon_\parallel$
- k

ii. Output:

- r_{ss}
- r_{pp}

iii. Calculates the reflection coefficients for a basal plane as given in [Lek91], using the notation of that paper.

(e) Lekpar.m (used in par.m)

i. Input:

- θ_i
- $\varepsilon_\perp$
- $\varepsilon_\parallel$

- α
- k

ii. Output:

- r_{ss}
- r_{sp}
- r_{ps}
- r_{pp}

iii. Calculates the reflection coefficients for when the reflecting plane is parallel to the optic axis as given in [Lek91], using the notation of that paper.

(f) gen.m

i. Input: same as par.m except for a new fifth option for the variable 'gamma'. There are no requirements for the values of the material parameters this time.

ii. Output: same as par.m except that the values of the reflection coefficients as given by [Lek91] come from Section 4 of that paper.

iii. This function was designed as a generalization of basal.m and par.m, making them obsolete. It uses Lekgen.m to compute the reflection coefficients given by [Lek91] in the most general case. With the right input (i.e. the requirements given for the above programs), gen.m will duplicate their results.

iv. This code was used to test the code for the formulas based off of [Che83] for another special case mentioned in [Lek91]: when the optic axis is in the plane of incidence. This is the special case when $\beta = 0$.

(g) Lekgen.m (used in gen.m)

i. Input:

- θ_i
- $\varepsilon_\perp$
- $\varepsilon_\parallel$
- α
- γ
- k

ii. Output: same as Lekpar.m

iii. Calculates the reflection coefficients for any arbitrary geometrical relationship between the incoming wave and crystal as given in [Lek91], using that paper's notation.

(h) lin.m: the function used to generate Figure 4.2

i. Input: same as gen.m except for new sixth and seventh options, 'pp', and '3', and the value of theta must be in single quotes. Also, a third element of the wave sctructure, thetap, is used. Its value is the LaTeXversion of theta. For example, if theta is 'pi/9', then thetap needs to be '\pi/9'.

ii. Output

- S_{HH}
- S_{HV}
- S_{VH}
- S_{VV}
- S^l_{HH}
- S^l_{HV}
- S^l_{VH}
- S^l_{VV}

iii. Similarly to gen.m, this function computes the reflection coefficients as given by [Che83] over a range of values for the desired variable, where all the other input parameters are fixed. It then plots the results. However, instead of comparing the results to [Lek91], this uses the aforementioned ourlin.m to compute the reflection coefficients given by the linearized framework. These results are then plotted on the same axes as the reflection coefficients given by [Che83] so that the general and linearized reflection coefficients can be compared and contrasted.

iv. Note: If 'pp' is the input variable, the program will assume the value entered for $\varepsilon_\perp$ is the only permittivity, making the medium isotropic. Because they are zero, it will not plot the cross-polarized terms.

v. Note: If '3' is the input variable, the program will generate a plot that combines elements from the 'pe', 'pa', and 'pp' options. This is really more for plotting purposes, and the numerical output will be the same as that for the 'pa' option.

vi. To get the results seen in Figure 4.2, the actual command is (all typed in one line)

$[Ghh, Ghv, Gvh, Gvv, Ghhl, Ghvl, Gvhl, Gvvl] =$
lin(struct('pe',1.05,'pa',1.05','alpha',.75,'gamma',0),
struct('k',3,'theta','pi/9','thetap','\pi/9'),'3');

(i) Ghvmax.m is a short function for analyzing the differences for the $\alpha = 0$ case of $S^{\max}_{\mathrm{HV}}$ for different values of θ_i.

Appendix Q

Matlab code used in Chapter 4 and Appendix O

Q.1 Appendix O code: scatterer4.m

Here is the main function used to generate the plots in Appendix O, scatterer4.m:

```
function scatterer4(pemm,pamm,gammamm,p,func)
%scatterer4([epsilonperpmin epsilonperpmax],[epsilonparallelmin
%epsilonparallel max],[gammamin gammamax],'pe', 'pa', or 'norm',@ourlin
%or @refcoef)

%It calls the external functions @ourlin, @ourlinn, @refcoef, and
%@refcoefn.

sorp='S';
%sorp='\Gamma'; %also sometimes used in the literature
alpha=0;
%theta=pi/7;  %If just one plot is needed, this is a good example.
d=9;
for ia=1:floor(d/2)
%The last number should be the last whole number such
    %that ia/d<1/2.

    theta=ia*pi/d;
    K=3;  %This isn't ksin(theta) but just regular k.
    %pe=pemm(1):range(pemm)/(10^5-1):pemm(2);
    %pa=pamm(1):range(pamm)/(10^5-1):pamm(2);
    pe=logspace(log10(pemm(1)),log10(pemm(2)),10^5); %generates better
```

```
%spaced dots

pa=logspace(log10(pamm(1)),log10(pamm(2)),10^5);
gamma=gammamm(1):range(gammamm)/(10^5-1):gammamm(2);
%The next two lines randomize the input (sort of).
rng(374);  %seeds the random number generator
pa=pa(randperm(length(pa)));
rng(583);  %different seed just for the fun of it
gamma=gamma(randperm(length(gamma)));


Ghh=zeros(2*length(pe),1); Ghv=Ghh; Gvh=Ghh; Gvv=Ghh;



if isequal(func,@ourlin)==1
    for i=1:length(pe)
        [Ghh(i),Ghv(i),Gvh(i),Gvv(i)]=func(theta,pe(i),pa(i),...
            alpha,gamma(i),K);
        [Ghh(i+length(pe)),Ghv(i+length(pe)),Gvh(i+length(pe)),...
            Gvv(i+length(pe))]=ourlinn(theta,pe(i),pa(i),alpha,...
            gamma(i),K);

    end
else
    for i=1:length(pe)
        [Ghh(i),Ghv(i),Gvh(i),Gvv(i)]=func(struct('pe',pe(i),...
            'pa',pa(i),'alpha',alpha,'gamma',gamma(i)),...
            struct('k',K,'theta',theta));
        [Ghh(i+length(pe)),Ghv(i+length(pe)),Gvh(i+length(pe)),...
            Gvv(i+length(pe))]=refcoefn(struct('pe',pe(i),'pa',...
            pa(i),'alpha',alpha,'gamma',gamma(i)),...
            struct('k',K,'theta',theta));
    end
end
%The next two lines are needed for both signs of beta.
pe=[pe pe];
pa=[pa pa];

%hmin=min(Ghv);  Needed if using whole range of Ghv
hmax=max(Ghv);
```

```
%figure('OuterPosition',[680 431 955 718])
%figure('OuterPosition',[680 399 694 750])
figure('OuterPosition',[680 396 922 753])
for k=1:9 %Each k corresponds to a subplot.
    clear bounddown boundup bottom top left right xtreme ytreme

    j=find(Ghv>(k-1)*hmax/9 & Ghv<=k*hmax/9);
    %j=find(Ghv>hmin+(k-1)*(hmax-hmin)/9 & Ghv<=hmin+k*...
    %(hmax-hmin)/9);

    Ghhs=Ghh(j); Gvvs=Gvv(j);
    Gh=min(Ghhs):.001:max(Ghhs);
    Gv=min(Gvvs):.001:max(Gvvs);

    GHV=(k-1)*hmax/9;
    %GHV=hmin+(k-1)*(hmax-hmin)/9;
    %if GHV<0
    %    GHV=hmin+k*(hmax-hmin)/9;
    %end

    sbp(k)=subplot(3,3,k);

    for i=1:length(Gh)
        bounddown(i)=-sqrt(4*cos(2*theta)*GHV^2)-cos(2*theta)*Gh(i);
        boundup(i)=sqrt(4*cos(2*theta)*GHV^2)-cos(2*theta)*Gh(i);
    %    bottom(i)=0;
    %    top(i)=(pemm(2)*cos(theta)-sqrt(pemm(2)-sin(theta)^2))/...
    %       (pemm(2)*cos(theta)+sqrt(pemm(2)-sin(theta)^2));
    end

    %for i=1:length(Gv)
    %    left(i)=(cos(theta)-sqrt(pamm(2)-sin(theta)^2))/...
    %       (cos(theta)+sqrt(pamm(2)-sin(theta)^2));
    %    right(i)=0;
    %end

    %for i=1:length(pe)
    %    xtreme(i)=(cos(theta)-sqrt(pe(i)-sin(theta)^2))/...
    %       (cos(theta)+sqrt(pe(i)-sin(theta)^2));
    %    ytreme(i)=(pe(i)-sqrt(pe(i)))/(pe(i)+sqrt(pe(i)));
```

```
%end

if isequal(p,'pe')
    callScatterc(Ghhs,Gvvs,pe(j));
    pp=', \epsilon_\perp ';
elseif isequal(p,'pa')
    callScatterc(Ghhs, Gvvs, pa(j));
    pp=', \epsilon_{||} ';
elseif isequal(p,'norm')
    callScatterc(Ghhs, Gvvs, sqrt(pe(j).*pa(j)));
    pp=', norm,';
end
hold on
%I think the last condition is all that is needed, but I want to
%be thorough just in case.
if isreal(bounddown)==1 && isreal(boundup)==1  && ia/d<1/4
    plot(Gh,bounddown,'r',Gh,boundup,'r','LineWidth',2)
end
%plot(Gh,bottom,'b--',Gh,top,'b--',left,Gv,'b--',...
%   right,Gv,'b--','LineWidth',2)
%plot(xtreme,ytreme,'y--','LineWidth',2)
set(gca,'FontSize',15)
colorbar
if isequal(p,'pe')
    caxis([pemm(1) pemm(2)])
elseif isequal(p,'pa')
    caxis([pamm(1) pamm(2)])
elseif isequal(p,'norm')
    caxis([sqrt(pemm(1)*pamm(1)) sqrt(pemm(2)*pamm(2))])
end

if k==5
    %xlabel([sorp,'_{HH}'],'FontSize',15)
    %ylabel([sorp,'_{VV}'],'FontSize',15)
    a=axis;
    if ia==2
        text(-.06,-.16,[sorp,'_{HH}'])
        text(-.49,.53,[sorp,'_{VV}'])
    elseif ia==3
        text(-.14,-.36,[sorp,'_{HH}'])
        text(-.99,.34,[sorp,'_{VV}'])
```

```
    else
        text(a(2),a(3),[sorp,'_{HH}'])
        text(a(1),a(4),[sorp,'_{VV}'])
    end
    if isequal(p,'pe')
        xlabel(colorbar,'\epsilon_\perp','FontSize',15)
    elseif isequal(p,'pa')
        xlabel(colorbar,'\epsilon_{||}','FontSize',15)
    elseif isequal(p,'norm')
        xlabel(colorbar,'sqrt{\epsilon_\perp\epsilon_{||}}',...
            'FontSize',15)
    end
end
hold off
if isequal(func,@ourlin)==1
    %title([num2str((k-1)*hmax/9),'<=Ghv<=',...
    %num2str(k*hmax/9),':linearized'])
    %If you want detailed titles for each subplot use this.

     title([sorp,'_{HV}=',num2str((2*k-1)*hmax/18,'%5.3g')])
     annotation('textbox',[0 .9 1 .1],'String',['\theta=',...
         num2str(ia),'\pi/',num2str(d),pp,', ','max(',sorp,...
         '_{HV})=',num2str(hmax,'%5.3g'),', Linearized'],...
         'EdgeColor','none','HorizontalAlignment','center',...
         'FontSize',18)
     %annotation('textbox',[0 .9 1 .1],'String',['\theta=',...
     %  num2str(ia),'\pi/',num2str(d),pp,'min(Ghv)=',...
     %  num2str(hmin),', ','max(Ghv)=',num2str(hmax),...
     %  ', Linearized'],'EdgeColor','none',...
     %  'HorizontalAlignment','center','FontSize',18)
else
    %title([num2str((k-1)*hmax/9),'<=Ghv<=',...
    %num2str(k*hmax/9),':  Chen'])
     title([sorp,'_{HV}=',num2str((2*k-1)*hmax/18,'%5.3g')])
     annotation('textbox',[0 .9 1 .1],'String',['\theta=',...
         num2str(ia),'\pi/',num2str(d),pp],'EdgeColor',...
         'none','HorizontalAlignment','center','FontSize',18)
     %annotation('textbox',[0 .9 1 .1],'String',...
     %  ['\theta=',num2str(ia),'\pi/',num2str(d),pp,', ',...
     %  'max(',sorp,'_{HV})=',num2str(hmax,'%5.3g'),',...
     %  Chen'],'EdgeColor','none','HorizontalAlignment',...
```

```
        %  'center','FontSize',18)
        %annotation('textbox',[0 .9 1 .1],'String',...
        %  ['\theta=',num2str(ia),'\pi/',num2str(d),pp,...
        %  'min(Ghv)=',num2str(hmin),', ','max(Ghv)=',...
        %  num2str(hmax),', Chen'],'EdgeColor','none',...
        %  'HorizontalAlignment','center','FontSize',18)
    end
end
set(gcf,'PaperPositionMode','auto')
if ia==2
    if isequal(p,'pe')
        if isequal(func,@ourlin)==1
            print -depsc2 pelgap9c
        elseif isequal(func,@refcoef)==1
            print -depsc2 peggap9c
        end
    elseif isequal(p,'pa')
        if isequal(func,@ourlin)==1
            print -depsc2 palgap9c
        elseif isequal(func,@refcoef)==1
            print -depsc2 paggap9c
            %print -djpeg paggap9c
        end
    end
elseif ia==3
    if isequal(p,'pe')
        if isequal(func,@ourlin)==1
            print -depsc2 pelno9c
        elseif isequal(func,@refcoef)==1
            print -depsc2 pegno9c
        end
    elseif isequal(p,'pa')
        if isequal(func,@ourlin)==1
            print -depsc2 palno9c
        elseif isequal(func,@refcoef)==1
            print -depsc2 pagno9c
        end
    end
end
%The rest of the code is for plotting the second subplot of each
%iteration separately.  Note that which subplot is plotted can be
```

```
%changed in the argument of sbp.
figure(2*ia)
cop=copyobj(sbp(2),2*ia);
colorbar
if isequal(p,'pe')
        caxis([pemm(1) pemm(2)])
    elseif isequal(p,'pa')
        caxis([pamm(1) pamm(2)])
    elseif isequal(p,'norm')
        caxis([sqrt(pemm(1)*pamm(1)) sqrt(pemm(2)*pamm(2))])
end
set(cop,'Position','default')
set(gca,'FontSize',15)
xlabel([sorp,'_{HH}'],'FontSize',18, 'FontWeight', 'bold')
ylabel([sorp,'_{VV}'],'FontSize',18, 'FontWeight', 'bold')
%a=axis;
%text(a(2),a(3),[sorp,'_{HH}'])
%text(a(1),a(4),[sorp,'_{VV}'])
if isequal(p,'pe')
    xlabel(colorbar,'\epsilon_\perp','FontSize',15)
elseif isequal(p,'pa')
    xlabel(colorbar,'\epsilon_{||}','FontSize',15)
elseif isequal(p,'norm')
    xlabel(colorbar,'sqrt{\epsilon_\perp\epsilon_{||}}',...
        'FontSize',15)
end
if ia==2
    if isequal(p,'pe')
        if isequal(func,@ourlin)==1
            print -depsc2 pelgap1c
        elseif isequal(func,@refcoef)==1
            print -depsc2 peggap1c
        end
    elseif isequal(p,'pa')
        if isequal(func,@ourlin)==1
            print -depsc2 palgap1c
        elseif isequal(func,@refcoef)==1
            print -depsc2 paggap1c
        end
    end
end
```

```
end


end % main function


function callScatterc(h,v,c)
    scatter(h,v,.1,c,'filled')
end
```

The following four functions are needed for scatterer4.m to run:

Q.1.1 ourlin.m

```
function [Ghh,Ghv,Gvh,Gvv]=ourlin(theta,pe,pa,alpha,gamma,k)
K=k*sin(theta); q=k*cos(theta);
beta=sqrt(1-alpha^2-gamma^2);
xi=pe-1; zeta=pa-pe;

Ghh=-(1/4)*(k^2/q^2)*(xi+beta^2*zeta);
Gvv=(1/4)*((xi+alpha^2*zeta)-(K^2/q^2)*(xi+gamma^2*zeta));
Gvh=-(1/4)*(k/q)*(alpha-(K/q)*gamma)*zeta*beta;
Ghv=(1/4)*(k/q)*(alpha+(K/q)*gamma)*zeta*beta;
```

Q.1.2 ourlinn.m

```
function [Ghh,Ghv,Gvh,Gvv]=ourlinn(theta,pe,pa,alpha,gamma,k)
K=k*sin(theta); q=k*cos(theta);
beta=-sqrt(1-alpha^2-gamma^2); %beta is negative
xi=pe-1; zeta=pa-pe;

Ghh=-(1/4)*(k^2/q^2)*(xi+beta^2*zeta);
Gvv=(1/4)*((xi+alpha^2*zeta)-(K^2/q^2)*(xi+gamma^2*zeta));
Gvh=-(1/4)*(k/q)*(alpha-(K/q)*gamma)*zeta*beta;
Ghv=(1/4)*(k/q)*(alpha+(K/q)*gamma)*zeta*beta;
```

Q.1.3 refcoef.m

```
function [Ghh,Ghv,Gvh,Gvv]=refcoef(material, wave)
    k = wave.k;
    theta = wave.theta;
```

```
    pe = material.pe;
    pa = material.pa;
    alpha = material.alpha;
    gamma = material.gamma;
%theta,pe,pa,alpha,gamma

%pe is epsilon perp and pa is epsilon parallel
%ebar=[pe 0 0;0 pe 0;0 0 pa];
%adj=[pe*pa 0 0;0 pe*pa 0;0 0 pe^2];
q=[0;0;1];
a=[0;-k*sin(theta);0];
b=[k*sin(theta);0;0];
%hat{c} = [alpha;beta;gamma]
c=[alpha;sqrt(1-alpha^2-gamma^2);gamma];
%This assumes beta is positive...

ebar=pe*eye(3)+(pa-pe)*(c*c');
adj=pe*(pa*eye(3)+(pe-pa)*(c*c'));
ac=sqrt(1-alpha^2-gamma^2)*k*sin(theta);%So does this.
bc=alpha*k*sin(theta);
%a_dot_c = ac
%b_dot_c = bc
%q_dot_c = gamma


a2=k^2*(sin(theta))^2;
qi=k*cos(theta);
qp=k*sqrt(pe-(sin(theta))^2);
z=sqrt(k^2*pe*pa*q'*ebar*q-a'*adj*a);
qm=(-b'*ebar*q+z)/(q'*ebar*q);
%qm=k*sqrt(pe-(pe/pa)*(sin(theta))^2); basal
X=k^2*qi*pe*(-a2*gamma+qp*bc)*(-a2*gamma+qm*bc);
Y=k^2*(-a2*gamma+qp*bc)*(qp^2*bc-qm*a2*gamma);
U=k^4*pe*qp*ac^2;
Z=k^4*pe^2*qi*ac^2;
V=k^3*pe*qi*qp*ac*bc;
L=k^3*pe*qi*a2*ac*gamma;
delta1=(qi+qp)*(X+Y)+(qi+qm)*(U+Z);
Ghh=((qi-qp)*(X+Y)+(qi-qm)*(U+Z))/delta1;
Ghv=(2*(qp-qm)*(V-L))/delta1;
Gvh=(2*(qm-qp)*(V+L))/delta1;
```

```
Gvv=((qi+qp)*(X-Y)+(qi+qm)*(Z-U))/delta1;
```

Q.1.4 refcoefn.m

```
function [Ghh,Ghv,Gvh,Gvv]=refcoefn(material, wave)
    k = wave.k;
    theta = wave.theta;

    pe = material.pe;
    pa = material.pa;
    alpha = material.alpha;
    gamma = material.gamma;
%theta,pe,pa,alpha,gamma

%pe is epsilon perp and pa is epsilon parallel
%ebar=[pe 0 0;0 pe 0;0 0 pa];
%adj=[pe*pa 0 0;0 pe*pa 0;0 0 pe^2];
q=[0;0;1];
a=[0;-k*sin(theta);0];
b=[k*sin(theta);0;0];
%hat{c} = [alpha;beta;gamma]
c=[alpha;-sqrt(1-alpha^2-gamma^2);gamma];
%This assumes beta is negative...

ebar=pe*eye(3)+(pa-pe)*(c*c');
adj=pe*(pa*eye(3)+(pe-pa)*(c*c'));
ac=-sqrt(1-alpha^2-gamma^2)*k*sin(theta);%So does this.
bc=alpha*k*sin(theta);
%a_dot_c = ac
%b_dot_c = bc
%q_dot_c = gamma


a2=k^2*(sin(theta))^2;
qi=k*cos(theta);
qp=k*sqrt(pe-(sin(theta))^2);
z=sqrt(k^2*pe*pa*q'*ebar*q-a'*adj*a);
qm=(-b'*ebar*q+z)/(q'*ebar*q);
%qm=k*sqrt(pe-(pe/pa)*(sin(theta))^2); basal
X=k^2*qi*pe*(-a2*gamma+qp*bc)*(-a2*gamma+qm*bc);
Y=k^2*(-a2*gamma+qp*bc)*(qp^2*bc-qm*a2*gamma);
U=k^4*pe*qp*ac^2;
```

```
Z=k^4*pe^2*qi*ac^2;
V=k^3*pe*qi*qp*ac*bc;
L=k^3*pe*qi*a2*ac*gamma;
delta1=(qi+qp)*(X+Y)+(qi+qm)*(U+Z);
Ghh=((qi-qp)*(X+Y)+(qi-qm)*(U+Z))/delta1;
Ghv=(2*(qp-qm)*(V-L))/delta1;
Gvh=(2*(qm-qp)*(V+L))/delta1;
Gvv=((qi+qp)*(X-Y)+(qi+qm)*(Z-U))/delta1;
```

Q.2 Code for Figure 4.2: lin.m

To generate the plots seen in Figure 4.2, we used lin.m (See 7h in Appendix P for details):

```
function [Ghh,Ghv,Gvh,Gvv,Ghhl,Ghvl,Gvhl,Gvvl]=...
    lin(material,wave,variable)
%It calls the external functions @refcoef and @ourlin.
k = wave.k;
    theta = wave.theta;
    thetap = wave.thetap;

    pe = material.pe;
    pa = material.pa;
    alpha = material.alpha;
    gamma = material.gamma;
if strcmp(variable,'theta')==1
    theta=0:.01:pi/2;
    Ghh=zeros(length(theta),1);
    Ghv=Ghh; Gvh=Ghh; Gvv=Ghh; Ghhl=Ghh; Ghvl=Ghh; Gvhl=Ghh; Gvvl=Ghh;
    for i=1:length(theta)
        [Ghh(i),Ghv(i),Gvh(i),Gvv(i)]=refcoef(struct('pe',pe,'pa',pa,...
            'alpha',alpha,'gamma',gamma),struct('k',k,...
            'theta',theta(i)));
        [Ghhl(i),Ghvl(i),Gvhl(i),Gvvl(i)]=ourlin(theta(i),pe,pa,...
            alpha,gamma,k);
    end
    plot(theta,Ghh,'b-*',theta,Ghv,'g-*',theta,Gvh,'y-*',theta,Gvv,...
        'c-*',theta,Ghhl,'r',theta,Ghvl,'k--',theta,Gvhl,'k',theta,...
        Gvvl,'m')
    xlabel('Incidence angle','FontSize',15)
    ylabel('Reflection coefficient','FontSize',15)
    title(['Exact vs. linearized:',' \epsilon_\perp=',num2str(pe),...
        ', \epsilon_{||}=',num2str(pa),', \alpha=',num2str(alpha),...
        ', \gamma=',num2str(gamma)],'FontSize',18)
```

```
    legend('Shh','Shv','Svh','Svv','Shh lin','Shv lin','Svh lin',...
        'Svv lin','Location','SouthWest')
elseif strcmp(variable,'pe')==1
    pe=1:.01:5;
    Ghh=zeros(length(pe),1);
    Ghv=Ghh; Gvh=Ghh; Gvv=Ghh; Ghhl=Ghh;
    Ghvl=Ghh; Gvhl=Ghh; Gvvl=Ghh;
    Q=Ghh; Ql=Ghh; z=Ghh;
    for i=1:length(pe)
        [Ghh(i),Ghv(i),Gvh(i),Gvv(i)]=refcoef(struct('pe',pe(i),'pa',...
            pa,'alpha',alpha,'gamma',gamma),struct('k',k,'theta',...
            str2num(theta)));
        [Ghhl(i),Ghvl(i),Gvhl(i),Gvvl(i)]=ourlin(str2num(theta),...
            pe(i),pa,alpha,gamma,k);
        Q(i)=Gvv(i)/Ghh(i);
        Ql(i)=Gvvl(i)/Ghhl(i);
    end
        figure('OuterPosition',[680 396 922 753])

    subplot(2,1,1)
    plot(pe,Ghh,'b-',pe,Ghv,'g-',pe,Gvh,'y-',pe,Gvv,'c-',pe,Ghhl,'r',...
    pe,Ghvl,'k--',pe,Gvhl,'k',pe,Gvvl,'m',pe,z,'k:')
    %hold on
    %o=axis;
    %plot(pe,Q,'b:',pe,Ql,'r:',zi,z,'k:')
    %axis([o(1),o(2),min(Q(length(Q)),Ql(length(Ql))),o(4)]);
    xlabel('\epsilon_{\perp}','FontSize',15)
    ylabel('Reflection coefficient','FontSize',15)
    title(['Exact vs. linearized:',' \epsilon_{||}=',num2str(pa),...
        ', \alpha=',num2str(alpha),', \gamma=',num2str(gamma),...
        ', \theta_i=',thetap],'FontSize',18)
    legend('Shh','Shv','Svh','Svv','Shh lin','Svh lin','Shv lin',...
        'Svv lin','Location','BestOutside')
    subplot(2,1,2)
    plot(pe,Q,'b:',pe,Ql,'r:')
    xlabel('\epsilon_{\perp}','FontSize',15)
    ylabel('Polarization ratio','FontSize',15)
    title(['Exact vs. linearized:',' \epsilon_{||}=',num2str(pa),...
        ', \alpha=',num2str(alpha),', \gamma=',num2str(gamma),...
        ', \theta_i=',thetap],'FontSize',18)
    legend('Q','Q lin','Location','BestOutside')
```

```
    print -depsc2 linvgenpare
elseif strcmp(variable,'pa')==1
    pa=1:.01:5;
    Ghh=zeros(length(pa),1);
    Ghv=Ghh; Gvh=Ghh; Gvv=Ghh;
    Ghhl=Ghh; Ghvl=Ghh; Gvhl=Ghh; Gvvl=Ghh;
    Q=Ghh; Ql=Ghh; z=Ghh;
    for i=1:length(pa)
        [Ghh(i),Ghv(i),Gvh(i),Gvv(i)]=refcoef(struct('pe',pe,...
            'pa',pa(i),'alpha',alpha,'gamma',gamma),...
            struct('k',k,'theta',str2num(theta)));
        [Ghhl(i),Ghvl(i),Gvhl(i),Gvvl(i)]=ourlin(str2num(theta),pe,...
            pa(i),alpha,gamma,k);
        Q(i)=Gvv(i)/Ghh(i);
        Ql(i)=Gvvl(i)/Ghhl(i);
    end
        figure('OuterPosition',[680 396 922 753])

    subplot(2,1,1)
    plot(pa,Ghh,'b-',pa,Ghv,'g-',pa,Gvh,'y-',pa,Gvv,'c-',pa,...
        Ghhl,'r',pa,Ghvl,'k--',pa,Gvhl,'k',pa,Gvvl,'m',pa,z,'k:')
    %hold on
    %o=axis;
    %plot(pa,Q,'b:',pa,Ql,'r:',zi,z,'k:')
    %axis([o(1),o(2),min(Q(length(Q)),Ql(length(Ql))),o(4)]);
    xlabel('\epsilon_{||}','FontSize',15)
    ylabel('Reflection coefficient','FontSize',15)
    title(['Exact vs. linearized',' \epsilon_\perp=',num2str(pe),...
        ', \alpha=',num2str(alpha),', \gamma=',num2str(gamma),...
        ', \theta_i=',thetap],'FontSize',18)
    legend('Shh','Shv','Svh','Svv','Shh lin','Svh lin','Shv lin',...
        'Svv lin','Location','BestOutside')
    subplot(2,1,2)
    plot(pa,Q,'b:',pa,Ql,'r:')
    xlabel('\epsilon_{||}','FontSize',15)
    ylabel('Polarization ratio','FontSize',15)
    title(['Exact vs. linearized:',' \epsilon_\perp=',num2str(pe),...
        ', \alpha=',num2str(alpha),', \gamma=',num2str(gamma),...
        ', \theta_i=',thetap],'FontSize',18)
    legend('Q','Q lin','Location','BestOutside')
    print -depsc2 linvgenpara
```

```
elseif strcmp(variable,'alpha')==1
    al=-1:.01:1;
    j=1;
    for i=1:length(al)
        if 1-al(i)^2-gamma^2>=0
            alpha(j)=al(i);
            j=j+1;
        end
    end
    Ghh=zeros(length(alpha),1);
    Ghv=Ghh; Gvh=Ghh; Gvv=Ghh; Ghhl=Ghh; Ghvl=Ghh; Gvhl=Ghh; Gvvl=Ghh;
    for i=1:length(alpha)
        [Ghh(i),Ghv(i),Gvh(i),Gvv(i)]=refcoef(struct('pe',pe,'pa',pa,...
            'alpha',alpha(i),'gamma',gamma),...
            struct('k',k,'theta_i',str2num(theta)));
        [Ghhl(i),Ghvl(i),Gvhl(i),Gvvl(i)]=ourlin(str2num(theta),...
            pe,pa,alpha(i),gamma,k);
    end
    plot(alpha,Ghh,'b-*',alpha,Ghv,'g-*',alpha,Gvh,'y-*',alpha,Gvv,...
        'c-*',alpha,Ghhl,'r',alpha,Ghvl,'k--',alpha,Gvhl,'k',...
        alpha,Gvvl,'m')
    xlabel('\alpha','FontSize',15)
    ylabel('Reflection coefficient','FontSize',15)
    title(['Exact vs. linearized',' \epsilon_\perp=',num2str(pe),...
        ', \epsilon_{||}=',num2str(pa),', \gamma=',num2str(gamma),...
        ', \theta=',thetap],'FontSize',18)
    legend('Shh','Shv','Svh','Svv','Shh lin','Shv lin','Svh lin',...
        'Svv lin','Location','SouthWest')
elseif strcmp(variable,'gamma')==1
    ga=-1:.01:1;
    j=1;
    for i=1:length(ga)
        if 1-alpha^2-ga(i)^2>=0
            gamma(j)=ga(i);
            j=j+1;
        end
    end
    Ghh=zeros(length(gamma),1);
    Ghv=Ghh; Gvh=Ghh; Gvv=Ghh; Ghhl=Ghh; Ghvl=Ghh; Gvhl=Ghh; Gvvl=Ghh;
    for i=1:length(gamma)
        [Ghh(i),Ghv(i),Gvh(i),Gvv(i)]=refcoef(struct('pe',pe,'pa',pa,...
```

```
            'alpha',alpha,'gamma',gamma(i)),...
            struct('k',k,'theta_i',str2num(theta)));
        [Ghhl(i),Ghvl(i),Gvhl(i),Gvvl(i)]=ourlin(str2num(theta),...
            pe,pa,alpha,gamma(i),k);
    end
    plot(gamma,Ghh,'b-*',gamma,Ghv,'g-*',gamma,Gvh,'y-*',...
        gamma,Gvv,'c-*',gamma,Ghhl,'r',gamma,Ghvl,'k--',...
        gamma,Gvhl,'k',gamma,Gvvl,'m')
    xlabel('\gamma','FontSize',15)
    ylabel('Reflection coefficient','FontSize',15)
    title(['Exact vs. linearized',' \epsilon_\perp=',num2str(pe),...
        ', \epsilon_{||}=',num2str(pa),', \alpha=',num2str(alpha),...
        ', \theta=',thetap],'FontSize',18)
    legend('Shh','Shv','Svh','Svv','Shh lin','Shv lin','Svh lin',...
        'Svv lin','Location','SouthWest')
elseif strcmp(variable,'pp')==1
    pe=1:.01:3;
    Ghh=zeros(length(pe),1);
    Ghv=Ghh; Gvh=Ghh; Gvv=Ghh;
    Ghhl=Ghh; Ghvl=Ghh; Gvhl=Ghh; z=Ghh; Gvvl=Ghh;
    Q=Ghh; Ql=Ghh;
    for i=1:length(pe)
        [Ghh(i),Ghv(i),Gvh(i),Gvv(i)]=refcoef(struct('pe',pe(i),'pa',...
            pe(i),'alpha',alpha,'gamma',gamma),...
            struct('k',k,'theta',str2num(theta)));
        [Ghhl(i),Ghvl(i),Gvhl(i),Gvvl(i)]=ourlin(str2num(theta),...
            pe(i),pe(i),alpha,gamma,k);
        Q(i)=Gvv(i)/Ghh(i);
        Ql(i)=Gvvl(i)/Ghhl(i);
    end
    plot(pe,Ghh,'b-',pe,Gvv,'c-',pe,Ghhl,'r',pe,Gvvl,'m',pe,Q,'b:',...
        pe,Ql,'r:',pe,z,'k')
    xlabel('\epsilon','FontSize',15)
    ylabel('Reflection coefficient, Ratio','FontSize',15)
    title(['Exact vs. linearized:',' \theta_i=',thetap],'FontSize',18)
    legend('Shh','Svv','Shh lin','Svv lin','Q','Q lin',...
        'Location','NorthWest')
    print -depsc2 linvgeniso
elseif strcmp(variable,'3')==1
    p=1:.01:3;
    Ghh=zeros(length(p),1);
```

```
Ghv=Ghh; Gvh=Ghh; Gvv=Ghh;
Ghhl=Ghh; Ghvl=Ghh; Gvhl=Ghh; z=Ghh; Gvvl=Ghh;
Q=Ghh; Ql=Ghh;
for i=1:length(p)
    [Ghh(i),Ghv(i),Gvh(i),Gvv(i)]=refcoef(struct('pe',p(i),'pa',...
        p(i),'alpha',alpha,'gamma',gamma),...
        struct('k',k,'theta',str2num(theta)));
    [Ghhl(i),Ghvl(i),Gvhl(i),Gvvl(i)]=ourlin(str2num(theta),p(i),...
        p(i),alpha,gamma,k);
    Q(i)=Gvv(i)/Ghh(i);
    Ql(i)=Gvvl(i)/Ghhl(i);
end
%scrsz=get(0,'ScreenSize');
%figure('Position',[1 scrsz(4) scrsz(3) scrsz(4)])
    figure('OuterPosition',[680 396 922 753])
subplot(2,2,[1 3])
%p1=plot(p,Ghh,'b-.',p,Gvv,'b:',p,Ghhl,'m-.',p,Gvvl,'m:',...
%   p,Q,'g--',p,Ql,'k--',p,z,'k:');
p1=plot(p,Ghh,'b--',p,Ghhl,'b',p,Gvv,'m--',p,Gvvl,'m',p,Q,'r--',...
    p,Ql,'k',p,z,'k:');
set(p1(1),'LineWidth',2);
set(p1(2),'LineWidth',2);
set(p1(3),'LineWidth',4);
set(p1(4),'LineWidth',4);
set(p1(5),'LineWidth',6);
set(p1(6),'LineWidth',6);
set(gca,'FontSize',14,'LineWidth',2,'YTick',-1:.2:.5);
xlabel('\epsilon','FontSize',22)
ylabel('Polarization ratio, Reflection coefficient','FontSize',18)
title(['(a) Isotropic;',' \theta_i=',thetap],'FontSize',18)
leg1=legend('S_{HH}^{exact}','S_{HH}','S_{VV}^{exact}','S_{VV}',...
    'Q^{exact}','Q','Location','NorthWest');
set(leg1,'FontSize',14)
p=1:.01:5;
Ghh=zeros(length(p),1);
Ghv=Ghh; Gvh=Ghh; Gvv=Ghh; Ghhl=Ghh;
Ghvl=Ghh; Gvhl=Ghh; Gvvl=Ghh;
Q=Ghh; Ql=Ghh; z=Ghh;
for i=1:length(p)
    [Ghh(i),Ghv(i),Gvh(i),Gvv(i)]=refcoef(struct('pe',p(i),'pa',...
        pa,'alpha',alpha,'gamma',gamma),...
```

```
        struct('k',k,'theta',str2num(theta)));
    [Ghhl(i),Ghvl(i),Gvhl(i),Gvvl(i)]=...
        ourlin(str2num(theta),p(i),pa,alpha,gamma,k);
    Q(i)=Gvv(i)/Ghh(i);
    Ql(i)=Gvvl(i)/Ghhl(i);
end

subplot(2,2,2)

%p2=plot(p,Q,'g--',p,Ql,'k--');
p2=plot(p,Q,'r--',p,Ql,'k');
set(p2(1),'LineWidth',6);
set(p2(2),'LineWidth',6);
set(gca,'FontSize',14,'LineWidth',2);
xlabel('\epsilon_{\perp}','FontSize',22)
ylabel('Polarization ratio','FontSize',18)
title(['(b) Anisotropic;',' \epsilon_{||}=',num2str(pa),...
    ', \alpha=',num2str(alpha),', \gamma=',num2str(gamma),...
    ', \theta_i=',thetap],'FontSize',18)
leg2=legend('Q^{exact}','Q','Location','SouthEast');
set(leg2,'FontSize',14)
p=1:.01:5;
Ghh=zeros(length(p),1);
Ghv=Ghh; Gvh=Ghh; Gvv=Ghh; Ghhl=Ghh;
Ghvl=Ghh; Gvhl=Ghh; Gvvl=Ghh;
Q=Ghh; Ql=Ghh; z=Ghh;
for i=1:length(p)
    [Ghh(i),Ghv(i),Gvh(i),Gvv(i)]=refcoef(struct('pe',pe,...
        'pa',p(i),'alpha',alpha,'gamma',gamma),...
        struct('k',k,'theta',str2num(theta)));
    [Ghhl(i),Ghvl(i),Gvhl(i),Gvvl(i)]=...
        ourlin(str2num(theta),pe,p(i),alpha,gamma,k);
    Q(i)=Gvv(i)/Ghh(i);
    Ql(i)=Gvvl(i)/Ghhl(i);
end


subplot(2,2,4)

%p3=plot(p,Q,'g--',p,Ql,'k--');
p3=plot(p,Q,'r--',p,Ql,'k');
```

```
    set(p3(1),'LineWidth',6);
    set(p3(2),'LineWidth',6);
    set(gca,'FontSize',14,'LineWidth',2);
    xlabel('\epsilon_{||}','FontSize',22)
    ylabel('Polarization ratio','FontSize',18)
    title(['(c) Anisotropic;',' \epsilon_\perp=',num2str(pe),...
        ', \alpha=',num2str(alpha),', \gamma=',num2str(gamma),...
        ', \theta_i=',thetap],'FontSize',18)
    leg3=legend('Q^{exact}','Q','Location','NorthEast');
    set(leg3,'FontSize',14)
    set(gcf,'PaperPositionMode','auto')
    print -depsc2 linvgen3
end
```

It should be noted that ourlin.m and refcoef.m from the previous section are also called within lin.m.

Q.3 Other useful code

There were other programs written over the course of the research that the reader may find useful. These did not contribute directly to any results in the dissertation, but they helped in the development of the code that did.

Q.3.1 fresnel.m

Plot the Fresnel curves $S_{HH}(\theta_i)$ and $S_{VV}(\theta_i)$ for a given permittivity. Also, display the Brewster angle numerically and graphically.

```
function fresnel(perm)
    if ~exist('perm', 'var')
        perm = 1.7;
    end

    theta=0:.01:pi/2;
    Ghh=zeros(numel(theta),1);
    Ghv=Ghh; Gvh=Ghh; Gvv=Ghh;

    for i=1:length(Ghh)
        [Ghh(i),Ghv(i),Gvh(i),Gvv(i)]=refcoef(struct('pe',perm,...
            'pa',perm,'alpha',0.3,'gamma',0.4),...
            struct('k',3,'theta',theta(i)));
    end
```

```
    theta_deg = rad2deg(theta);
    plot(theta_deg,Ghh,theta_deg,Gvv)

    theta_b = atan(sqrt(perm)); % Brewster angle
    theta_b_deg = rad2deg(theta_b);
    hold on; plot(theta_b_deg, 0, 'rs'); hold off
    hold on; plot([min(theta_deg), max(theta_deg)], [0 0], 'r')

    xlabel('Incidence angle, degrees')
    ylabel('Reflection coefficient')
    title(sprintf('Fresnel curves; Brewster = %6.3f deg', theta_b_deg))
    legend('Ghh','Gvv')


end
```

Q.3.2 basal.m

Plot the reflection coefficients off the basal plane of a uniaxial crystal from both [Che83] and [Lek91] for compare/contrast purposes.

```
function [Ghh,Ghv,Gvh,Gvv,rss,rpp]=basal(material,wave,variable)
%theta,pe,pa,alpha,gamma)

k = wave.k;
    theta = wave.theta;

    pe = material.pe;
    pa = material.pa;
    alpha = material.alpha;
    gamma = material.gamma;

if strcmp(variable,'theta')==1

    Ghh=zeros(length(0:.01:pi/2),1);
    Ghv=Ghh; Gvh=Ghh; Gvv=Ghh; rss=Ghh; rpp=Ghh;
    theta=0:.01:pi/2;
    %qi=k*cos(theta)
    for i=1:length(Ghh)
        [Ghh(i),Ghv(i),Gvh(i),Gvv(i)]=refcoef(struct('pe',pe,'pa',pa,...
            'alpha',alpha,'gamma',gamma),struct('k',k,...
            'theta',theta(i)));
```

```
        %rss(i)=(k*cos(theta(i))-k*sqrt(pe-(sin(theta(i)))^2))/...
        %   (k*cos(theta(i))+k*sqrt(pe-(sin(theta(i)))^2));


        [rss(i),rpp(i)]=rppcheck(theta(i),pe,pa,k);

    end
    plot(theta,Ghh,'b-*',theta,Gvv,'c-*',theta,rss,'r',theta,-rpp,'m')
    xlabel('Incidence angle')
    ylabel('Reflection coefficient')
    title('Chen vs. Lekner:  Basal')
    legend('Ghh','Gvv','rss','-rpp')
elseif strcmp(variable,'pe')==1
    pe=0:.1:5;
    Ghh=zeros(length(pe),1);
    Ghv=Ghh; Gvh=Ghh; Gvv=Ghh; rss=Ghh; rpp=Ghh;
    for i=1:length(pe)
        [Ghh(i),Ghv(i),Gvh(i),Gvv(i)]=...
            refcoef(struct('pe',pe(i),'pa',pa,...
            'alpha',alpha,'gamma',gamma),struct('k',k,'theta',theta));
        %rss(i)=(k*cos(theta)-k*sqrt(pe(i)-(sin(theta))^2))/...
        %   (k*cos(theta)+k*sqrt(pe(i)-(sin(theta))^2));
        [rss(i),rpp(i)]=rppcheck(theta,pe(i),pa,k);
    end
    plot(pe,Ghh,'b-*',pe,Gvv,'c-*',pe,rss,'r',pe,-rpp,'m')
    xlabel('Epsilon perp')
    ylabel('Reflection coefficient')
    title('Chen vs. Lekner:  Basal')
    legend('Ghh','Gvv','rss','-rpp')
elseif strcmp(variable,'pa')==1
    pa=0:.1:5;
    Ghh=zeros(length(pa),1);
    Ghv=Ghh; Gvh=Ghh; Gvv=Ghh; rss=Ghh; rpp=Ghh;
    for i=1:length(pa)
        [Ghh(i),Ghv(i),Gvh(i),Gvv(i)]=...
            refcoef(struct('pe',pe,'pa',pa(i),...
            'alpha',alpha,'gamma',gamma),struct('k',k,'theta',theta));
        %rss(i)=(k*cos(theta)-k*sqrt(pe-(sin(theta))^2))/...
        %   (k*cos(theta)+k*sqrt(pe-(sin(theta))^2));
        [rss(i),rpp(i)]=rppcheck(theta,pe,pa(i),k);
    end
```

```
    plot(pa,Ghh,'b-*',pa,Gvv,'c-*',pa,rss,'r',pa,-rpp,'m')
    xlabel('Epsilon parallel')
    ylabel('Reflection coefficient')
    title('Chen vs. Lekner:  Basal')
    legend('Ghh','Gvv','rss','-rpp')
end
```

Q.3.3 rppcheck.m (used in basal.m)

Calculate the reflection coefficients for a basal plane of a uniaxial crystal as given in Section 5.1 of [Lek91].

```
function [rss,rpp]=rppcheck(theta,pe,pa,k)
qm=k*sqrt(pe-(pe/pa)*(sin(theta))^2);
K=k*sin(theta); q=k*cos(theta); qp=sqrt(pe*k^2-K^2);
%Eo=[0;-1;0]; Ee=Ne*[qm;0;-(pe/pa)*K];
Ne=sqrt(qm^2+((pe/pa)*K)^2);
Eo=[0;-1;0]; Ee=Ne*[-qm;0;(pe/pa)*K];
A=(qp+q+K*tan(theta))*Eo(1)-K*Eo(3);
B=(qm+q+K*tan(theta))*Ee(1)-K*Ee(3);
D=(q+qm)*A*Ee(2)-(q+qp)*B*Eo(2);
qt=q+K*tan(theta);
rpp=(2*qt/D)*((q+qm)*Eo(1)*Ee(2)-(q+qp)*Ee(1)*Eo(2))-1;
rss=((q-qm)*A*Ee(2)-(q-qp)*B*Eo(2))/D;
```

Q.3.4 par.m

Plot the reflection coefficients off a plane parallel to the optic axis of a uniaxial crystal from both [Che83] and [Lek91] for compare/contrast purposes.

```
function [Ghh,Ghv,Gvh,Gvv,rss,rsp,rps,rpp]=par(material,wave,variable)
%Note that for this one, gamma=0.
k = wave.k;
    theta = wave.theta;

    pe = material.pe;
    pa = material.pa;
    alpha = material.alpha;
    gamma = material.gamma;

if strcmp(variable,'theta')==1
    theta=0:.01:pi/2;
```

```
    Ghh=zeros(length(theta),1);
    Ghv=Ghh; Gvh=Ghh; Gvv=Ghh; rss=Ghh; rsp=Ghh; rps=Ghh; rpp=Ghh;
    for i=1:length(theta)
        [Ghh(i),Ghv(i),Gvh(i),Gvv(i)]=refcoef(struct('pe',pe,'pa',pa,...
            'alpha',alpha,'gamma',gamma),struct('k',k,...
            'theta',theta(i)));
        [rss(i),rsp(i),rps(i),rpp(i)]=Lekpar(theta(i),pe,pa,alpha,k);
    end
    plot(theta,Ghh,'b-*',theta,Ghv,'g-*',theta,Gvh,'y-*',...
        theta,Gvv,'c-*',theta,rss,'r',theta,-rsp,'k--',theta,rps,'k',...
        theta,-rpp,'m')
    xlabel('Incidence angle')
    ylabel('Reflection coefficient')
    title('Chen vs. Lekner:  Parallel')
    legend('Ghh','Ghv','Gvh','Gvv','rss','-rsp','rps','-rpp',...
        'Location','SouthWest')
elseif strcmp(variable,'pe')==1
    pe=0:.1:5;
    Ghh=zeros(length(pe),1);
    Ghv=Ghh; Gvh=Ghh; Gvv=Ghh; rss=Ghh; rsp=Ghh; rps=Ghh; rpp=Ghh;
    for i=1:length(pe)
        [Ghh(i),Ghv(i),Gvh(i),Gvv(i)]=...
            refcoef(struct('pe',pe(i),'pa',pa,...
            'alpha',alpha,'gamma',gamma),struct('k',k,'theta',theta));
        [rss(i),rsp(i),rps(i),rpp(i)]=Lekpar(theta,pe(i),pa,alpha,k);
    end
    plot(pe,Ghh,'b-*',pe,Ghv,'g-*',pe,Gvh,'y-*',pe,Gvv,'c-*',...
        pe,rss,'r',pe,-rsp,'k--',pe,rps,'k',pe,-rpp,'m')
    xlabel('Epsilon perp')
    ylabel('Reflection coefficient')
    title('Chen vs. Lekner:  Parallel')
    legend('Ghh','Ghv','Gvh','Gvv','rss','-rsp','rps','-rpp',...
        'Location','SouthWest')
elseif strcmp(variable,'pa')==1
    pa=0:.1:5;
    Ghh=zeros(length(pa),1);
    Ghv=Ghh; Gvh=Ghh; Gvv=Ghh; rss=Ghh; rsp=Ghh; rps=Ghh; rpp=Ghh;
    for i=1:length(pa)
        [Ghh(i),Ghv(i),Gvh(i),Gvv(i)]=...
            refcoef(struct('pe',pe,'pa',pa(i),...
            'alpha',alpha,'gamma',gamma),struct('k',k,'theta',theta));
```

```
        [rss(i),rsp(i),rps(i),rpp(i)]=Lekpar(theta,pe,pa(i),alpha,k);
    end
    plot(pa,Ghh,'b-*',pa,Ghv,'g-*',pa,Gvh,'y-*',pa,Gvv,'c-*',...
        pa,rss,'r',pa,-rsp,'k--',pa,rps,'k',pa,-rpp,'m')
    xlabel('Epsilon parallel')
    ylabel('Reflection coefficient')
    title('Chen vs. Lekner:  Parallel')
    legend('Ghh','Ghv','Gvh','Gvv','rss','-rsp','rps','-rpp',...
        'Location','SouthWest')
elseif strcmp(variable,'alpha')==1
    alpha=-1:.01:1;
    Ghh=zeros(length(alpha),1);
    Ghv=Ghh; Gvh=Ghh; Gvv=Ghh; rss=Ghh; rsp=Ghh; rps=Ghh; rpp=Ghh;
    for i=1:length(alpha)
        [Ghh(i),Ghv(i),Gvh(i),Gvv(i)]=refcoef(struct('pe',pe,'pa',pa,...
            'alpha',alpha(i),'gamma',gamma),struct('k',k,...
            'theta',theta));
        [rss(i),rsp(i),rps(i),rpp(i)]=Lekpar(theta,pe,pa,alpha(i),k);
    end
    plot(alpha,Ghh,'b-*',alpha,Ghv,'g-*',alpha,Gvh,'y-*',...
        alpha,Gvv,'c-*',alpha,rss,'r',alpha,-rsp,'k--',alpha,rps,'k',...
        alpha,-rpp,'m')
    xlabel('Alpha')
    ylabel('Reflection coefficient')
    title('Chen vs. Lekner:  Parallel')
    legend('Ghh','Ghv','Gvh','Gvv','rss','-rsp','rps','-rpp',...
        'Location','SouthWest')
end
```

Q.3.5 Lekpar.m (used in par.m)

Calculate the reflection coefficients for a plane parallel to the optic axis of a uniaxial crystal as given in Section 5.2 of [Lek91].

```
function [rss,rsp,rps,rpp]=Lekpar(theta,pe,pa,alpha,k)
K=k*sin(theta); q=k*cos(theta);
beta=sqrt(1-alpha^2);
qp=sqrt(pe*k^2-K^2);
qm=sqrt(qp^2+((pa-pe)/pe)*(pe*k^2-alpha^2*K^2));
No=1/sqrt((-beta*qp)^2+(alpha*qp)^2+(beta*K)^2);
Ne=1/sqrt((alpha*qp^2)^2+(beta*pe*k^2)^2+(-alpha*qm*K)^2);
Eo=No*[-beta*qp;alpha*qp;beta*K];
```

```
Ee=Ne*[alpha*qp^2;beta*pe*k^2;-alpha*qm*K];
A=(qp+q+K*tan(theta))*Eo(1)-K*Eo(3);
B=(qm+q+K*tan(theta))*Ee(1)-K*Ee(3);
D=(q+qm)*A*Ee(2)-(q+qp)*B*Eo(2);
qt=q+K*tan(theta);
rss=((q-qm)*A*Ee(2)-(q-qp)*B*Eo(2))/D;
rsp=2*k*(A*Ee(1)-B*Eo(1))/D;
rps=2*k*(qm-qp)*Eo(2)*Ee(2)/D;
rpp=(2*qt/D)*((q+qm)*Eo(1)*Ee(2)-(q+qp)*Ee(1)*Eo(2))-1;
```

Q.3.6 gen.m

Plot the reflection coefficients off a uniaxial crystal for any geometrical configuration from both [Che83] and [Lek91] for compare/contrast purposes.

```
function [Ghh,Ghv,Gvh,Gvv,rss,rsp,rps,rpp]=gen(material,wave,variable)

k = wave.k;
    theta = wave.theta;

    pe = material.pe;
    pa = material.pa;
    alpha = material.alpha;
    gamma = material.gamma;

if strcmp(variable,'theta')==1
    theta=0:.01:pi/2;
    Ghh=zeros(length(theta),1);
    Ghv=Ghh; Gvh=Ghh; Gvv=Ghh; rss=Ghh; rsp=Ghh; rps=Ghh; rpp=Ghh;
    for i=1:length(theta)
        [Ghh(i),Ghv(i),Gvh(i),Gvv(i)]=refcoef(struct('pe',pe,'pa',pa,...
            'alpha',alpha,'gamma',gamma),struct('k',k,...
            'theta',theta(i)));
        [rss(i),rsp(i),rps(i),rpp(i)]=...
            Lekgen(theta(i),pe,pa,alpha,gamma,k);
    end
    plot(theta,Ghh,'b-*',theta,Ghv,'g-*',theta,Gvh,'y-*',...
        theta,Gvv,'c-*',theta,rss,'r',theta,-rsp,'k--',theta,rps,'k',...
        theta,-rpp,'m')
    xlabel('Incidence angle')
    ylabel('Reflection coefficient')
    title('Chen vs. Lekner:  General')
```

```
    legend('Ghh','Ghv','Gvh','Gvv','rss','-rsp','rps','-rpp',...
        'Location','SouthWest')
elseif strcmp(variable,'pe')==1
    pe=0:.1:5;
    Ghh=zeros(length(pe),1);
    Ghv=Ghh; Gvh=Ghh; Gvv=Ghh; rss=Ghh; rsp=Ghh; rps=Ghh; rpp=Ghh;
    for i=1:length(pe)
        [Ghh(i),Ghv(i),Gvh(i),Gvv(i)]=...
            refcoef(struct('pe',pe(i),'pa',pa,...
            'alpha',alpha,'gamma',gamma),struct('k',k,'theta',theta));
        [rss(i),rsp(i),rps(i),rpp(i)]=...
            Lekgen(theta,pe(i),pa,alpha,gamma,k);
    end
    plot(pe,Ghh,'b-*',pe,Ghv,'g-*',pe,Gvh,'y-*',pe,Gvv,'c-*',...
        pe,rss,'r',pe,-rsp,'k--',pe,rps,'k',pe,-rpp,'m')
    xlabel('Epsilon perp')
    ylabel('Reflection coefficient')
    title('Chen vs. Lekner:  General')
    legend('Ghh','Ghv','Gvh','Gvv','rss','-rsp','rps','-rpp',...
        'Location','SouthWest')
elseif strcmp(variable,'pa')==1
    pa=0:.1:5;
    Ghh=zeros(length(pa),1);
    Ghv=Ghh; Gvh=Ghh; Gvv=Ghh; rss=Ghh; rsp=Ghh; rps=Ghh; rpp=Ghh;
    for i=1:length(pa)
        [Ghh(i),Ghv(i),Gvh(i),Gvv(i)]=...
            refcoef(struct('pe',pe,'pa',pa(i),...
            'alpha',alpha,'gamma',gamma),struct('k',k,'theta',theta));
        [rss(i),rsp(i),rps(i),rpp(i)]=...
            Lekgen(theta,pe,pa(i),alpha,gamma,k);
    end
    plot(pa,Ghh,'b-*',pa,Ghv,'g-*',pa,Gvh,'y-*',pa,Gvv,'c-*',...
        pa,rss,'r',pa,-rsp,'k--',pa,rps,'k',pa,-rpp,'m')
    xlabel('Epsilon parallel')
    ylabel('Reflection coefficient')
    title('Chen vs. Lekner:  General')
    legend('Ghh','Ghv','Gvh','Gvv','rss','-rsp','rps','-rpp',...
        'Location','SouthWest')
elseif strcmp(variable,'alpha')==1
    al=-1:.01:1;
    j=1;
```

```
    for i=1:length(al)
        if 1-al(i)^2-gamma^2>=0
            alpha(j)=al(i);
            j=j+1;
        end
    end
    Ghh=zeros(length(alpha),1);
    Ghv=Ghh; Gvh=Ghh; Gvv=Ghh; rss=Ghh; rsp=Ghh; rps=Ghh; rpp=Ghh;
    for i=1:length(alpha)
        [Ghh(i),Ghv(i),Gvh(i),Gvv(i)]=refcoef(struct('pe',pe,'pa',pa,...
            'alpha',alpha(i),'gamma',gamma),struct('k',k,...
            'theta',theta));
        [rss(i),rsp(i),rps(i),rpp(i)]=...
            Lekgen(theta,pe,pa,alpha(i),gamma,k);
    end
    plot(alpha,Ghh,'b-*',alpha,Ghv,'g-*',alpha,Gvh,'y-*',...
        alpha,Gvv,'c-*',alpha,rss,'r',alpha,-rsp,'k--',alpha,rps,'k',...
        alpha,-rpp,'m')
    xlabel('Alpha')
    ylabel('Reflection coefficient')
    title('Chen vs. Lekner:  General')
    legend('Ghh','Ghv','Gvh','Gvv','rss','-rsp','rps','-rpp',...
        'Location','SouthWest')
elseif strcmp(variable,'gamma')==1
    ga=-1:.01:1;
    j=1;
    for i=1:length(ga)
        if 1-alpha^2-ga(i)^2>=0
            gamma(j)=ga(i);
            j=j+1;
        end
    end
    Ghh=zeros(length(gamma),1);
    Ghv=Ghh; Gvh=Ghh; Gvv=Ghh; rss=Ghh; rsp=Ghh; rps=Ghh; rpp=Ghh;
    for i=1:length(gamma)
        [Ghh(i),Ghv(i),Gvh(i),Gvv(i)]=refcoef(struct('pe',pe,'pa',pa,...
            'alpha',alpha,'gamma',gamma(i)),struct('k',k,...
            'theta',theta));
        [rss(i),rsp(i),rps(i),rpp(i)]=...
            Lekgen(theta,pe,pa,alpha,gamma(i),k);
    end
```

```
    plot(gamma,Ghh,'b-*',gamma,Ghv,'g-*',gamma,Gvh,'y-*',...
        gamma,Gvv,'c-*',gamma,rss,'r',gamma,-rsp,'k--',gamma,rps,'k',...
        gamma,-rpp,'m')
    xlabel('Gamma')
    ylabel('Reflection coefficient')
    title('Chen vs. Lekner:  General')
    legend('Ghh','Ghv','Gvh','Gvv','rss','-rsp','rps','-rpp',...
        'Location','SouthWest')
end
```

Q.3.7 Lekgen.m (used in gen.m)

Calculate the reflection coefficients off a uniaxial crystal for any geometrical configuration as given in Section 4 of [Lek91]

```
function [rss,rsp,rps,rpp]=Lekgen(theta,pe,pa,alpha,gamma,k)
K=k*sin(theta); q=k*cos(theta);
beta=sqrt(1-alpha^2-gamma^2);
qp=sqrt(pe*k^2-K^2);
d=pe*(pa*(pe+gamma^2*(pa-pe))*k^2-(pa-beta^2*(pa-pe))*K^2);
qm=(sqrt(d)-alpha*gamma*K*(pa-pe))/(pe+gamma^2*(pa-pe));
No=1/sqrt((-beta*qp)^2+(alpha*qp-gamma*K)^2+(beta*K)^2);
Ne=1/sqrt((alpha*qp^2-gamma*qm*K)^2+(beta*pe*k^2)^2+...
    (gamma*(pa*k^2-qm^2)-alpha*qm*K)^2);
Eo=No*[-beta*qp;alpha*qp-gamma*K;beta*K];
Ee=Ne*[alpha*qp^2-gamma*qm*K;beta*pe*k^2;gamma*(pe*k^2-qm^2)-alpha*qm*K];
A=(qp+q+K*tan(theta))*Eo(1)-K*Eo(3);
B=(qm+q+K*tan(theta))*Ee(1)-K*Ee(3);
D=(q+qm)*A*Ee(2)-(q+qp)*B*Eo(2);
qt=q+K*tan(theta);
rss=((q-qm)*A*Ee(2)-(q-qp)*B*Eo(2))/D;
rsp=2*k*(A*Ee(1)-B*Eo(1))/D;
rps=2*k*(qm-qp)*Eo(2)*Ee(2)/D;
rpp=(2*qt/D)*((q+qm)*Eo(1)*Ee(2)-(q+qp)*Ee(1)*Eo(2))-1;
```

Q.3.8 Ghvmax.m

Analyze the differences for the $\alpha = 0$ case of $S_{HV}^{\max}$ for different values of θ_i.

```
gamma=-1:.0001:1;
for i=1:4
    theta=i*pi/9;
```

```
    for j=1:length(gamma)
        Ghv(j)=(sin(theta)*gamma(j)*sqrt(1-gamma(j)^2)...
            *((1+4*gamma(j)^2)...
            *cos(theta)-sqrt(5+20*gamma(j)^2-(1+4*gamma(j)^2)*...
            (sin(theta))^2)))/((1-gamma(j)^2*(cos(theta))^2)*...
            (cos(theta)*(1+4*gamma(j)^2)+sqrt(5+20*gamma(j)^2-...
            (1+4*gamma(j)^2)*(sin(theta))^2)));
    end
    if i==1
        p(1)=plot(gamma,Ghv,'r');
    elseif i==2
        p(2)=plot(gamma,Ghv,'b');
    elseif i==3
        p(3)=plot(gamma,Ghv,'g');
    elseif i==4
        p(4)=plot(gamma,Ghv,'y');
    end

    hold on
end
xlabel('\gamma','FontSize',15)
ylabel('S_{HV}','FontSize',15)
title('\epsilon_\perp=1 and \epsilon_{||}=5','FontSize',18)
legend(p,'\theta=\pi/9','\theta=2\pi/9','\theta=3\pi/9','\theta=4\pi/9')
```